Particle suspensions in complex formulations

Anastasia Papadopoulou

A dissertation submitted in partial fulfilment

of the requirements for the degree of

Doctor of Philosophy

of

University College London

Department of Mechanical Engineering

University College London

September, 2020

''*Not everything that can be counted counts, and not everything that counts can be counted*''

Albert Einstein

Abstract

Particle suspensions are ubiquitous in nature and engineering/manufacturing applications. Suspensions exhibit complex rheological phenomena even in the simplest cases of monodisperse rigid spheres in Newtonian media. To complicate matters further, industrial formulations, toothpaste being a typical example, often involve particles that vary in size, surface morphology and porosity, suspended in non-Newtonian and viscoelastic solvent media. Such systems entail new particle and polymer dynamics which are poorly understood, introducing new challenges in manufacturing and product stability. Experimental evidence considering the combined effects of these parameters on suspension rheology is limited.

The present study attempts to address this gap by examining two types of non-colloidal, commercial silica particles, commonly used in toothpaste formulations and differing in surface area, roughness and porosity, suspended in various non-aqueous Newtonian and non-Newtonian solvents. Their suspension rheology was investigated under steady state and oscillatory shear at different volume fractions (φ) and compared to that of relatively smooth glass sphere suspensions with a similar size distribution, used as a control system and investigated under the same experimental and solution conditions.

Particle surface roughness and porosity increased suspension viscosity and induced non-Newtonian rheological phenomena at lower particle volume fractions in both the Newtonian and non-Newtonian suspending media. This was due to the increased particle specific surface area and effective volume fraction, as the solvent gets absorbed into the pores, leading to enhanced particle-particle or particle-solvent interactions.

Glycerol and mineral oil were first used as the suspending medium to probe two mechanisms for suspension shear thinning: a friction driven and an adhesion driven respectively. Suspensions in glycerol exhibited shear thinning at $\varphi \geq 0.25$ due to the elastic deformation of the surface asperities at increasing shear leading to a reduction in the friction coefficient. In contrast, suspensions in mineral oil showed pronounced shear thinning and elasticity at $\varphi \geq 0.02$ due to particle agglomeration; this was due to the agglomerates breaking down upon increasing the shear rate. The use of an optical shearing technique enabled the monitoring of particle deagglomeration in situ which was quantified using image analysis and aggregation metrics. Based on these findings, tuning of suspension shear thinning was demonstrated by inhibiting particle agglomeration through particle surface chemistry modification.

To explore the effects of solvent elasticity and shear thinning on suspension rheology and provide links with industrially relevant formulations, the same particles were studied in two non-Newtonian solvents: a viscoelastic Boger fluid and a shear thinning and weakly viscoelastic Xanthan gum solution. Elastic thickening was induced for certain suspensions in the Boger fluid. The shear thinning nature of the Xanthan gum solution seemed to suppress this phenomenon giving rise to strong shear thinning response, compared to the same suspensions in the corresponding Newtonian solvents, especially in the dilute concentration regime.

The effect of temperature on suspension rheology was also investigated by heating the suspensions to 60^{o}C, a typical temperature that solids are added in industrial manufacturing. Heating significantly decreased suspension viscosity and suppressed the shear thickening response. The suppression of the shear thickening response was either due to a decrease in the possibility of hydroclustering in the Newtonian solvents or the decrease in the flexibility of the polymer chains at elevated temperature, requiring higher stresses to show strain hardening. In contrast, suspension shear thinning was found to both increase and decrease with temperature.

The thesis offers new insights in tuning suspension rheology through the particle surface morphology and chemistry as well as the physical and chemical properties of the suspending media. Suspension rheology is complex and thus, understanding the mechanisms governing it, will aid manufacturers in addressing challenges during industrial processing and developing guidelines for the design and optimization of formulations tailored to specific applications.

This work forms part of an EPSRC funded research programme on addressing manufacturing challenges of Future Formulations and in particular, non-aqueous paste formulations. It also involves the collaboration with leading companies in the pharmaceutical and inkjet printing fields (GlaxoSmithKline, Xaar Plc).

Impact statement

Particles are ubiquitous in industry and nature and their suspension rheology has been the focus of research for decades. Particle suspensions exhibit a wide range of rheological phenomena, including shear thinning, shear thickening and yield stress. Despite the huge amount of research conducted on investigating the specific mechanisms that govern the complex rheology of particle suspensions, it still remains unclear how exactly particle surface morphology and surface functional groups as well as the physical properties of the solvent-carrier medium influence particle interactions and thus, rheology.

The present study investigated the combined effects of particle surface irregularity and porosity in non-aqueous solvents on suspension rheology and elucidated two mechanisms for the shear thinning response, i.e. a friction driven and an adhesion driven mechanism. The effect of viscoelasticity and shear thinning nature of the suspending medium were also investigated in an attempt to resemble real industrially employed formulations. Three scientific articles have been published in peer-reviewed journals extending the scientific literature to more complex systems and providing a deeper understanding of suspension shear thinning rheology. A bespoke rheo-optics set up was developed to resolve suspension microstructure which will also aid future research activities on particle suspensions and biological fluids microstructure *in situ*.

The project involved the participation in international conferences and activities for public engagement, sharing the research findings with the scientific community as well as with general audiences to promote STEM and collaborations with industrial and academic partners.

This work was conducted in close collaborations with industrial partners in the oral healthcare sector (GSK) and inject printing (Xaar Plc.). Linking academic research with such widely used everyday products as toothpastes and inks will aid manufacturers in resolving challenges during industrial processing of complex fluids and develop more energy and cost efficient manufacturing procedures.

The thesis opens new insights for tuning and optimizing suspension rheology through the particle surface morphology and chemistry as well as the physical and chemical properties of the suspending media leading to the engineering of formulations tailored to specific applications. Lastly, the research herein provides extended data sets that can be utilized for the development or optimization of computational tools predicting the rheology of complex particulate formulations both in academia and industry.

Acknowledgements

Completing this PhD has been a long and life-changing journey full of experiences both educational and personal. I am thankful to a number of people without whom the completion of my work would have been very difficult. First and foremost, I am grateful to my supervisors Professor Stavroula Balabani and Professor Manish K. Tiwari for giving me the opportunity to undertake this challenging project and also learn to live independently in such a big city as London. Special thanks go to Prof. Balabani whose guidance, advice, encouragement and support throughout all stages of my research and writing of the thesis were substantial to successfully complete this work.

I would also like to take this opportunity to give my thanks and appreciation to the Department of Mechanical Engineering at UCL for providing financial support for my studies as part of the EPSRC project-Complex ORAL health products (CORAL): Characterisation, modelling and manufacturing challenges (EP/N024915/1) and also, our industrial partners, GSK and Xaar Plc for their support and fruitful input to the project. I would like to particularly thank Dr. Bob Sochon, Mr. Mark Jackson, Dr. Andrew Johnson and Dr. Sophie Darragh in GSK who have been helpful for endlessly providing me with the raw materials and made me feel very welcome when I have been visiting their site in Weybridge. Further thanks to Prof Mackley and his team in Cambridge University for initial experiments on extensional rheology and Dr. Maëlle Douaire and Mr. John Tatum from Xaar Plc. who were happy to open their facilities and discuss some of the challenges of my project.

Heartfelt thanks go to all my colleagues and friends in the FluME, Nanoengineered Systems Lab and CORAL groups for their support, guidance, discussions and most of all, their friendship. Special thanks go to Andreas, Rallia, Nikos B., Nikos K., Antonis and Yao for being such wonderful lab/office mates and friends accompanying me on many lunch and coffee breaks. I would like to express my deep appreciation to Dr. Jurriaan J.J. Gillissen for the stimulating discussions and for generously sharing his expertise and knowledge with me. I gratefully acknowledge Dr. Vikramjeet Sigh, Dr. Bagchi, Biswajoy and Mr. Norbert Janowicz for helping me with the chemistry stuff as well as Dr. Neil Cagney and Dr. Tom Lacassagne for teaching me MATLAB.

Last but by no means least, I would like to express my sincere gratitude to all my best friends and family members in Greece, my parents, my beloved brother and grandparents for their endless support, encouragement and love over the last four years and throughout my life. I am especially thankful to my wonderful mother, Argiro, my amazing father, Christos and my brother, Paul, for always being behind me, supporting me in my decisions and making me laugh with their jokes during the difficult times of this journey.

Scientific dissemination

Articles

A. Papadopoulou, J.J.J. Gillissen, H.J. Wilson, M.K. Tiwari, S. Balabani, 'On the shear thinning of non-Brownian suspensions: Friction or Adhesion', 2020. *Journal of non-Newtonian Fluid Mechanics*, 281, p. 104298. (invited)

A. Papadopoulou, J.J.J. Gillissen, H.J Wilson, M.K. Tiwari, S. Balabani, 2020. 'Effect of particle specific surface area on the rheology of non-Brownian silica suspensions.', *Materials,* 13, p.4628. (invited)

J.J.J. Gillissen, A. Papadopoulou, M.K. Tiwari, S. Balabani, H. J. Wilson, 'Suspension rheology of adhesive particles at high shear rates', 2020. *Phys. Rev. Fluids* 5, 053302.

J.J.J. Gillissen, N. Cagney, T. Lacassagne, A. Papadopoulou, S. Balabani, H.J. Wilson, 'Taylor couette instability in disk suspensions: experimental observation and theory'. *Physical Review Fluids* 5, p. 053302

Y. Lu, J.J.J. Gillissen, A. Papadopoulou, G. He, M.K. Tiwari, 'Measurement and modelling of rigid particle-surface adhesion in viscous liquids'. *Submitted to Langmuir* (under revision)

S. Aabith, R. Caulfield, A. Papadopoulou, S. Homer-Vanniasinkam, M.K. Tiwari, '3D direct-write printing of water-soluble micromoulds for rapid prototyping'. *Submitted to Additive Manufacturing* (under revision)

International Conferences

A. Papadopoulou, M.K. Tiwari, S. Balabani. 'Rheology and Microstructure of Silica Particle Suspensions in Non-aqueous Media', *9th Hellenic Society of Rheology Meeting*, Samos, Greece, 23-27 June 2019 (Oral)

A. Papadopoulou, M.K. Tiwari, S. Balabani. 'Particles in Complex Formulations: Rheology, Dynamics & Microstructure', *Annual European Rheology Conference*, Sorrento, Italy, 17-20 April 2018 (Oral)

Industrial meetings

A. Papadopoulou, M.K. Tiwari, S. Balabani. 'Particles in Complex Formulations: Rheology, Dynamics & Microstructure', *GSK PhD Annual Symposium 2018*, Weybridge, UK, 13-14 June 2018 (Poster)

A. Papadopoulou, M.K. Tiwari, S. Balabani. 'Particles in Complex Formulations: Rheology, Dynamics & Microstructure', *GSK PhD Annual Symposium 2017*, Weybridge, UK, 11-12 October 2017 (Oral)

UK meetings

A. Papadopoulou, M.K. Tiwari, S. Balabani. 'Shear Rheology and Microstructure of Particle Suspensions in Complex Oral Formulations', *British Society of Rheology Midwinter Meeting*, Edinburgh, Scotland, 17-18 December 2018 (Oral)

A. Papadopoulou, M.K. Tiwari, S. Balabani. 'Rheological Characterization of Rough Particles in Complex Formulations', *ChemEngDay UK,* Leeds, UK, 27-28 March 2018 (Poster)

A. Papadopoulou, M.K. Tiwari, S. Balabani. 'Rheological Characterization of Rough Particles in Complex Formulations', *Annual meeting of the British Society of Rheology*, Cambridge, UK, 15 March 2018 (Poster)

A. Papadopoulou, M.K. Tiwari, S. Balabani. 'Understanding the Flow Properties of Particles in Complex Formulations', *Clever Characterization for Smarter Formulations*, London, UK, 10 November 2017 (Poster)

UCL internal meetings

A. Papadopoulou, M.K. Tiwari, S. Balabani. 'Rheology of Particle Suspensions for Oral Healthcare', *UCL Institute of Healthcare Engineering – Autumn Research Symposium*, London, UK, 1 October 2018 (Poster)

A. Papadopoulou, M.K. Tiwari, S. Balabani. 'Rheological Characterization of Rough Particles in Complex Formulations', *2nd Meeting of the UCL Cross-Disciplinary Network on Soft Materials*, London, 11 June 2018 (Poster)

A. Papadopoulou, M.K. Tiwari, S. Balabani. 'Particles in Complex Formulations: Rheology, Dynamics and Microstructure', *1st Meeting of the UCL Cross-Disciplinary Network on Soft Materials*, London, 19 June 2017 (Poster)

A. Papadopoulou, M.K. Tiwari, S. Balabani. 'Particles in Complex Formulations: Rheology, Dynamics and Microstructure', *UCL Mechanical Engineering - PhD Conference 2017*, London, 9 June 2017 (Poster)

A. Papadopoulou, M.K. Tiwari, S. Balabani. 'Rheological Characterization of Rough Particles in Complex Formulations', *UCL Mechanical Engineering - PhD Conference 2018*, London, 7 June 2018 (Oral)

Outreach events

International Women in Engineering Day, UCL, 22 June 2018 (outreach event)

Public engagement film 'Linking an everyday product - toothpastes - with research in engineering', UCL Mechanical Engineering, London, 2 August 2017
https://www.youtube.com/watch?list=PLXXq6t7B9L_7ItyGo7kzG224AA3QOnpIN&time_continue=6&v=qRolFxZAw0w

Awards

IChemE **Competition winner**:
'How your research is making a difference to the world'
ChemEngDay UK, Leeds, UK, 27-28 March 2018

Table of Contents

List of figures

List of tables

Nomenclature

English symbols

A	aggregation index	–
B	intrinsic viscosity	–
b	fitting parameter to account for particle surface roughness	–
C	fitting parameter to account for polydispersity	–
D	particle diameter	μm
E	Young modulus	Pa
F_A	adhesion force	μN
f	frequency	Hz
g	gravitational acceleration	m^2/s
G	shear modulus	Pa
G'	storage modulus	Pa
G''	loss modulus	Pa
G^*	complex modulus	Pa
G'_M	dynamic minimum strain elastic modulus	Pa
G'_L	dynamic large strain elastic modulus	Pa
h	parallel plate gap	μm
h_r	particle surface roughness	μm
$I_{3/1}$	relative intensity of the 3rd harmonic under LAOS	–
k_B	Boltzmann constant, $1.38 \cdot 10^{-23}$	J/K
k	consistency index	–
L_c	critical load for shear thinning	N
M	torque	$N.m$
M_w	polymer molecular weight	g/mol
n	flow index	–
R	geometry radius	mm
$\bar{\bar{p}}$	particle aspect ratio	–
S	stiffening ratio	–

S_p	particle specific surface area	m^2/g
S_s	particle sphericity	–
T	thickening ratio	–
t	time	s
t_e	elastic relaxation time	s
t_v	viscous relaxation time	s
V_0	plate velocity	m/s
Y_o	Yield strength	Pa

Latin Symbols

a	particle radius	μm
Γ	2nd order fitting parameter in Batchelor equation	–
γ	strain amplitude	–
γ_0	input strain amplitude	–
$\dot{\gamma}$	shear rate	s^{-1}
$\dot{\gamma}_0$	input shear rate	s^{-1}
$\dot{\gamma}_R$	shear rate at the rim of geometry (max radius)	s^{-1}
δ	phase angle	°
ε	porosity	–
η	shear viscosity	$Pa.s$
η_0	zero shear rate viscosity	$Pa.s$
η_∞	infinite shear rate viscosity	$Pa.s$
η_r	relative viscosity	–
$\eta_{r,e}$	extent of shear thinning	–
$\eta_{r,t}$	extent of shear thickening	–
η_f	suspending medium viscosity	$Pa.s$
η'_L	dynamic large strain rate viscosity	$Pa.s$
η'_M	dynamic minimum strain rate viscosity	$Pa.s$
θ	temperature	°C
λ	viscous relaxation time	s

ν	Poisson ratio	–
ρ_f	suspending medium density	g/ml
ρ_p	particle density	g/ml
τ	shear stress	Pa
τ_0	input shear stress	Pa
τ_c	critical stress for shear thinning	Pa
τ_{true}	corrected/true shear stress	Pa
τ_y	yield stress	Pa
φ	particle volume fraction	–
φ_m	maximum packing fraction	–
φ_{m1}	maximum packing fraction related to surface morphology	–
ω	angular frequency	rad/sec
ω_v	angular velocity	rad/sec

Abbreviations

LAOS	Large Amplitude Oscillatory Shear
LVR	Linear Viscoelastic Region
PDMS	Poly-Di-Methyl-Siloxane
PMMA	Poly-Methyl-Meth-Acrylate
PS	Poly-Styrene
PVC	Poly-Vinyl Chloride
SAOS	Small Amplitude Oscillatory Shear

Chapter 1

Introduction

1.1 Background

Particle suspensions are ubiquitous in industry and nature. From everyday products, such as paints, detergents and toothpastes to biological fluids, such as blood, fluids comprise particles suspended in various media. Environmental applications, processing of slurries, mixing of solids in fluids, the effectiveness of a paint or coating and the packaging at the end of the production line are only a few examples, where rheology plays a significant role in ensuring the efficiency of the applied manufacturing process and defining the quality of the end mixture/formulation.

Rheology comes from the Greek work '*rheo*' and it simply describes the science of flow and deformation of matter. It was firstly introduced by Professor Eugene C. Bingham at Lafayette College in Indiana (Barnes, 1989; Iordan, 2009) and since then it has gone through major technological advances. Figure 1.1 depicts the simplest case of steady state shear flow experiments. The sample is placed between two parallel plates where the top one moves with a velocity, V_0, while the bottom plate is stationary. The rate of displacement between the upper and the bottom plane is described by x. According to Newton, 'the resistance which arises from the lack of slip among the parts of the liquid, is proportional to the velocity with which the parts of the liquid are separated from one another'. The resistance to flow is expressed through the 'viscosity', mostly denoted with the Greek letter η, and it is a synonym of the 'internal friction' or else the 'absence of slipperiness'. The current SI unit for viscosity is Pascal-second (Pa.s). In this type of flow where the fluid is set in motion by the action of the plate, the force per unit area required to initiate the motion is F/A and is proportional to the velocity gradient or shear rate: V_0/y.

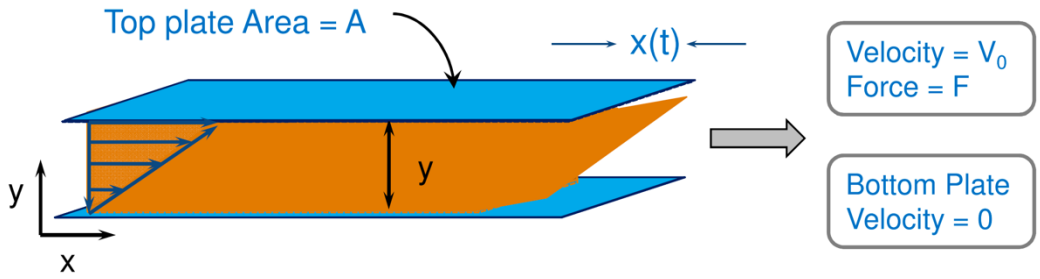

Figure 1.1: Representation of the velocity profile in a steady state shear experiment (adopted from (TA Instruments, 2014)).

1.2 Motivation

One typical application, where rheology is important during both manufacturing and usage, is toothpaste. Due to their significance in oral healthcare, toothpastes hold the highest share in the oral care industry and constitute one of the highest income sources in the global industry market, reaching an annual revenue of 26 billion dollars in 2018 globally (Businesswire, 2019). Therefore, over the last years many efforts have been devoted onto improving toothpaste quality, effectiveness and functionality (Stamm, 2007) in order to satisfy consumers' needs and meet the market demand. Understanding the rheology of its individual components comprise a significant step in toothpaste formulation optimisation and thus, it served as a motivation for this work. Toothpastes generally comprise dense suspensions of solid particles with irregular shapes, acting as abrasives and fillers, flavours and therapeutic substances suspended in polymeric water based or mostly nowadays water free fluids; this is illustrated in the microscopic image shown in Figure 1.2a. This complex composition is what classifies toothpastes as non-Newtonian (shear thinning) yield-stress pastes with time-dependent rheological properties (Ardakani, 2014; Coussot, 2014; Liu et al., 2015). They exhibit yield stress and shear thinning rheology, i.e. they behave like elastic solids under no or small stress, while they flow like liquids when subjected to large stresses; for example, when squeezed out from the tube (Liu et al., 2015). However, a strong force to overcome the yield stress needs be applied for the paste to flow out of the tube (Ardakani, 2014). Indicative examples of the rheological behaviour of three different commercial toothpaste formulations are depicted in Figure 1.2b. All samples show thixotropic response and yield stress under steady state. Among the various parameters influencing the rheological behaviour of the toothpaste composites under steady state, e.g. viscosity, yield stress, storage and loss modulus,

the thickness of the polymeric network and the particle size were reported to cause the most pronounced effects (Liu et al., 2015).

The flow curves presented in Figure 1.2b highlight that toothpastes are complex multiphase systems, whose rheology is closely dependent on the interactions of the different ingredients, mainly between the particles and a polymeric matrix. Using modern toothpastes as an exemplar complex particle suspension system, this study aims to obtain a deeper understanding on the interactions between particles, with varying surface morphology and porosity, such as those encountered in industry, suspended in non-aqueous media and their effect on suspension rheology. This will ultimately offer new insights into the design and optimisation of complex formulations, with rheological properties tailored to specific applications.

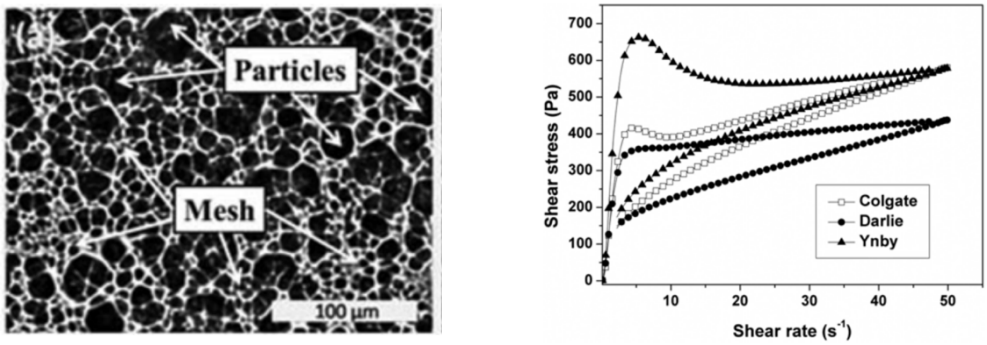

(a) (b)

Figure 1.2: a) Microscopic image of an indicative toothpaste example; b) shear stress versus shear rate response of three difference commercial toothpastes (adopted from (Liu et al., 2015)).

1.3 Basic fluid rheology

Fluids comprise an endless list of materials, either liquids or gases, and are an integral part of everyday life. According to their response under steady state shearing conditions, fluids can be divided into two main categories: Newtonian and non-Newtonian. The rheological response of the fluids under oscillatory shear is described through their viscoelasticity.

1.3.1 Steady state shear rheology

Figure 1.3 summarises the shear stress response of typical fluids as a function of shear rate (Figure 1.3a) and time (Figure 1.3b). The viscosity of a Newtonian fluid is independent of time and shear rate and thus, its shear stress increases linearly with

shear rate (Barnes, 2000; Chhabra and Richardson, 2008; Macosko, 1994), as depicted in Figure 1.3a. Any behaviour that deviates from this linearity is referred to as non-Newtonian. On the other hand, the viscosity of a Newtonian fluid depends on temperature and pressure. More specifically, the viscosity of a fluid decreases with increasing the temperature due to the increasing Brownian motion of its molecules, while it increases almost linearly when the pressure is increased (Barnes, 2000).

The viscosity of the non-Newtonian fluids is both time and shear rate dependent. Time-dependent fluids can be further categorized as thixotropic, where the viscosity decreases with time and rheopectic, when the viscosity increases with time; these phenomena are depicted in Figure 1.3b. Experiments to detect thixotropy or rheopexy and obtain the hysteretic loops shown in Figure 1.3b involve either the application of successive increasing and decreasing shear rate steps over a couple of decades (Chhabra and Richardson, 2008) or creep tests. In the latter a constant shear stress is applied for some time and the recovery of the samples rheological behaviour is monitored after ceasing the applied deformation.

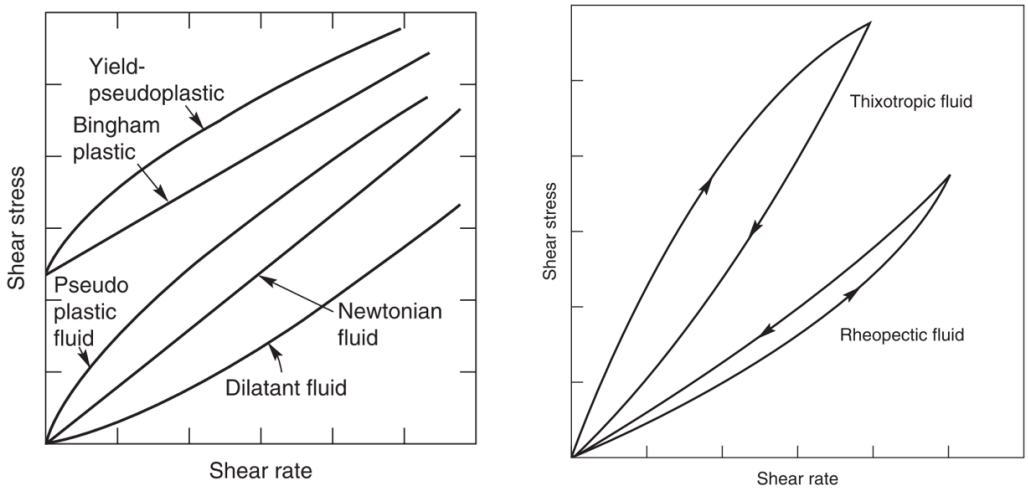

Figure 1.3: Rheological behaviour of common fluids expressed as the shear stress as a function of shear rate; a) time independent rheological behaviour (shear thinning/shear thickening, yield stress); b) time dependent rheology (thixotropy, rheopexy) (adopted from (Chhabra and Richardson, 2008)).

In terms of shear rate dependency, fluids can be further divided into shear thinning, when the viscosity decreases with increasing the shear rate, and shear thickening if the viscosity values increase with shear rate. Typical examples of shear thinning fluids include toothpastes, paints, inks, whipped cream and even blood, while the most common shear thickening example is the cornstarch in water mixture.

Various mathematical models have been proposed in the literature to describe the rheology of both Newtonian and non-Newtonian fluids. The most commonly used equations are summarised in Table 1.1. The Newtonian fluids can often exhibit yield stress as well, which is denoted as τ_y and represents the minimum stress that needs to be overcome for a fluid to flow. Determining an accurate value of the material's yield stress has often proven difficult as this property highly depends on the experimental technique used; these vary from direct stress ramps, where the applied shear stress is increased linearly with time until the viscosity curve exhibits a peak value to yield stress estimation by model fitting and extrapolation of the acquired data to the zero shear rate regime (Malvern Instruments, 2012).

The empirical equations describing the behaviour of the non-Newtonian fluids are more complex and require additional parameters to be identified in order to fully capture the non-Newtonian behaviour. The flow index, n, is the most common parameter defining whether a fluid is shear thinning ($n < 1$) or shear thickening ($n > 1$). In the Newtonian case $n = 1$.

Table 1.1: Summary of the most commonly used Newtonian and non-Newtonian fluid models to describe the shear stress (τ)/viscosity (η) dependence on the shear rate ($\dot{\gamma}$) (Barnes, 2000; Rao, 2014).

Fluid model name	τ or $\eta = f(\dot{\gamma})$
Newtonian	
without yield stress	$\tau = \eta\dot{\gamma}$
with yield stress (Bingham)	$\tau = \tau_y + \eta\dot{\gamma}$
non-Newtonian	
Power law	$\tau = k\dot{\gamma}^n$
Herschel-Bulkley	$\tau = \tau_y + k\dot{\gamma}^n$
Casson	$\sqrt{\tau} = \sqrt{\tau_y} + \sqrt{\eta\dot{\gamma}}$
Carreau-Yasuda	$\eta = \eta_\infty + (\eta_0 - \eta_\infty)\left[1 + (\lambda\dot{\gamma})^\beta\right]^{\frac{n-1}{\beta}}$ (Carreau model was obtained with $\beta = 2$)
Cross	$\eta = \eta_\infty + (\eta_0 - \eta_\infty)\frac{1}{1+k\dot{\gamma}^n}$

* explanation of symbols: τ is the shear stress, η is the steady state viscosity, $\dot{\gamma}$ is the shear rate, τ_y is the yield stress, k is the consistency index, n is the flow index, η_0 is the zero shear rate viscosity, η_∞ is the infinite shear rate viscosity, λ is the relaxation time and β is the transition index or the index that controls the transition from the Newtonian to the power law behaviour.

1.3.2 Viscoelasticity

Viscoelastic materials behave both as ideal solids (Hooke's law) and ideal liquids (Newton's law) according to the deformation that is applied on them (TA Instruments, 2014). The different parameters required to characterize this type of fluids are mainly the storage (elastic) modulus, G', the loss (viscous) modulus, G'', the phase angle, δ, and its tangent, $\tan(\delta)$. In particular, G' represents the amount of energy the material can store, whereas the G'' is a measure of the energy the material dissipates as heat upon the application of deformation. Both moduli are expressed in Pascals (Pa) and their measure is called complex modulus, G^*. The phase angle corresponds to the phase difference between the applied stress/strain and the measured response and is indicative of the viscoelastic nature of the material. For example, when $\delta = 0^o$ the material is purely elastic ($G' > G''$). If $\delta = 90^o$, the material is purely viscous ($G' < G''$), while for viscoelastic materials δ takes values between 0^o and 90^o. $\tan(\delta)$ is also defined as the ratio of G'' to G' (Barnes, 2000; Macosko, 1994; TA Instruments, 2014). In order to determine the viscoelasticity of a material, the above properties are measured under oscillatory shear; i.e. the applications of a sinusoidal signal, as a function of strain, frequency, time and temperature, using the equations summarised in Table 1.2.

Table 1.2: Summary of the basic equations to describe viscoelastic fluids.

Viscoelastic parameters
$\gamma = \gamma_0 \cos(\omega t + \delta)$
$\tau = \tau_0 cos(\omega t + \delta)$
$G' = (\tau_0/\gamma_0)\cos(\delta)$
$G'' = (\tau_0/\gamma_0) sin(\delta)$
$G^* = \sqrt{(G')^2 + (G'')^2}$
$\tan(\delta) = G''/G'$

The range of strain amplitudes (γ) where the material does not go through any microstructural rearrangements but stays close to equilibrium defines the Linear Viscoelastic Region (LVR). Within the LVR both moduli, G' and G'', remain independent of the applied strain and this region is typically defined through conducting small amplitude oscillatory shear measurements (SAOS). Viscoelastic materials exhibit time and frequency dependent rheological properties. Oscillatory frequency sweeps are usually performed in the LVR so that only the time dependent

properties can be probed. The most typical rheological responses under oscillatory shear are three and presented in Figure 1.4.

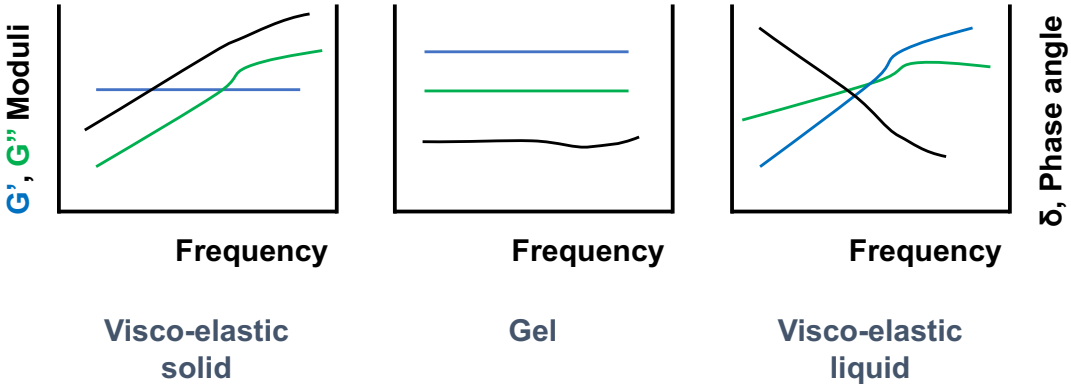

Figure 1.4: Representative examples of the frequency dependence of viscoelastic materials. The storage, G', and loss, G'', moduli as well as the corresponding phase angles, δ, are presented as a function of frequency. The figure reproduced from (Malvern Instruments, 2012).

Industrial applications often involve large and rapid material deformations. Under these conditions, microstructure changes can occur that drive the response of the material outside the linearity due to the contribution of higher odd harmonics of the input frequency. The materials lose their ability to restore their equilibrium state within the short measurement time leading to permanent changes in microstructure, e.g. changes in the microscale structure of particles or particle-polymer networks and agglomerates break down. Therefore, probing the non-linear properties of various fluids is of high importance to industrial manufacturing. Large Amplitude Oscillatory Shear (LAOS) experiments have been widely conducted in recent years to explore that range of high deformation rates.

Figure 1.5 summarises the four different responses reported in the literature during LAOS experiments. Type I response under LAOS (Figure 1.5a) is observed when both G' and G'' moduli exhibit strain thinning, while in Type II response (Figure 1.5b) both moduli show strain thickening outside the LVR. Type III response (Figure 1.5c) under LAOS shows more complex phenomena with G' exhibiting only strain thinning and G'' showing strain overshoot and a peak value. In Type IV response (Figure 1.5d) under LAOS, G' and G'' show strain overshoot followed by strain thinning at increasing strain amplitudes (Hyun et al., 2011). However, the G' and G'' taken directly from the rheometer lose their physical meaning and further analysis of each single stress waveform is required in order to obtain more meaningful parameters that correspond to the material's microstructural representations; these are described

through the elastic and viscous Lissajous-Bowditch plots respectively. The Lissajous-Bowditch plots appear elliptical within the LVR while they take irregular shapes outside the LVR (Ewoldt et al., 2008; Hyun et al., 2011). A more detailed description of the raw stress waveform analysis and the information derived from it, is given in Chapter 2.

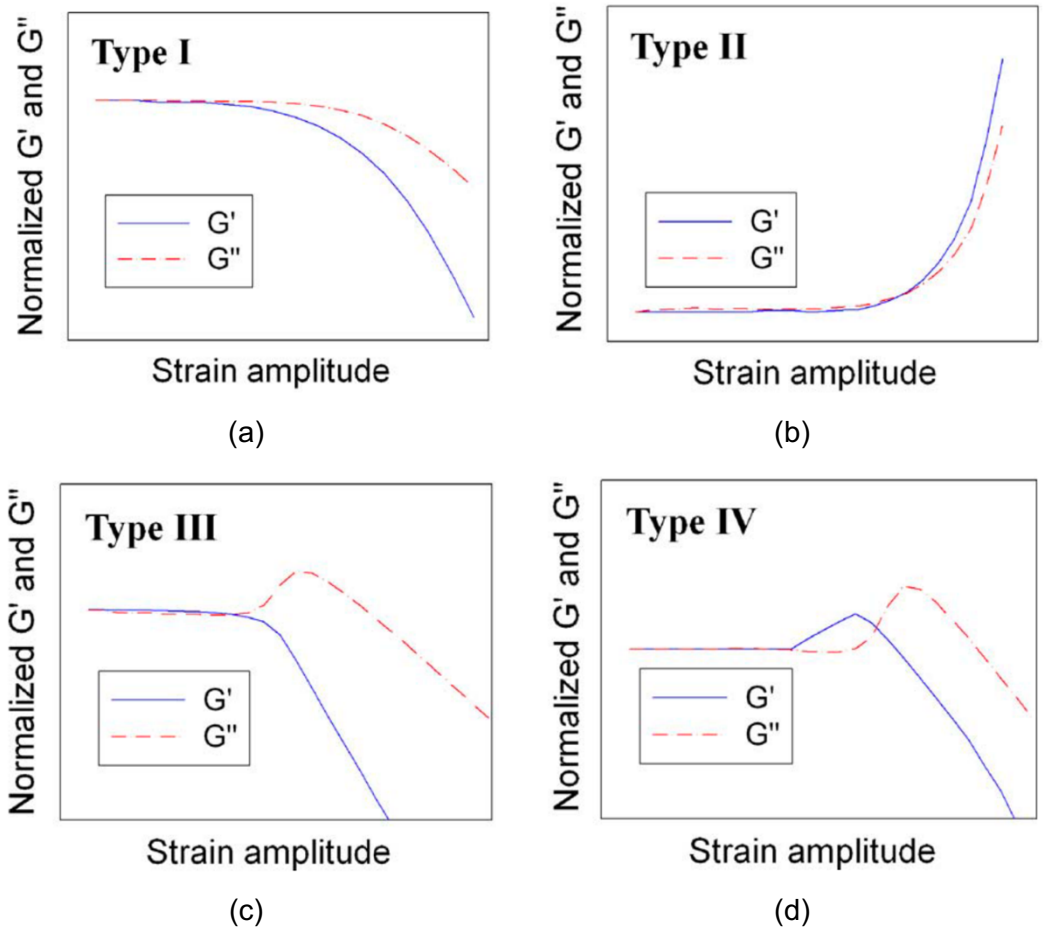

Figure 1.5: Typical responses under LAOS; Type I shows strain thinning of both moduli, Type II shows strain hardening of both moduli, in Type III only the G'' exhibits weak strain overshoot, Type IV consists of strong strain overshoot of both moduli (adopted from (Hyun et al., 2011)).

1.4 Particle suspension rheology

Particle suspension rheology is of significant importance in numerous industrial and natural applications and has been the focus of extensive research, as it can pose challenges during material handling, manufacturing processes as well as product quality and stability. Many modern consumer goods, including food (e.g. ice cream, whipped creams), healthcare and cosmetics products (e.g. body creams, exfoliating gels), biological fluids (e.g. blood) as well as building materials (e.g. gypsum plaster, concrete pastes with gas inclusions) consist of multiphase suspensions of solid particles and/or gas bubbles in different liquids. Natural hazards, such as lava flows, can also be associated with fluid flow properties and thus, managing them requires a very good knowledge on the likely rheological behaviour of these fluids. This section is divided in two main categories: suspensions in Newtonian and non-Newtonian suspending media. The emphasis of this review will be on non-colloidal particle suspensions. In industrial formulations, particles are often highly polydisperse with size spanning from the colloidal to the non-colloidal regime. Thus, references to colloidal systems will also be included to probe how their behaviour differs from the non-colloidal ones and also cover the rheological properties of suspensions with high degrees of polydispersity.

1.4.1 Suspensions in Newtonian media

Particle suspensions are complex multiphase systems and can exhibit a wide range of non-linear rheological phenomena, such as shear thinning, shear thickening and yield stress, even in the simplest case of spheres suspended in Newtonian solvents. The complex rheological response and the relevant microstructure changes responsible for such phenomena are being described in Figure 1.6. Experimental evidence suggests that several factors influence suspension rheology, such as particle volume fraction, surface morphology, shape, size and size distribution as well as the physical and chemical of the suspending medium (e.g. viscosity and its relevance with the applied deformation rate, the presence of reactive groups) or the applied experimental conditions (Chen et al., 2010; Genovese, 2012; Mueller et al., 2010; Stickel and Powell, 2005).

At low particle volume fractions, hard-sphere suspensions generally exhibit Newtonian behaviour, i.e. their viscosity remains independent of shear. Increasing the particle volume fraction, $\varphi \geq 0.40$, promotes the onset of non-Newtonian phenomena,

which can evolve in three stages. Firstly, a zero shear plateau or yield stress behaviour is observed followed by shear thinning (i.e. decrease of the viscosity values with the shear rate) which reaches a limiting high shear plateau; this is a typical Carreau fluid. Suspension shear thinning has been attributed to particle ordering and alignment to the direction of the applied flow field, particle agglomeration or frictional contacts between them.

At sufficiently high particle volume fractions ($\varphi \geq 0.50$) and shear rates, shear thickening, i.e. the increase of the viscosity values with the shear rate, can also occur. In that regime, further increase of the shear rate disrupts particle ordering leading to hydrocluster formation. Frictional contacts between particles under large shear rate conditions have also been reported in the literature as being responsible for the onset of shear thickening (Cwalina and Wagner, 2016; Hermes et al., 2016; Lee et al., 2020; Lin et al., 2016; Mari et al., 2015a).

These non-Newtonian phenomena observed in suspension rheology, i.e. shear thinning and shear thickening, will be discussed in more detail in sections 1.4.1.5 and 1.4.1.6 respectively.

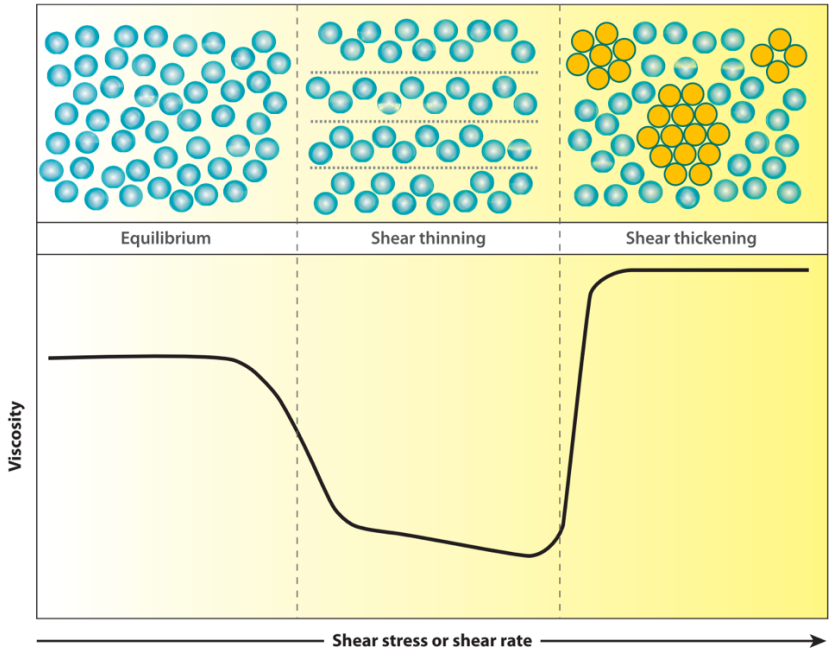

Figure 1.6: Representation of the typical rheology of a particle suspension under steady state shear and the relevant microstructure transitions at increasing the deformation rate (e.g. shear stress or shear rate) (adopted from (Chen et al., 2010)).

1.4.1.1 Effect of particle volume fraction

In general, the presence of solid particles increases the viscosity of a Newtonian solvent as their presence imposes additional stresses and higher resistance of the fluid to the applied flow field. Three main concentration regimes have been established in the literature (Mueller et al., 2010): 1) A dilute regime including volume fractions up to 0.05 where relative viscosity remains approximately constant showing Newtonian behaviour; 2) A semi-dilute regime with $\varphi \leq 0.25$ where although the relative viscosity shows a higher dependence on particle concentration, the rheology in most of the cases is still Newtonian; 3) A dense regime, starting at $\varphi = 0.25$, where the relative viscosity increases rapidly leading to non-Newtonian behaviour. Interparticle distance or the possibility of particle contacts constitute other measures to define if a suspension is in the dilute or dense concentration range. For example, a suspension is considered dense when (i) the average particle-particle distance is smaller or equal to the particle size and (ii) multi-body interactions or two-body lubrication extensively influence the rheology of the suspension (Mueller et al., 2010; Stickel and Powell, 2005).

Various empirical and theoretical models have been proposed in the literature to describe the relation between the suspension relative viscosity (η_r) and particle volume fraction (φ); the most commonly used are summarised in Table 1.3 and have been mainly developed based on the rheology of suspensions of nearly monodisperse spherical particles suspended in Newtonian media. Einstein was the first to introduce an analytical model to show the linear relationship between η_r and φ for suspensions in the dilute regime. The parameter B is a material's property representing its intrinsic viscosity and, in the Einstein equation, takes the value of 2.5. However, variations in particle size as well as deformability have been found to affect the value of B and thus, researchers have identified a wide range of values for the intrinsic viscosity varying from 1.5 to 5 (Genovese, 2012; Jeffrey and Acrivos, 1976; Mueller et al., 2010; Rutgers, 1962).

Following Einstein, other researchers derived more complex equations to include higher particle volume fractions. Krieger and Dougherty (1959) reported that a power law relationship exists between suspension viscosity and particle volume fraction for suspensions of spheres in the semi-dilute regime. The variable φ_m in their equation corresponds to the maximum packing of the suspensions; its value has been found to vary widely from 0.50 to 0.74 with $\varphi_m = 0.64$ being the equivalent to a random close packing state (Denn and Morris, 2014; Pavlik, 2009; Stickel and Powell, 2005). Batchelor and Green (1972) extended Einstein's theory by adding a quadratic term of

the φ dependence. The parameter B was assumed again 2.5, while the parameter Γ was found to vary from 5.2 in the case of simple rigid spheres to 7.6 for non-Brownian particles in simple shearing flow (Batchelor and Green, 1972; Stickel and Powell, 2005). Lastly, Quemada simplified Krieger-Dougherty equation by assuming that the factor $B\varphi_m$ is equal to 2 for monodisperse and spherical particles.

Table 1.3: Summary of the most commonly empirical models used to describe the relation between the suspensions relative viscosity (η_r) with the particle volume fraction (φ) (Batchelor and Green, 1972; Genovese, 2012; Irvin M. Krieger and Dougherty, 1959; Quemada, 1978; Stickel and Powell, 2005).

Models of η_r	$\eta_r = f(\varphi)$
Einstein	$\eta_r = 1 + B\varphi$
Batchelor & Green	$\eta_r = 1 + B\varphi + \Gamma\varphi^2$
Krieger-Dougherty	$\eta_r = \left(1 - \frac{\varphi}{\varphi_m}\right)^{-B\varphi_m}$
Quemada	$\eta_r = \left(1 - \frac{\varphi}{\varphi_m}\right)^{-2}$

The equations summarised in Table 1.3 have been mainly derived from suspensions of monodisperse spheres in Newtonian solvents. However, in real systems particles are far from these ideal conditions while the maximum packing volume fraction can significantly differ from the theoretical value, φ_m. Therefore, in these cases φ_m is replaced by an effective maximum packing fraction, $\varphi_{m,eff}$, for describing particles other than hard spheres (Genovese, 2012). Different factors such as particle shape, surface morphology and size distribution can also influence the relative viscosity of the suspension; despite extensive research on suspension rheology, current theoretical models fail to describe the behaviour of more complex systems than sphere suspensions.

1.4.1.2 Effect of particle shape

Non-spherical particles are encountered in a number of applications and thus, the rheological properties of their suspensions merit investigation. Suspensions of non–spherical particles, such as rods, oblate and prolate spheroids, fibers and discs, have been widely studied in the literature and their rheology is well understood. However, all the aforementioned types of particles have at least one axis of rotational symmetry and they are normally defined by their aspect ratio ($\bar{p}$), which corresponds to the ratio

of the length of the particle at the axis of rotational symmetry to the maximum length of the particle at the axis orthogonal to the flow.

Kitano et al. (1981) studied the effect of the shape and volume fraction of different inorganic fillers, including glass fibers, carbon fibers, talc, precipitated and natural calcium carbonate powder, at varying concentrations, on the rheology of a polymer melt (polyethylene) and proposed an empirical model to describe the relation between suspension relative viscosity, particle volume fraction and particle aspect ratio; the model is given by:

$$\eta_r = \left(1 - \frac{\varphi}{0.54 - 0.0125\bar{\bar{p}}}\right)^{-2} \quad (1.1)$$

η_r is the relative viscosity of the suspensions, φ is the particle volume fraction and $\bar{\bar{p}}$ represents the average particle aspect ratio (Kitano et al., 1981).

In a more recent study, Niu et al (2015) investigated the effect of particle shape on the microstructure and rheology of carbon-based particle suspensions. Four different types of particles were used with different aspect ratios (spherical–like carbon black, rod–like multi-wall carbon nanotube, sheet–like graphene and hollow carbon spheres) suspended in polydimethylsiloxane (PDMS). The PDMS used in this study had a constant viscosity and almost zero normal stress differences in the range of shear rates applied. Rheological measurements were complemented with optical techniques to provide a link between the rheological behaviour and changes in the microstructure of the suspensions. The study showed shear thinning (i.e. a decrease of the viscosity values with increasing the shear rate) for the carbon black, multi-wall carbon nanotubes and graphene suspensions. This behaviour was mainly attributed to the vorticity alignment of the particles to the direction of the flow. On the contrary, no significant microstructure changes were observed in the case of the hollow carbon spheres leading to less pronounced non-Newtonian rheology (Niu et al., 2015).

Katepalli et al. (2017) studied the effects of particle shape and interparticle interactions on the microstructure and rheological properties of spherical and fumed silica particle stabilized emulsions in bromohexadecane ($C_{16}H_{33}Br$). The irregularly shaped fumed silica created more stable emulsions with smaller droplet sizes as well as showing higher storage moduli compared to spherical particles. The higher degree of elasticity was attributed to the formation of volume-filling particle networks in the aqueous phase due to the irregularly shaped particles offering a higher density of available contact areas between them compared to the spherical ones (Katepalli et al., 2017).

In summary, there have been some fundamental observations related to the effect of particle shape on suspension rheology. As particle shape deviates from sphericity (i.e. $\bar{\bar{p}} \neq 1$), the intrinsic viscosity increases due to the extra energy dissipation occurring under shear flow, while the effective maximum packing fraction decreases as depicted in Figure 1.7a (Mader et al., 2013). However, their product should generally remain equal to 2 (Gaudio et al., 2013; Genovese, 2012; Mueller et al., 2011; Stickel and Powell, 2005). The onset of non-linear rheology and yield stress is also dependent on particle aspect ratio. Increasing the particle $\bar{\bar{p}}$ value leads to more pronounced shear thinning rheology and yield stress behaviour (D 'Avino et al., 2015; Mader et al., 2013; Maurath et al., 2016). The relative viscosity increases with increasing particle aspect ratio followed by a decrease in the effective maximum packing, as described in Figure 1.7b (Genovese, 2012).

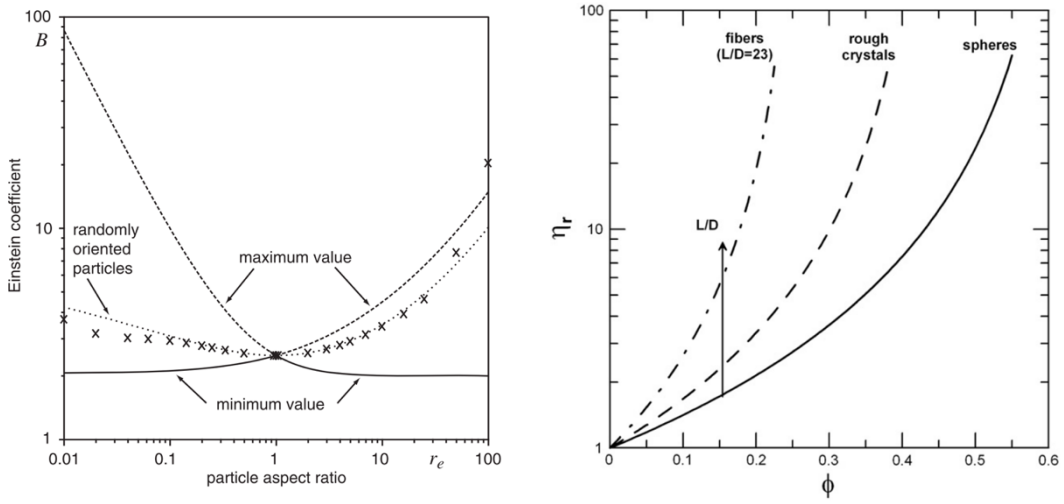

(a) (b)

Figure 1.7: a) Intrinsic viscosity or Einstein coefficient, B, as a function of the particle aspect ratio and particle orientation (adopted from (Mader et al., 2013)); b) Relative viscosity as a function of particle volume fraction for particle suspensions of varying aspect ratios (L/D) (adopted from (Genovese, 2012)).

1.4.1.3 Effect of particle surface morphology

The effect of particle surface morphology and more specifically, surface roughness, was investigated by Moon et al. (2015). This study utilised polymethylmethacrylate (PMMA) ($D = 40 \pm 4.0\,\mu m$), polystyrene (PS) ($D = 40 \pm 2.8\,\mu m$ & $D = 80 \pm 1.7\,\mu m$) and glass spheres ($D = 40 \pm 8.8\,\mu m$) with surface roughness varying from 0.15% to 0.45% in relation to the average particle size. The surface roughness was induced through mechanical grinding and the particles were suspended in a silicone oil matrix. The particle volume fraction varied from $\varphi = 0.30$

to $\varphi = 0.50$. It was shown that particle surface roughness increases both the viscosity and the normal stress differences ($N_1 - N_2$), whereas the maximum packing fraction decreased by 2.6% (Moon et al., 2015).

The work of Moon et al. (2015) was complemented by Tanner and Dai (2016) who induced a higher roughness ratio to the particles up to 5%. At such high degrees of surface roughness, the particles lose their sphericity and particle contacts are favoured through the extended surface asperities (Davis et al., 2003; Hoyle et al., 2020; Tanner and Dai, 2016a). Similar phenomena were also observed by comparing the rheology of smooth and etched colloidal silicas with controlled roughness (Hsiao et al., 2017). The surface frictional contacts between rough particles under shear have been associated with both shear thinning and shear thickening rheology (Hsiao et al., 2017; Lobry et al., 2019). An empirical formula was introduced to estimate the maximum packing fraction of a particle suspension as a function of particle shape and roughness and the relation is given by:

$$\varphi_m = \varphi_{m1} exp\left[-\frac{(log_{10}\bar{\bar{p}})^2}{2b^2}\right] \tag{1.2}$$

where φ_{m1} and b are constant variables related to the degree of surface roughness. In particular $\varphi_{m1} = 0.66$ and $b = 1.08$ for smooth particles, whereas $\varphi_{m1} = 0.55$ and $b = 1.00$ for relatively rough particles (Mader et al., 2013; Truby et al., 2015).

On the contrary, Fusier et al. (2018) studied the yield stress and the elastic modulus of two different silica particle suspensions in aqueous solutions, i.e. highly controlled monodisperse silica beads with varying size from 0.7μm to 1.4μm and crushed silica particles with average diameters of $D = 2\mu m$ and $D = 4\mu m$. In this study, it was demonstrated that both yield stress and elastic modulus depend on the ionic strength, the resting time and the solid volume fraction, while there was no experimental evidence that suspension rheology was dependent on particle surface morphology (Fusier et al., 2018).

It can be seen that in most studies mentioned in this section, particle surface roughness can be controlled by mechanical grinding, chemical etching and crushing; methods that do not affect significantly the initial particle size distribution. However, commercial particles often exhibit high degrees of polydispersity and uncontrolled surface characteristics and their suspension rheology is yet to be fully understood. For example, silica particles very often comprise irreducible aggregates of primary particles indicating high degrees of surface irregularity and porosity.

1.4.1.4 Effect of particle size and size distribution

Particle size and size distribution comprise additional factors affecting suspension rheology. The particles with smaller sizes result in suspensions with lower viscosity values and more linear behaviour close to the Batchelor equation (Pavlik, 2009). For example, Konijn et al. (2014) studied the rheological properties of nearly monodisperse PMMA particles with four different diameters ($D = 6.3\ \mu m$, $D = 15\ \mu m$, $D = 30\ \mu m$, $D = 40\ \mu m$) in glycerine. The relative viscosity of the suspensions was found to be independent of particle size in a highly viscous solvent (glycerine in room temperature), while in the case of a lower viscosity suspending medium (heated glycerine) the consistency index in the Herschel -Bulkley was found to decrease by increasing the particle size. In both suspending media shear thinning behaviour was observed at $\varphi \geq 0.40$, whereas shear thickening was also observed for the suspensions with the smaller particles, i.e. $D = 6.3\ \mu m$ (Konijn et al., 2014).

The effect of particle size and size distribution on suspension shear thickening behaviour has also been investigated by several researchers (Guy et al., 2015; Heussinger, 2013; Maranzano and Wagner, 2001a, 2001b). For example, Maranzano and Wagner (2001) reported a decrease in the critical stress for the onset of shear thickening with increasing the particle diameter. The latter was attributed to enhanced frictional contacts between the particles at increasing the shear rate. On the contrary, the critical stress was found to be unaffected by the polydispersity index, while suspensions with wide particle size distributions showed a suppressed shear thickening response.

Gaudio et al. (2013) studied the rheology of suspensions consisting of magmatic crystals with diameters ranging from 63 to 500 μm suspended in a silicone oil. In this study, smaller particles exhibited higher relative viscosities which was mainly associated with the tendency of smaller particles to form clusters more easily due to the smaller particle–particle distance (Gaudio et al., 2013; Mewis and Wagner, 2012). Other studies have also shown a dependence of suspension viscosity on the particle size; in particular, viscosity has shown to increase with decreasing particle size at concentrations in the dense regime (Gamonpilas et al., 2016a; Nguyen et al., 2007) due to particle agglomeration.

The maximum packing fraction, φ_m, of the suspensions can also be affected by particle polydispersity. In particular, φ_m increases for polydisperse systems, compared to monodisperse ones, since the smaller particles act as lubricants facilitating the flow through filling the gaps between the larger particles (Gamonpilas et al., 2016a; Genovese, 2012; Konijn et al., 2014; Mwasame et al., 2016). The value

of φ_m depends not only on the polydispersity index but also on the size ratio of the particles, defined as the ratio of the large particles to the smaller ones. More importantly, φ_m increases with increasing the size ratio of the particles in the suspension (Mwasame et al., 2016). In contrast to φ_m, the relative viscosity decreases by increasing the particle size distribution, as shown in Figure 1.8.

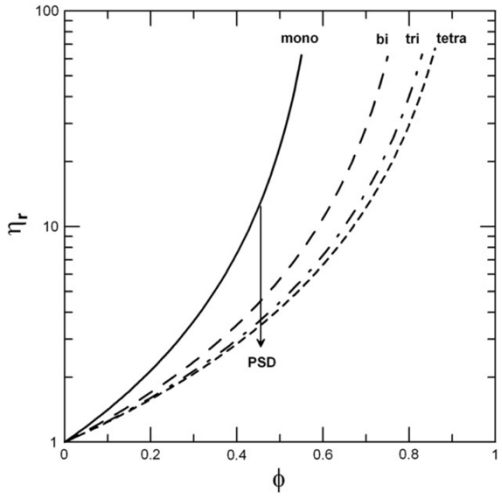

Figure 1.8: Relative viscosity of particle suspensions with varying particle size distribution (PSD) and particle volume fraction (adopted from (Genovese, 2012)).

A modification of the Krieger-Dougherty model has been proposed in the literature to include the effect of particle size distribution, and its formula is given by:

$$\eta_r = \left[1 + \left(\frac{C\varphi}{1 - {}^{\varphi}/_{\varphi_m}}\right)\right]^{3.3\varphi_m} \tag{1.3}$$

where η_r is the relative viscosity, φ the particle volume fraction, φ_m the maximum packing and C is a fitting parameter related to the particle size distribution (Servais et al., 2002).

As depicted in Figure 1.6, suspension rheology is complex and can exhibit several flow regimes including shear thinning, shear thickening and yield stress (Denn and Morris, 2014; Gaudio et al., 2013; Konijn et al., 2014; Stickel and Powell, 2005). The specific mechanisms leading to the abovementioned non-Newtonian rheology will be described in the following subsections.

1.4.1.5 Shear thinning rheology

Shear thinning is a typical non-Newtonian behaviour encountered in numerous particle suspensions and has been mainly attributed to interparticle and particle-fluid interactions as well as changes in the microstructure under shear. Suspension microstructure refers to the structure/organisation of particles in a solution at the microscale level, made visible through a microscope. Particle structuring involves but is not limited to, their alignment to the direction of the applied flow field at increasing shear rate or particle agglomeration. Several researchers have investigated the origins of shear thinning for particle suspensions over the years; the main mechanisms proposed in the literature are mainly related to particle structuring under shear, shear thinning of interparticle gap fluids, frictional and adhesive interparticle interactions.

Gadala-Maria and Acrivos (1980) were among the first to explore the mechanism behind shear thinning through studying the rheology of highly concentrated ($\varphi \geq 0.3$) non-Brownian polystyrene spheres (40-50 μm) in a mixture of silicone oils. The shear thinning behaviour of these suspensions was attributed to an anisotropic structuring and migration of the particles under shear. Particle alignment to the direction of the flow has also been observed, especially for non-spherical (i.e. rod-like or sheet-like shaped) particles. The latter leads to shear thinning rheology as the particles align to the direction of the applied flow field imposing less resistance to the fluid flow (Gunes et al., 2008; Niu et al., 2015).

In a more recent study, Vàzquez-Quesada et al. (2016) used a numerical approach and showed that the shear thinning of non-colloidal particles in a macroscopically Newtonian fluid (silicone oil) stems from the shear thinning behaviour of the suspending medium at extremely high shear stresses experienced within the interparticle gaps. This is understandable considering that silicone oils consist of polymer chains with various lengths, which align in the direction of flow at sufficiently high shear rates, inducing thus a shear thinning response.

More recent research eluded a very strong role played by interparticle interactions in determining shear thinning behaviour. More specifically, shear thinning was found to be dominated by frictional contacts between the particles at sufficiently high normal loads, as evidenced by the experiments of Chatté et al. (2018) with smooth polyvinyl chloride (PVC) particles with few asperities in a Newtonian plasticizer. Considering the surface irregularities as elastically deformable and based on the theory of Archard (1957) for the elastic deformation of rough surfaces, they were able to demonstrate that shear thinning stems from a reduced microscopic friction coefficient between

particles as the asperities deform during contact. The microscopic friction coefficient was estimated using Atomic Force Microscopy experiments and measuring the frictional force arising during the frictional contacts between two particle surfaces at increasing normal load. Lobry et al. (2019) further supported this shear thinning mechanism by studying the rheology of relatively smooth polystyrene (PS) particles in silicone oil.

Blanc et al. (2018) provided additional evidence in support of the theory introduced by Chatté et al. (2018). In their study, the rheology of relatively smooth and monodisperse polystyrene spheres ($d{\sim}80\mu m$) and irregularly shaped (faceted) sugar particles ($d{\sim}80-100\mu m$) in a Newtonian silicone oil matrix was investigated. Irregularly shaped particles were shown to exhibit higher zero shear viscosities and pronounced shear thinning compared to the polystyrene spheres at the same particle volume fractions. The non-Newtonian rheology of the faceted particles was attributed to the higher contribution of the contact viscosity to the total viscosity value of the suspension at increasing particle volume fraction and decreasing applied shear stress; as particle contacts are favoured in the case of irregularly shaped particles (Blanc et al., 2018; Gallier et al., 2014; Jones et al., 2002). In contrast, suspensions of relatively smooth spheres showed weak shear thinning response due to mild surface deformation (non-linear Hertz contact).

On the other hand, when particles are suspended in solvents which promote particle attraction, adhesion forces are expected to dominate suspension rheology. Therefore, in the presence of adhesive systems, the shear thinning rheology is governed by the formation of agglomerates which break down under increasing applied deformations. This leads to the large structures reducing to smaller units and thus, lowering the viscosity values with increasing shear rate, as has been demonstrated in biological fluids such as blood as well as silica particle suspensions (Eberle et al., 2014; Kaliviotis and Yianneskis, 2007; Min Kim et al., 2014). Thus, the shear induced microstructural changes of suspensions of adhesive particles play a key role in the shear thinning of such particle systems; these are also highly dependent on particle size distribution, volume fraction and surface characteristics (Blanc et al., 2018; Mewis and Wagner, 2012). For example**,** when Brownian motion is significant, due to the presence of small, submicron particles, agglomeration is favoured by the larger available surface for particle contacts leading to more pronounced shear thinning rheology (Mewis and Wagner, 2012).

Wall slip and viscous dissipation are common for particle suspensions and can lead to shear thinning response as well. Wall slip is related to the shear induced migration of the particles away from the wall and the formation of a dilute layer of the

sample therein. This derives from the shear gradient near the wall and leads to an abrupt decrease in the viscosity values (Chinesta and Ausias, 2015; Macosko, 1994). Wall slip is undesirable in rheological measurements and can be prevented by using the appropriate experimental tools, i.e. sandblasted rheometer components or vane rotors (Barnes, 1995; Chang et al., 2003; Chinesta and Ausias, 2015; Denn and Morris, 2014; Trofa et al., 2016; Yüce and Willenbacher, 2017). Viscous dissipation is described by the local increase of the sample's temperature generated at sufficiently high deformation rate. This leads to a decrease in the suspension viscosity and thus, shear thinning (Frankei and Acrivos, 1967; Mueller et al., 2010). Frictional contacts between the particles have also been observed to enhance viscous dissipation and hence, are more likely to occur in suspensions of rough particles (Mari et al., 2015a; Trulsson et al., 2017).

1.4.1.6 Shear thickening rheology

Shear thickening of suspensions has been the subject of extensive research for several decades due to its relevance in many industrial applications such as drilling, in the manufacturing of smart clothes (body armours) and power transfer in all wheel vehicles. Shear thickening is divided in two categories, i.e. continuous (CST), where the viscosity shows a smooth increase with shear rate, and discontinuous (DST), where suspension viscosity increases abruptly with shear rate, often expanding in several decades (Mari et al., 2015a). The formation of particle aggregates through hydroclustering due to increased lubrication forces or the distortion of particle alignment with the direction of the flow due to instabilities generated at high shear rates have been strongly associated with the onset of shear thickening rheology (Khandavalli and Rothstein, 2015; Lin et al., 2016; Ness and Sun, 2016a; Qin Xu et al., 2014; Royer et al., 2016; Warren et al., 2015).

Barnes (1989), in his thorough review on the shear thickening of non-aggregating particle suspensions in Newtonian fluids, concluded that the onset of shear thickening depends both on the particle and suspending medium properties (i.e. particle volume fraction, particle size distribution and shape, inter-particle interactions, medium viscosity and characteristics of deformation). Firstly, Barnes drew the conclusion that the critical shear rate for shear thickening to occur ($\dot{\gamma}_c$) decreases with increasing φ or the particle size. In particular, $\dot{\gamma}_c$ is inversely proportional to the particle diameter squared as also demonstrated by more recent studies on (Maranzano and Wagner, 2001b; Ness and Sun, 2016a).

Secondly, $\dot{\gamma}_c$ is strongly dependent on the maximum packing fraction (φ_m) and thus, the onset of shear thickening can be delayed by widening the particle size distribution (Genovese, 2012) or lowering the particle aspect ratio (Brown et al., 2011a) as both lead to an increase in φ_m. Anisotropic particles have also been found to induce more pronounced shear thickening. According to Barnes, any solid particle suspension can show shear thickening if placed under the right conditions. Solvent viscosity also influences the $\dot{\gamma}_c$ for the onset of shear thickening, i.e. higher solvent viscosities lead to more pronounced shear thickening (Barnes, 1989; Genovese, 2012).

Hydrocluster formation is one of the main mechanisms leading to shear thickening response. This phenomenon occurs at sufficiently high shear rates, where the attractive hydrodynamic forces overcome the repulsive particle forces leading to cluster formation and a subsequent increase in the viscosity values. However, there is more evidence in the literature supporting that frictional contacts between the particles induce more pronounced shear thickening behaviour (Hoyle et al., 2020; Mari et al., 2015a; Ness and Sun, 2016a; Pan et al., 2015; Qin Xu et al., 2014; Sarkar et al., 2017; Seto et al., 2013). In this case, confinement and crowding results in adjacent particles jamming while trying to respond to the applied flow field. Frictional forces arise from particle contacts leading to increased stresses and shear thickening. Shear reversal experiments, where the flow direction is suddenly reversed, have been mainly used to decouple the hydrodynamic from the particle contact forces and thus, reveal the mechanism of shear thickening (Lin et al., 2015). Contact forces have been found to govern both continuous and discontinuous shear thickening in suspensions of non-Brownian particles and this has been proven by numerical simulations (Mari et al., 2015b; Ness and Sun, 2016b, 2015; Seto et al., 2013; Townsend and Wilson, 2017) and experimental work (Lin et al., 2015; Royer et al., 2016).

Cornstarch–water solutions comprise a very typical example of suspensions which show discontinuous shear thickening due to jamming at sufficiently high cornstarch concentrations (Brown and Jaeger, 2014; Khandavalli and Rothstein, 2015). In the study of Madraki et al. (2018) a transition from continuous to discontinuous shear thickening was observed by adding large solid particles with average diameters of $D = 49\mu m$, $D = 100\mu m$ and $D = 150\mu m$) in a cornstarch suspension initially showing CST. The CST to DST transition was associated with a local increase in cornstarch concentration in certain areas of the suspensions as it gets excluded from the near proximity of the large particle surface (Madraki et al., 2018). Hsiao et al. (2017) demonstrated that increasing the surface roughness of the particles shifts the shear thickening onset to lower particle volume fractions and critical stresses by using

smooth and rough silica particles (Hsiao et al., 2017). On the other hand, Clavaud et al. (2017) used a model suspension of negatively charged non-Brownian silicas to investigate the origins of shear thickening. In this study, shear thickening was eliminated by the addition of salt, which lowered the repulsive forces range between the particles below that of the particle surface roughness (Clavaud et al., 2017).

Hsu et al. (2018) fabricated raspberry-like particles with tunable surface roughness through electrostatic absorption of silica nanoparticles (namely berries) on the surface of larger silica colloids (namely cores). A clear link between surface roughness and discontinuous shear thickening (DST) rheology was provided by combining rheology with lateral force microscopy experiments. Increasing particle surface roughness shifted the onset of DST behaviour to lower shear rates and particle volume fractions (φ) explained through an interlocking mechanism of the surface asperities under shear (Hsu et al., 2018). Numerical simulations by Cheal and Ness (2018) for dense granular suspensions also showed that the frictional contacts induced by rough particles lead to jamming and shear thickening rheology at lower φ, compared to frictionless particles. The latter was attributed to the more anisotropic contacts between the frictional particles (Cheal and Ness, 2018).

1.4.1.7 Effect of temperature

Significant variations in temperature can occur during manufacturing. Many industrial processes involve heating of the formulation to either facilitate the mixing procedure or to promote a chemical reaction. High temperatures can also occur unintentionally in local areas or the bulk formulation during mixing due to high shear rates and the heat energy dissipation in the sample. In general, an increase in temperature results in decreasing the suspension viscosity due to a decrease in the viscosity of the suspending medium (Burlawar et al., 2019; Elbishari et al., 2011; Jia et al., 2007; Pavlik, 2009; Rathee et al., 2019; Vryzas et al., 2017). The applied temperature conditions can also significantly influence suspension rheology by altering interparticle interactions.

Increasing the temperature has been found to suppress shear thickening due to a decrease in the hydrodynamic forces, which require higher shear rates to overcome the repulsive forces between the particles (Amiri et al., 2012; Gao et al., 2017). In contrast, in the case of frictional shear thickening, Rathee et al. (2019) observed an increase in the shear thickening response of the suspension with increasing the temperature. In that study, colloidal silica rods were grafted with thermo-responsive

polymer brushes in order to tune the frictional contacts between the particles by changing an external stimulus, i.e. temperature. In particular, at intermediate temperatures below the transition temperature (T_{LCST}), an increase in the shear thickening occurred due to the gradual collapse of the polymer brushes, which favoured frictional contacts between the silicas. However, increasing the temperature beyond T_{LCST} led to particle adhesion and high values of yield stress, which obscured shear thickening (Brown et al., 2010; Rathee et al., 2019). A similar behaviour was observed by Gao et al. (2017) for colloidal silicas in an inorganic solvent. A loss in the stability of the suspensions and a suppression of the shear thickening behaviour were observed at temperatures higher than 30°C followed by pronounced shear thinning and yield stress. This behaviour was attributed to a decrease in the thickness of the solvation layer able to induce repulsive forces between adjacent particles, which was measured by small angle neutron scattering (SANS) experiments (Gao et al., 2017).

Vryzas et al. (2017) investigated the effect of temperature on aqueous suspensions of bentonite particles ($D = 36\ \mu m$) due to their high importance in drilling processes. Although the suspensions exhibited Newtonian behaviour at all temperature conditions applied, an increase in the yield stress with temperature was observed, which arose from enhanced particle adhesion (Vryzas et al., 2017, 2016). On the contrary, the study of Burlawar et al. (2019) showed a decrease in the yield stress values with increasing the temperature of aqueous suspensions of fibers, which was attributed to fiber deformation and bending upon shear.

1.4.2 Suspensions in non-Newtonian media

The above studies refer to suspensions of particles with varying surface morphologies and size characteristics suspended in Newtonian solvents. However, in real systems and industrial formulations, the suspending media often involve polymer solutions with complex non-Newtonian rheology. Blending such solvents with particles can alter both the particle and polymer dynamics leading to hybrid composites with completely different rheological properties (Zenit and Feng, 2018). Two main categories of non-Newtonian fluids have been generally reported in the literature as suspending media of particle suspensions, i.e. shear thinning or shear thickening with weak viscoelasticity (Daugan et al., 2004; Liard et al., 2014; Ovarlez et al., 2015) and highly elastic but with constant viscosity, namely Boger fluids (Scirocco et al., 2005, 2004; Tanner, 2019a; Vázquez-Quesada et al., 2019; Yang and Shaqfeh, 2018a).

The key effects of suspending medium viscoelasticity and shear thinning nature are summarised in the reviews of Yang and Shaqfeh (2018) and Tanner (2019).

1.4.2.1 Shear thinning and shear thickening solvents

Among the first to report the effect of a shear thinning suspending medium on the rheology of particle suspensions were Nicodemo et al. (1974). In that study, polydisperse glass beads ($D = 4 - 44\ \mu m$) were suspended in aqueous solutions of polymers typically known for their shear thinning nature. Increasing the particle volume fraction increased the viscosity values of the suspending medium, while maintaining the same degree of shear thinning with that of the suspending medium. More complex rheological phenomena and enhanced shear thinning were observed at the highly concentrated suspensions of $\varphi \geq 0.30$ (Nicodemo et al., 1974). Several years later, Ye et al. (2014) reported shear thickening behaviour for polydisperse colloidal silica suspensions in PEO (polyethylene oxide)-water solutions and particle concentration of 17% wt, whereas the shear thickening was absent in the case of monodisperse silicas. This behaviour was attributed to the fact that small particles penetrate the polymer coils forcing them to expand, while larger particles effectively bind on the different polymer coils leading to a polymer network and thus, an increase in the viscosity values with shear rate (Ye et al., 2014).

Liard et al. (2014) studied the rheology of glass spheres with two size distribution groups ($D = 50 - 70\ \mu m$ & $D = 100 - 140\ \mu m$) suspended in a shear thinning and a shear thickening fluid and observed no effect of particle addition on the power law index of both suspending media. Therefore, using a power law relation, Liard et al. (2014) were able to construct a single master curve where the viscosity curves of the suspensions were superimposed onto that of the corresponding suspending medium. The ability to construct a single master curve can further aid in minimising the number of experiments required to describe the rheological properties of such particle suspension types (Liard et al., 2014). Pal (2015) also investigated experimentally the rheological properties of glass beads with an average diameter of $D = 92\ \mu m$ suspended in power law shear thinning solvents. Four different models were proposed to describe the constant shear rate relative viscosity of the suspensions as a function of the flow index, n, and volume fraction, φ, and the most representative one is described by:

$$\eta_r = exp\left[\frac{\left\{2.5\left(\frac{n+1}{2}\right)+\left(\frac{n-1}{2}\right)\right\}\varphi}{1-{}^{\varphi}/_{\varphi_m}}\right] \quad (1.4)$$

where, n is the flow index of the suspending medium indicative of its shear thinning or shear thickening nature.

Trofa and D'Avino (2020) studied the effect of the solvent shear thinning on the rheology of a dilute suspension of irregularly shaped aggregates. The intrinsic viscosity of the suspensions exhibited a linear decrease with increasing the shear thinning degree of the suspending fluid (i.e. decreasing the flow index, n), which was related to the fractal dimension and the aspect ratio of the formed aggregates (Trofa and D'Avino, 2020). Shear thinning fluids have also been found to influence particle sedimentation in a vertical cell. Daugan et al. (2004) observed a delay in the sedimentation of non-Brownian monodisperse spheres suspended in shear thinning Xanthan gum solutions due to the formation of strong like particle aggregates, required for sedimentation to occur.

1.4.2.2 Boger fluids

Boger fluids have been widely used in the literature as model fluids to isolate the elastic effects of the suspending medium on the rheology of particle suspensions in the absence of shear thinning rheology. Boger fluids generally consist of a low concentration of a high molecular weight polymer dissolved in a solution (James, 2009). Shear thickening has been widely observed in several studies of particles suspended in these highly elastic solvents, which has been mainly attributed to the extensional thickening of the viscoelastic matrix and is known as elastic thickening (Scirocco et al., 2004).

Scirocco et al. (2004, 2005) studied the rheology and microstructure of monodisperse polystyrene (PS) spheres with two different diameters ($D = 2.7 \pm 0.1$ & $D = 1.9 \pm 0.1$) in various shear thinning and Boger fluids. String like structures and particle alignment was observed for the suspensions in the shear thinning fluids. The onset of string formation, the degree of particle alignment and the possibility of the string structures to aggregate were highly dependent on the degree of shear thinning in the suspending medium (D'Avino and Maffettone, 2015; Scirocco et al., 2004). On the contrary, no specific microstructural features or hydrocluster formation occurred for the suspensions in the Boger fluids. Microscopic images showed that the particles remained randomly distributed in the solvent independently of the shearing condition applied. In particular, the shear thickening behaviour of the suspensions in the Boger

fluids was linked to the strain hardening of the long polymer chains under the influence of the extensional flows generated in the narrow interparticle gaps (Scirocco et al., 2005, 2004).

Recent numerical studies further supported the theory that the strain hardening of the polymer chains originating from extensional stresses is responsible for the shear thickening behaviour of particle suspensions in Boger fluids. For example, Yang & Shaqfeh (2018) combined numerical simulations with experiments using non-colloidal polyethylene microspheres ($D = 32 - 38\,\mu m$) to probe the extensional thickening of the suspensions in the high molecular weight polymer solutions (i.e. the Boger fluids). The onset of shear thickening was observed at particle volume fractions as low as $\varphi = 0.025$, while the increase in viscosity with shear rate was more pronounced at the closed streamlines around the particles, where the flow is governed by extensional stresses (Shaqfeh, 2019; Yang and Shaqfeh, 2018a, 2018b). Vazquez-Quesada et al. (2019) extended the work of Yang and Shaqfeh (2018) to higher particle volume fractions in the semi-concentrated regime ($\varphi \leq 0.30$). The shear thickening of suspensions of non-colloidal particles suspended in a Boger fluid was investigated through three-dimensional numerical simulations. Shear thickening rheology was observed at particle volume fractions as low as $\varphi = 0.10$. The simulations were able to predict the elastic thickening of suspensions in the dilute and semi-dilute particle concentration regime, showing a good qualitative agreement with experimental studies by other researchers. In contrast, the model showed high deviations from the available experimental data for suspensions in the concentrated regime ($\varphi = 0.30$) due to the interparticle frictional contacts affecting suspension rheology more rigorously (Vázquez-Quesada et al., 2019).

Tanner and Dai (2016) revealed the presence of elongation stresses in a Boger fluid suspension by conducting filament stretching experiments. The suspensions consisted of non-colloidal smooth or rough PMMA and PS particles suspended in a Boger fluid, made from corn syrup, glycerine and an aqueous solution of polyacrylamide. In this study, the suspensions of smooth spheres exhibited mild shear thickening in agreement with the afore-mentioned studies. In contrast, the suspensions of rough particles exhibited pronounced shear thinning response under steady state at particle volume fractions of $\varphi \geq 0.30$. This behaviour was associated with a partial deformation of the polymer molecules at the areas near the rough surface of the particles (Tanner and Dai, 2016b, 2016a).

1.4.2.3 Particle and polymer dynamics

As mentioned above, blending particles with polymers can significantly alter the particle and polymer dynamics (D'Avino and Maffettone, 2015). For example, Marcovich et al. (2004) observed an increase in the relaxation times of the polymer melt with increasing the particle volume fraction for wood flour suspensions ($D \approx 17\,\mu m$) in polypropylene. However, the rheology of the hybrid composite was governed by the polymer dynamics (Marcovich et al., 2004). Ndong and Russel (2012) showed that absorption of the polymer molecules on the particle surface can significantly decrease the relative viscosity of the hybrid composite. In particular, the rheology of titanium dioxide (TiO_2) nanoparticles was investigated in binary blends of polydimethylsiloxane (PDMS). The decrease in the relative viscosity of the suspensions was attributed to a preferential absorption of the higher molecular weight polymer chains on the particle surface, which prevented particle attraction (Ndong and Russel, 2012). He et al. (2006) showed a decrease in the viscosity of a limestone slurry with the addition of appropriate polymeric dispersants. The presence of dispersants provided the suspensions with good electro-steric stabilisation for the effective avoidance of depletion flocculation (He et al., 2006).

On the contrary, Massaro et al. (2020) observed a decrease in the viscosity values of colloidal PMMA suspensions in PDMS solution. The latter was attributed to enhanced densification of the particle aggregates in the viscoelastic media, which decreased the effective particle volume fraction in the suspension (Massaro et al., 2020). Similar observations were made for porous zeolite particles ($D = 130 \pm 6\,nm$) suspended in polymer solutions (Olanrewaju et al., 2013). In this case, the viscosity values of the suspensions were significantly increased in the presence of polymers, as the pores absorbed part of the pure solvent leading to an increase of both the effective particle volume fraction and the polymer concentration in suspension. Bossis et al. (2017) were also able to inhibit the jamming transition of calcium carbonate particle suspensions in the presence of PEO molecules reaching a volume fraction of $\varphi = 0.69$ with negligible yield stress. They observed that a small polymer densely absorbed on the particle surface can more effectively prevent direct particle frictional contacts and thus, jamming, compared to a large molecule less densely absorbed (Bossis et al., 2017).

1.4.2.4 Viscoelasticity driven particle migration

Particle migration have also been associated with particle suspensions in polymer viscoelastic solutions and they have been found to depend on the applied flow field, confinement and the degree of viscoelasticity of the suspending medium. (D'Avino et al., 2017; D'Avino and Maffettone, 2015; Datt and Elfring, 2018). Shear induced migration is a well known phenomenon in particle suspensions and more specifically, the particles have been observed to migrate towards the low shear rate (maximum velocity) regions of the applied flow field. Such phenomena have been obtained both through numerical simulations (Patankar and Hu, 2001) and experimental studies (Kim, 2001; Ovarlez et al., 2015). In particular, Kim (2001) investigated concentrated suspensions of spherical PMMA particles ($D = 550 \pm 50\ \mu m$) in a 200ppm polyacrylamide solvent under Poiseuille and torsional flows. The particles migrated towards the centre of the pipe (Kim, 2001), i.e. in the zero shear rate area. In a more recent study, Ovarlez et al. (2015) studied the rheology of polystyrene spheres ($D = 250\ \mu m$ & $D = 140\ \mu m$) in yield stress fluids using a Couette geometry. In that case, the particles migrated from the inner (rotating) to the outer cylinder (non-rotating) (Ovarlez et al., 2015).

However, D'Avino and Maffettone (2015), in their extensive review on the particle dynamics in viscoelastic liquids, reported that although viscoelasticity drives the particles towards the low shear rate regions due to normal stress differences, shear thinning media induce the opposite effect. This phenomenon was observed for all types of flows, i.e. planar, Couette and Poiseuille (D'Avino and Maffettone, 2015). Wall slip results from both shear induced and viscoelasticity driven particle migration and its effect on the dynamics of viscoelastic suspensions has been studied by Trofa et al (2016) through numerical simulations. In particular, in parallel plate shear flow condition, the presence of wall slip was found to reverse the migration direction towards the channel middle plane compared to the no-slip condition, where the particles migrated towards the wall (Trofa et al., 2016). Viscoelasticity induced particle migration and particle inertia have also been exploited in the context of microfluidics. By utilizing the appropriate suspending media the particles can be driven in fixed positions of the microchannel to serve specific applications/flow requirements (D'Avino et al., 2017; Giudice et al., 2017).

1.5 Suspension microstructure

Microstructure changes under shear play a crucial role in suspension rheology. Suspension microstructure generally refers to particle organisation in the microscale, including their position in the solvent when subjected to shearing conditions, alignment, particle agglomeration and/or migration effects. Various methods have been employed to probe such changes, including simulations, spectroscopic techniques and oscillatory shear rheology (Egres et al., 2006; Gadala-Maria and Acrivos, 1980; Kalman and Wagner, 2009; Morris, 2009; Sierou and Brady, 2002). In spectroscopic techniques the intensity of the scattered light can be used as a guide to identify patterns in the microstructure of the suspension.

In the studies of Egres et al. (2006) and Kalman and Wagner (2009), rheometric experiments were combined with small angle neutron scattering (Rheo-SANS) experiments to elucidate the mechanisms behind the shear thickening of colloidal suspensions with varying particle shapes. The shear thickening in these experiments was found to stem from a disruption of the flow alignment of the particles and the formation of transient hydroclusters at sufficiently high shear rates (Egres et al., 2006; Egres and Wagner, 2005; Kalman and Wagner, 2009; Maranzano and Wagner, 2001a).

Niu et al. (2015) obtained microscopic images of carbon-based particle suspensions under shear. Different types of particles were used including hollow carbon spheres with an average diameter of $D = 91\ nm$, multiwall carbon nanotubes (rod-like particles with $D = 10\text{–}20\ nm$ and $Length = 10\text{–}30\ \mu m$) and sheet-like graphene ($thickness < 5\ nm$, $size$: $0.1\text{–}5\ \mu m$). The particles were suspended in a Newtonian poly-dimethyl-siloxane (PDMS) solution. The microscopic images under shear showed an alignment of the particles to the direction of flow at sufficiently high shear rates for the non-spherical rod-like and sheet-like carbon black particles (max particle concentration: 2% wt.). In contrast, spherical particles remained randomly distributed in the suspension for the whole range of shear rates investigated. Massaro et al. (2020) used confocal microscopy for enhanced optical resolution to complement the rheology of weakly attractive colloidal suspensions in a Newtonian and a viscoelastic fluid. Denser and slightly larger aggregates were seen to form in the viscoelastic fluid leading to lower suspension viscosities at high shear compared to these in the Newtonian solvent (Massaro et al., 2020).

The microstructure of non-Brownian particle suspensions has also been investigated both numerically and experimentally. For example, Sierou and Brady

(2002) used numerical simulations to study the rheology and microstructure of dense non-colloidal suspensions. Non-Newtonian rheological phenomena were found to arise from an anisotropy in the microstructure of the suspensions with increasing the deformation rate, which was further enhanced at higher particles volume fractions (Sierou and Brady, 2002). Won and Kim (2004) utilized a custom-made flow cell to investigate the microstructure of non-colloidal spherical PMMA ($D = 300 - 355\ \mu m$) suspensions in shear thinning and viscoelastic fluids at a fixed particle volume fraction of $\varphi = 0.10$. Microscopic images revealed the formation of string-like structures in shear thinning fluids, while no such patterns were observed in viscoelastic media in the absence of shear thinning (Won and Kim, 2004).

Blanc et al. (2013) used a transparent Couette cell to allow the visualisation of the shear induced microstructure of rough non-Brownian particle suspensions. The suspensions consisted of large non-Brownian PMMA particles ($D = 172 \pm 8\ \mu m$) in an index matched Newtonian mineral oil. The experimental study was complemented with numerical simulations using simple shear flows at zero Reynolds numbers. A pair distribution function (PDF) was used to analyse the relative location of particle pairs upon shear and its function is described as follows:

$$g_{2D}(\rho, \theta) = \langle \frac{1}{n_{OS}} \frac{N(\rho, \theta)}{N_1 \rho \Delta \rho \Delta \theta} \rangle \tag{1.5}$$

where ρ is the distance between two neighbouring particles, θ is the divergence of the ρ vector from the mean flow direction, N is the total number of particles, N_1 is the number of the reference particles and n_{OS} is the average surface number density of the particles. Anisotropic PDFs were observed in this study attributed to the particle surface roughness as the particles were not allowed to approach at distances lower than the height of the surface asperities. The data obtained from simulations showed a good quantitative agreement with the experimental results at particle volume fractions of $\varphi \leq 0.45$. At higher particle volume fractions, the model failed to fully capture the experimental data due to an effect of the flow cell size but also the multi-body interactions induced in the dense concentration regime. Indicative PDFs are shown in Figure 1.9.

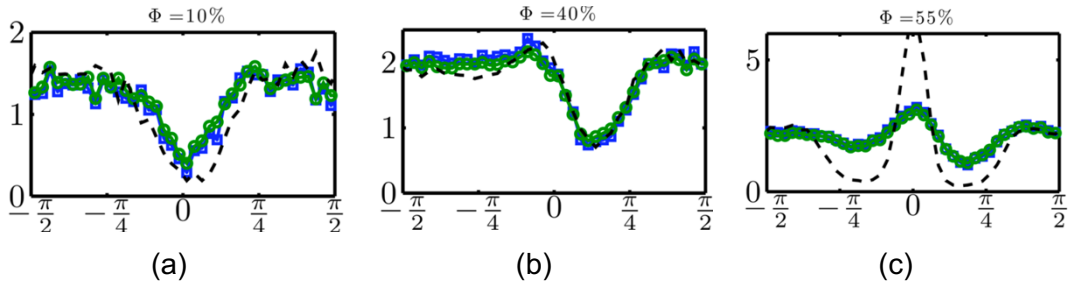

Figure 1.9: Indicative angular PDFs expressed by g_{2D} as a function of angular position at three different particle volume fractions. Dashed lines correspond to the numerical simulations, while open circles refer to the experimental data (images adopted from (Blanc et al., 2013))

Although bulk rheology and spectroscopic techniques have been widely used in the literature to probe structural changes of different materials under shear, direct visualisation of the microstructure of dense sheared suspensions including irregularly shaped particles has proven challenging. Therefore, optical imaging and actual quantification of the shear-induced characteristics of such systems has been fairly limited; to date very few relevant studies exist mainly focusing on smooth or spherical particles and biological samples, such as blood (Gunes et al., 2008; Kaliviotis et al., 2016; Lin et al., 2018; Massaro et al., 2020; Tanner, 2015; Varga et al., 2019).

In this case, other techniques should be employed to derive meaningful information about suspension microstructure based on bulk rheology. Large amplitude oscillatory shear (LAOS) experiments have gained a lot of interest in recent years as suitable for investigating the microstructure of the material. In these experiments, the strain amplitude enters the non-linear region and permanent deformation of the microstructure is induced to the material. The types of fluids investigated under LAOS so far range from polymer solutions (Ewoldt et al., 2008; Hyun et al., 2011) and particle suspensions (Khandavalli and Rothstein, 2015) to biological fluids, such as blood or its equivalents (Lamer et al., 2017; Sousa et al., 2016). For example, Khandavalli and Rothstein (2015) investigated the shear thickening origins of three particle suspensions that thicken through different mechanisms, i.e. polymer bridging (fumed silica in polyethylene oxide), hydrocluster formation (fumed silica in polypropylene glycol) and jamming (cornstarch in water). Lamer et al. (2017) applied the LAOS technique to investigate the rheology of fully formed fibrin clots resembling the in vivo high shear stress conditions.

1.6 Silica suspension rheology

Despite the huge amount of research conducted on investigating the specific mechanisms governing shear thinning behaviour in particle suspensions (Gallier et al., 2014; Marunaka and Kawaguchi, 2014; Moon et al., 2015; Selimovic et al., 2007; Tanner, 2018), it still remains unclear how exactly particle surface morphology and surface functional groups as well as the physical properties of the solvent-carrier media influence particle interactions and thus rheology. Silica particles have been widely used as model systems in many studies (Chen et al., 2007; De Kruif et al., 1985; Galindo-Rosales and Rubio-Hernandez, 2009; Katepalli et al., 2017; Maranzano and Wagner, 2001b; Raghavan et al., 2000; Selimovic et al., 2007; Zhou et al., 1995) not only due to their high relevance to both industrial and natural applications, but also due to their unique properties of being eminently amenable to variations in morphology and surface chemistry.

Silica particles include certain active groups on their surface, namely silanol hydroxyl groups, that enable them to form hydrogen bonds either with adjacent particles or with the solvent molecules. The typical surface chemistry of a silica particle is described in Figure 1.10; the groups capable of interacting with the environment are the isolated silanols. Several researchers have investigated the rheological properties of suspensions of silica particles with varying size distributions and surface chemistry (i.e. hydrophilic and hydrophobic) in a wide range of suspending media, both Newtonian and non-Newtonian.

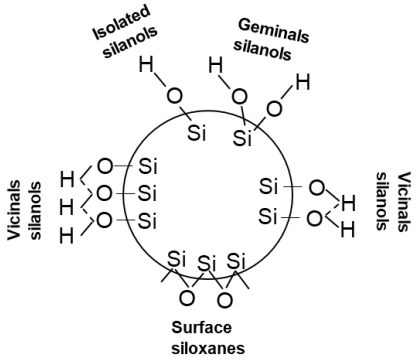

Figure 1.10: Representation of the chemical groups present on the silica surface (reproduced from (Zhuravlev and Potapov, 2006)).

Selimovic et al. (2007) and Selimovic and Hu (2014) investigated suspensions of precipitated silica particles in three different solvents – i.e. silicone oil, mineral oil and a glycerol/water mixture at a fixed particle volume fraction of $\varphi = 0.053$. They reported

that in non-polar media, such as the mineral oil, the silicas form a stable gel network, which retained its rheological properties (steady state and viscoelasticity) over a time period of 4 weeks. Similar behaviour has also been observed for suspensions of fumed silicas in mineral oil (Sugino and Kawaguchi, 2017). On the other hand, when a polar solvent was used, i.e. a water/glycerol mixture, the hydroxyl groups present in the water and glycerol molecule could occupy the free silanol groups on the silica surface forming a solvation layer. The latter led to a viscous dominated response of these suspensions, whose rheological properties and stability deteriorated over time. The suspensions in the silicone oil exhibited an intermediate behaviour compared to the rheology of the suspensions in the mineral oil and the glycerol/water mixture. More specifically, the suspensions showed a solid-like behaviour during the first days followed by dramatic aging (reduction of the viscosity and viscoelastic properties with time) and a transition from solid-like to viscous dominated behaviour. The silicone oil molecules were speculated to break the particle gel network as the hydroxyl groups penetrate through and destroy the hydrogen bonds between the silica particles.

The significant role of a solvation layer formed around silica particles suspended in polar solvents have also been highlighted by other researchers (Amiri et al., 2012; Raghavan et al., 2000; Saint-Michel et al., 2019). For instance, Amiri et al. (2012) studied the rheology of fumed silica suspensions in water/glycerol solutions. They observed that increasing the glycerol content in the suspending medium led to more stable suspensions, despite a decrease in the z-potential. This behaviour revealed the existence of a new stabilisation force, which was again related to the formation of a solvation layer around the particles and the subsequent hindering of interparticle contacts. Similar behaviour was observed for non-Brownian glass spheres in an aqueous Newtonian solvent (Saint-Michel et al., 2019).

The inherently hydrophilic chemistry of the silica surface can be easily altered through the addition of hydrophobic groups providing a route to tune suspension rheology. Chen et al. (2007) investigated the rheology of hydrophilic and hydrophobic silica particles with varying size distributions from the colloidal to the non-colloidal scale suspended in mineral oil. The hydrophobic fumed silicas exhibited higher maximum packing fraction compared to their hydrophilic counterparts, indicating a lower degree of particle aggregation in the former silicas (Chen et al., 2007).

The rheology of hydrophobic fumed silicas modified with hexadecyl chains has also been investigated in various alkanes (octane, dodecane, hexadecane) and aromatic suspending media (toluene, o-xylene, m-xylene, p-xylene) (Marunaka and Kawaguchi, 2017, 2014). All suspensions exhibited gel-like response ($G' > G''$), while the hexadecane molecules were found to be the most effective in getting incorporated

into the particle network; the suspensions of hydrophobic silicas showed higher viscoelastic moduli but reduced shear thinning behaviour compared to the suspensions in the rest of the solvents. Overall, the rheology of these suspensions was found to be governed by the mutual interactions between the suspending media and the hydrophobic hexadecyl groups attached on the silica surface. In a similar study, where precipitated silicas were modified with PDMS and suspended in benzyl alcohol, the suspensions gelation was shifted to higher particle volume fractions by increasing the degree of surface modification (Hayashi and Kawaguchi, 2017a).

Ma et al. (2017) investigated the rheology of hydrophilic and hydrophobic fumed silicas in polydimethylsiloxane (PDMS) solutions with varying polymer molecular weights (M_w). It was shown that particle gelation was promoted in the low-M_w solvent due to bridging effects of the short chains; the suspensions in that case showed solid-like response at a low concentration of 5 phr (phr: parts per rubber). In contrast, the transition from a liquid-like to a solid-like system was shifted to higher particle concentrations in the case of the high-M_w solvent. A possible explanation for the observed behaviour could be that longer polymer chains include a lower density of available contact areas and thus, polymer bridging and gelation could be suppressed (Ma et al., 2017).

In the study of Domenech and Velankar (2017) silica particles ($D \approx 2\ \mu m$) in a fixed volume fraction of $\varphi = 0.35$ were suspended in an emulsion of two immiscible polymers, i.e. polyethylene oxide (PEO) and polyisobutylene (PIB). PEO was added as a wetting agent for the silica particles, while PIB showed no interaction with the suspended silicas. Tuning the concentration ratio of the two polymers, several microstructural features were identified. At low PEO concentration (excess of PIB), polymer induced bridging led to the formation of capillary aggregates. On the other extreme, i.e. excess of PEO (low PIB concentration), the silica particles appeared to be well dispersed in the suspending medium, with the PIB part of the solvent appearing as droplets (Domenech and Velankar, 2017).

Aliabadian et al. (2018) highlighted the effectiveness of polyacrylamide molecules to control the aggregate size of two types of fumed silicas (hydrophilic, AEROSIL 300 (300 being an approximation of the particle specific surface area) and their hydrophobic counterparts, AEROSIL R816). The particle surface chemistry was also found to play a key role in the rheology of the hybrid composite. In particular, the hydrophobic silicas exhibited a stronger binding capability with the polyacrylamide molecules compared to the hydrophilic AEROSILs. Two types of bonds are likely to occur between the silicas and the polymer molecules. First, hydrogen bonds can be formed between the free silanol groups on the silica surface and the carbonyl group

or the nitrogen atom in the polyacrylamide molecule. These bonds are available at both the hydrophilic and the hydrophobic silica suspensions. However, an additional type of bond can occur in the case of the AEROSIL R816 suspensions between the hydrophobic backbone of the polyacrylamide molecules and the hydrophobic hexadecylsilane functional group on the surface of the particles. The latter could be responsible for the higher elasticity and the subsequent higher relaxation times of the hydrophobic silica suspensions in the polyacrylamide solution (Aliabadian et al., 2018).

Lastly, the effect of the polymer characteristics on the rheology of three types of non-colloidal precipitated silica suspensions was investigated by Potanin (2019). These studies were conducted in relevance to toothpaste development. Xanthan gum and carboxyl-methyl cellulose (CMC) were dissolved in a water/glycerol (1:1) mixture and served as the shear thinning suspending media for the precipitated silicas. The silica dispersions in the pure Newtonian medium exhibited a two-yield step, which was also maintained for the suspensions in the CMC solution. On the contrary, when the silicas were suspended in the Xanthan gum solution, the two-step yielding was found to be eliminated. In that sense, the Xanthan gum molecules were able to bind onto the silica surface and form a stable particle-polymer network, whereas, the CMC molecules, being smaller than the Xanthan gum ones, were unable to induce any permanent structuring effects (Potanin, 2019).

Interparticle interactions and solvent mediated interactions play an important role in silica suspension rheology. These interactions have been mainly quantified through Atomic Force Microscopy (AFM) measurements (Jones et al., 2002; Varga et al., 2019). Dishon et al. (2009) controlled the repulsive and attractive forces between micron-sized silica beads in aqueous solutions containing salts (NaCl, KCl and CsCl). Increasing the salt concentration of the aqueous solution leads to more cations absorbing on the negatively charged silicas. The latter suppresses the repulsive forces between the silicas and gives rise to particle attraction. Cation absorption also increases with cation radius from Na^+ to Cs^+. Further increase of the salt concentrations caused particle repulsion to re-emerge due to a reversal in the surface charge stemming from the saturation of the absorbed cations on the silica surface (Dishon et al., 2009). The strength of dispersion forces between silicas with $D = 5\mu m$ in an aqueous solution were also measured using AFM by Valmacco et al. (2016). By heating the particles at 1200°C they were able to tune the nanoscale roughness of the particle surface and hence improve suspension stability through an increase in the Van der Waals dispersion forces.

Thus, varying temperature conditions provides another route to control silica suspension rheology. The latter has been mainly investigated in the context of shear thickening. Studies of suspensions of fumed silicas suspended in polyethylene glycol (PEG) (Liu et al., 2019; Warren et al., 2015) have shown that the shear thickening response is suppressed by increasing the temperature, while the critical shear rate for the onset of the non-Newtonian behaviour is shifted to higher values. Warren et al. (2015) attributed the suppression of the shear thickening to the stiffening of the polymer molecules at the elevated temperatures. On the other hand, Liu et al. (2019) associated that phenomenon with the decrease of the hydrodynamic forces with temperature and their inability to induce hydrocluster formation. Moreover, thermal pre-treatment of the fumed silicas at temperatures above 120^{o}C was observed in the literature to enhance shear thickening (Chu et al., 2014). The latter was attributed to the increase of the hydroxyl groups on the silica surface induced by heating, which led to a thicker solvation layer when the pre-heated silicas were suspended in ethylene glycol; this increased the degree of short range repulsive forces between the silicas and subsequently, promoted the shear thickening.

1.7 Summary of key findings

Particle suspension rheology has been widely studied over the years due to its major role in a great variety of industrial applications. The literature review-which is by no means exhaustive-shows that a significant amount of research has been conducted on the rheology of particle suspensions, especially in Newtonian suspending media under a great range of experimental conditions. A number of scientific gaps and opportunities for fundamental investigation have been identified from the literature review and summarised below, alongside the key findings:

- Particle suspensions exhibit several flow regimes and rheological features, such as shear thinning and shear thickening, yield stress and thixotropy under applied shear. The mechanisms of these phenomena depend strongly on suspension characteristics and need be investigated specifically for each type of particles.

- Theoretical and empirical equations relating the relative viscosity with particle volume fraction, φ, capture well the behaviour of monodisperse spherical particles in the dilute and semi-dilute regime. The application of these equations to dense suspensions of highly irregular particles is still debatable.

- Particle roughness increases suspension viscosity due to the extra energy dissipation occurring under shear flow. Investigations of rough particle suspension rheology focus on particles with controlled roughness or colloidal fumed silicas. Rheological studies of suspensions involving non-Brownian particles with uncontrolled surface roughness are generally limited.

- Non-Newtonian rheological phenomena are mostly attributed to changes in the suspension microstructure under shear; hence microstructure needs be resolved for better understanding of the specific mechanisms governing suspension rheology.

- The different parameters affecting suspension rheology have only been studied individually so far. The combined effects of morphology, roughness and polydispersity encountered in industrial formulations are not fully explored.

- Particle porosity can also play a crucial role to the rheological properties of the suspensions as part of the solvent gets absorbed into the pores leading to substantial increase of the effective particle volume fraction in the suspension.

- Although a significant amount of research has been focused on the rheological properties of particles suspended in Newtonian carrier media, industrial formulations often involve non-Newtonian base fluids. The studies available in the literature on such suspensions are fairly limited and mainly focus on spherical and nearly monodisperse particles.

- The rheology of silica particle suspensions has been widely investigated by several researchers due to their high importance in both industrial and natural applications. However, most of the studies have been focused on colloidal fumed silicas, which exhibit high specific surface areas and pronounced non-linear rheology. To the best of the researcher's knowledge, there are limited studies involving non-Brownian precipitated silicas and their rheological properties in various solvents are yet to be fully understood.

1.8 Aims and objectives

Industrial formulations, an exemplar being toothpastes, very often involve particles with complex morphologies, non-uniform asymmetric shapes, high values of surface roughness and porosity as well as large size distributions. These uncontrolled characteristics in addition to the complex rheology of the base fluids, can impose

many challenges during manufacturing processes. They can significantly influence the rheological properties of the end product and/or lead to problems associated with the consistency between different batch productions of the same formulation.

The complex rheological responses of such industrial non-idealized particles are not well understood. Therefore, the overall aim of this project is to probe the specific mechanisms governing the rheology of non-idealized and non-Brownian dense solid particle suspensions, akin to those involved in oral healthcare applications, in non-aqueous, non-Newtonian environments as well as provide a link between changes in microstructure and the macroscopic flow properties of the suspensions. This will ultimately provide clues on tuning suspension rheology and achieve the design of formulations with rheological properties tailored to specific applications.

Several methods have been employed in this study, from steady state and oscillatory shear rotational rheometry to direct visualisation of the suspension microstructure, to obtain a fundamental understanding of how differently these non–idealized particles behave compared to the spherical ones. Three types of silica particles with varying specific surface areas were used: polydisperse glass spheres, serving as a baseline of a well-studied and not very complex system and two types of non-Brownian rough and porous precipitated silica that are commonly used as abrasives and fillers in novel non-aqueous toothpaste formulations was also investigated.

By employing three different non-aqueous solvents, namely glycerol, mineral oil and glycerol polymer mixtures, the study sets out to:

- Explore the frictional and adhesive contacts in commercial silicas with uncontrolled surface roughness and porosity investigating their effect on the non-Newtonian behaviour of suspensions and propose various routes to tune suspension rheology of such complex systems.
- Elucidate the competing effects between interparticle and particle-solvent interactions in non-Brownian silica particles suspended in a non-aqueous polar solvent and the effect of industrial process conditions such as temperature on their suspension rheology.
- Probe the effect of polymers, i.e. non-Newtonian matrices, on silica particle rheology; particularly decoupling the effects of the suspending medium viscoelasticity and shear thinning behaviour on the rheology of suspensions of commercial silica particles.

1.9 Outline of the thesis

The thesis is structured as follows:

- Chapter 2 presents the experimental methods employed in this study and explains the data analysis and image processing techniques.

- Chapter 3 elucidates the friction-enabled shear thinning rheology of suspensions of silica particles with varying specific surface area suspended in a non-aqueous polar solvent (glycerol). An extensive study of the rheological properties of these suspensions is provided under steady state and small and large amplitude oscillatory shear measurements at different temperature conditions. The effects of particle surface morphology and porosity as well as the particle-particle and particle-solvent interactions will be discussed.

- Chapter 4 discusses another mechanism of suspension shear thinning based on particle agglomeration. In this case the particles are suspended in a non-polar solvent, i.e. mineral oil, and the rheological properties are presented under steady state and oscillatory shear. Bulk rheology will also be complemented with direct visualisation of the suspension microstructure under shear.

- Chapter 5 studies the effect of two discrete polymer solutions, i.e. a viscoelastic one with constant viscosity, namely Boger fluid, and a shear thinning and weakly viscoelastic Xanthan gum solution, on the shear thinning and shear thickening rheology of selected suspensions in the highly concentration regime. Comparisons with the same suspensions in the corresponding Newtonian solvents will be provided alongside to further elucidate the effects of the different polymer solutions.

- The main findings and contributions of the research are summarised in Chapter 6 alongside suggestions for future work.

Chapter 2

Experimental methods

This chapter presents the characteristics of the particles and solvents used in the present study as well as the methods used for sample preparation. Particle surface chemistry modification was conducted to induce hydrophobicity and the steps taken are explained later in this chapter. The methods used for the rheological characterisation of the suspensions follow. Suspension microstructure is also investigated using two different techniques: direct visualisation under shear through an optical shearing cell and Large Amplitude Oscillatory Shear (LAOS) measurements. The techniques are described in detail followed by an explanation of the data analysis methods and the metrics used to quantify rheological responses and microstructure changes. The repeatability and errors in the measurements are also discussed.

2.1 Particle suspensions

Two types of commercial grade silica particles, noted as abrasives ($D = 17.5 \pm 15.2\ \mu m$) and fillers ($D = 12.5 \pm 4.0\ \mu m$) hereafter, supplied in-kind by our industrial partners (GSK), and hollow glass spheres ($D = 11 \pm 5.5\ \mu m$) (Sigma Aldrich) were suspended in various Newtonian and non-Newtonian media. Table 2.1 summarizes the size, size distribution and morphological properties of the three types of particles used in this study. The size distribution of the particles was derived using laser diffraction, the surface morphology was evaluated through Scanning Electron Microscopy (SEM) and image analysis, whereas the specific surface area and porosity were calculated using the Brunauer-Emmet-Teller (BET) method, explained later in this section. SEM micrographs of all particles are shown in Figure 2.1. It should also be noted that commercial silicas are produced through precipitation of an aqueous solution of silicate salts, consisting of primary particles with diameter ~10 nm, which are fused together to irreducible aggregates of irregular shapes (Figure 2.1 b and c).

Table 2.1: Size, size distribution and morphological properties of the three types of particles used in this study.

Particle properties	Glass spheres	Abrasive silicas	Filler silicas
Density (ρ_p, g/ml)	1.1	2.0	2.0
Diameter (*D, μm*)	11±5.5	17.5±15.2	12.5±4.0
Span[*1]	1.66	1.94	1.47
Specific surface area (S_p, m^2/g)	1.6	51.9	226.2
Sphericity[*2] (S_s)	0.97±0.02	0.93±0.04	0.90±0.04
Porosity[*3] (ε)	-	68.5%	89.2%
Refractive index	1.46	1.46	1.46

[*1]: $span = (d(0.9) - d(0.1))/d(0.5)$ and is indicative of the width of the particle size distribution (i.e. the smaller the span number, the narrower the distribution is); [*2]: deviation of particle shape from a circle; computed from the particle analyser using single particle images as $C = 4\pi A^*/P^2$, $C = 1$ corresponds to a perfect circle (A^*: area of the object, P: perimeter of the object); [*3]: calculated from the BET method.

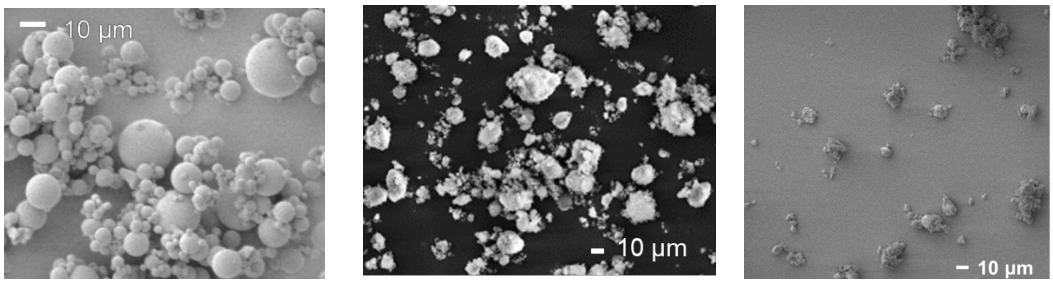

(a) (b) (c)

Figure 2.1. SEM micrographs of a) hollow glass spheres; b) abrasive silicas; c) filler silicas.

Figure 2.2 shows a comparison of the size distributions of the particles investigated in the present study. It can be seen that all three particle types have similar size distributions with the abrasive silicas showing a slightly wider distribution as also indicated by the greater span number (Figure 2.1).

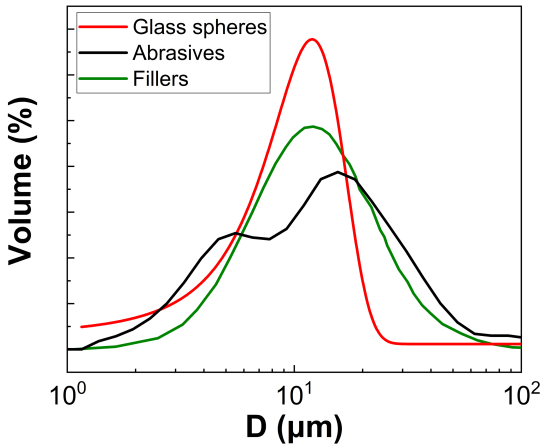

Figure 2.2: Comparison of the size distributions of the three types of particles.

The two types of commercial silicas used in the present study are highly porous. Their porosity was evaluated through the BET method by monitoring the adsorption and desorption of nitrogen under different relative pressures varying from 0 to 1, as well as through mercury porosimetry. As mercury is much heavier (atomic number: 80) compared to nitrogen (atomic number: 7), it can deposit to even smaller pores and provide more comprehensive information about the porosity of the particles. The results of the two techniques are presented in Figure 2.3. The presence of a porous structure is evidenced by the appearance of hysteretic loops in the isotherm curves (Figure 2.3a) of the abrasive and filler silicas; the glass spheres are non-porous and thus, show no hysteresis between the adsorption and desorption process. It can also be seen that as the porosity increases from the abrasive to the filler silicas, the area in the hysteretic loop increases proportionally (i.e. abrasives: ~2.1 and fillers: ~ 9.5).

The results from the mercury porosimetry (Figure 2.3b) were utilised to obtain a better insight on the size distribution of the pores but also their shape. For example, for both porous silicas 100% of the pores is filled with mercury during intrusion. However, during extrusion, mercury recovery is only ~40% for the abrasives and ~20% for the filler silicas. Based on these observations, an indicative pore shape can be obtained. Schematic representations of the pores are described in Figure 2.4. As can be seen, abrasive silicas have v-shaped pores, which makes it easier for a gas or a liquid to move in and out, while the filler silicas show a bottle shape pore, which can restrict the extrusion of the fluid once it gets into the pores.

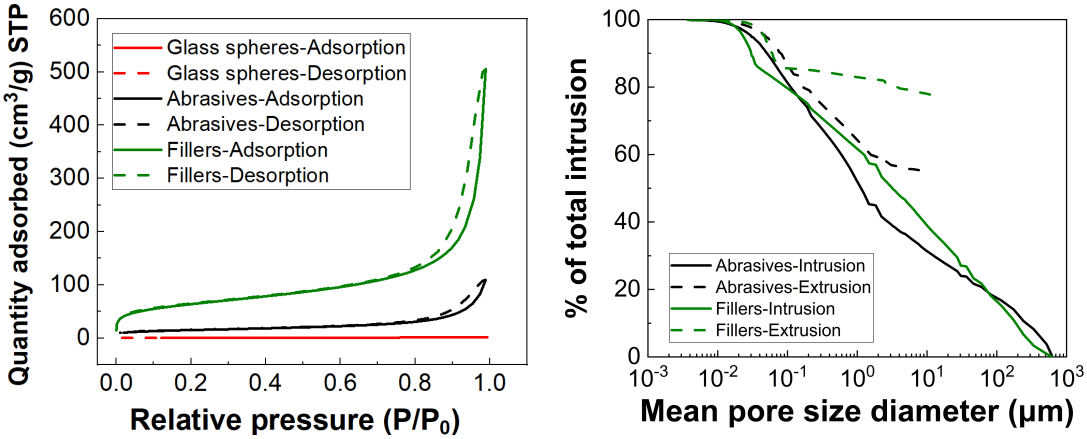

Figure 2.3: a) Volume of absorbed nitrogen as a function of relative pressure as derived from the BET method; b) Mercury porosimetry results for the porous silica particles, i.e. abrasives and fillers.

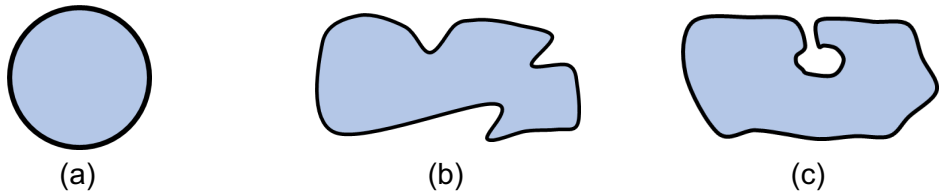

Figure 2.4: Schematic representation of the pore shapes of a) glass spheres (no pores); b) abrasives (v-shaped pores) & c) filler silicas (bottle shaped pores).

Tables 2.2 to 2.4 summarise the physical and rheological properties of the Newtonian and non-Newtonian media utilised as solvents (the grey columns in Tables 2.3 and 2.4 represent the non-Newtonian fluids used in the present study); their viscosity as a function of shear rate is presented in Figure 2.5. Two different types of non-Newtonian solvents were employed in the present study including Xanthan gum solutions with a concentration of 0.1% w/v in glycerol and in a water/glycerol mixture (1/9 by volume) and a typical Boger fluid (200 ppm polyacrylamide in 1% water and 99% glycerol by weight). Different concentrations of Xanthan gum were investigated varying from 1% w/v to 0.07% w/v in glycerol. The concentration of 0.1% w/v was selected as the one fulfilling the following requirements: allowed the xanthan gum to be well dispersed in both pure glycerol and the water/glycerol mixtures, the solutions gave moderate viscosity values so that high particle loadings could be achieved and showed a high degree of shear thinning and weak viscoelasticity. Xanthan gum and polyacrylamide (Sigma Aldrich) had molecular weights of $M_w = 1.7 \cdot 10^6\ g/mol$ and $M_w = 5.5 \cdot 10^6\ g/mol$ respectively. Further details and analysis on the non-Newtonian fluids will be presented in Chapter 5.

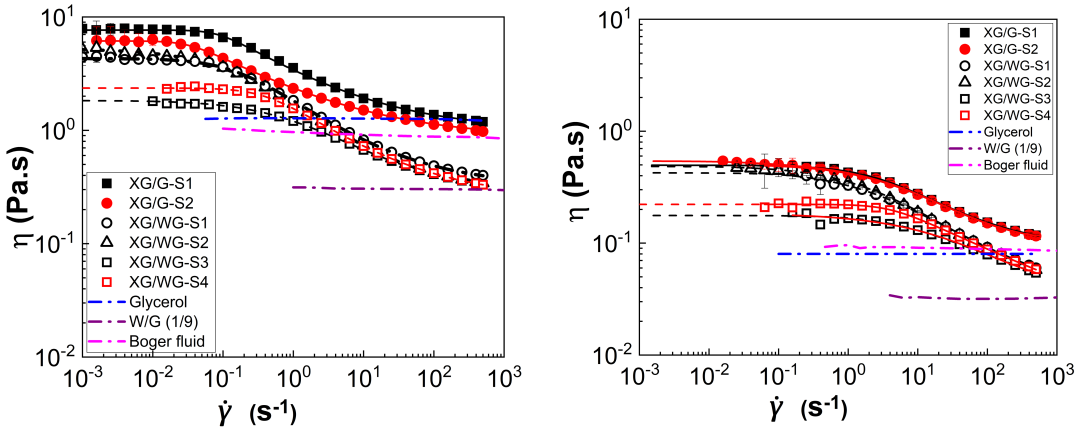

(a) (b)

Figure 2.5: Viscosity (η) values as a function of the shear rate ($\dot{\gamma}$) for all solvents, Newtonian and non-Newtonian at the two temperature conditions investigated: a) 20°C and b) 60°C.

Table 2.2: Density and viscosity values of the Newtonian fluids used in this study.

Newtonian fluids	**Glycerol**		**Water/Glycerol (1/9 – volume)**		**Water/Glycerol (0.1/9.9 – weight)**	
	20°C	**60°C**	**20°C**	**60°C**	**20°C**	**60°C**
Density (ρ_f, g/ml)	1.25	1.24	1.24	1.22	1.25	1.23
Viscosity (η_f, $Pa.s$)	1.30	0.08	0.3	0.03	0.87	0.07
Refractive index	1.47		1.46		1.47	
Mineral oil-20°C						
Density (ρ_f,g/ml)	0.87					
Viscosity (η_f,$Pa.s$)	0.03					
Refractive index	1.47-1.48					

Table 2.3: Rheological properties of all non-Newtonian suspending media used in the present study at 20°C. * The columns in grey refer to the fluids used. XG: Xanthan Gum, G: Glycerol, WG: Water Glycerol, S(No.): Sample number.

Fluids	Boger fluid	XG/G-S1	XG/G-S2	XG/WG-S1	XG/WG-S2	XG/WG-S3	XG/WG-S4
Density (ρ_f, g/ml)	1.25	1.25	1.25	1.24	1.24	1.24	1.24
Zero viscosity ($\eta_{,0}$, $Pa.s$)	0.97	7.65±0.73	6.13±0.18	4.30±0.03	5.24±0.09	1.84±0.01	2.36±0.05
Infinite viscosity (η_∞, $Pa.s$)		1±0.01	0.86±0.01	0.32±0.01	0.30±0.02	0.27±0.01	0.25±0.01
Relaxation time (s)-viscous[*1] (t_v)	-	11.82±3.40	30.46±2.61	6.68±0.35	5.89±1.45	1.19±0.22	2.46±0.15
Relaxation time (s)-elastic[*2] (t_e)	1.25	3.96	9.96	0.16	1.58	0.4	0.63
Flow index, n	-	0.59	0.63	0.51	0.41	0.49	0.53

[*1]: viscous relaxation time, t_v, corresponds to the one derived from fitting the Carreau-Yasuda model to the viscosity curve; [*2]: elastic relaxation time, t_e, calculated from the crossover point in the frequency sweep after subtracting the solvent' s viscosity from the G' , values.

Table 2.4: Rheological properties of all non-Newtonian suspending media used in the present study at 60°C. * The columns in grey refer to the fluids used. XG: Xanthan Gum, G: Glycerol, WG: Water Glycerol, S(No.): Sample number.

Fluids	Boger fluid	XG/G-S1	XG/G-S2	XG/WG-S1	XG/WG-S2	XG/WG-S3	XG/WG-S4
Density (ρ_f, g/ml)	1.23	1.24	1.24	1.22	1.22	1.22	1.22
Zero viscosity ($\eta_{,0}$, $Pa.s$)	0.09	0.50±0.01	0.53±0.01	0.44±0.04	0.49	0.18 ± 0.01	0.22±0.003
Infinite viscosity (η_∞, $Pa.s$)		0.09±0.003	0.10±0.01	0.03±0.01	0.03	0.04±0.01	0.04±0.01
Relaxation time (s)-viscous[*1] (t_v)	-	0.33±0.05	0.06±0.07	0.50±0.24	0.5	0.20±0.05	0.25±0.12
Relaxation time (s)-elastic[*2] (t_e)	0.1	0.16	N/A	1	1	1	0.1
Flow index, n	-	0.47	0.47	0.49	0.46	0.70	0.69

2.2 Sample preparation

Particle suspensions: The required amount of particle mass to achieve a given volume fraction was dispersed to any of the suspending media and mixed using a high shear mixer (Silverson, Model L5M). Mixing time varied from 5 to 10 minutes at a rotating speed between 3500 and 4000 rpm. Microscopic images of the suspensions after preparation showed that high shear mixing did not induce any particle breakage. Particle concentrations varied between 0-62% v/v depending on particle type and dispersion capacity, resulting in volume fractions, φ, ranging from 0 to 0.62. Air bubbles trapped during mixing were removed under vacuum and the rheological measurements were conducted immediately after that step to minimize particle sedimentation.

It should be noted that the suspensions in the Boger fluid were mixed at the lowest speed of the mixer (~100-300 rpm) to avoid degradation of the polyacrylamide molecules. The pure Boger fluid was also tested at the same shearing conditions and its G' and G'' values were monitored before and after mixing through frequency sweeps. No significant changes were observed in the mechanical properties of the Boger fluid due to the applied mixing procedure.

Xanthan gum solutions in glycerol: The required mass of xanthan gum was dispersed in a certain volume of glycerol under high shear mixing. The samples were heated during mixing to lower the viscosity of glycerol and facilitate the dissolution process. The slight difference in the rheological properties of these two Xanthan gum batches, denoted as XG/G-S1 and XG/G-S2 in Tables 2.3 and 2.4, might be attributed to changes in the conformation of Xanthan gum chains due to heating. To evaluate this effect on suspension rheology, only suspensions of the three particle types at the onset of the shear thinning response in pure glycerol were investigated, i.e. glass spheres at $\varphi = 0.50$, abrasive silicas at $\varphi = 0.30$ and filler silicas at $\varphi = 0.10$. A small amount of water (10% by volume) was added in glycerol for the rest of the Xanthan gum solutions to facilitate the dissolution of the polymer powder at room temperature.

Xanthan gum solutions in water/glycerol (1/9): In these solutions, xanthan gum was first dissolved in a small amount of water (10% v/v) using magnetic stirring and then glycerol was gradually added to the mixture. The preparation process was conducted using high shear mixing at room temperature. The solvents denoted with XG/WG-S1, XG/WG-S3 and XG/WG-S4 (Tables 2.3 and 2.4) were used as solvents for the suspensions of abrasive silicas, glass spheres and filler silicas respectively

due to them showing similar flow indices, n and subsequently similar shear thinning degree. Only suspensions in the highly concentrated regime for each particle type were considered in this case to explore the competing effects of the non-Newtonian behaviour induced by the suspending medium and that induced by the particles.

Boger fluid: The polymer (PAA) was first dissolved in water under strong magnetic stirring and then added to hot glycerol (~70°C), to ease the mixing of the two highly viscous fluids. The solution was kept under magnetic stirring at low speed (150 rpm) and at the same temperature for *ca* a week to achieve complete dispersion/dissolution of the polyacrylamide in the water/glycerol mixture.

2.3 Particle surface chemistry modification

To demonstrate rheology control via tuning interparticle interactions and improve particle dispersion in mineral oil, the surface chemistry of the glass spheres was modified. Two agents, i.e. 1H,1H,2H,2H-Perfluorooctyltriethoxysilane and palmitic acid (Sigma Aldrich) were employed to induce hydrophobic groups on the particle surface. The treatment process was conducted as follows: solutions of the hydrophobic chemicals with specified concentrations were prepared in ethanol for the palmitic acid and in hexane for the fluorosilane and then the particles were added in different mass ratios in relation to the reagent. The suspensions were kept under strong magnetic stirring for at least two hours to ensure good dispersion and sufficient contact time between the particles and the silane or the palmitic acid respectively. Finally, the particles were separated from the solvent by centrifugation and left to dry overnight.

2.4 Shear rheology

The rheological properties of the suspensions were measured using a hybrid stress controlled rotational rheometer (DHR-3, TA Instruments) equipped with a sandblasted (R_a= 1.8−2 μm) parallel plate geometry with a diameter of 40 mm. The rheometer is operated through the TRIOS software. The average gap between the two parallel plates was kept at 650±50 μm, which is at least 30 times larger than the average particle diameter (Mewis and Wagner, 2012; Peyla and Verdier, 2011). The rheological properties of the pure solvents were measured using a cone plate geometry with a diameter of 60 mm, angle of 1° and truncation gap equal to 27 μm.

A schematic representation of the geometries used in this study is presented in Figure 2.6.

In a cone-plate geometry the edge of the cone has been trimmed so that the cone does not touch the bottom plate. The trimmed area and the angle of the cone define the truncation gap, which is fixed for each geometry type and ensures that a uniform shear rate is applied along the radius of the geometry, as shown in Figure 2.6a. The uniform shear rate is achieved through the gap (h) changing proportionally to the radius (R) of the geometry ranging from the center ($r = 0$) to the edge ($r = R$).

$$\dot{\gamma} = \frac{\omega_v R}{h} \tag{2.1}$$

, where ω_v is the angular velocity, R is the geometry radius and h is the gap height.

Unlike the cone plate geometry where a uniform shear rate is applied to the whole sample volume, in a parallel plate geometry a shear rate gradient occurs in the gap between the two parallel plates. Conventional rheometers normally are programmed to record the viscosity at the edge of the geometry where the shear rate is maximum. However, this might lead to misinterpretation of the acquired rheological data since the measured viscosity is different from the real material viscosity, especially for the non-Newtonian fluids, whose viscosity is highly dependent on shear rate. Therefore, to account for this non-uniformity in the shear rate, the Rabinowitsch correction, known also as the single point correction, was applied to the steady state rheological data acquired using this geometry (Gamonpilas et al., 2016b). The corrected formula of the shear stress is given by:

$$\tau_{true} = \frac{M}{2\pi R^3}\left(3 + \frac{dlnM}{dln\dot{\gamma}_R}\right) \tag{2.2}$$

where τ_{true} is the corrected shear stress (Pa), M is the measured torque (N.m), R is the radius of the measuring system (m) and $\dot{\gamma}_R$ is the maximum shear rate at the rim of the geometry (s^{-1}).

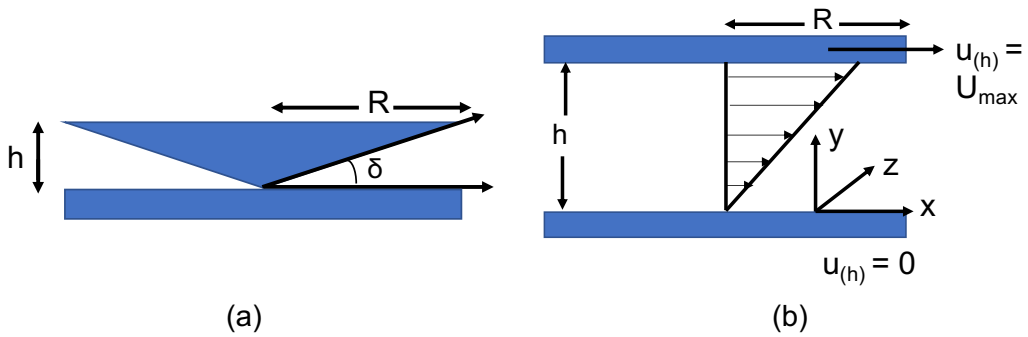

Figure 2.6: Schematic representation of a) a cone-plate geometry & b) a parallel plate geometry.

The rheological measurements were conducted at two different temperatures, i.e. room temperature (20°C) and a higher temperature of 60°C, commonly applied during manufacturing processes to facilitate the mixing of particles in the formulation. The temperature of the lower plate was controlled through a Peltier system with an accuracy of ± 0.1 °C. A custom made solvent evaporation trap made of acrylic material, to enable direct visualisation of the sample, was used to hinder sample evaporation during all measurements. The solvent evaporation trap was also used as a means to enclosing the sample during measurements and minimise its exposure to atmospheric moisture. Both glycerol and silicas are highly hygroscopic which renders them sensitive to humidity. To minimize the effect of moisture absorption on the rheological measurements the following measures were applied: i. the viscosity of glycerol was measured prior to sample preparation to evaluate its quality and purity, ii. the suspensions were transferred to enclosed containers after sample preparation to minimise the free surface area exposed to the atmosphere and iii. the samples were measured right after preparation. Therefore, although humidity might have an effect on the measured rheology, this can be considered negligible.

At first, small amplitude oscillatory shear (SAOS) tests were performed at $f = 1Hz$ and $\gamma = 0.01 - 10\%$ to determine the linear viscoelastic region (LVR) of all samples, i.e. the range of strain amplitudes where both G' and G'' are independent from the applied deformation. An indicative example is presented in Figure 2.7 below.

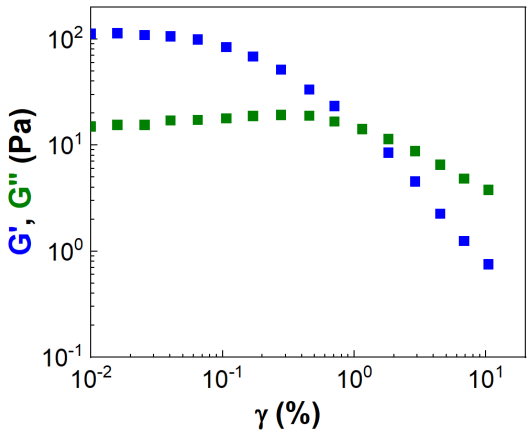

Figure 2.7: Indicative example of a small amplitude oscillatory shear test. The data correspond to a 10% v/v glass spheres suspension in mineral oil.

Subsequently, a fresh sample was loaded to the rheometer and steady state flow sweeps were conducted. Particle suspensions are sensitive to shearing conditions and therefore, the samples were first pre-sheared at a constant shear rate of 200 s^{-1} for 300 s to ensure the same shear history, followed by a resting period of 300 s to allow sample equilibration (Khandavalli and Rothstein, 2015; Ma et al., 2017; Varga et al., 2019). An exception is the suspensions in the Boger fluid, which were exposed to a lower pre-shear of $\dot{\gamma} = 50\ s^{-1}$ to avoid any damage of the long polymer chains during the pre-shearing state. Minimally destructive frequency sweeps were performed after the resting period at angular frequencies (ω) from 0.1 rad/s to 100 rad/s. Steady state flow sweeps were conducted at increasing shear rates ($\dot{\gamma}$) from 10^{-3} s^{-1} to 10^{3} s^{-1}. The presence of hysteretic loops under shear was evaluated by performing a subsequent steady state flow sweep with decreasing shear rate values in the same range. Samples were allowed to rest for 5 min between the flow sweeps, while non-destructive low amplitude time sweeps were performed in parallel to evaluate any particle restructuring or sedimentation during the equilibration time. An indicative example is presented in Figure 2.8.

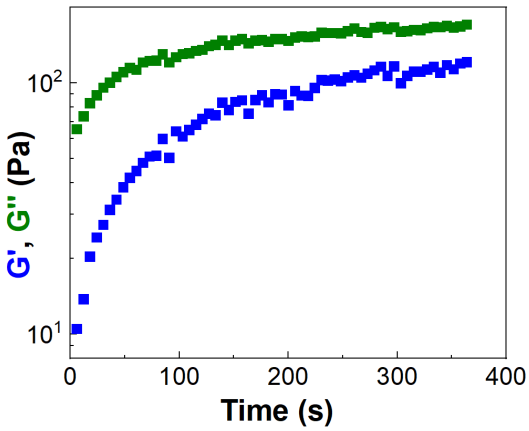

Figure 2.8: Indicative example of a time sweep during the resting period following the pre-shear step. The data correspond to 28% v/v abrasive silica suspension in glycerol.

Due to the density mismatch between the particles and the suspending medium, especially in the case of mineral oil, the flow sweeps need be performed at sufficiently high stresses to avoid particle sedimentation. This critical stress is determined using the dimensionless Shields parameter, defined as the ratio of the fluid force acting on the particle to the particle weight (Lobry et al., 2019).

$$Sh = \frac{\tau}{2a\Delta\rho g} \tag{2.3}$$

where τ is the shear stress (Pa), a the particle radius (m), $\Delta\rho$ the particle-fluid density difference (kg/m^3) and g the gravitational acceleration (m/s^2). Therefore, only data at stresses higher than the limit of $Sh = 1$ are considered in the measured flow curves. The stress values meeting this requirement for the suspensions in glycerol at 20°C are 0.01 Pa for the glass spheres and 0.09 Pa for the abrasive and filler silicas. The Shields number mainly depends on the solvent and particle density; these values are not significantly affected by the addition of water in glycerol, the presence of polymers or temperature and thus, the same stress values are taken for the corresponding suspensions in the non-Newtonian solvents and at 60°C. Accordingly, the stress values in the case of mineral oil suspensions are 0.14 Pa and 1.2 Pa for the glass spheres and the abrasive silicas respectively. The data below these stress values are excluded from the viscosity and shear stress curves in the following chapters.

The *Pèclet* number (Pe) was also estimated in order to examine the extent of Brownian effects introduced by the smallest submicron particles in the distribution. The *Pèclet* number is a measure of the ratio of the thermal energy transferred to the fluid to the thermal energy carried within the fluid and is defined as:

$$Pe = 6\pi\alpha^3\dot{\gamma}\eta_f/k_B\theta \quad (2.4)$$

, where α is the particle radius, $\dot{\gamma}$ is the shear rate, η_f the viscosity of the fluid, k_B is the Boltzmann constant and θ is the temperature. The estimated values of the Pe numbers for all cases are presented in Table 2.5.

Table 2.5: Pe number values for all particle suspensions at the two temperatures using the average diameter of each particle type. In the case of the shear thinning fluids (Xanthan gum solutions) an average viscosity was estimated from the values in the whole shear rate range.

Solvents	Glass spheres	Abrasive silicas	Filler silicas
Glycerol-20ºC	$2\cdot10^5$ - $2\cdot10^{11}$	$7.3\cdot10^5$ - $7\cdot10^{11}$	$2.7\cdot10^5$ - $2.6\cdot10^{11}$
Glycerol-60ºC	$3.4\cdot10^6$ - $3.2\cdot10^{12}$	$1.2\cdot10^7$ - $1.1\cdot10^{13}$	$4.3\cdot10^6$ - $4.2\cdot10^{12}$
Mineral oil-20ºC	$9\cdot10^6$ - $8.7\cdot10^{12}$	$3.2\cdot10^7$ - $3.1\cdot10^{13}$	$1.2\cdot10^7$ - $1.1\cdot10^{13}$
Boger fluid-20ºC	$3\cdot10^5$ - $2.9\cdot10^{11}$	$1\cdot10^6$ - $1\cdot10^{12}$	$3.8\cdot10^5$ - $3.7\cdot10^{11}$
Boger fluid-60ºC	$3\cdot10^6$ - $2.9\cdot10^{12}$	$1\cdot10^7$ - $1\cdot10^{13}$	$3.8\cdot10^6$ - $3.7\cdot10^{11}$
Xanthan gum-20ºC	$2\cdot10^5$ - $2.5\cdot10^{11}$	$4\cdot10^5$ - $4\cdot10^{11}$	$2.7\cdot10^5$ - $2.6\cdot10^{12}$
Xanthan gum-60ºC	$2\cdot10^6$ - $2\cdot10^{12}$	$4\cdot10^6$ - $3.8\cdot10^{12}$	$2.2\cdot10^6$ - $2.1\cdot10^{12}$

It can be seen that the estimated Pe numbers using the average particle diameter are well above the limit for Brownian motion to play a significant role in suspension rheology ($Pe > 10$). However, the particles used in the present study are highly polydisperse and some sizes fall in the submicron scale responsible to induce some degree of Brownian effects. The critical shear rate values beyond which the Brownian effects can be neglected are estimated by calculating the required particle size at $Pe = 10$. The critical shear rate (summarised in Table 2.6) is estimated based on the size distribution of each particle type for which the ratio of the particles able to induce colloidal effects to the total number of particles is below 1%. It can be seen that Brownian effects are more pronounced at 60ºC and the glass sphere suspensions as higher shear rate limits are observed in these cases.

Table 2.6: Critical shear rate values to exclude Brownian motion effects from suspension rheology. N/A in the mineral oil case indicates that no Brownian effects are expected to occur in these suspensions, as the critical shear rate for Brownian motion is below the one required to prevent particle sedimentation.

Solvents	Glass spheres	Abrasive silicas	Filler silicas
Glycerol-20°C	0.04 s^{-1}	0.004 s^{-1}	<0.001 s^{-1}
Glycerol-60°C	0.63 s^{-1}	0.063 s^{-1}	0.01 s^{-1}
Mineral oil-20°C	N/A	N/A	N/A
Boger fluid-20°C	0.063 s^{-1}	0.004 s^{-1}	0.001 s^{-1}
Boger fluid-60°C	0.63 s^{-1}	0.04 s^{-1}	0.016 s^{-1}
Xanthan gum-20°C	0.04 s^{-1}	0.003 s^{-1}	<0.001 s^{-1}
Xanthan gum-60°C	0.63 s^{-1}	0.016 s^{-1}	0.01 s^{-1}

In order to evaluate if fluid inertia affects suspension rheology, the particle Reynolds number (Re) was estimated using the equation given below. The estimated values ranged between 10^{-15} and 10^{-6} for all fluid and particle types used in the present study. This indicates that fluid inertia can be considered negligible as $Re \ll 1$.

$$Re = \rho_f r^2 \dot{\gamma} / \eta_f \tag{2.5}$$

The Stokes number (St) was also utilised as a measure of the degree of coupling between the solid and fluid phases. St is the ratio of the characteristic time of the motion of a particle to the characteristic time of the motion of the bulk suspension and is estimated using the equation below:

$$St = \rho_p r^3 \dot{\gamma} / \lambda \eta_f \tag{2.6}$$

The estimated St values were well below 1 ($St = 10^{-16} - 10^{-7}$) indicating that the fluid phase dictates particle motion, i.e. particles follow the fluid flow (Mueller et al., 2010).

The shear thinning response of the concentrated suspensions in glycerol and the corresponding non-Newtonian solvents as a function of shear rate was mostly described by the Carreau equation (Boyd et al., 2007).

$$\eta = \eta_\infty + (\eta_0 - \eta_\infty)(1 + (\lambda \dot{\gamma})^2)^{\frac{n-1}{2}} \tag{2.7}$$

where η_0 and η_∞ are the zero-shear rate and infinite-shear rate viscosities (Pa.s) respectively, λ is the relaxation time (s) and n is the flow index (n=1 corresponds to Newtonian fluids, while n<1 describes the shear thinning response) (Macosko, 1994).

A modified Herschel-Bulkley model was used to fit the viscosity data derived from the suspensions in mineral oil (Dinkgreve et al., 2016).

$$\eta = \eta_\infty + \frac{\tau_y}{\dot{\gamma}}(1 + (\lambda\dot{\gamma})^n) \tag{2.8}$$

where η_∞ is the suspensions viscosity at infinite shear rate (Pa.s), τ_y is the yield stress (Pa) and λ is the relaxation time (s). Eq. (2.8) implies that at small shear rates ($\dot{\gamma} \to 0$) the suspensions show yield stress behaviour, while at the high rate limit the viscosity curve reaches an asymptotic value to an infinite viscosity with a power law relation and a flow index n.

The relative viscosity (η_r) values as a function of particle volume fraction (φ) were well fitted with the Krieger-Dougherty model (Krieger and Dougherty, 1959), given by:

$$\eta_r = \left(1 - \frac{\varphi}{\varphi_m}\right)^{-B\varphi_m} \tag{2.9}$$

where φ_m is the maximum packing fraction, B is the intrinsic viscosity.

Two additional empirical equations accounting for particle polydispersity and surface irregularities were used to fit the relative viscosity data as a function of particle volume fraction consudered to better suit the particle systems examined in this study. These are the well-known Quemada model (Quemada, 1978):

$$\eta_r = \left(1 - \frac{\varphi}{\varphi_m}\right)^{-2} \tag{2.10}$$

and the model by Servais et al. (2002):

$$\eta_r = \left[1 + \left(\frac{b\varphi}{1 - {}^{\varphi}/_{\varphi_m}}\right)\right]^{3.3\varphi_m} \tag{2.11}$$

, where φ_m is the maximum packing fraction and b is an adjustable parameter accounting for particle polydispersity.

2.5 Suspension microstructure

2.5.1 Optical shearing measurements-low particle concentration limit

An optical shearing method was implemented to investigate the microstructure changes of the suspensions under shear. The method allows visualisation of the suspension microstructure during shearing in a viscometric flow. The experimental set up is depicted in Figure 2.9. The sample was placed between the two quartz plates of a Couette shearing cell (CSS-450, Linkam Scientific Ltd.) and pre-sheared at a constant shear rate of $\dot{\gamma} = 200\ s^{-1}$ for 5 min. Shearing was applied after a resting period of 5 mins at shear rates varying from 5 s^{-1} to 500 s^{-1} (i.e. 5 s^{-1}, 10 s^{-1}, 25 s^{-1}, 40 s^{-1}, 60 s^{-1}, 100 s^{-1}, 250 s^{-1}, 500 s^{-1}). The sample was kept at each shear rate for 1 or 2 mins before image acquisition. The above procedure was followed to mimic the bulk rheological measurements performed with the rheometer. All experiments were conducted using a gap of 100 μm, to minimise the effects of the out of plane particles and at room temperature (ca 25°C). The sheared suspensions were illuminated using a fiber optic LED (SugarCube Ultra, Edmund Optics) and images were acquired using a high-speed CMOS camera (IDT X3) attached on a microscope assembly. The latter was equipped with a 20x objective (NA: 0.6). On average, 2000 images were acquired for each case at frame rates varying from 30 Hz to 300 Hz, depending on the shear rate, and at a resolution of 1280x1024 px^2. The visualisation was made in the flow (velocity) plane and thus, shear banding effects in the depth (vorticity) direction could not be observed.

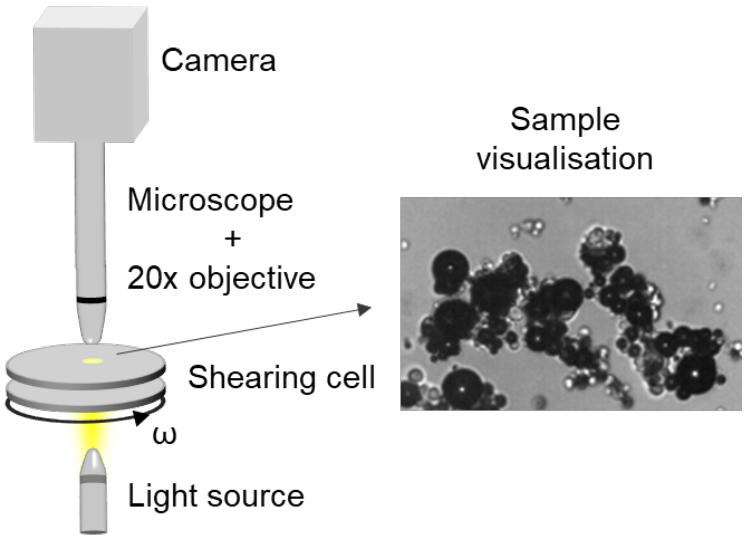

Figure 2.9. Experimental setup of the optical shearing technique. The system consists of an optical shearing cell, a microscope assembly, a high-speed camera and LED illumination.

The captured images were analysed in MATLAB and various aggregation indices and metrics were estimated in order to quantify the degree of particle clustering in some of the suspensions. These are: the aggregation index (A) (Kaliviotis et al., 2016), the image intensity correlation (Dusting et al., 2009), the mean standard deviation of the image intensity (Kaliviotis et al., 2016) and the ratios of the particle free areas in the image (void) to either the corresponding areas covered with particles (solid) or the total image area (total). The image intensity correlation is a measure of the difference in mean intensity between successive images for a given shear rate and is expected to vary as shear increases. Estimates of all these parameters were produced through image analysis and normalised with the corresponding values at maximum shear rate.

The aggregation index (A) is defined as the ratio of the total observed particle free area to the expected particle free area according to the applied particle volume fraction (φ) (eq. (2.10)). In the non-aggregated case, particles are arranged mostly to a monolayer due to the small gap (100 μm). However, when agglomeration occurs the particles form a 3D structure which is inaccessible through the conventional microscope. This results in decreasing the 2D projected area covered with particles observed under the microscope and gives rise to the estimated aggregation index.

$$A = \frac{Total\ particle\ free\ area}{(1-\varphi)\ Total\ area}\ 100\% \tag{2.12}$$

Other metrics based on image analysis were also employed to evaluate and quantify particle aggregation under varying shear rates, such as the image intensity correlation (I_{ij}) given in eq. (2.11), as well as the A_{void} and A_{total} defined in eqs. (2.12) and (2.13).

$$I_{ij} = \frac{\sum_{i=1}^{w}\sum_{j=1}^{w}(A_{ij}-\bar{A})(B_{ij}-\bar{B})}{\sqrt{\sum_{i=1}^{w}\sum_{j=1}^{w}(A_{ij}-\bar{A})^2\sum_{i=1}^{n}\sum_{j=1}^{n}(B_{ij}-\bar{B})^2}}\ 100\% \tag{2.13}$$

where I_{ij} is the image intensity of two subsequent images A and B at pixel location (i, j) and w the interrogation window, taken equal to the whole image in the present case.

$$A_{void} = \frac{Total\ particle\ free\ area}{Total\ area\ covered\ by\ particles}\ 100\% \tag{2.14}$$

$$A_{total} = \frac{Total\ particle\ free\ area}{Total\ \text{image}\ area}\ 100\% \quad (2.15)$$

Custom-made algorithms built in MATLAB were used to perform the various image processing steps required to estimate the particle free areas in the acquired images. A sample describing the basic steps followed is shown in Figure 2.10. First, the original images (Figure 2.10a) were filtered to correct for the non-uniform illumination but also remove static image artefacts arising from dirt/dust on the optics and the resulting image is shown in Figure 2.10b. Subsequently, a local thresholding function was applied to obtain the binarized images (Figure 2.10c), which would enable the quantification of the areas in pixel of the agglomerates. The next few steps (Figure 2.10d-f) involved morphological processing of the images using the dilate and erode functions to allow to reconstruct the particle agglomerate structures. A mask was constructed and applied at the last stage of the image processing to fill the smaller empty areas within the agglomerates. Structures that were irrelevant to the particles were also removed at the last stage (Figure 2.10g). The areas free of particles, turned to white in the final binarized images, were labelled and then measured by applying the regionprops function incorporated in MATLAB in order to derive the necessary parameters for estimating the aggregation indices.

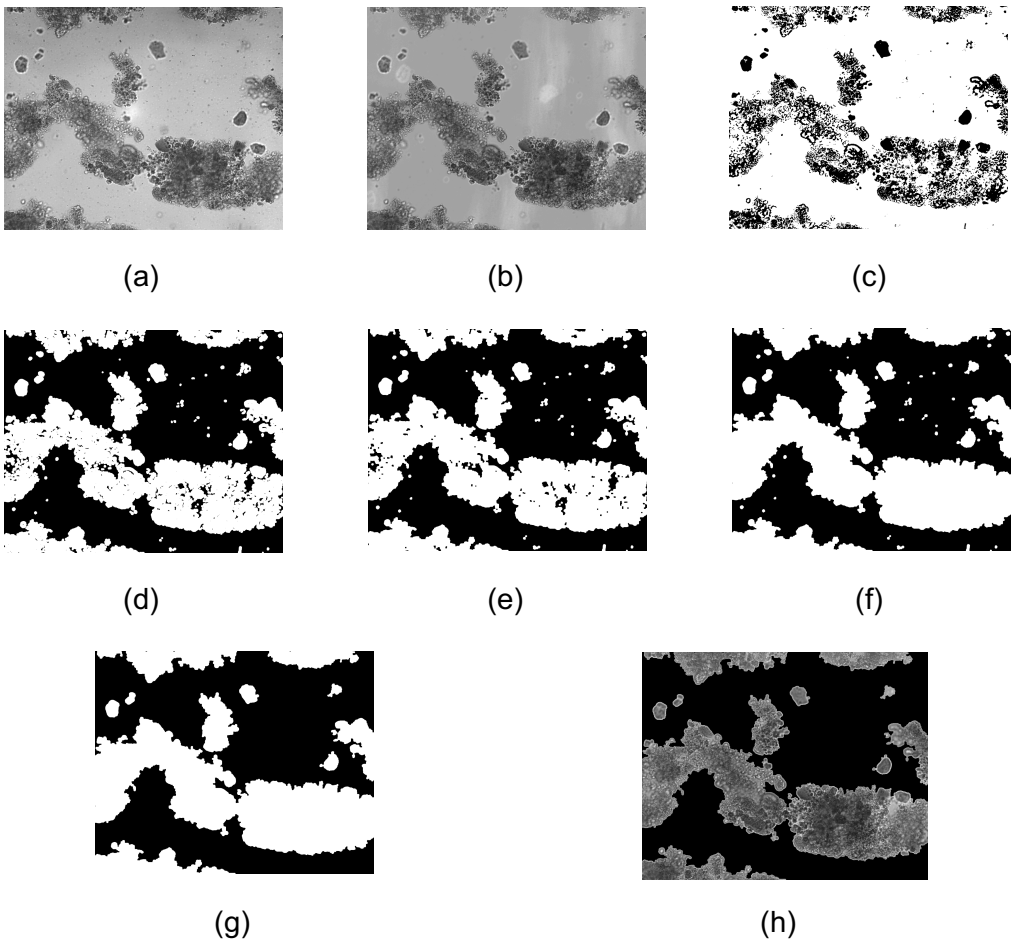

Figure 2.10: Sample images describing the basic steps of the image processing starting from a) the original image; b) original image after subtracting the background; c) binarized image by applying local thresholding; d)-f) applying dilation and erosion to the edges of the agglomerates to obtain closed structures; g) final binarized image & h) binarized image superimposed on the original image. The images correspond to a 3% v/v suspension of abrasives in mineral oil.

However, optical methods are not always applicable, especially at very high particle concentrations where the suspension becomes opaque and thus, the image is completely covered with particles. The latter makes it very hard to monitor particle agglomeration and disaggregation using optical techniques. In such cases, meaningful information about the material microstructure can be derived through bulk rheology and especially, Large Amplitude Oscillatory Shear (LAOS) measurements, commonly used to study the microstructure and also, classify complex fluids including filled rubbers and particle suspensions.

2.5.2 Large Amplitude Oscillatory shear (LAOS)–high particle concentration limit

LAOS measurements were performed for strain amplitudes between 0.01 and 1000% at various frequencies ranging from 0.5 to 30 Hz. LAOS measurements aimed at investigating the nonlinear viscoelastic properties of the suspensions that reflect the evolution of microstructure changes under large strains, which are very common during large scale batch manufacturing. The raw oscillatory stress waveforms were analysed using the Fast Fourier Transform (FFT), incorporated in TRIOS software, to derive the non-linear viscoelastic parameters. In the linear viscoelastic region (LVR), the Fourier spectrum is expected to contain only one frequency, while in the non-linear regime higher odd harmonics can also be present (odd multiples of the input frequency). The highest harmonic to be considered for the stress signal reconstruction is selected from the Fourier spectrum, so as to maximize the signal to noise ratio and the smoothed signals are then reconstructed accordingly (Ewoldt et al., 2008). This processing enables the derivation of the non-linear parameters related to LAOS measurements, such as the Lissajous-Bowditch plots, the minimum/maximum strain-dynamic moduli and the minimum/maximum strain rate-dynamic viscosity. The validity of the analysis was evaluated by comparing the raw data (storage and loss moduli) with the reconstructed ones from the FFT and a very good agreement between the two was observed.

More specifically, the G' and G'' moduli values obtained directly from the rheometer are based on the assumption that the stress response of the material under testing is a pure sinusoid ($\tau = \tau_0 sin(\omega t + \delta)$). However, under LAOS the existence of higher harmonics leads to non-linear and non-sinusoidal stress waveforms that comprise the sum between the first and additional harmonic stresses ($\tau = \sum_1^{N=odd} \tau_n sin(n\omega t + \delta_n)$). Under these non-linear conditions, the storage and loss moduli measured experimentally lose their physical meaning and thus, Ewoldt et al. (2008) introduced more physically meaningful non-linear viscoelastic moduli based on the local material response at small and large instantaneous strains and strain rates in one oscillatory cycle. These moduli are illustrated in Figure 2.11 and the corresponding equations are presented below that.

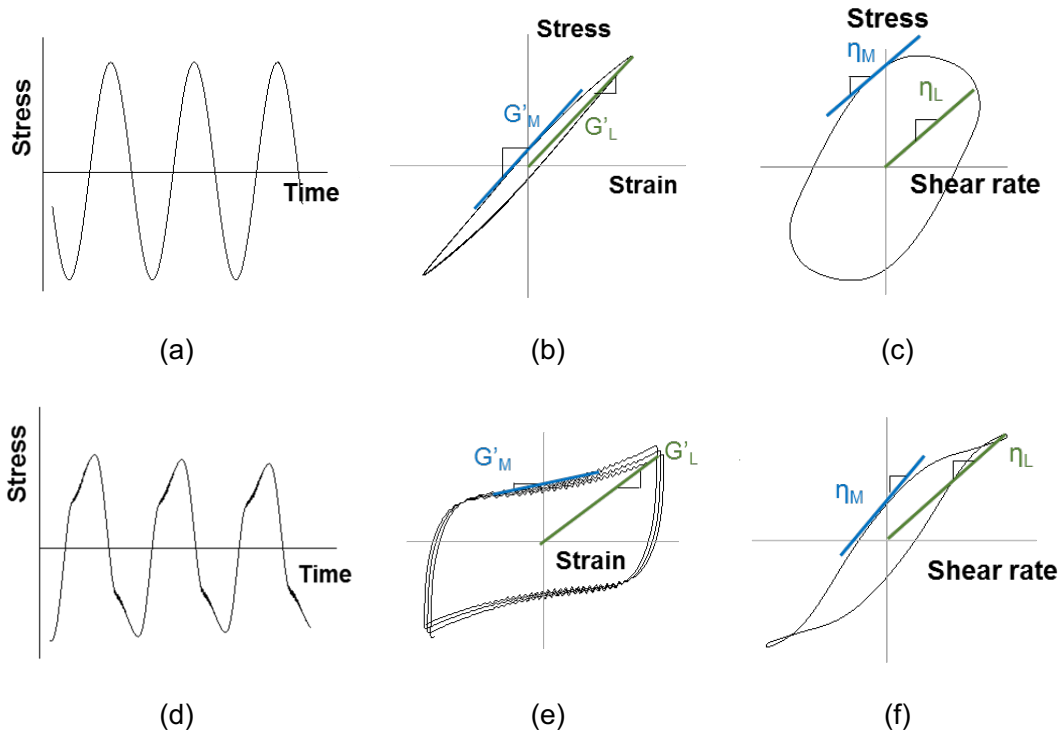

Figure 2.11: a) & d) Raw stress waveforms; b) & e) typical elastic Lissajous-Bowditch plots, c) & f) typical viscous Lissajous-Bowditch plots in the LVE (top) and non-linear strain amplitude range (bottom).

$$G'_M = \left|\frac{d\tau}{d\gamma}\right|_{\gamma=0} \tag{2.16}$$

$$G'_L = \left|\frac{\tau}{\gamma}\right|_{\gamma=\pm\gamma_0} \tag{2.17}$$

$$\eta_M = \left|\frac{d\tau}{d\dot{\gamma}}\right|_{\dot{\gamma}=0} \tag{2.18}$$

$$\eta_L = \left|\frac{\tau}{\dot{\gamma}}\right|_{\dot{\gamma}=\pm\dot{\gamma}_0} \tag{2.19}$$

where G'_M and G'_L represent the dynamic elastic moduli and η_M and η_L the corresponding dynamic viscosities at minimum and maximum instantaneous strain in one oscillatory cycle. γ_0 is the input strain and $\dot{\gamma}_0$ is the input strain rate. At an oscillatory cycle the strain and strain rate are orthogonal to each other, which means that when the strain is zero the strain rate is maximum and vice versa. In the linear viscoelastic region, both G'_M and G'_L reduce to the first order harmonic moduli, G'_1, which corresponds to the measured modulus. The same principle applies to the

dynamic viscosities as well. Those elastic and viscous components can be further used to quantify the intra-cycle viscoelastic non-linearities through the stiffening ratio, S, and the thickening ratio, T, defined as follows:

$$S = \frac{G'_L - G'_M}{G'_L} \tag{2.20}$$

$$T = \frac{\eta_L - \eta_M}{\eta_L} \tag{2.21}$$

In the LVR both S and T should be equal to zero whereas in the non-linear region S and T can take negative or positive values. In particular, the elastic response is strain hardening when $S > 0$ and strain softening when $S < 0$. Accordingly, the viscous response is intra-cycle strain rate thickening if $T > 0$ and strain rate thinning if $T < 0$. However, the sign of these parameters should not be confused with the strain thinning or strain thickening behaviour of the viscoelastic moduli by increasing the strain amplitude. S and T comprise measures of the difference in magnitude between the minimum and large local response of the material and thus, by calculating them we can derive information on the origins of the intra-cycle non-linearities. For example, if the G'_M or η_L (maximum strain rate) decrease more rapid than G'_L or η_M correspondingly ($S > 0$ and $T < 0$), the non-linearities originate from the viscous component of the material since they are strain rate driven. When the opposite behaviour is observed (i.e. the G'_L or η_M decreases faster than G'_M or η_L), the non-linearities are strain driven and the elastic component of the material dominates the response (Ewoldt et al., 2008; Hyun et al., 2011; Khandavalli and Rothstein, 2015).

2.6 Repeatability and error

All rheological measurements were conducted in triplicate to ensure repeatability of the results. The measured data were mainly obtained from different loadings of the same sample batch on the rheometer. The average values of the rheological properties were then estimated from the three sets of data along with the errors/standard deviation of the mean value. In the case of errors higher than 5%, the data from this measurement were excluded and a new measurement was performed either using the same batch or a new one. In the following sections, the data are presented as mean values with their corresponding error bars. To further minimise errors occurring during sample preparation, the same batch of solvent either

Newtonian or non-Newtonian was used for each series of measurements, while extra care was taken to achieve correct sample loading to the rheometer. The glycerol was stored under appropriate conditions and in tightly closed containers to avoid moisture absorption, while its rheological properties, i.e. viscosity, were always checked before use to evaluate its quality.

The viscosity and shear stress data influenced by Brownian motion or particle sedimentation were excluded from the flow curves based on the values of Pe and Sh numbers to avoid additional complication of the observed rheological phenomena. The samples were measured right after preparation to prevent particle sedimentation in the container.

The fittings of the different empirical models to the data, e.g. Carreau, Krieger-Dougherty, Quemada, were selected based on the R^2 values as being above 0.90. The values of R^2 were automatically estimated from Origin. To minimise the error during image processing, the images were initially filtered, and the background noise was subtracted before the binarization step. Shearing time in the rheo-optics cell as well as image acquisition time were adjusted at each shear rate to ensure a steady state condition was achieved. This was selected based on initial experiments at different time periods.

2.7 Concluding remarks

This chapter presented the characteristics of the particles and solvents used in the present study. The different techniques employed to study/tune suspension rheology and microstructure were described alongside an explanation of the data analysis performed. The next chapter (Chapter 3) will present the rheological properties of the three types of particle suspensions in glycerol and the shear thinning response of the suspensions will be described on the basis of a friction driven mechanism.

Chapter 3

Frictional particle suspensions [1]

The aim of this chapter is to explore the friction-driven mechanism of shear thinning in non-colloidal smooth and rough silica particle suspensions in a non-aqueous Newtonian solvent (glycerol). The rheology of suspensions of two types of commercial silicas, commonly used as abrasives and fillers in toothpaste formulations, in glycerol will be compared with that of suspensions of relatively smooth glass spheres with a similar size distribution under the same experimental conditions, to investigate how differently the non-idealized particles behave compared to the spherical particles. The effect of the different parameters, such as particle surface morphology, porosity and specific surface area, on the shear thinning of the suspensions will be discussed in the light of microstructural changes under shear and interparticle and particle-solvent interactions.

The chapter is divided in four main sections. Section 3.1 will provide a brief introduction of the different parameters affecting suspension rheology and the main mechanisms inducing non-Newtonian behaviour reported in the literature. Section 3.2 will firstly present the measured rheological properties, i.e. relative viscosity (η_r) and shear stress (τ), of the three types of particles with different surface morphologies suspended in glycerol as a function of shear rate and particle volume fraction at room temperature. The dynamic response of the suspensions investigated under small amplitude oscillatory shear and frequency sweeps in the linear regime will follow.

[1] Part of this chapter has been published in the Journal of non-Newtonian Fluid Mechanics and Materials.

A. Papadopoulou, J.J.J. Gillissen, H.J. Wilson, M.K. Tiwari, S. Balabani, 2020. ' On the shear thinning of non-Brownian suspensions: friction or adhesion?', *Journal of non-Newtonian fluid Mechanics*, 281, p.104298.

A. Papadopoulou, J.J.J. Gillissen, H.J. Wilson, M.K. Tiwari, S. Balabani, 2020. 'Effect of particle specific surface area on the rheology of non-Brownian silica suspensions.', *Materials, 13, p.4628*.

The rheological behaviour of the suspensions will be discussed in the light of microstructure measurements under applied deformation examined using two different methods: an optical shearing technique for relatively dilute suspensions and large amplitude oscillatory shear (LAOS) measurements for the more concentrated cases.

Rheological measurements acquired at a higher temperature of 60^{o}C, typically encountered in industrial manufacturing, were also acquired and presented in the last part of the results section. These were motivated by the lack of studies on the effect of temperature on highly polydisperse non-Brownian suspensions in contrast to colloidal dispersions that have been extensively studied due to their high importance in heat transfer and many other applications.

The effects of particle surface morphology and porosity on suspension rheology are discussed in section 3.3 on the basis of their specific surface area. A friction-led mechanism, as mentioned above, is utilized to explain the observed shear thinning behaviour, based on the elastic deformation of particle surface asperities leading to a reduced microscopic friction coefficient (Chatté et al., 2018; Lobry et al., 2019). The effects of particle and suspending medium chemical properties are discussed due to their important role in defining interparticle and particle-solvent interactions. The chapter will end with concluding remarks in section 3.4.

3.1 Introduction

Several factors influencing suspension rheology have been reported in the literature. Although particle volume fraction seems to play the most important role, experimental evidence suggests that parameters such as particle surface morphology, shape, size distribution and/or electrical charges combined with the suspending medium physical flow properties and the type of flow/deformation applied, to name just a few, can significantly affect suspension rheology (Gaudio et al., 2013; Jeffrey and Acrivos, 1976; Luckham and Ukeje, 1999; Moon et al., 2015; Niu et al., 2015). Therefore, the effective viscosity of a particulate system can be described as a function of various parameters:

$$\eta_r = f(r, \rho_p, \rho_f, \varphi, \eta_f, k_B\theta, \dot{\gamma}, t) \tag{3.1}$$

where φ is the particle volume fraction, r a characteristic particle size, ρ_p the particle density, ρ_f the fluid density, η_f the viscosity of the suspending medium, $k_B\theta$ the

thermal energy (k_B: Boltzmann constant = $1.38 \cdot 10^{-23}$ JK^{-1}), $\dot{\gamma}$ the shear rate and t the time.

More specifically, the addition of particles to a Newtonian medium increases the viscosity of the solvent and can induce non-Newtonian rheology at sufficiently high φ values. Solid particles act as rigid objects which can move and rotate with the fluid upon shearing conditions, but they can also resist the applied flow field due to inertia. This resistance imposes an additional stress in the flow leading to a rise in the viscosity values (Chen et al., 2010; Zarraga et al., 2000); this increase highly depends on particle volume fraction (φ). Many empirical models exist in the literature describing the relative viscosity of the suspension as a function of φ and can be well applied to dilute and semi-dilute suspensions (Batchelor and Green, 1972; Genovese, 2012; Irvin M Krieger and Dougherty, 1959). However, most of them fail to predict the dense concentration regime.

Not only the particle concentration but also other parameters such as particle size and size distribution and particle surface morphology and shape can significantly affect suspension rheology. For monodisperse suspensions comprising particles in the non-Brownian regime, i.e. particle diameter $d > 1\,\mu m$, smaller particles are expected to show lower viscosity values and require higher φ to induce non-Newtonian rheology. This is due to the smaller particles moving more freely into the solvent compared to the larger particles that tend to 'lock' in certain positions due to the large interparticle gaps, inducing higher resistance to the applied flow field (Konijn et al., 2014; Pavlik, 2009).

In industrial formulations, particles are often widely polydisperse and this leads to more complex rheological phenomena that are yet to be fully understood. Polydisperse systems show lower relative viscosities and higher maximum packing fractions compared to monodisperse particle suspensions which has been widely attributed to a lubrication effect caused by the smaller particles filling the gaps between the larger ones (Chang and Powell, 1994; Gamonpilas et al., 2016a; Genovese, 2012; Luckham and Ukeje, 1999; Stickel and Powell, 2005). A modification of the Krieger-Dougherty equation has also been proposed in the literature to relate the relative viscosity and the maximum packing fraction with the particle size distribution, as depicted in eq. (2.11) ($\eta_r = [1 + (b\varphi/(1 - \varphi/\varphi_m))]^{3.3\varphi_m}$) (Servais et al., 2002).

The surface morphology and porosity of particles typically used in manufacturing also contribute to the complex rheological phenomena in particulate formulations. In general, rough particles increase suspension viscosity due to the extra energy

dissipation occurring under shear flow. Most recently, the presence of surface asperities has been found responsible for inducing shear thinning rheology. Considering the surface irregularities (roughness) as elastically deformable, it was demonstrated that shear thinning stems from a reduced microscopic friction coefficient between the particles as their surface asperities deform during contact (Chatté et al., 2018; Lobry et al., 2019; Vázquez-Quesada et al., 2017). Increasing particle porosity is also expected to affect suspension rheology by increasing the viscosity values and inducing non-Newtonian phenomena at lower particle volume fractions. This can be understood on the basis of the solvent being absorbed into the particle pores, thus increasing the effective volume fraction of the particles in the suspension (Olanrewaju et al., 2013).

The relation between the particle and fluid density can affect suspension rheology and lead to a misinterpretation of the acquired data. The suspensions need to be neutrally buoyant in order to avoid sedimentation effects during rheological measurements. In the case that particle and fluid densities cannot be fully matched, sufficiently high shear stresses need to be applied so as to ensure particle redispersion across the sample in the measuring system. The required amount of stress to induce particle redispersion is described through the dimensionless Shields number, as described in Chapter 2 (eq. (2.3), $Sh = \tau/(D\Delta\rho g) > 1$). Since the particles in a suspension interact via the suspending medium, a highly viscous fluid or a fluid whose chemical properties are close to those of the particles can restrict interparticle interactions and suppress the non-linear rheology.

It is clear that a great number of parameters influence suspension rheology. Despite the huge amount of research effort on investigating the specific mechanisms that control suspension rheology, it still remains unclear how the combined effects of particle surface morphology, roughness and polydispersity (especially, in the non-Brownian regime), commonly encountered in industrial formulations, as well as the physical properties of the carrier media affect interparticle interactions and thus, rheology. The work presented in this chapter aims to elucidate the effects of particle surface roughness and porosity on silica suspension rheology and provide a framework for their behaviour under shear. This will further aid in the optimization of manufacturing processes but also the development of constitutive models that can fully capture suspension rheology independent of particle characteristics.

3.2 Results

3.2.1 Shear rheology as a function of particle volume fraction

The measured relative viscosity (η_r=$\eta_{\text{suspension}}/\eta_{\text{fluid}}$) and the shear stress ($\tau$), of the three types of particles described in Chapter 2 suspended in glycerol are presented in Figure 3.1. A clear dependence of suspension rheology, and in particular, the extent of non-Newtonian rheology, on shear rate ($\dot{\gamma}$) and particle surface characteristics and porosity can be observed. In the range of concentrations studied, the 'smooth' glass spheres (Figure 3.1a and b) show very weak shear thinning behaviour, while mild shear thickening is observed at sufficiently high particle volume fractions close to the maximum packing (i.e. $\varphi \geq 0.50$). On the contrary, the abrasive silicas suspensions (Figure 3.1c and d) exhibit pronounced shear thinning response at much lower particle volume fractions, i.e. $\varphi \geq 0.25$. Interestingly, the onset of shear thinning occurs at even lower φ values for the filler silica particles (Figure 3.1e and f) compared to the other two types of suspensions, $\varphi \geq 0.10$. A mild shear thickening response can also be observed for the filler silicas at $\varphi \geq 0.15$. It should be noted that the filler particles could only be dispersed up to $\varphi = 0.20$ during sample preparation. The Carreau equation can well describe the shear thinning response of the suspensions and the fittings to the data are presented as continuous lines in Figure 3.1c and e.

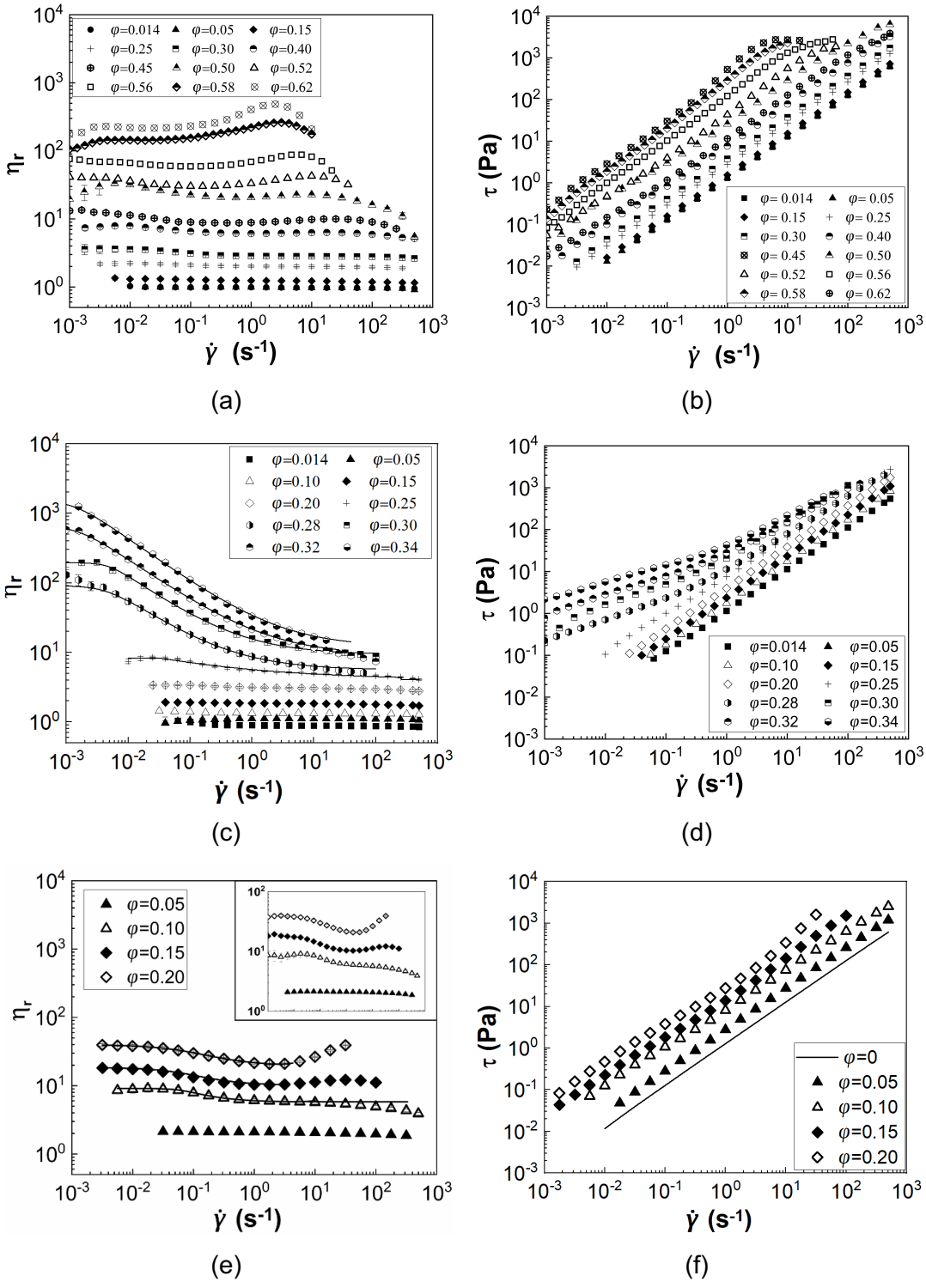

Figure 3.1: Relative viscosity (η_r) (left) and shear stress (τ) (right) of all three types of suspensions as a function of shear rate ($\dot{\gamma}$) and particle volume fraction (φ) at 20°C; a) & b) glass spheres, c) & d) abrasive silicas; e) & f) filler silicas. Continuous lines in figures c) and e) correspond to the Carreau fittings of the viscosity data.

The effect of particle volume fraction is better depicted in Figure 3.2, where the zero shear rate ($\eta_{r,0}$) and the infinite shear rate ($\eta_{r,\infty}$) relative viscosities are plotted against φ, while fittings of the data with the corresponding theoretical models

described in Chapter 2 with eqs. (2.9) to (2.11). The Carreau fittings are used to estimate the $\eta_{r,0}$ and $\eta_{r,\infty}$ of the abrasive and filler silica suspensions, while for the glass sphere suspensions they are estimated by extrapolating the viscosity data at $\dot{\gamma} = 0.001\ s^{-1}$ and $\dot{\gamma} = 500\ s^{-1}$ respectively. The $\eta_{r,\infty}$ values for all suspensions were taken at the shear thinning region, i.e. before the onset of shear thickening occurred As expected, increasing the particle volume fraction increases suspension viscosity due to the additional stress dissipated from the movement of the solids under shear; this is also dependent on particle surface morphology and porosity.

The glass sphere suspensions (Figure 3.2a) show the typical behaviour of spherical particles suspended in a Newtonian fluid and can be described sufficiently well by all the empirical models applied. The relative viscosities at the selected shear rates almost overlap over the whole φ range, since no shear thinning was observed for these suspensions. Abrasive silicas (Figure 3.2b) increase the viscosity of glycerol at a higher rate compared to the glass spheres due to the presence of surface roughness offering a higher area available for particle contacts (Blanc et al., 2018; Moon et al., 2015), while the pronounced shear thinning response is depicted through the large difference of the η_r values between the zero ($\eta_{r,0}$) and infinite shear rate ($\eta_{r,\infty}$). The $\eta_{r,\infty}$ values were well fitted with all three empirical models applied similar to the glass sphere suspensions. In contrast, only the Quemada model (eq. (2.10)) can fit well the $\eta_{r,0}$ values.

The filler silicas (Figure 3.2c) appear to induce a steeper increase on the viscosity of glycerol compared to the other two types of suspensions. The mild shear thinning behaviour of these suspensions can be seen by the small differences between the $\eta_{r,0}$ and $\eta_{r,\infty}$ values. The Krieger-Dougherty (eq. (2.9)) and the model for polydisperse systems (eq. (2.11)) completely failed to describe the complex behaviour of the filler silicas, while the Quemada equation provides a poor fit to the experimental data. In general, the Quemada model (eq. (2.10)) seems to describe most of the experimental data. The latter might be attributed to the fact that the Quemada model has only one degree of freedom, i.e. the maximum packing fraction, rendering easier the adjustment of one parameter to fit the data, compared for example, to Krieger-Dougherty, which has two unknown parameters (maximum packing fraction and intrinsic viscosity).

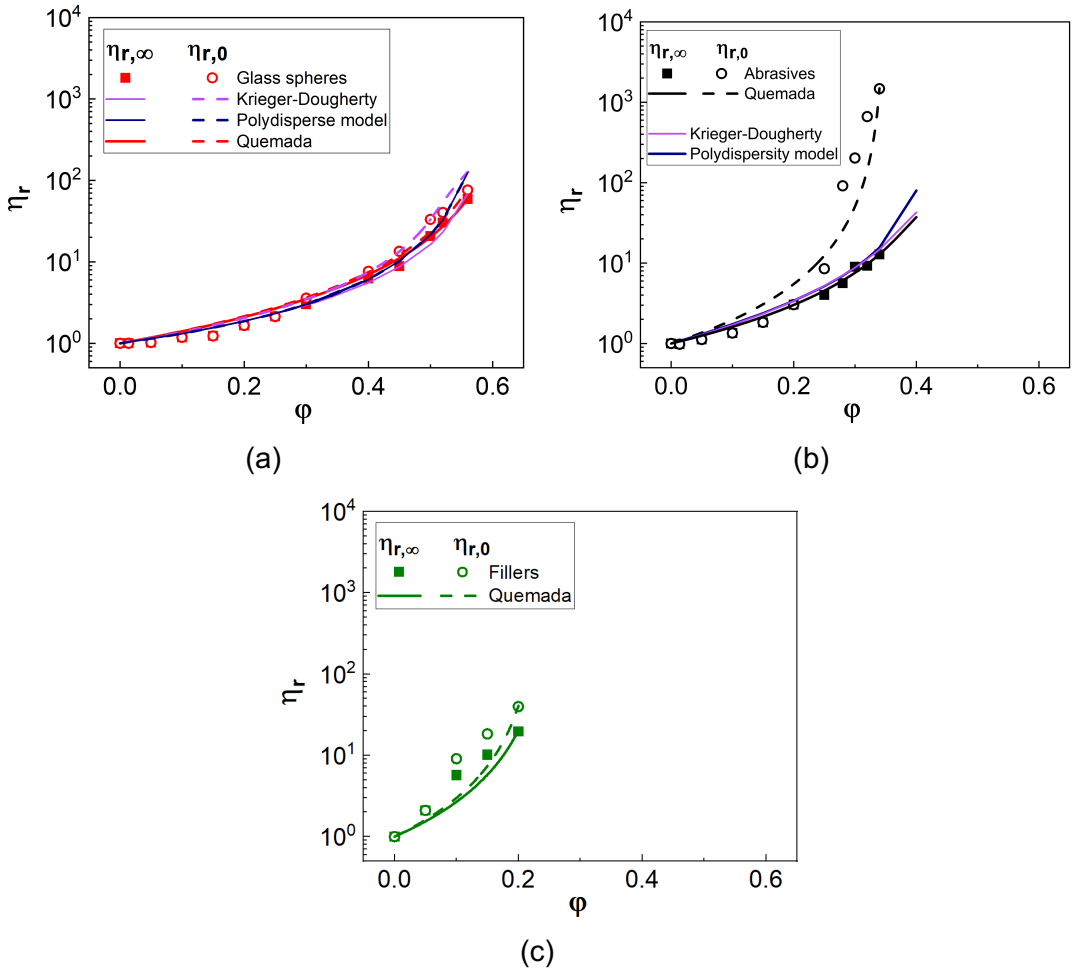

Figure 3.2: Zero shear rate ($\eta_{r,0}$) and infinite shear rate ($\eta_{r,\infty}$) relative viscosities as a function of particle volume fraction (φ) at 20°C. Continuous lines correspond to fittings of the empirical equations to the $\eta_{r,\infty}$, while dashed lines refer to the fittings of the $\eta_{r,0}$ data. a) glass spheres, b) abrasive silicas and c) filler silicas. The $\eta_{r,\infty}$ values for all suspensions were taken at the shear thinning region, i.e. before the onset of shear thickening occurred. The Quemada equation managed to fit most of the datasets sufficiently well which could most likely be attributed to the one degree of freedom of this model.

Table 3.1 lists the estimated parameters derived from the fittings of the different empirical equations to the data in Figure 3.2. It can be seen that glass spheres show lower intrinsic viscosities (B) and higher maximum packing fractions (φ_m) compared to both types of rough silicas. The presence of surface roughness can increase the B values, while in parallel, decreasing φ_m by increasing the density of the available contact areas between the particles and leading to stronger interparticle interactions. Additionally, although the glass spheres are highly polydisperse as shown in Figure 2.2, the estimated φ_m values for both shear rate areas are close to those reported in the literature for random closed packed monodisperse spheres ($\varphi_m = 0.64$) (Denn and Morris, 2014; Stickel and Powell, 2005). This might be attributed to the use of glycerol as a suspending medium which prevents the particles from coming in close

proximity. No specific values of the φ_m are reported in the literature for rough and polydisperse particles as the abrasives and fillers to compare against.

Slightly lower φ_m values were also obtained for the zero shear rate relative viscosity ($\eta_{r,0}$) fitting for all particle suspensions. At low shear rates particles might experience frictional contacts with the neighboring particles leading to lower particle loading loadings and thus, decreasing the maximum packing of the suspension (Mewis and Wagner, 2012). On the other hand, at sufficiently high shear rates, particle contacts are less constrained due to a reduction in the microscopic friction coefficient, leading to higher φ_m values.

Table 3.1: Fitting parameters estimated from the different empirical equations ((2.9) to (2.11)) applied to the relative viscosity versus φ data of the glass sphere, the abrasive silica and the filler silica suspensions at 20°C. B is the intrinsic viscosity, φ_m is the maximum packing fraction and b is a fitting parameter to account for particle polydispersity.

Estimated parameters / η_r	**Krieger-Dougherty (1959)**		**Servais et al. (2002)**		**Quemada (1978)**
	$\boldsymbol{B}$	$\boldsymbol{\varphi_m}$	$\boldsymbol{\varphi_m}$	$\boldsymbol{b}$	$\boldsymbol{\varphi_m}$
Glass spheres					
$\boldsymbol{\eta_{r,0}}$	2.92	0.57	0.60	1.24	0.63
$\boldsymbol{\eta_{r,\infty}}$	2.60	0.60			0.64
Abrasive silicas					
$\boldsymbol{\eta_{r,0}}$	-	-	-	-	0.35
$\boldsymbol{\eta_{r,\infty}}$	4.80	0.51	0.43	3.65	0.47
Filler silicas					
$\boldsymbol{\eta_{r,0}}$	-	-	-	-	0.24
$\boldsymbol{\eta_{r,\infty}}$	-	-	-	-	0.26

The above results should be interpreted in the light of strong interaction between particles (glass sphere or irregular silicas) with glycerol, which will dominate inter-particle interactions and/or particle agglomeration. Both glycerol and silicas are hydrophilic with a copious amount of hydroxyl groups (-OH). Although, silicas tend to attract to themselves through the free hydroxyl groups on their surface, when suspended in a polar solvent equipped with hydroxyl groups, such as glycerol, a so-called solvation layer is formed around the particles (Amiri et al., 2012; Raghavan et al., 2000), which acts as a lubricant preventing interparticle attraction. The thickness and strength of this solvation layer is strongly dependent on glycerol's viscosity, which

can be modified through temperature variations or the addition of water (Amiri et al., 2012; Gao et al., 2017; Saint-Michel et al., 2019). Therefore, we should expect the rheology of both glass sphere and silica suspensions in glycerol to be strongly influenced by the particle-solvent interactions.

3.2.2 Elucidating the frictional nature of shear thinning

Friction enabled thinning offers a plausible means to understand the results in Figure 3.1. This theory employs the concept of a critical normal load to describe the shear thinning behaviour (Archard, 1957; Chatté et al., 2018; Lobry et al., 2019). More specifically, Lobry et al. (2019) and Chattè et al. (2018) combined simulations with experiments, using non-Brownian polystyrene (PS) particles in silicone oil and polyvinyl chloride (PVC) particles in a plasticizer respectively. Their work confirmed the findings of Archard (1957), reporting that in a few-asperity system (i.e. where particles contain relative sparse number of asperities) elastic deformation of the surface topology occurs when two surfaces (i.e. particles in the case of suspension) are pushed together; this further leads to a reduction in the friction coefficient and shear thinning rheology. In other words, particle surface asperities are directly linked to modulation of friction between particles responsible for shear thinning rheology. At sufficiently high normal loads, plastic deformation of the surface asperities can occur as well, but this effect was found weak and hence not considered in their model.

Clearly for smooth glass spheres, the surface asperities are negligible and alongside the presence of a thick solvation layer formed around the particles from glycerol, leads to limiting interparticle contacts, resulting thus in a significant suppression of the shear thinning response. This is in contrast to the observations of Saint-Michel et al. (2019) who reported considerable shear thinning of glass sphere suspensions in an aqueous solution. However, in the presence of water a higher interparticle interaction is expected due to the much lower viscosity of the solvent and the fact that water molecules have only one hydroxyl group (-OH) to bind onto silicas, compared to glycerol which has three. On the other hand, at very high particle loadings, beyond which long range, jamming networks occur, i.e. at $\varphi > 0.50$, shear thickening, is observed for the glass sphere suspensions.

The commercial silica particles employed in the present study comprise aggregates of primary (nanoscale) particles, which effectively can serve as asperities in this case. Although a solvation layer also exists around these particles, it is speculated that the surface asperities can deform or even penetrate it easier compared to the relatively smooth glass spheres and thus, induce a shear thinning

rheology. The shape of the particles as shown in Figure 2.4, also indicates that abrasive silicas appear slightly rougher than filler silicas, implying that abrasive silicas might be more efficient in penetrating that solvation layer. The theory of Lobry et al. (2019) will thus be applied to explain the pronounced shear thinning exhibited by the abrasive silica suspensions. The PS particles used in the work of Lobry et al. (2019) have a much lower Young modulus ($3 \cdot 10^9$Pa) than the abrasive silicas (Young modulus: $66.3 \cdot 10^9$Pa). However, the shear stresses presented in Figure 3.1d extend to slightly higher values compared to these reported in the experiments of Lobry et al. (2019). Thus, frictional shear thinning could serve as a plausible explanation for the observed shear thinning rheology of the abrasive silica suspensions.

It should be recalled that a solvation layer also exists for the abrasive silicas which can act as a barrier to the interparticle contacts, especially at low shear rates/stresses. Many researchers have reported the effect of the solvation layer formed by the suspending medium around the particles on suspension rheology (Amiri et al., 2012; Chu et al., 2014; Gao et al., 2017; Raghavan et al., 2000). However, very little knowledge exists about its strength and subsequently its possible deformation or even rupture under shear.

Shear thinning due to interparticle frictional contacts has been reported in recent studies for non-Brownian lubricated particles. For example, Saint-Michel et al. (2019) highlighted the contribution of the contact viscosity to the shear thinning behaviour of glass beads ($d_{average} = 250\mu m$) in an aqueous solution. In this study, shear reversal experiments revealed the presence of interparticle frictional contacts at shear stresses as low as 11 Pa (Saint-Michel et al., 2019). Blanc et al. (2018) also related suspension shear thinning with interparticle frictional contacts by using polystyrene particles ($d_{average} = 80\mu m$) in a Newtonian silicone oil. The measured shear stress in the latter were between $\tau = 10\ Pa$ and $\tau = 100\ Pa$.

The shear stresses in Figure 3.1c span several decades, i.e. between $\tau = 10^{-1}Pa$ and $\tau = 10^{3}Pa$. The abrasive silicas are rough, irregularly shaped and highly porous, leading to an increase in the effective volume fraction at least by a factor of 2 compared to the apparent. It can thus, be postulated that shear thinning in the dense abrasive silica suspensions is initiated by the deformation of the solvation layer formed by glycerol. Increasing the shear rate leads to gradual rupturing of the solvation (hydration) layer, which enables the frictional contacts between the particle surface asperities and gives rise to the observed shear thinning rheology. A further analysis of this mechanism is provided in the following paragraphs.

The shear thinning flow curves (Figure 3.1c) of these suspensions is described well by the Carreau model for 0.25≤ φ ≤0.34, while the estimated parameters (relaxation time, λ and flow index, n) are summarised in Table 3.2. A critical stress (τ_c) required for frictional contacts to occur needs to be estimated, in order to apply this theory to the acquired data. To this end, the $\lambda\dot{\gamma}$ term in the Carreau model is equated to the ratio of the suspension total stress to the critical stress (i.e. $\lambda\dot{\gamma} = \eta_r\eta_f\dot{\gamma}/\tau_c$), which gives:

$$\tau_c = \frac{\eta_r\eta_f}{\lambda} \tag{3.2}$$

The above relation was utilised as a means to convert the shear rate parameter in the Carreau model to an equivalent shear stress and is based on the assumption as follows: The suspension relative viscosity (η_r) was taken in the middle of the shear thinning region of the relative viscosity versus shear rate curve (Figure 3.1c), which was more indicative for the λ estimation during fitting, and the corresponding shear rates are also presented in Table 3.2 (Papadopoulou et al., 2020).

Table 3.2: Relaxation time (λ) as derived from the Carreau fittings in Figure 3.1c. Relative viscosities (η_r) and the corresponding shear rates ($\dot{\gamma}$) for the estimation of the critical stress values (τ_c) and the critical load (L_c) for the abrasive silica suspensions at 20°C.

φ	**0.25**	**0.28**	**0.30**	**0.32**	**0.34**
$\boldsymbol{\lambda}$ **(s)**	34.2	225.8	202.2	640.7	677.5
$\boldsymbol{\eta}$	8.3	45.1	48.6	149.8	167.7
$\dot{\boldsymbol{\gamma}}$ **(s^{-1})**	0.2	0.025	0.1	0.03	0.08
$\boldsymbol{\tau_c}$ **(Pa)**	0.2	0.2	0.2	0.2	0.3
$\boldsymbol{L_c}$ **(nN)**	0.2 ($\boldsymbol{\tau_{c,average}}$=0.2±0.02 Pa)				
$\boldsymbol{h_r}$ **(μm)**	0.8				

Interestingly, the estimated critical stress values (Table 3.2) appear to be independent of particle volume fraction, in agreement with the findings of Lobry et al. (2019), as this theory is based on a single-asperity contact state. The critical stress values enabled the estimation of the critical load (L_c) above which frictional contacts occur leading to shear thinning rheology as follows:

$$L_c = \tau_c 6\pi\alpha^2 \tag{3.3}$$

where L_c is the critical load, τ_c the critical stress and α the particle average radius.

The estimated critical load (L_c) was found equal to 0.2 nN (Table 3.2), which is almost two orders of magnitude lower than the one found by Lobry et al. (2019). The low critical normal load estimated for the abrasive silicas can be attributed to the relative high roughness of the particles ($h_r = 0.8\ \mu m$) that facilitates contacts between neighbouring particles at lower loads compared to the relatively smooth particles ($h_r = 0.04\ \mu m$) with very few asperities considered by Lobry et al. (2019).

Based on the Hertzian contact law, which refers to the local stresses generated when two curved surfaces come in contact and slightly deform under the imposed load, the L_c variable is related to the material's mechanical properties (Young modulus, E, Yield strength, Y_0 and Poisson's ratio, n), given in Table 3.3, and the relative radius of the contacting surface asperities; these are described in eqs. (3.4) to (3.7) below:

$$L_c = \overline{L_c}\pi^3 \frac{Y_o}{6} {C_v}^3 \left(h_r \frac{2(1-\nu^2)}{E} Y_0 \right)^2 \tag{3.4}$$

where h_r is the average diameter of the surface asperities, $\overline{L_c}$ represents the full stick contact condition and accounting for the elastic-plastic deformation of the surface asperities at full contact defined as:

$$\overline{L_c} = [8.88\nu - 10.13(\nu^2 + 0.089)] \tag{3.5}$$

and C_v describes the ability of extension or contraction of a material in the direction perpendicular to the direction of the applied deformation, defined as:

$$C_v = 1.234 + 1.256\nu \tag{3.6}$$

By rearranging eq. (3.4) and utilising the data presented in Table 3.3 enabled the estimation of the h_r value (eq. (3.7)) for the abrasive silicas.

$$h_r = \frac{E\sqrt{{L_c}/{\overline{L_c}\pi^3 \frac{Y_o}{6} {C_v}^3}}}{2(1-\nu^2)Y_0} \tag{3.7}$$

A roughness ratio ($= \%\, h_r/\alpha$) of 9% was estimated, which could explain the high relative viscosities measured for the silica particles compared to those reported in the literature for a maximum roughness ratio of 5.3%; the latter was induced by

mechanical grinding on the surface of spherical polystyrene particles with an average diameter of 40 μm suspended in a silicone oil matrix (Tanner and Dai, 2016b).

Table 3.3: Mechanical properties of silicas to estimate the relative roughness of abrasives.

Young modulus, E	66.3 GPa
Yield strength, Y_0	45 MPa
Poisson's ratio (ν)	0.15

An attempt was made to apply the same approach to describe the weak shear thinning response of the filler silica suspensions presented in Figure 3.1e. The corresponding estimated parameters, i.e. relaxation time (λ), viscosity (η) and shear rate ($\dot{\gamma}$) as well as the critical stress (τ_c) are summarised in Table 3.4. For these suspensions the estimated critical stress appeared to be highly dependent on particle volume fraction and no further analysis based on the theory of Lobry et al. (2019) could be conducted. The deviation of the rough fillers from the theory applied to the abrasive silicas might arise from either the limited particle concentration range investigated or the presence of both shear thinning and shear thickening areas in the same curve, which might lead to higher uncertainties in the Carreau model fitting.

Table 3.4: Relaxation time (λ) as derived from the Carreau fittings in Figure 3.1e. Viscosity values (η) and the corresponding shear rates ($\dot{\gamma}$) for the estimation of the critical stress values (τ_c) of the filler silica suspensions at 20°C.

φ	**0.10**	**0.15**	**0.20**
$\boldsymbol{\lambda}$ $(\boldsymbol{s})$	15.0	12.98	8.9
$\boldsymbol{\eta}$	6.3	10.6	22.8
$\dot{\boldsymbol{\gamma}}$ $(\boldsymbol{s^{-1}})$	0.56	0.56	0.56
$\boldsymbol{\tau_c}$ $(\boldsymbol{Pa})$	0.5	1.1	3.3

To further evaluate the effects of surface roughness and induced frictional contacts on the rheology of the suspensions presented above, the 'bootstrap' mechanism proposed by Tanner et al. (2018) was implemented to estimate the microscopic friction coefficients. In essence, this theory is based on the surface roughness increasing the stress between the particles by intensifying the frictional contacts, which subsequently, increases the total stress of the suspension. Assuming that the total shear stress of the suspension is a sum of two components, i.e. the frictionless,

τ^*, and the frictional shear stresses, τ^f, Tanner et al. (2018) proposed the following equation (eq. (3.8)) to describe the relative viscosity of the suspension:

$$\eta_{r,exp} = \frac{\eta_r^*}{\{1 - k\mu_r^* P/\tau\}} \tag{3.8}$$

where $\eta_{r,exp}$ is the relative viscosity obtained from experimental data, η_r^* is the frictionless relative viscosity for smooth particles, k is a constant, μ_r^* is the microscopic friction coefficient for rough particles and P/τ is the particle pressure versus the shear stress. The value of k was taken equal to 1.75 and the P/τ values were taken from literature data derived through mainly numerical studies at $\mu = 0.9$, which is the estimated macroscopic dry friction coefficient between two 'smooth' glass surfaces (Gallier et al., 2014; Tanner et al., 2018).

By rearranging eq. (3.8) the microscopic friction coefficient can be obtained from the experimentally derived relative viscosities using eq. (3.9):

$$\mu_r^* = \frac{\{1 - \eta_r^*/\eta_{r,exp}\}}{k(P/\tau)} \tag{3.9}$$

Table 3.5 summarizes the values of frictionless relative viscosity and the pressure to stress ratio as a function of particle volume fraction (Gallier et al., 2014; Tanner et al., 2018) used to estimate the microscopic friction coefficients proposed by Tanner et al. (2018).

Table 3.5: Particle volume fraction (φ), frictionless relative viscosity (η_r^*) and pressure to stress ratio as estimated by computational studies (P/τ) from Tanner et al. 2018.

φ	η_r^*	P/τ	φ	η_r^*	P/τ
0.10	1.36	0.0023	0.34	4.38	0.34
0.15	1.73	0.0392	0.40	6.12	0.61
0.20	2.10	0.0533	0.50	13.90	1.17
0.28	3.00	0.156	0.52	14.72	1.58
0.30	3.22	0.23	0.56	17.93	2.06
0.32	3.80	0.26			

The estimated friction coefficients using eq. (3.9) for the three types of suspensions in glycerol at 20°C are plotted in Figure 3.3 as a function of the shear rate ($\dot{\gamma}$); the insets in Figure 3.3a and b represent an expanded view of the data estimated to better evaluate the effect of particle volume fraction in each case. The 'smooth' glass spheres (Figure 3.3a) exhibit very low values of the friction coefficient, as expected; the latter are almost totally independent of the shear rate and φ. A slight reduction of μ with shear rate is only observed for the suspension with $\varphi = 0.40$, which also shows

mild shear thinning in the viscosity curve (Figure 3.1a). Overall, these suspensions exhibited negligible shear thinning behaviour under steady state shear.

The estimated μ values for the abrasive silica suspensions (Figure 3.3b) are at least two times higher than those of the glass spheres, and they appear to be highly dependent on both the particle volume fraction and the shear rate (Tanner et al., 2018). The latter is closely related to the shear thinning rheology of the abrasive silicas as depicted in Figure 3.1c. Increasing particle volume fraction, increases the probability of collisions between neighbouring particles, which can give rise to a higher degree of surface asperities deformation at lower shear rates. This phenomenon will lead to a decrease in the microscopic friction coefficient at increasing φ and thus, result in a more pronounced shear thinning rheology of the suspensions according to the theories of Lobry et al. (2019) and Chatté et al. (2018). For shear thinning rheology to occur, the friction coefficient should be a decreasing factor of the sliding speed between the solid surfaces and more specifically, the friction coefficient should decrease at increasing shear rates as more fluid can squeeze through the interparticle gaps acting as a lubricant (Moon et al., 2015; Tanner et al., 2018). At sufficiently high shear rates where the relative viscosity values tend to reach a plateau in Figure 3.1c, the difference between the friction coefficients at different φ becomes relatively smaller.

Filler silica suspensions exhibit higher friction coefficients in relation to the other two types of suspensions. A substantial difference between the values for $\varphi = 0.10$ and $\varphi = 0.15$ and 0.20 can be observed, which shows no relation to the relative viscosities (Figure 3.1e), where both the shear thinning response and the $\eta_{r,0}$ and $\eta_{r,\infty}$ values (Figure 3.2c) appear to increase with φ. Most importantly, a weak dependence of the friction coefficients on the shear rate is observed for this type of suspensions at all φ, which might be associated with the large number of contacting asperities due to the increased surface roughness. The latter can lead to the saturation of the frictional contacts between the particles and the levelling off of the μ values (Lobry et al., 2019).

The estimated μ values for the abrasive and filler silicas are relatively large and much higher than $\mu = 0.9$, i.e. the static friction coefficient for silicas, which can be attributed to the presence of surface roughness and the subsequent increase of the static friction coefficients between the solids (Blair et al., 2001). For example, Blair et. al. reported a threefold increase of the static friction coefficient of rough soda lime glass spheres compared to that of corresponding smooth particles. Therefore, since the P/τ values have been estimated for $\mu = 0.9$, which might be significantly lower

than the real static friction coefficient of the rough particles used in the present study, the microscopic μ shown in Figure 3.3b and c should be subject to uncertainty and treated with caution.

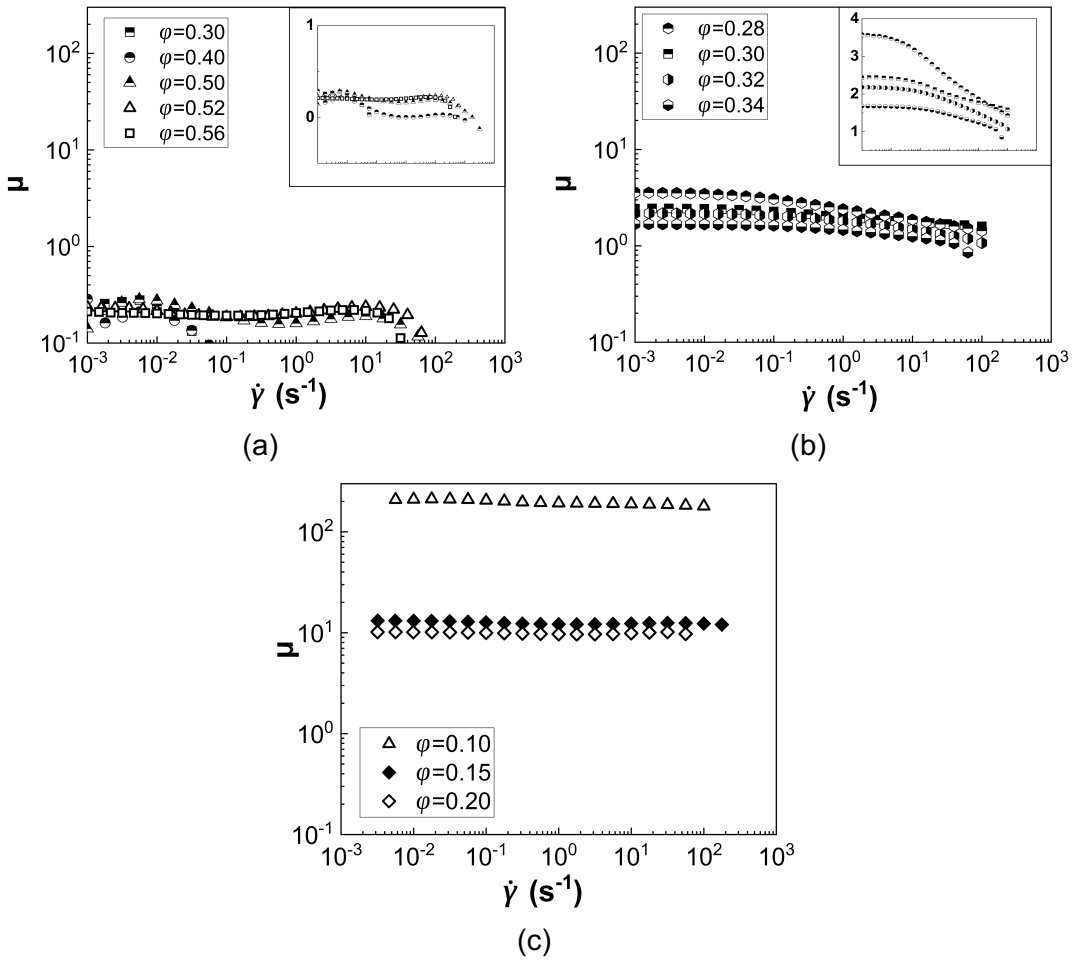

Figure 3.3: Microscopic friction coefficients (μ) for the suspensions of a) glass spheres, b) abrasive silicas and c) filler silicas suspended in glycerol at 20°C. The insets in a) and b) represent the same data with an expanded y-axis scale.

The fact that the shear thinning response of the filler silica suspensions does not completely follow the theory related to the elastic deformation of the surface asperities implies that there are also other factors affecting suspension rheology except surface morphology. The following section will elucidate the effect of particle specific surface area to the suspension rheological response, which is also affected by particle size, surface roughness and porosity.

3.2.3 Effect of particle specific surface area

The particles used in the present study have similar size and size distributions and thus the effect of these parameters on suspension rheology can be considered negligible. However, the particles used vary a lot in the surface characteristics and porosity, parameters that significantly alter their particle specific surface area. Hence, the flow curves shown in Figure 3.1 will be discussed on the basis of the particle specific surface area (S_p) in an attempt to employ a single parameter expressing both particle surface irregularity (roughness) and porosity (ε).

In the previous section, it was shown that increasing the surface roughness shifted the onset of non-Newtonian rheological phenomena (shear thinning and shear thickening) to lower particle volume fractions compared to that of the glass sphere suspensions. Particle porosity can induce similar effects since part of the solvent gets absorbed into the pores increasing the effective particle volume fraction in the suspension. The intrinsic viscosity (B) increased and the maximum packing (φ_m) decreased (Table 3.1) with increasing the particle surface roughness and porosity, which can be described in terms of an increase in the S_p value of the particles under investigation.

The abovementioned phenomena are better illustrated in Figure 3.4 to Figure 3.6. Figure 3.4a is replotted from Figure 3.2 and compares the relative viscosities at zero ($\eta_{r,0}$) and infinite ($\eta_{r,\infty}$) shear rate as a function of φ for all three types of particle suspensions. The continuous and dashed lines represent the Quemada fittings to the data. Figure 3.4b presents the infinite relative viscosity as a function of the normalized particle volume fraction (φ/φ_m) along with published data for suspensions including rough or smooth particles suspended in Newtonian media.

It can be seen that for the same φ values, $\eta_{r,0}$ and $\eta_{r,\infty}$ values increase at a much higher rate for the filler silicas compared to the other two types of suspensions due to the increased specific surface area. However, normalizing the particle concentration (φ) with the estimated maximum packing fraction (φ_m) from the Quemada fitting in each case nearly collapses the experimental data with data from the literature regardless of the particle surface morphology and specific surface area. The latter indicates that the maximum packing fraction can capture the effect of particle characteristics on suspension rheology sufficiently well. However, small variations in the relative viscosity between smooth and rough particle suspensions still exist and thus, a universal scaling based only on the maximum packing fraction cannot be

obtained as has also been reported by other researchers (Blanc et al., 2018; Mewis and Wagner, 2012).

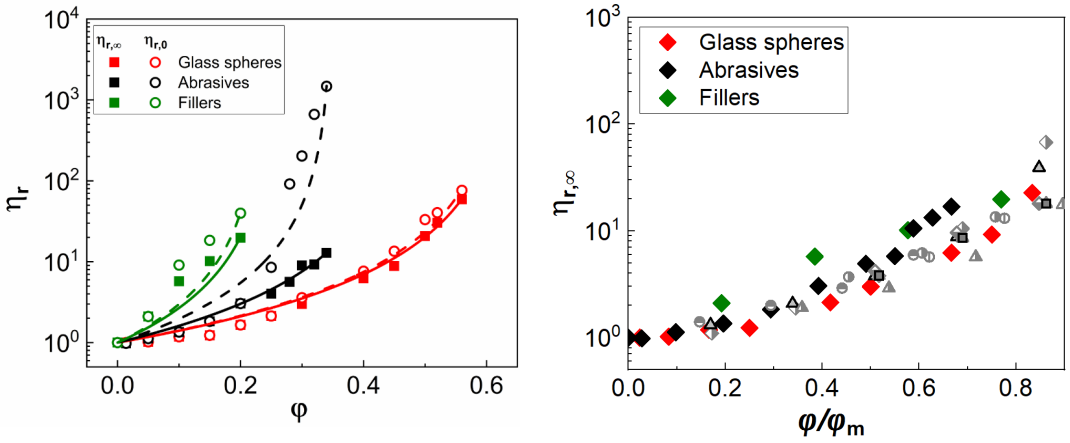

Figure 3.4: a) Comparison of the zero shear ($\eta_{r,0}$) and the infinite shear ($\eta_{r,\infty}$) relative viscosity of all three types of suspensions in glycerol as a function of particle volume fraction (φ) at 20°C. Continuous and dashed lines correspond to the fittings of the Quemada equation to the experimental data; b) Infinite shear relative viscosity of all suspensions in glycerol as a function of particle volume fraction normalised with the maximum packing fraction (φ_m) of each suspension (i.e. Glass spheres φ_m=0.60, abrasives φ_m=0.51, fillers φ_m=0.26). Grey points correspond to relevant data reported in literature for frictional suspensions with varying friction coefficients (μ), ◆: Mari et. all ($\mu = 1$) (2014), ▲: Cheal and Ness ($\mu = 0.5$) (2018), ◆: Tanner and Dai (5.3% roughness ratio) (2016) and non-frictional suspensions, ▲: Guy et al. (2015), ●: Mari et al. (2014), ●: Gallier et al. (2014), ■: Tanner and Dai (smooth) (2016), ●: Cheal and Ness ($\mu = 0$) (2018).

As mentioned above, in suspensions consisting of porous particles, part of the suspending medium is absorbed into the particle pores. This reduces the amount of solvent in the suspension and thus, leads to increased suspension viscosities due to a higher effective particle volume fraction (φ_{eff}). The latter is defined as (Olanrewaju et al., 2013):

$$\varphi_{eff} = \frac{w_p}{\frac{\rho_p}{\rho_{susp}} - \varepsilon w_p \frac{\rho_p}{\rho_f}} \tag{3.10}$$

where, w_p is the weight fraction of the particles in suspension, ε represents the particle porosity and ρ_{susp} indicates the suspension density defined as:

$$\rho_{susp} = \varphi(\rho_p - \rho_f) + \rho_f \tag{3.11}$$

where, ρ_p is the density of the solid particles, ρ_f refers to the density of the suspending medium and φ is the apparent particle volume fraction.

The estimated φ_{eff} values as a function of φ are presented in Figure 3.5a. The maximum packing fraction (φ_m) derived for each type of suspensions from the Quemada fitting is shown in Figure 3.5b as a function of particle porosity and specific surface area. It should be noted that in Figure 3.5a two sets of data are shown for the filler silicas. These refer to the estimation of the φ_{eff} using either the material's density (filled green diamonds), i.e. $\rho_p = 2\ g/ml$, or the experimentally derived particle density, i.e. $\rho_p = 1.24\ g/ml$, which is considerably lower compared to the pure silicon dioxide density. The latter can most probably be attributed to the high porosity of this particle type. Accordingly, as the specific surface area of the particles increase, the effective volume fraction of the particles significantly increases while the maximum packing decreases from $\varphi_m = 0.60$ for the glass spheres to $\varphi_m = 0.26$ for the filler silicas. Therefore, the increased φ_{eff} of the suspensions can explain the onset of non-Newtonian rheological phenomena at lower apparent φ values for the abrasive and the filler silica suspensions, described in Figure 3.1.

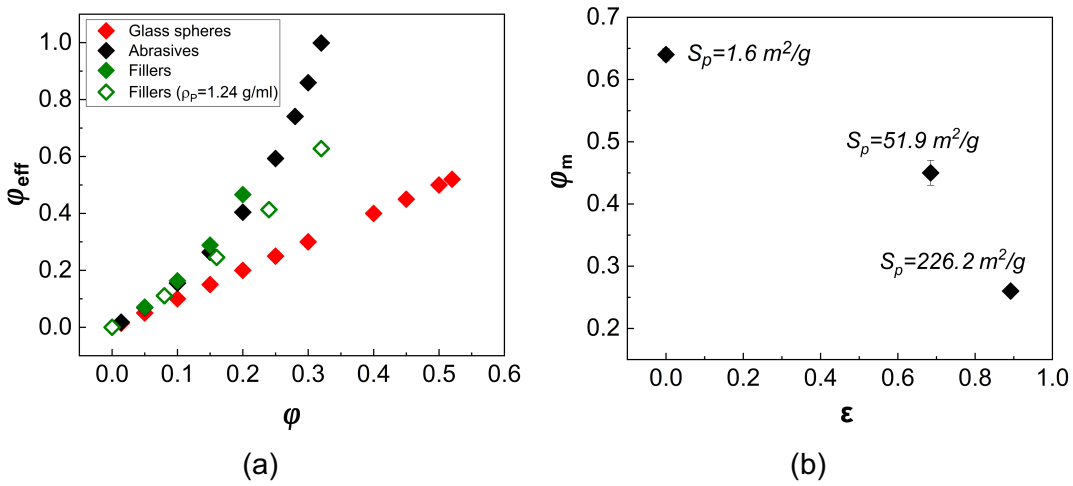

Figure 3.5: a) Effective volume fraction (φ_{eff}) estimated for the porous particles as a function of apparent particle volume fraction (φ) and b) maximum packing fraction of all suspensions at 20°C as a function of porosity (ε) and specific surface area (S_p). The φ_{eff} of the filler particles was estimated using both the material density ($\rho_p = 2\ g/ml$) (green filled diamonds) and the experimentally measured density ($\rho_p = 1.24\ g/ml$) (green open diamonds).

The extent of shear thinning ($\eta_{r,e}$, eq. (3.12)) is defined as the difference between the zero and the infinite shear rate relative viscosities divided by the value of the corresponding $\eta_{r,\infty}$ values, while the extent of shear thickening ($\eta_{r,t}$, eq. (3.13)) is defined in a similar manner:

$$\eta_{r,e} = \frac{\eta_{r,0} - \eta_{r,\infty}}{\eta_{r,\infty}} \tag{3.12}$$

$$\eta_{r,t} = \frac{\eta_{r,peak} - \eta_{r,\infty}}{\eta_{r,\infty}} \tag{3.13}$$

where $\eta_{r,peak}$ is the peak relative viscosity value of the shear thickening region.

The estimates of the above variables for all the non-Newtonian suspensions are plotted in Figure 3.6 as a function of the apparent φ volume fraction and the corresponding φ_{eff}. The data presented reflect the significant effect of particle characteristics on suspension rheology. In particular, the rough silicas induce both non-Newtonian phenomena at lower apparent φ values compared to the glass sphere suspensions. However, a non-monotonic effect of the particle specific surface area us observed. The abrasive silicas exhibit the most pronounced shear thinning response compared to the other two, while interestingly, the filler silicas show a behaviour similar to that of the glass spheres (Figure 3.6a). Shear thickening (Figure 3.6b) is only observed for the glass spheres and the filler silica suspensions, with the fillers exhibiting stronger non-Newtonian rheology.

By replotting the $\eta_{r,e}$ and $\eta_{r,t}$ values using the effective volume fraction for the abrasives and fillers (Figure 3.6c and d respectively), the data are shifted towards those of the glass sphere suspensions. However, the rough silicas still show stronger shear thinning and shear thickening response compared to the smooth and non-porous glass spheres despite scaling the data by the φ_{eff}. This implies that considering only porosity in the estimation of the effective volume fraction of the suspensions is not adequate to fully capture their non-Newtonian behaviour. The shape of the pores and their effectiveness in keeping the absorbed solvent inside comprise another factor that can influence the effective volume fraction of the particles in the suspension; this parameter is not considered in eq. (3.10).

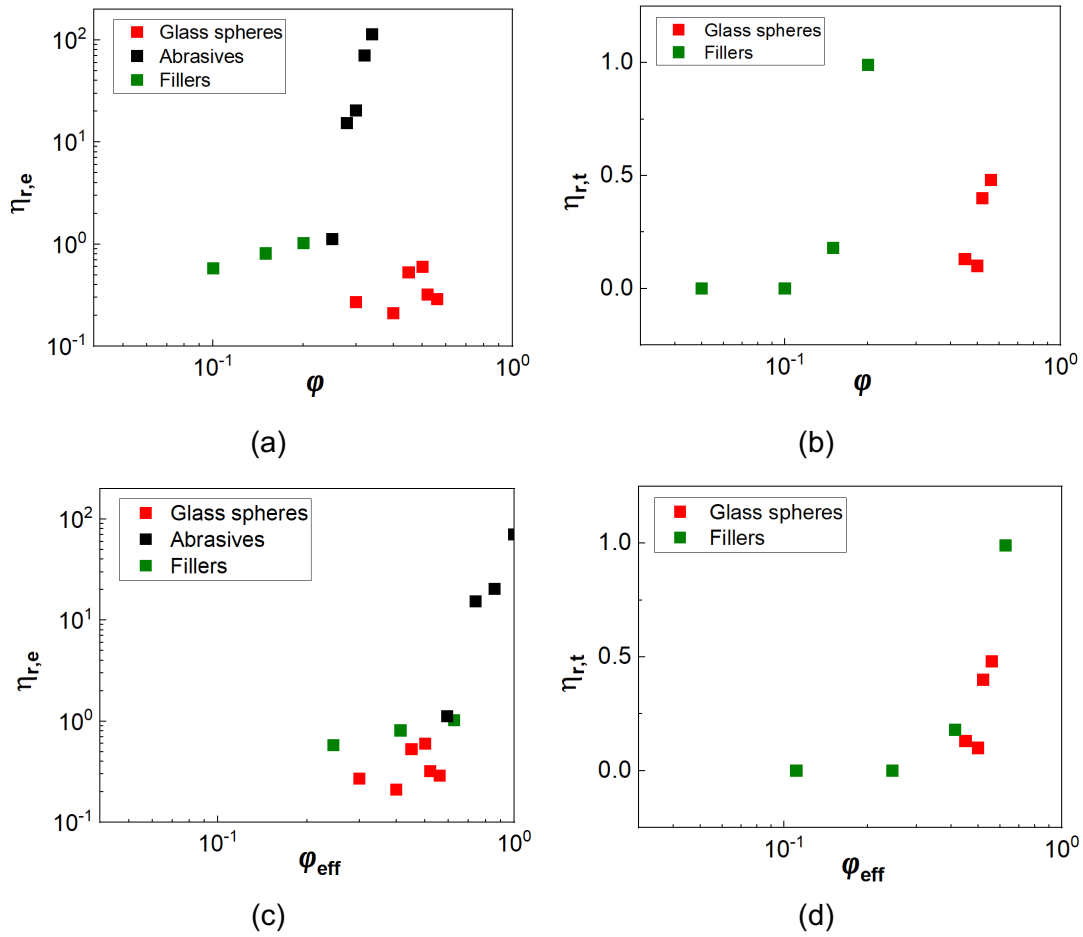

Figure 3.6 Extent of a) shear thinning and b) shear thickening as a function of the apparent particle volume fraction for all the suspensions in glycerol showing non-Newtonian rheology at 20°C. c) & d) The corresponding variables presented in a) & b) as a function of the effective particle volume fraction. In the case of the filler silicas, the effective volume fraction was estimated using the experimentally derived particle density.

The distance between the suspended particles comprises one of the main factors influencing interparticle interactions and thus, suspension rheology and this is closely related to φ_{eff} as shown in eq. (3.14) (Hoyle et al., 2020):

$$D_{pp} = D\left(\sqrt[3]{\frac{\pi}{6\varphi_{eff}}} - 1\right) \tag{3.14}$$

where, D_{pp} is the particle-particle distance and D the particle diameter.

It can be seen that the interparticle distance (D_{pp}) is proportional to the particle size (D), while the opposite relation holds for φ_{eff}; i.e. as the effective volume fraction-or equivalent the particle specific surface area- increases, the distance between the

particles decreases leading to stronger interparticle interactions, shifting the onset of non-Newtonian phenomena to lower φ. For example, at a fixed apparent particle volume fraction of $\varphi = 0.20$, the real interparticle distance is $D_{pp} = 4.2\,\mu m$ for the glass spheres, while it decreases to $D_{pp} = 1.6\,\mu m$ for the abrasive silicas and $D_{pp} = 0.5\,\mu m$ for the filler silicas respectively.

Although the particle volume fraction plays a crucial role in interparticle distance, there are also other factors affecting this parameter; these include the particle surface roughness, which increases the available area for particle contact, the solvent viscosity (Mewis and Wagner, 2012) as well as the particle specific surface area. For example, the high viscosity of glycerol at 20°C is responsible for the formation of a thick solvation layer around the particles, as mentioned previously, which leads to short-range repulsive solvation forces and stabilise the suspension (Amiri et al., 2012; Raghavan et al., 2000). It should also be noted that the density of the surface silanol groups (-OH) increases linearly with the particle specific surface area (eq. (3.15)) (Zhuravlev, 2000; Zhuravlev and Potapov, 2006) as follows:

$$\delta_{OH} = \frac{a_{OH} S_p}{N_A} \tag{3.15}$$

where δ_{OH} is the density of the surface silanol groups (mol OH/g of SiO_2), a_{OH} is a constant equal to 4.6 OH/nm^2, S_p is the particle specific surface area (m^2/g) and N_A is the Avogadro constant equal to $6.023 \cdot 10^{23}$ atoms/mol. The estimated densities of the silanol groups for the three types of particles are presented in Table 3.6. As expected, the δ_{OH} values increase with the specific surface area from $S_{p,GS} = 1.6\,m^2/g$ for the glass spheres to $S_{p,A} = 51.9\,m^2/g$ and $S_{p,F} = 226.2\,m^2/g$ for the abrasive and filler silicas respectively.

Table 3.6: Density of the surface silanol groups in the three types of particles used in the present study.

Particle type	$\boldsymbol{\delta_{OH}\ (mmol\ OH/g\ SiO_2)}$
Glass spheres	0.01
Abrasive silicas	0.40
Filler silicas	1.70

The impact of increasing the silanol groups on the surface of the silicas can be two-fold. On one hand, it can increase the strength of the solvation layer formed around the particles in the presence of glycerol due to providing a higher number of

available contact points between the particles and the suspending medium. On the other hand, a higher density of silanol groups in conjunction with particle porosity can promote interparticle interactions, through increasing both the available contact points on the particle surface and the effective particle volume fraction, leading to increased suspension viscosity and inducing non-Newtonian behaviour. Therefore, the observed rheology of the different suspensions investigated above results from the competition between these two phenomena, whose individual effect is hard to distinguish. For example, the high concentration of the surface silanol groups on the filler silicas might enhance the strength of the solvation layer, promoting short range repulsive forces between the particles and inducing shear thickening at sufficiently high shear rates; this can also prevent the frictional contacts at low shear and thus, explain the suppressed shear thinning response. In contrast, in the case of the abrasive silicas the δ_{OH} value is not adequate to induce such phenomena.

Several researchers have investigated the effect of the specific surface area on suspension rheology using fumed silica suspensions. For example, Asija Bhalla et al. (2015) used fumed silicas suspended in polyethylene glycol and reported an increase of the shear thinning response and a decrease in the shear thickening with increasing the specific surface area of the particles from 90 m^2/g to 200 m^2/g. However, the weakening of the shear thickening was attributed to the decrease of the average primary particle size as the surface area of the particles increases; this in turn resulted in a reduction of the hydrodynamic forces making them unable to overcome the sum of the repulsive forces (Asija et al., 2015). Other studies using fumed silicas with varying specific surface areas from 200 m^2/g to 380 m^2/g in organic and inorganic solvents did not show significant effects of this parameter on suspension rheological properties (Chen et al., 2007, 2005; Raghavan et al., 2000).

It should be noted that the results presented in this section will be further discussed in the last section of this chapter, in comparison with the data acquired at 60°C.

3.2.4 Linear Oscillatory shear rheology

The rheological properties of the suspensions under dynamic oscillatory shear in the linear viscoelastic regime (LVR) were investigated through small amplitude oscillatory shear and frequency sweeps.

Firstly, the LVR of the suspensions was identified through small amplitude oscillatory shear measurements (SAOS). Indicative examples are presented in Figure 3.7, where the normalized storage (G') and loss moduli (G'') for all three suspensions

at a fixed φ of 0.10 are plotted as a function of the applied % strain amplitude. It can be seen that the LVR is similar for the three types of particle suspensions and spans from $\gamma = 10^{-2}$ % to $\gamma = 1$ %. Therefore, a value of $\gamma = 10^{-1}$ % was selected for the subsequent frequency sweeps. Also, although the normalised loss moduli (G'') nearly overlap for the three types of particles, deviations occur for the storage moduli (G'). More specifically, increasing the specific surface area, increases the G' values of the suspension, implying stronger interparticle interactions, in accordance with the results obtained under steady state shear.

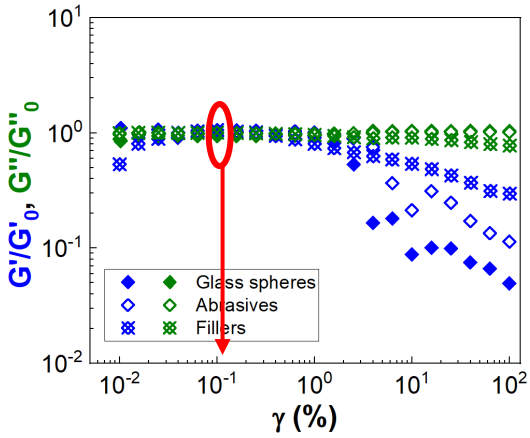

Figure 3.7: Indicative small amplitude oscillatory shear measurements conducted to define the linear viscoelastic region (LVR) at a frequency of $f = 1Hz$. Representative storage (G') and loss (G'') moduli normalised with the corresponding values of the moduli in the LVR, G'_0 and G''_0 respectively, as a function of % strain (γ). All measurements have been conducted with suspensions at $\varphi = 0.10$ in glycerol and at 20°C.

Figure 3.8 presents the G' and G'' values of all highly concentrated suspensions as a function of the angular frequency (ω) and the particle volume fraction (φ). Almost all suspensions exhibit viscous dominated behaviour, with the G'' values being higher than G', in all experimental conditions and particle characteristics, implying that hydrodynamic forces govern suspension rheology (Gao et al., 2017). Increasing the angular frequency increases both G' and G'', with the G'' following a power law indicative of viscous fluids (Barnes, 2000; Khandavalli and Rothstein, 2015; Ma et al., 2017). The particle volume fraction also affects the viscoelastic properties of the suspensions with both moduli increasing with φ_{eff}. Interestingly, the storage moduli appear to be more sensitive to volume fraction variations compared to the loss moduli in all cases. The latter can be explained in the light of interparticle interactions, which are mostly reflected in the variation of G'. In particular, by increasing the effective particle volume fraction and thus, decreasing particle-particle separation,

neighbouring particles are more likely to interact with each other giving rise to the elastic component of the suspension.

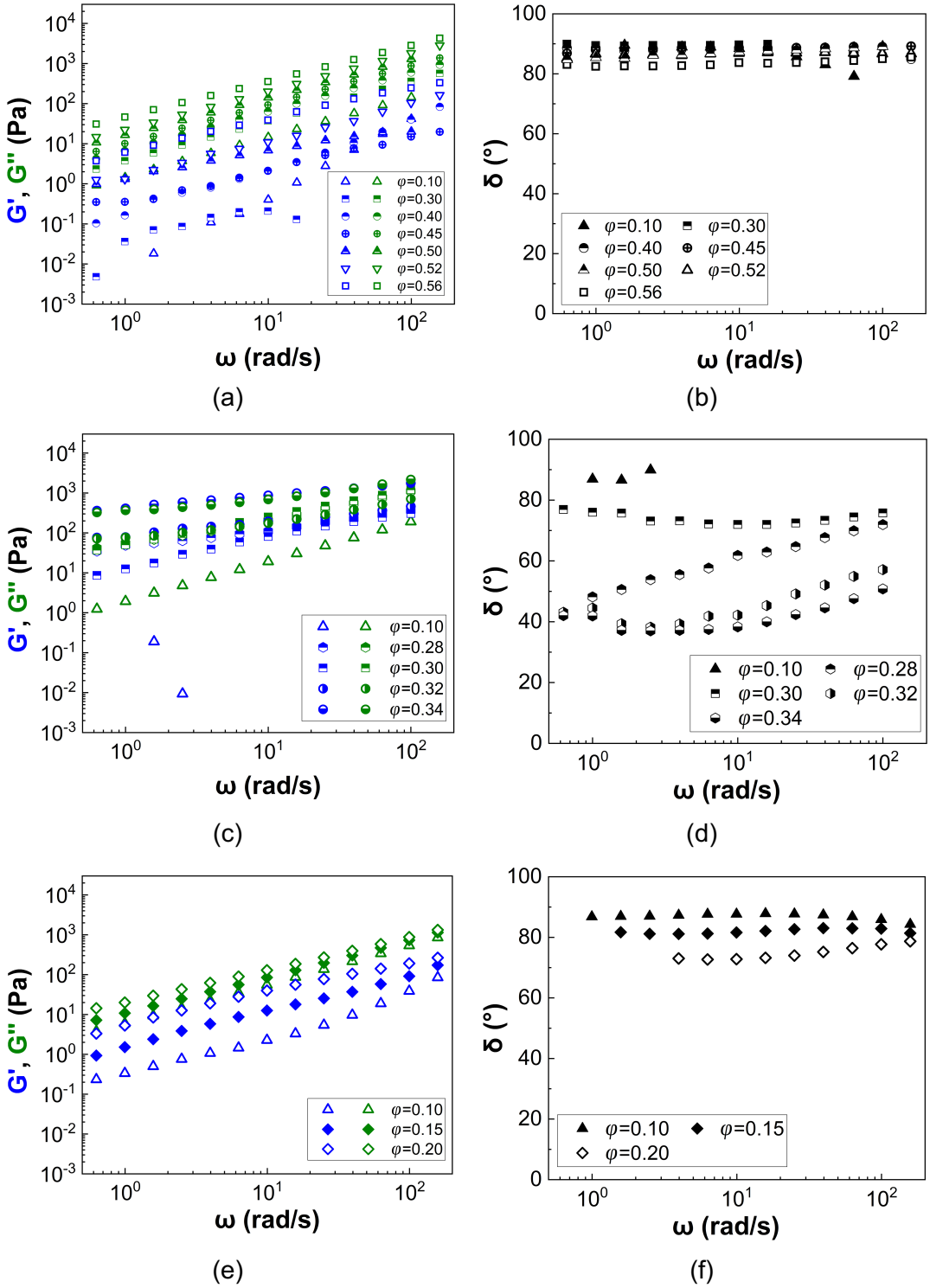

Figure 3.8: Storage (G') and loss moduli (G'') (left) as well as the phase angle (δ) (right) as a function of angular frequency (ω) generated from experimental frequency sweeps in the LVR of all highly concentrated suspensions in glycerol at 20°C. a) & b) glass spheres; c) & d) abrasive silicas and e) & f) filler silicas.

The corresponding phase angles (δ) of the suspensions are also shown in the right column of Figure 3.8 as a function of ω and φ. In general, a value of $\delta \approx 0^o$ indicates that the material behaves as an elastic solid, while $\delta \approx 90^o$ represents a liquid like behaviour. The phase angle values varying from 0^o to 90^o indicate that the material shows properties between a solid and a liquid, i.e. it is viscoelastic. The glass spheres suspensions show δ values very close to 90° and almost independent of the applied angular frequency. In contrast, the abrasive silicas show lower phase angles compared to the glass spheres, which also depend on the particle volume fraction. Increasing the φ values leads to a decrease in the phase angle and strengthens the viscoelasticity of the suspensions, especially, for $\varphi \geq 0.28$. This can be correlated with the shear thinning response observed for these suspensions under steady state shear in Figure 3.1c and the corresponding interparticle interactions underlying these phenomena. The equivalent of the shear rate under steady state in the dynamic frequency sweeps can be computed as $\dot{\gamma}_d = \omega\gamma_o$, where ω is the angular frequency and γ_o is the strain amplitude, i.e. $\gamma_o = 0.001$. This definition implies that the equivalent shear rate in the frequency sweeps presented in Figure 3.8d falls between $\dot{\gamma} = 0.001\ s^{-1}$ and $\dot{\gamma} = 0.1\ s^{-1}$, which correspond to the region of $\dot{\gamma}$ values that shear thinning occurs. It should be recalled that this low shear rate regime could be reached for these highly concentrated suspensions as the measured shear stresses were sufficiently high to overcome any sedimentation effects.

On the other hand, the observed phase angle values for the filler silica suspensions, although slightly lower, seem more comparable to those obtained for the glass spheres. In particular, δ is between ~90° (pure liquid) for the lowest concentration of $\varphi = 0.10$ to ~70° (weakly viscoelastic) at a particle concentration of $\varphi = 0.20$. This behaviour can be related to the weak shear thinning response of these suspensions under steady state shear in the corresponding shear rate region (Figure 3.1d).

3.2.5 Suspension microstructure

The rheology of suspensions is closely linked to changes in their microstructure under shear. In the present study, the microstructure of the suspensions was investigated using two different methods, one based on direct visualization, i.e. an optical shearing technique and another based on bulk rheology, i.e. large amplitude oscillatory shear (LAOS).

3.2.5.1 Optical shearing technique

Optical methods are limited by the opacity of the sample and thus, visualisation of the suspension microstructure could only be achieved under relatively dilute conditions; hence suspensions of 5% and 3% v/v were used for the glass spheres and the abrasive silicas respectively. It was not possible to visualise the filler silica suspensions, due to refractive index matching between particles and glycerol which coupled with the high porosity which turned the suspensions totally transparent for volume fractions up to $\varphi = 0.15$. Use of dye did not alleviate this problem but facilitated the visualisation of the abrasive silicas. No difficulties were experienced during the visualisation of the glass spheres, which might be attributed to a slightly lower refractive index compared to silicas due to the particles being hollow.

The optical shearing technique enables the quantification of the agglomeration (if any) and dispersion characteristics of the sheared suspensions *in situ*. Figure 3.9 presents sample images for the corresponding glass sphere and abrasive silica suspensions in glycerol at different shear rates, i.e. low ($\dot{\gamma}$=1 s^{-1}) (Figure 3.9a and b), medium ($\dot{\gamma}$=10 s^{-1}) (Figure 3.9c and d) and high ($\dot{\gamma}$=100 s^{-1}) (Figure 3.9e and f) shear rates. The microstructure of the suspensions in glycerol shows no apparent dependence either on the shear rate or the particle type, as the particles remain well dispersed at all shear rates applied; this also agrees with the Newtonian behaviour observed for the dilute conditions in Figure 3.1 and 3.10 (insets). In order to investigate whether there is any particle clustering in the suspension, the aggregation index defined in eq. (2.9) was utilised. Estimates are presented in Figure 3.10 in a normalised form, i.e. normalised with the aggregation index value obtained at the maximum shear rate applied, to facilitate comparison between the different cases images-in terms of particle type and volume fraction. Since no aggregation was observed in Figure 3.9, the aggregation indices for both glass spheres and abrasive silicas are constant and equal to 1 at all the shear rate range investigated, which highlights that the rheology of these suspensions is independent of $\dot{\gamma}$.

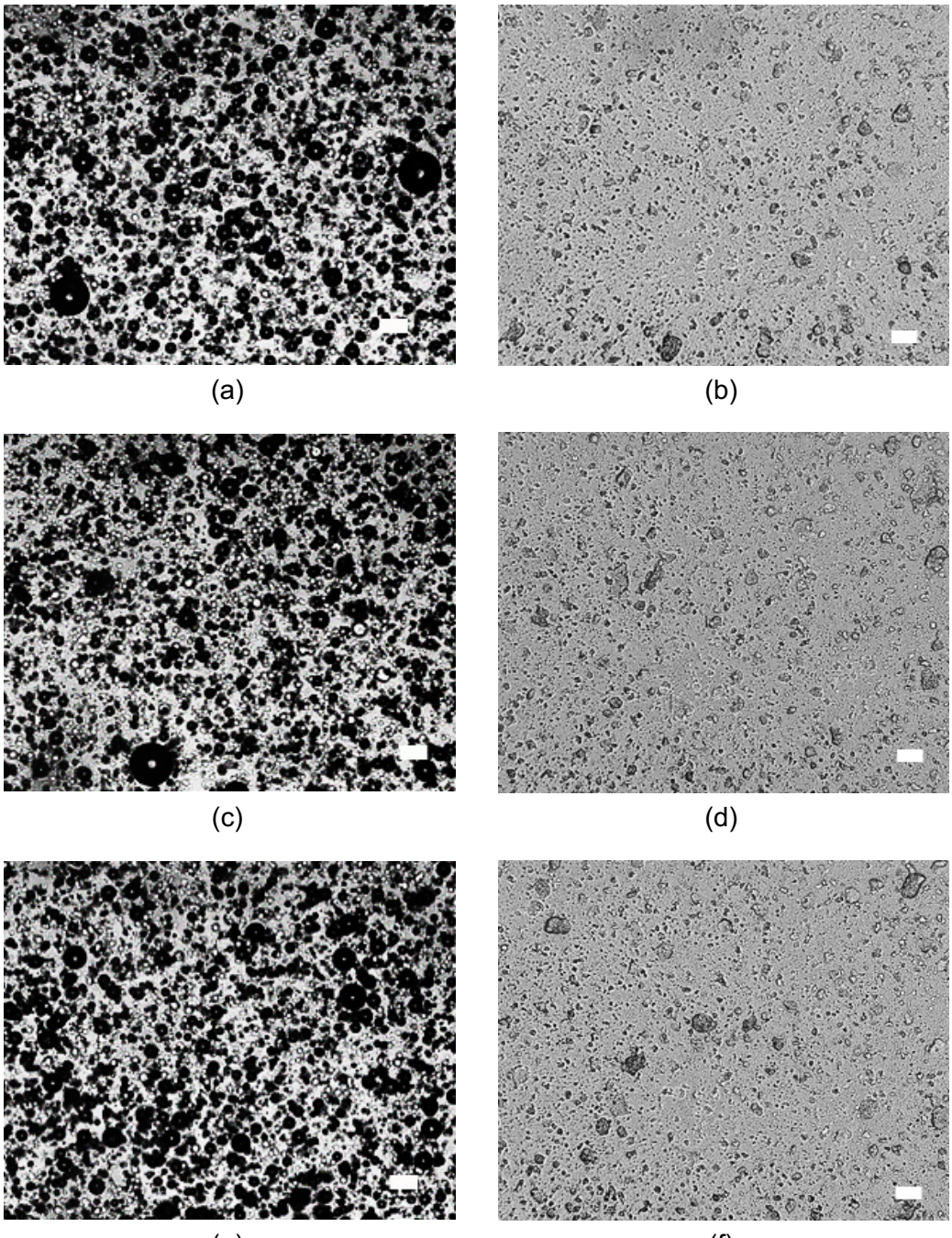

Figure 3.9: Sample images of the sheared suspensions obtained for 5% v/v glass sphere (left) and 3% v/v silica (right) suspensions in glycerol at shear rates of: $\dot{\gamma}$=1 s^{-1} (a, b); $\dot{\gamma}$=10 s^{-1} (c, d) & $\dot{\gamma}$=100 s^{-1} (e, f) and at room temperature. The scale bars (▬) correspond to 40 μm length.

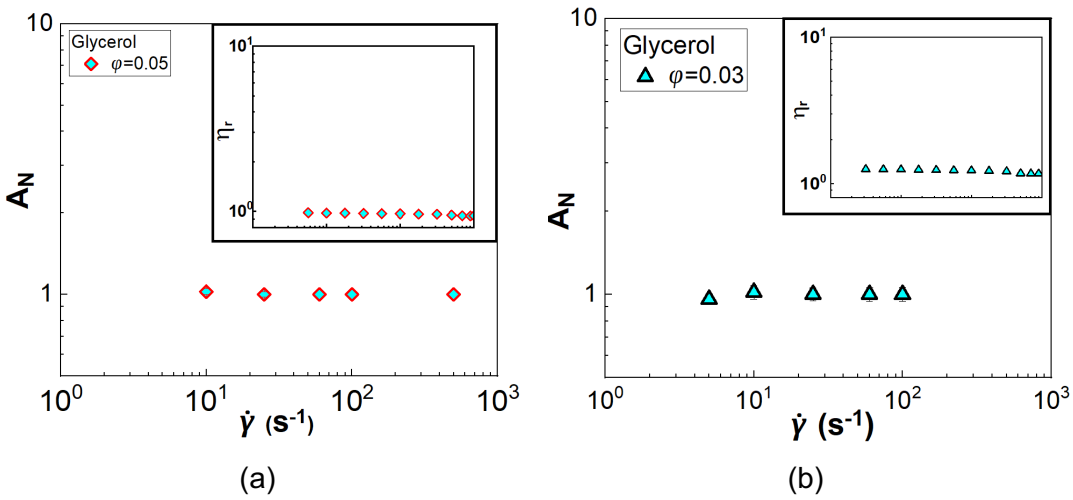

Figure 3.10: Normalised aggregation indices (A_N) for the suspensions presented in Figure 3.9 as a function of shear rate. The insets represent the relative viscosity values vs shear rate for the corresponding suspensions in glycerol at 20°C.

3.2.5.2 Large Amplitude Oscillatory shear (LAOS)

As mentioned above, optical techniques are limited to relatively dilute concentrations so that the microstructure comprising individual particles or small number of agglomerates can be identified and quantified. Other techniques based on bulk rheology are more suitable for denser suspensions, such as large amplitude oscillatory shear (LAOS) tests (Ewoldt et al., 2007; Hyun et al., 2011; McKinley, 2012; Narumi et al., 2005; Singh et al., 2015) as described in Chapter 2. During LAOS, the suspensions are subjected to large and rapid deformations, commonly encountered in industrial processing, leading to changes in suspension microstructure and revealing instabilities and non-linear responses of the materials under shear.

The response under LAOS of the three types of suspensions at a fixed particle volume fraction of $\varphi = 0.10$ is presented below. This concentration was selected as the lowest φ at which shear thinning behaviour was induced by the filler silicas. In contrast, the glass sphere and abrasive silica suspensions exhibited Newtonian response at $\varphi = 0.10$. Therefore, the difference in the particle dynamics (if any) in the different types of suspensions can be identified.

Figure 3.11 shows the LAOS results under different applied frequency and strain amplitude conditions. All suspensions exhibit strongly viscous dominated behaviour ($G'' > G'$) as also described in the above section. Interestingly, the loss modulus remains independent of the strain amplitude for both the glass sphere and the abrasive silica suspensions, while weak strain hardening is observed for the filler silica

suspensions. However, the values of both moduli (G', G'') increase with increasing the particle surface roughness and porosity.

The storage modulus, G', shows a more complex response than G'', with the LVR being followed by strain thinning and strain thickening with increasing the % strain amplitude, whose extent appear to depend on particle specific surface area. In general, the low G' values indicate that the elastic component is very weak in all suspensions, which could be attributed to the presence of the lubrication film around the particles formed by glycerol and the hindrance of real particle-particle contacts. The latter leads to the inability of particles to come in contact and form stable networks that would give rise to the G' values and a stronger viscoelastic behaviour.

The G' and G'' data as a function of frequency (f) generated from frequency sweeps and LAOS measurements at the same strain amplitude, i.e. $\gamma = 0.1\%$ are showin the right column of Figure 3.11. Both moduli increase with f, typical of viscous fluids, and with the particle surface roughness moving from the relatively smooth glass spheres to the rough abrasive and filler silicas. Good agreement is also observed between the storage and loss moduli obtained through the frequency sweep and the corresponding moduli obtained for the linear viscoelastic region in the amplitude sweep; this is expected as both measurements have been conducted in the linear viscoelastic region. The latter highlights the possibility and flexibility of using various techniques to characterise the rheology of complex fluids in the linear regime when one or the other method of measuring is inaccessible due to instrument limitations or limited amount of sample available.

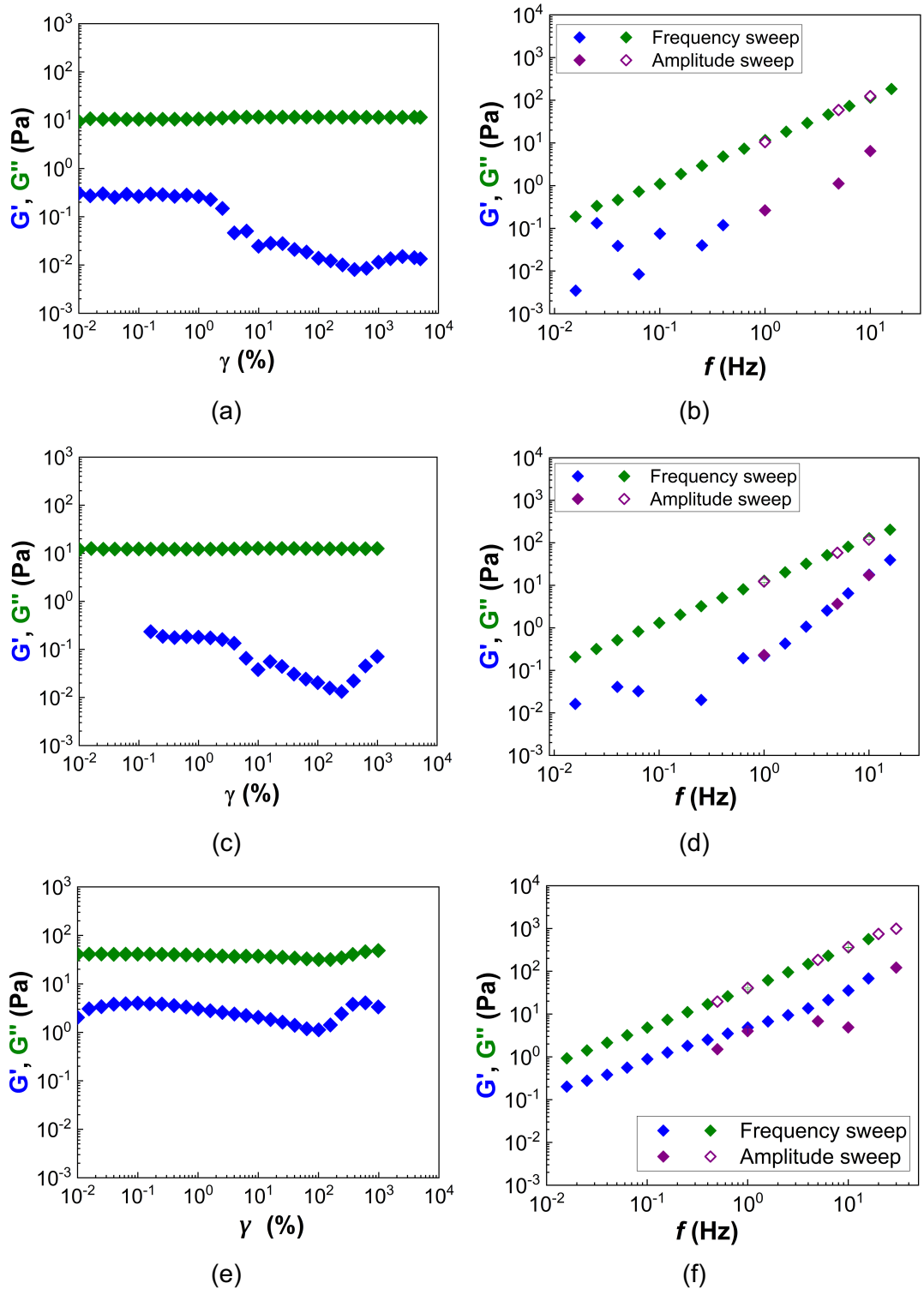

Figure 3.11: Storage (G') and loss (G'') moduli as a function of the % strain amplitude (γ) (left column) and the frequency (f) (right column) of all three particle suspensions at a fixed volume fraction of $\varphi = 0.10$ in glycerol and at 20°C. A comparison between the G' and G'' as a function of frequency (f) generated from the frequency sweep and the LAOS experiment at the same strain amplitude, i.e. $\gamma = 0.1\%$ is also included. a) and b) glass spheres; c) and d) abrasive silicas; e) and f) filler silicas.

The non-linear response of the suspension under LAOS can be described through the viscous and elastic Lissajous plots, which represent the raw stress signals as a function of strain rate and strain amplitude respectively in an oscillatory circle. The elastic Lissajous plots of the abrasive and filler silicas are presented in Figure 3.12, as a function of selected strain amplitudes in the non-linear regime ($\gamma \geq 10\%$) and a frequency of $f = 1\ Hz$. The corresponding curves of the glass sphere suspension are not included as the raw stress signals were very noisy and thus, subject to uncertainty. The maximum stress values of the filler silicas are at least two times higher than these obtained for the abrasive silicas, which is in agreement with the results obtained under steady state.

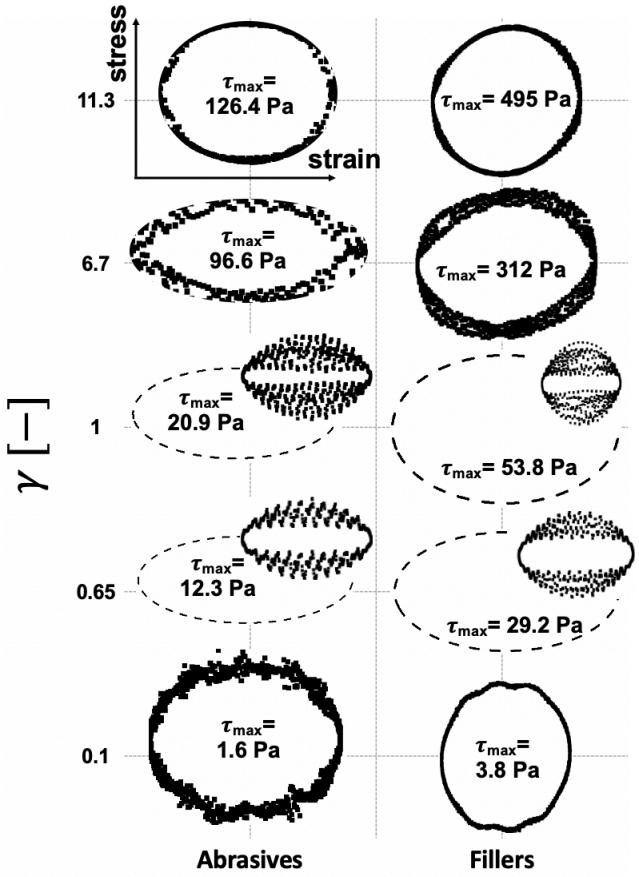

Figure 3.12: Raw LAOS data of the 10% v/v abrasive and filler silica suspensions in glycerol at 20°C, generated from experimental oscillatory tests shown as elastic Lissajous curves of total stress vs strain, at various strain amplitude (γ) and a fixed frequency of $f = 1\ Hz$. Insets represent the raw data, while the dashed line corresponds to the elliptical fitting to the data to smoothen the noise occurred at the maximum stress areas.

Although a non-linear response was observed in the G' and G'' values as a function of the strain amplitude, no significant instabilities are seen in the elastic Lissajous plots presented in Figure 3.12. The raw stress signals show a symmetric and elliptical

shape at the whole range of strain amplitudes reported, which is typical of linear response. This behaviour can be associated with the strongly viscous dominated response and the presence of the solvation layer around the silicas, which prevents direct interparticle contacts and results in weak instabilities.

Additional information regarding the LAOS measurements and the estimation of the non-linear parameter is provided in the following subsection for suspensions at the onset of non-Newtonian behaviour for each particle type, i.e. $\varphi = 0.50$ for the glass spheres, $\varphi = 0.30$ for the abrasive silicas and $\varphi = 0.10$ for the filler silicas. The next chapter will also present the response of adhesive suspensions at the same $\varphi = 0.10$ in comparison to the ones studied herein.

3.2.5.3 Microstructural study of suspensions at the onset of shear thinning

The response under LAOS of the three suspensions at the onset of non-Newtonian behaviour for each particle type, is shown in Figure 3.13a to c for glass spheres ($\varphi = 0.50$), abrasive silicas ($\varphi = 0.30$) and filler silicas ($\varphi = 0.10$) respectively.

All suspensions show viscous dominated response ($G'' > G'$) with the LVR being followed by strain thinning, strain thickening and strain thinning regions as a function of the % strain amplitude (γ) (Figure 3.13a to c). This behaviour is a combination of types I and IV responses under LAOS, i.e. a local minimum of both G' and G'' followed by strain hardening, and has been also observed for other systems, such as solid propellant dispersions, keratin filament and PMMA (polymethylmethacrylate) suspensions and peanut butter (Citerne et al., 2001; Heymann et al., 2002; Hyun et al., 2011; Ma et al., 1999; Miller et al., 1991). Such behaviour is generally thought to arise from the interplay between the formation and destruction of particle networks.

However, in the present study direct interparticle interactions are restricted by the formation of the solvation layer as the glycerol molecules form hydrogen bonds with the free silanol groups on the silica surface. This is responsible for the strongly viscous dominated response under oscillatory shear. The weak non-linear phenomena observed outside the LVR in Figure 3.13a to c are likely to stem from the transient deformation of the solvation layer under large oscillatory shear, which further influences the interparticle interactions and thus, suspension microstructure. It should be noted that a direct comparison of the non-linear rheological phenomena obtained for the three suspensions should be avoided due to the different particle volume fractions.

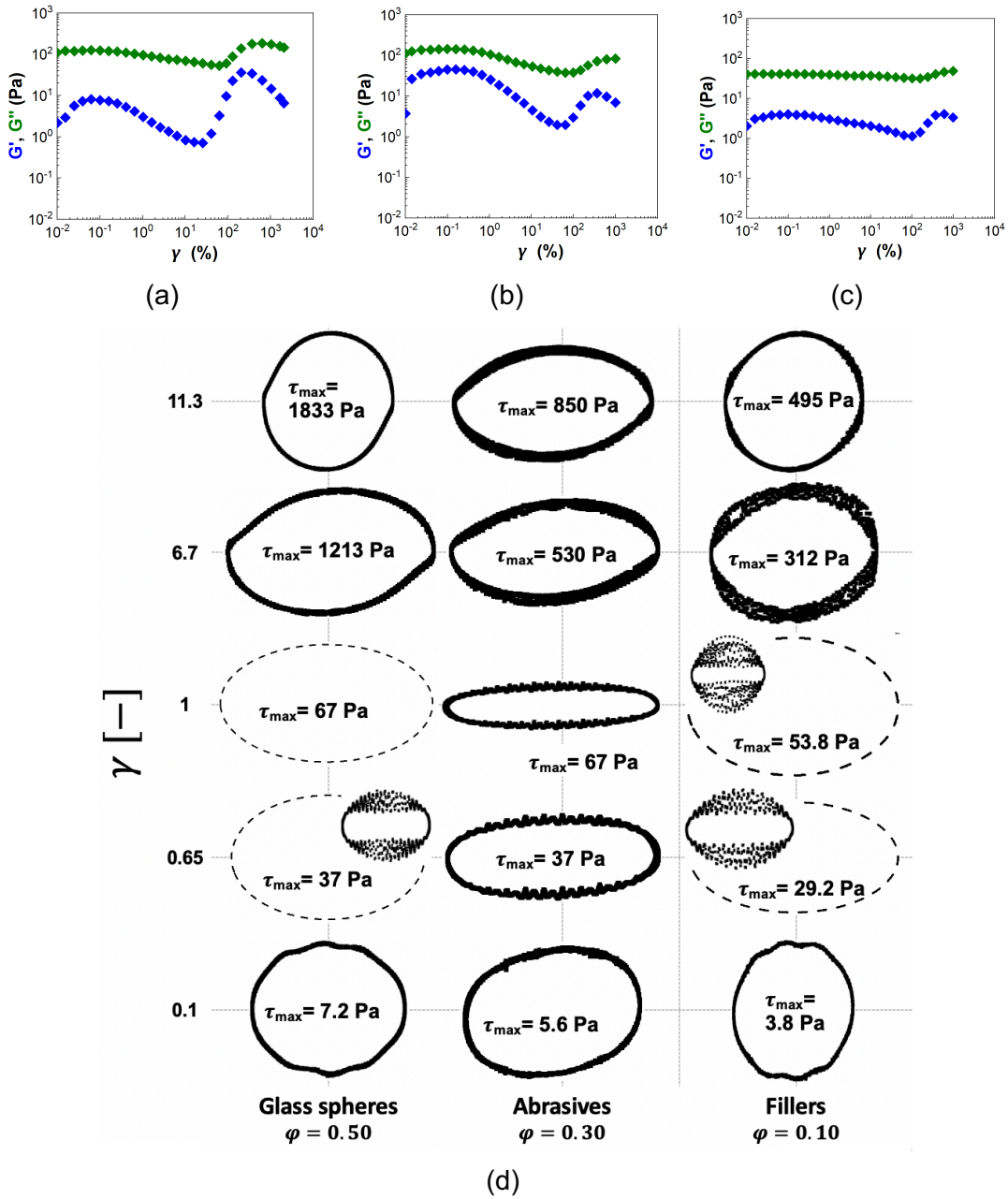

Figure 3.13: Raw storage (G') and loss (G'') moduli curves as a function of % strain amplitude (γ) at a fixed frequency of $f = 1Hz$ for the three suspensions: a) glass spheres $\varphi = 0.50$, b) abrasive silicas $\varphi = 0.30$ and filler silicas $\varphi = 0.10$; d) Elastic Lissajous curves of total stress vs strain, according to the values of strain amplitude (γ) and a frequency of $f = 1Hz$. Dashed lines correspond to the elliptical fittings to the raw data (shown as insets) to smoothen the noise occurred at the maximum stress area.

The origins of the non-linearities at sufficiently high strain amplitudes beyond the LVR can be further expressed through the raw stress signals acquired for each strain circle, namely the Lissajous plots. Indicative elastic Lissajous plots, i.e. stress vs strain, for the three suspensions at strain amplitudes in the non-linear regime ($\gamma \geq 10\%$) are presented in Figure 3.13d alongside the corresponding maximum stress values, which increase with the % γ, similar to measurements under steady state. It

can be seen that the stress signals are mostly symmetric and have an elliptical shape, which is typical of linear behaviour and does not imply any microstructural changes regardless of the particle type or the extent of the non-linear response. These curves can be further analysed to obtain the non-linear parameters, commonly used in LAOS experiments to get a more meaningful insight of the acquired data.

Figure 3.14 summarizes the non-linear parameters estimated from the analysis of the Lissajous curves as a function of the % strain amplitude: these include the dynamic minimum strain (G'_M) (hollow symbols) and large strain (G'_L) moduli (Figure 3.14a to c), dynamic minimum strain rate viscosity (η_M) (hollow symbols) and large strain rate viscosity (η_L) (filled symbols) (Figure 3.14d to f), stiffening ratio (S) and thickening ratio (T) (Figure 3.14g to i), Fourier spectra (Figure 3.14j to l) representing the intensity of the third harmonic, which arises in the non-linear regime giving rise to instabilities in the rheology of suspensions, relative to that of the first.

The non-linear moduli follow the same trend as the first order harmonic moduli (G', G'') (Figure 3.13a to c). The viscous component, η', shows no evidence of non-linear response as the minimum and maximum strain rate viscosities perfectly overlap (η'_M=η'_L) for all suspensions and at the whole range of strain amplitudes applied. This also results in nearly zero thickening ratios (green filled diamonds in Figure 3.14g to i).

On the contrary, slight deviations occur between the G'_M and G'_L moduli (Figure 3.14a to c), especially close to the minimum of the strain thinning and the maximum of the strain thickening region. The latter is also described by the non-zero values of the stiffening ratios (blue filled diamonds in Figure 3.14g to i) in these areas of the curve. It is important to note that a positive stiffening ratio (S) indicates strain rate driven instabilities (viscous component dominates), while negative S values imply the dominance of the elastic component of the measured material leading to strain driven instabilities. It can thus, be seen that the non-linear response of the suspensions is viscous dominated at low % γ (minimum of the strain thinning region), while it changes to elastic dominated in the strain thickening area (high % γ, $S < 0$). The observed instabilities of the elastic moduli are also reflected in the two maxima observed in the Fourier spectra of the third harmonic intensity at strain amplitudes of $\gamma > 5\%$.

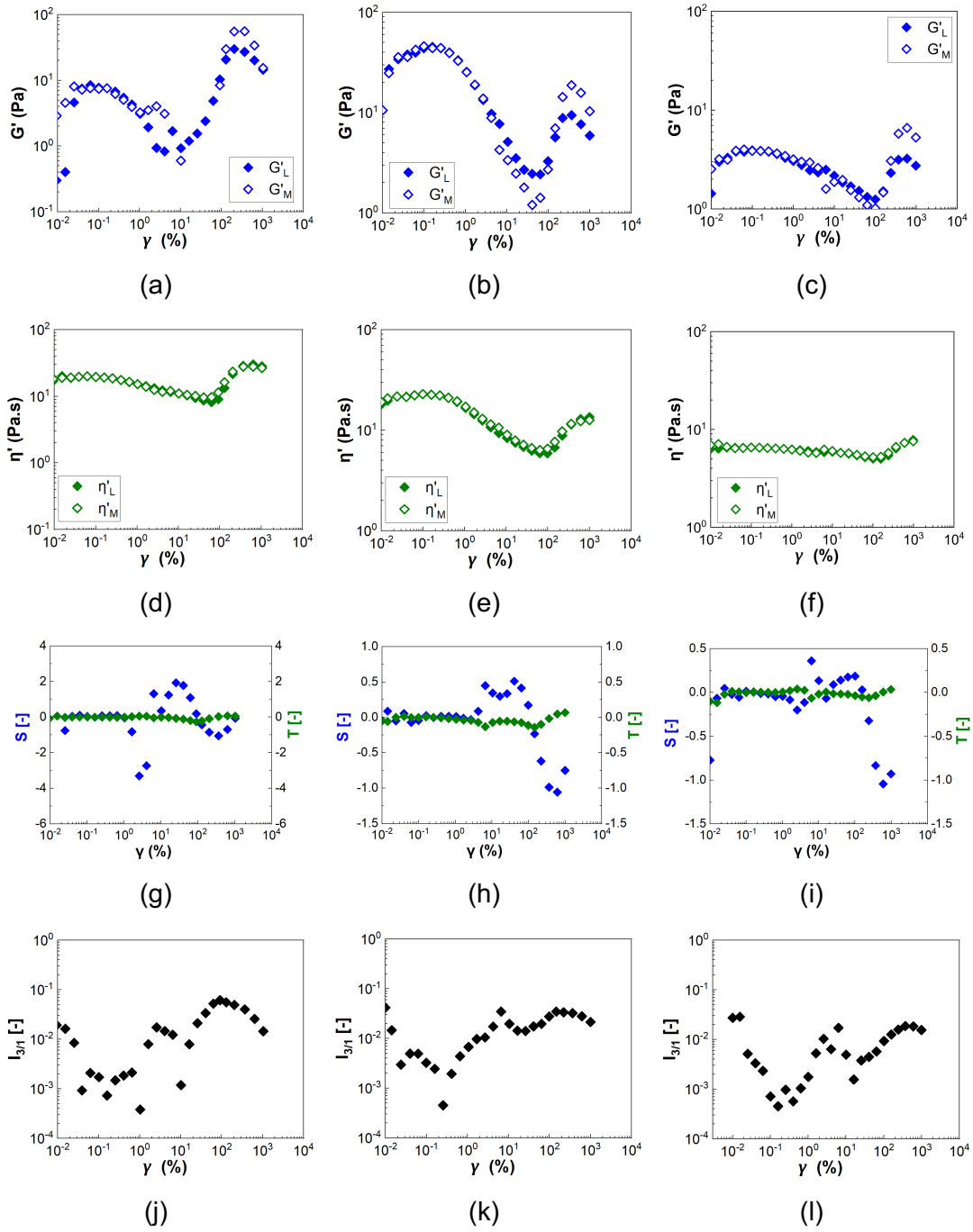

Figure 3.14: Non-linear viscoelastic measures estimated from the elastic Lissajous curves as a function of % strain amplitude for the three suspensions in glycerol at 20ºC and $f = 1Hz$. Dynamic minimum strain (G'_M) (hollow symbols) and large strain (G'_L) (filled sy.) moduli (a, b, c), dynamic minimum strain rate viscosity (η_M) (hollow symbols) and large strain rate viscosity (η_L) (filled symbols) (d, e, f), stiffening ratio (S) and thickening ratio (T) (g, h, i), Fourier spectra (j, k, l) representing the intensity of the third harmonic relative to that of the first harmonic.

Such shape in the $I_{3/1}$ vs $\gamma(\%)$ curve has been observed for weakly entangled micellar aggregates in a soft gel (Hyun et al., 2011) and fumed silica suspensions in

polypropylene glycol (Khandavalli and Rothstein, 2015) indicating the absence of direct interparticle contact due to the solvation layer.

In summary, all suspensions exhibited viscous dominated response under LAOS, $G'' > G'$, in the whole range of strain amplitudes applied, due to the presence of a solvation layer formed by glycerol molecules around the silicas. Although the recorded stress signals were mainly sinusoidal, implying absence of instabilities, the reconstructed signals after Fourier Transform revealed the presence of weak non-linearities mostly originating from the G' modulus. The latter indicates strain driven instabilities similar to the elastic dominated non-linearities observed in polymer solutions. The latter can be related to a transient deformation of the solvation layer under large applied strain amplitudes enabling weak interparticle contacts. It should be noted that the LAOS measurements were unable to fully capture the exact differences observed in the rheology of the three types of particle suspensions under steady state. Higher applied strain amplitudes (corresponding to higher equivalent strain rates), beyond the instrument limits, might have been required to induce the same phenomena as observed under steady state shear.

3.2.6 Effect of temperature on particle suspension rheology

Industrial manufacturing processes often operate at high temperature conditions so as to promote chemical reactions or improve the dispersion of solids into complex fluids. Mixing can also increase the temperature of a formulation due to the high stresses generated in the process. To account for these temperature variations, the rheological properties of all particle suspensions were measured not only at room temperature (20ºC) but also at a higher temperature of 60°C, typically employed in industrial processing to facilitate the addition and homogenization of particles in the formulation. Measurements were conducted under both steady state and oscillatory shear, i.e. frequency sweeps in the LVR. Selected particle suspensions at the onset of non-Newtonian behaviour at 20°C, i.e. $\varphi = 0.50$ for the glass spheres, $\varphi = 0.30$ for the abrasive silicas and $\varphi = 0.15$ for the filler silicas, were studied in the whole range of temperatures between 20°C and 60°C, to probe the evolution of the non-Newtonian phenomena observed; the data obtained are presented in Appendix I.

3.2.6.1 Steady state shear rheology

Figure 3.15 describes the relative viscosity (η_r) and the shear stress (τ) values for the three types of particle suspensions in glycerol as a function of shear rate ($\dot{\gamma}$) at 60°C. The data at $Sh < 1$ were excluded from the curves. The insets in the viscosity plots refer to the data obtained for the same suspensions at 20ºC. Continuous lines also represent the Carreau fittings to the shear thinning areas of the viscosity curves.

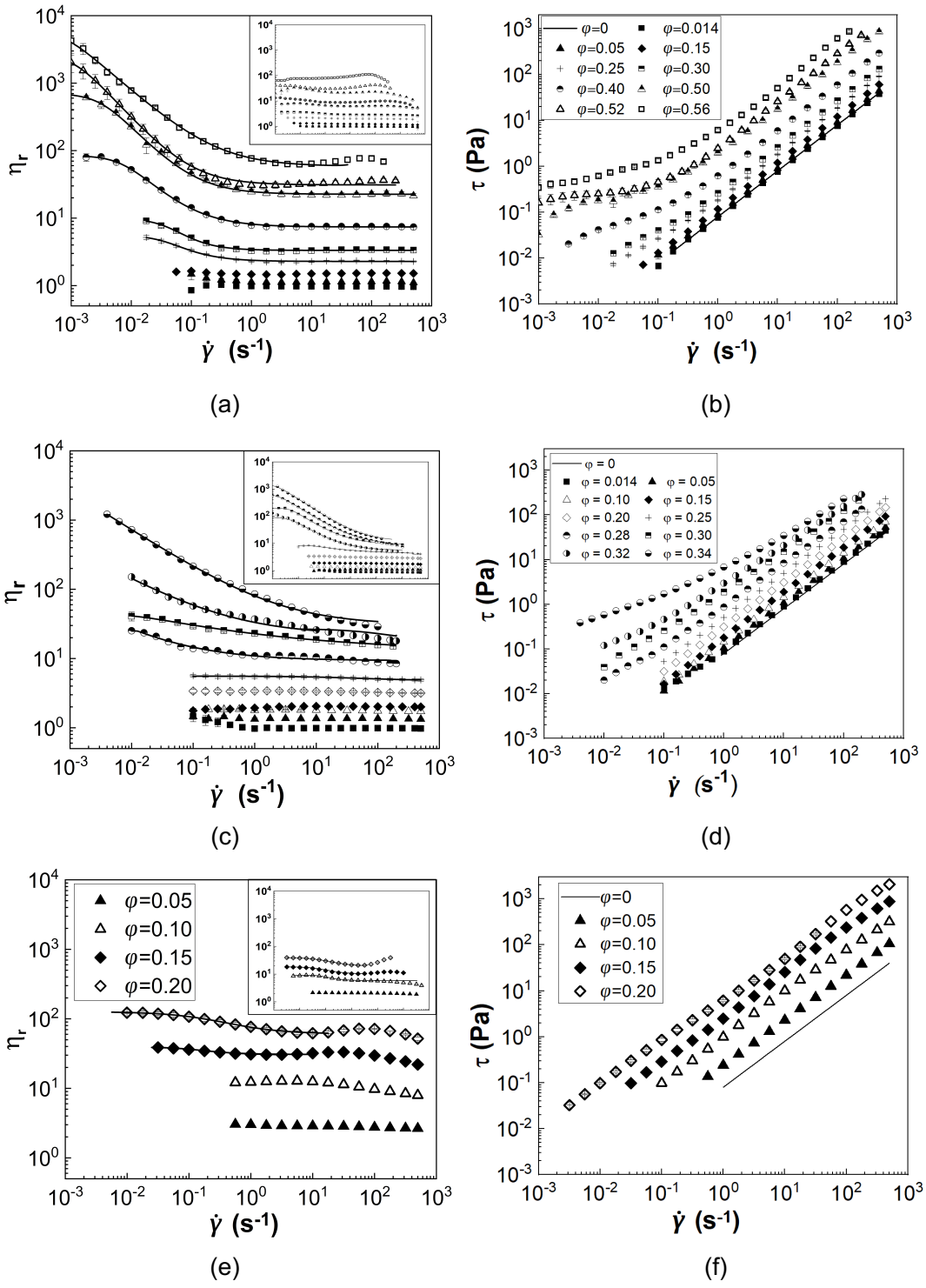

Figure 3.15: Relative viscosity (η_r) and b) shear stress (τ) of all the suspensions in glycerol at 60°C as a function of shear rate ($\dot{\gamma}$) and particle volume fraction (φ). a) and b) glass spheres; c) and d) abrasive silicas; e) and f) filler silicas. Insets in a), b) and c) show the corresponding data of the suspensions at 20°C for comparison reasons. Continuous lines represent the Carreau fittings to the shear thinning area of the viscosity curve.

Increasing the temperature to 60°C, shifts the onset of shear thinning response of the glass sphere suspensions (Figure 3.15a and b) to lower particle volume fractions, $\varphi \geq 0.25$, compared to 20°C, at which negligible shear thinning occurred even at the

highest concentrations reached. Yield stress behaviour at $\dot{\gamma}_{\to 0}$ is also observed by at 60°C, in contrast to 20°C. In contrast to the glass spheres, the shear thinning response of the abrasive silica suspensions (Figure 3.15c and d) is weakly suppressed by the increase in temperature and so does the apparent yield stress values. The shear thinning response of the filler silica suspensions (Figure 3.15e and f) is weak at both temperatures and shows low sensitivity to changes in the environmental conditions. On the other hand, the shear thickening behaviour of both glass sphere and filler silica suspensions appears significantly suppressed compared to that 20°C.

Figure 3.16 summarizes and compares the extent of both the shear thinning (Figure 3.16a) and the shear thickening (Figure 3.16b), as defined in eqs. (3.12) and (3.13) respectively, of the three types of suspensions in glycerol at 60°C, while the data at 20°C are included for comparison. Figure 3.16a clearly illustrates the sharp rise in the shear thinning behaviour of glass sphere suspensions with temperature, as evidenced by the higher $\eta_{r,e}$ values at $\varphi \geq 0.25$ compared to 20°C. In contrast, the abrasive silica suspensions show the same strong shear thinning behaviour at both temperatures, with the $\eta_{r,e}$ values being lower at 60°C. This contradictory behaviour is puzzling as according to the theory for hard sphere suspension rheology one would expect stronger interparticle interactions as well as more pronounced shear thinning to occur at higher temperatures or lower solvent viscosities (Konijn et al., 2014; Pavlik, 2009; Vryzas et al., 2017). The filler silica suspensions exhibit weak shear thinning at $\varphi \geq 0.10$, with low $\eta_{r,e}$ at 60°C similar to the estimated ones at 20°C.

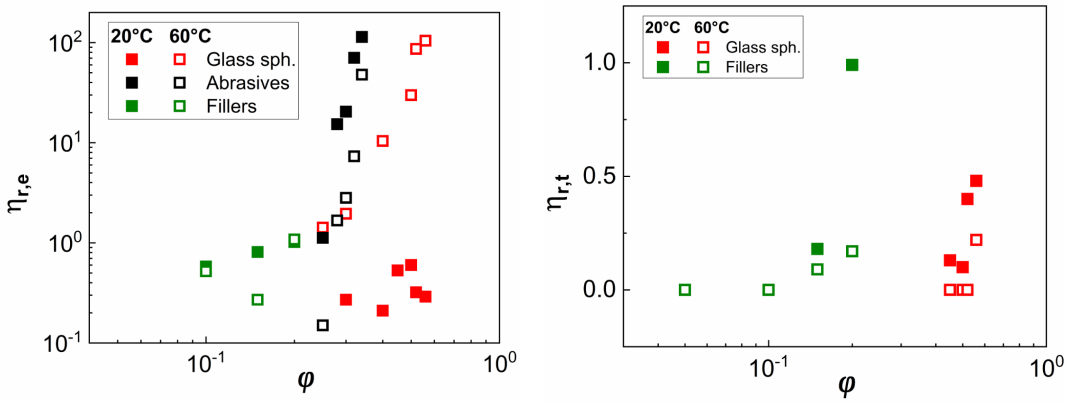

Figure 3.16: Comparison of the extent of a) shear thinning ($\eta_{r,e}$) and b) shear thickening ($\eta_{r,t}$) for the three suspensions in glycerol at 60°C. The data for 20°C are included for comparison.

On the other hand, the estimated values of $\eta_{r,t}$ (Figure 3.16b) show that the shear thickening response of both glass sphere and rough filler silica suspensions is

significantly suppressed by increasing the temperature from 20°C to 60°C. The filler silica suspensions show $\eta_{r,t}$ values that are similar to those estimated for the glass sphere suspensions but at much lower particle concentrations, attributed to their higher effective volume fraction due to porosity, as also described in section 3.2.3. Interestingly, the abrasive silica suspensions do not show shear thickening in any of the particle volume fractions or temperature conditions examined in the present study; this can be related to the strong shear thinning and yield stress behaviour responsible for screening shear thickening (Brown et al., 2010).

The friction driven mechanism based on the elastic deformation of surface asperities introduced by Lobry et al. (2019) was also utilized to describe the shear thinning response of the suspensions at 60°C. The raw variables and the estimated critical stress for each suspension are listed in Table 3.7 and Table 3.8. Although the glass spheres seem to have a smooth surface, a small degree of nanoscale asperities are expected on their surface topology. The critical stress (τ_c) estimated for the glass sphere suspensions at 60°C shows weak dependence on the particle volume fraction, except the lowest concentration of $\varphi = 0.25$, and thus, an average value with low uncertainty can be obtained. Also, the average critical stress value for the glass spheres appears to be similar to that estimated for the abrasive silicas at 20°C, indicating that similar particle dynamics apply to both cases. In contrast, the τ_c for the abrasive silicas at 60°C is two times higher than that of the same suspensions at 20°C indicative of the suppression of the shear thinning response. In the case of filler silicas, the estimated critical stress is again highly dependent on particle volume fraction, as observed at 20°C and thus, the corresponding results are omitted.

Table 3.7: Relaxation time (λ) as derived from the Carreau fittings in Figure 3.15a. Viscosity values (η) at the corresponding shear rates ($\dot{\gamma}$) for the estimation of the critical stress values (τ_c) and the critical load (L_c) for the glass sphere suspensions at 60°C.

φ	**0.25**	**0.30**	**0.40**	**0.50**	**0.52**	**0.56**
$\boldsymbol{\lambda\ (s)}$	28.9	26.1	146.3	325.3	921.2	1407.4
$\boldsymbol{\eta}$	0.3	0.5	2.1	5.1	16.7	24.6
$\boldsymbol{\dot{\gamma}\ (s^{-1})}$	0.056	0.1	0.032	0.056	0.016	0.04
$\boldsymbol{\tau_c\ (Pa)}$	0.2	0.2	0.2	0.2	0.2	0.2
$\boldsymbol{L_c\ (nN)}$	0.1 ($\boldsymbol{\tau_{c,average}}$=0.2 ±0.03 Pa)					

Table 3.8: Relaxation time (λ) as derived from the Carreau fittings in Figure 3.15c. Viscosity values (η) at the corresponding shear rates ($\dot{\gamma}$) for the estimation of the critical stress values (τ_c) and the critical load (L_c) for the abrasive silica suspensions at 60°C.

φ	**0.28**	**0.30**	**0.32**	**0.34**
$\boldsymbol{\lambda}$ $\boldsymbol{(s)}$	80.0	84.7	166.0	365.1
$\boldsymbol{\eta}$	1.8	2.0	3.7	8.8
$\dot{\boldsymbol{\gamma}}$ $\boldsymbol{(s^{-1})}$	0.021	0.56	0.25	0.52
$\boldsymbol{\tau_c}$ $\boldsymbol{(Pa)}$	0.4	0.4	0.4	0.4
$\boldsymbol{L_c}$ $\boldsymbol{(nN)}$	0.6 ($\boldsymbol{\tau_{c,average}}$=0.4±0.02 Pa)			

As shown earlier, the increase in temperature induces a yield stress behaviour to the glass sphere (Figure 3.15b) and abrasive silica suspensions (Figure 3.15d). The apparent yield stress values have been estimated from the limiting stress values at low shear rate and are plotted in Figure 3.17a as a function of particle volume fraction (φ). It is interesting to note that while a sharp increase in the yield stress behaviour with temperature is seen for the glass sphere suspensions, the opposite trend is observed for the abrasive silicas; the latter is in accordance with a weakening of the shear thinning with temperature. On the other hand, filler silicas exhibit zero shear viscosity response with no evidence of yield stress at all φ and temperatures studied.

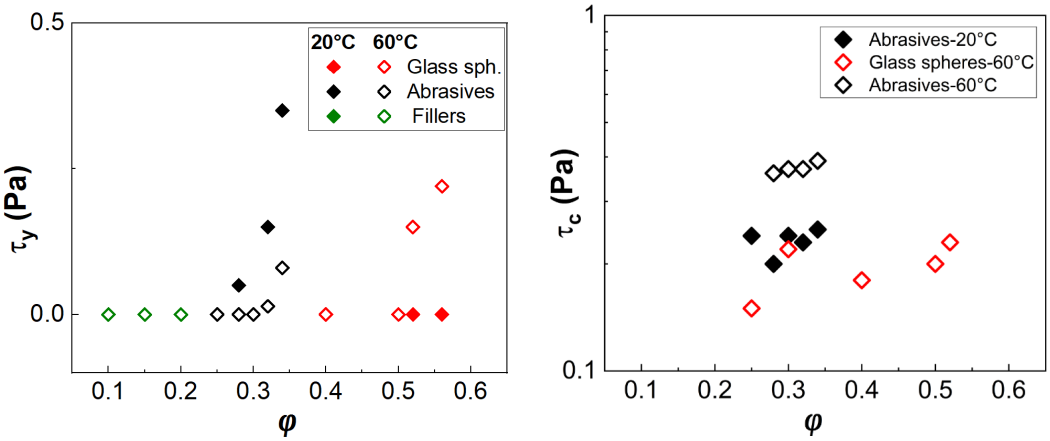

Figure 3.17: a) Apparent yield stress as a function of particle volume fraction (φ) of all suspensions in glycerol at 20°C and 60°C; b) Critical stress values for the onset of shear thinning behaviour as a function of particle volume fraction for the glass sphere and abrasive silica suspensions at 20°C and 60°C. Data for the glass spheres at 20ºC are not available as the

The critical stress values for the onset of shear thinning estimated from the viscosity curves of the glass sphere and abrasive silica suspensions at 60°C, are plotted in Figure 3.17b. As discussed previously, the τ_c values estimated for the glass sphere suspensions at 60°C are similar to the values obtained for abrasive silicas at 20°C highlighting the impact of temperature on the shear thinning of glass spheres. Increasing the temperature to 60°C can lead to a thinner solvation layer giving rise to the frictional contact of the glass surface nanoasperities. On the contrary, the critical stress of the abrasive silicas at 60°C is found to be higher than that at 20°C, which is indicative of the delay in shear thinning at elevated temperature conditions.

The friction coefficients (μ) of the suspensions at 60°C using the bootstrap method by Tanner et al. (2018) are summarized in Figure 3.18 as a function of shear rate ($\dot{\gamma}$) and particle volume fraction (φ). The corresponding μ values at 20°C are also included for comparison. A distinct increase of the friction coefficients with temperature can be observed for the glass sphere suspensions (Figure 3.18a) at low shear rates ($\dot{\gamma} \leq 0.01\ s^{-1}$) along with a more pronounced dependence on $\dot{\gamma}$. Increasing the particle volume fraction and thus, the shear thinning response, results in lower μ values at 60°C. On the contrary, the estimated friction coefficients for the abrasive silica suspensions (Figure 3.18b) show almost no change with temperature at low shear rates and an increase at $\dot{\gamma} \geq 0.5\ s^{-1}$. Raising the temperature to 60°C also results in the estimated μ values of the abrasive silicas to become less dependent on the shear rate, reflecting the reduction of the shear thinning in these suspensions with temperature. No apparent change in the friction coefficient values with temperature can be seen for the filler silicas (Figure 3.18c) probably due to the weak shear thinning response of these suspensions at both temperatures.

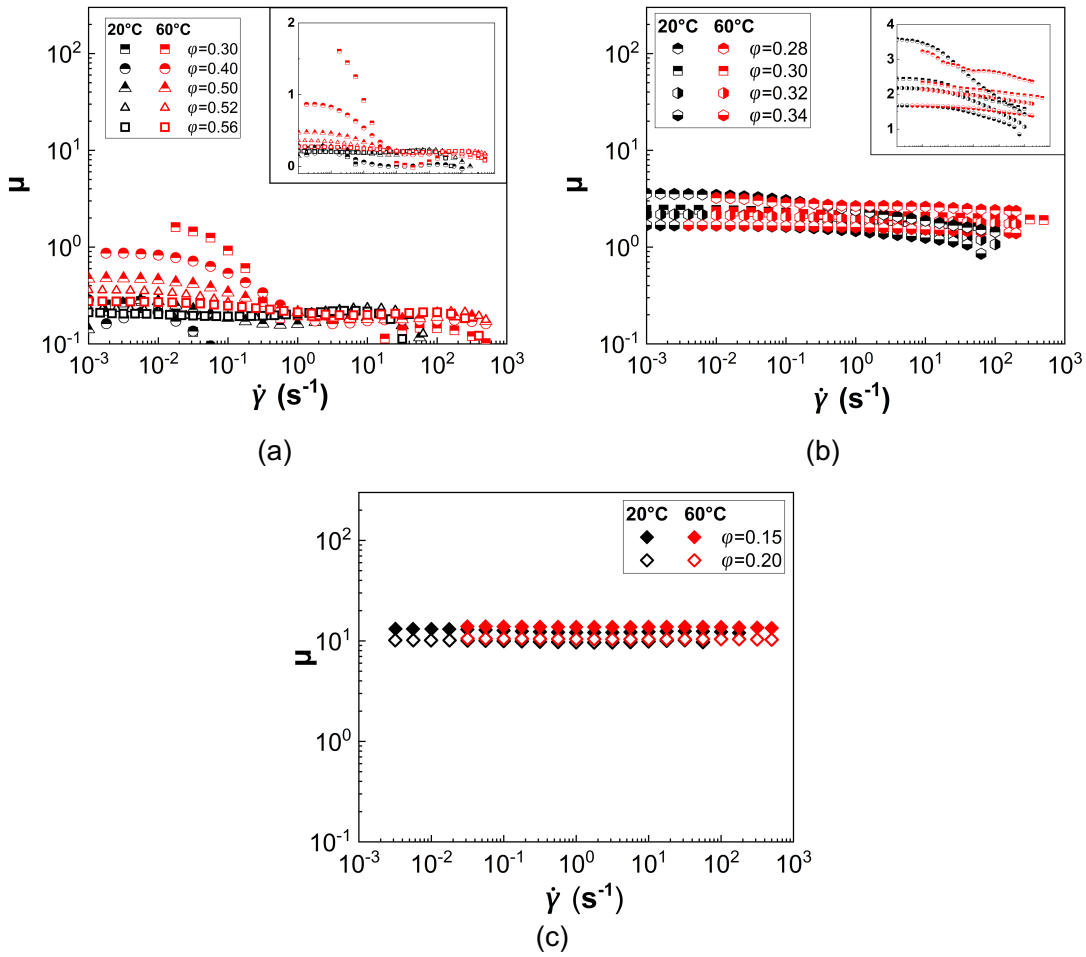

Figure 3.18: Microscopic friction coefficients for the suspensions of a) glass spheres (the inset represents the same estimates with expanded y-axis), b) abrasive silicas (the inset represents the same estimates with expanded y-axis) and c) filler silicas suspended in glycerol at 20°C and 60°C.

It should be noted that the calculation of the microscopic friction coefficient is based on a number of assumptions; the values of P/τ and η_r^* were taken from the literature and the same values were used for all particle types. Therefore, the estimated values might not fully capture the frictional characteristics of the two rough silicas, i.e. the abrasive and the filler particles. To probe this further, an additional method, based on the use of suspension shear stress (τ) and particle pressure (P) has been utilised to estimate the macroscopic friction coefficient (Blanc et al., 2018; Boyer et al., 2011; Gallier et al., 2014). Figure 3.19 plots the relative viscosity values (left column) for all the highly concentrated suspensions, i.e. those showing non-Newtonian rheology, at 60°C in comparison to the data at 20°C alongside the corresponding estimates of the macroscopic friction coefficient ($\mu_P = \tau/P$) (right column) as a function of a normalised shear rate, namely the viscous number, defined through the solvent viscosity and shear rate ($\eta_f\dot{\gamma}$) divided by the particle pressure and denoted as I_v ($I_v = \eta_f\dot{\gamma}/P$). The

particle pressure is assumed equal to the measured normal stress in this case, corresponding to the difference between the first and second normal stresses ($N_1 - N_2$). The insets in Figure 3.19 b, d and f show indicative plots of P as a function of the shear rate ($\dot{\gamma}$).

The estimated macroscopic friction coefficients (μ_P) for the glass spheres at 60°C (Figure 3.19b) exhibit two distinct regimes; the coefficient estimates seem to match those measured at 20°C and vary linearly with I_v for $I_v \geq 0.01$, while a deviation is observed for lower viscous numbers. μ_P shows an asymptotic behaviour characterised by higher values compared to those at 20°C and reaching a value of $\mu_p = 0.02$. This is in agreement with the increased shear thinning response of the glass sphere suspensions at 60°C compared to 20°C. The estimated μ_p value is much lower than that reported by Boyer et al. (2011), i.e. $\mu_P = 0.32$, for polymethylmethacrylate (PMMA, $d = 1.1 \pm 0.05\, mm$) and polystyrene (PS, $d = 0.58 \pm 0.01\, mm$) spheres suspended in index-matched Newtonian fluids and room temperature. This may be attributed to the smaller size of the particles used in the present study ($d = 11 \pm 5.5\, \mu m$) and the assumptions regarding particle pressure. The particle pressure was taken equal to $N_1 - N_2$; however, a more accurate estimation of N_2, which is closely related to particle contacts, is required to better reflect the particle pressure.

Figure 3.19d shows that the μ_P values for abrasive silica suspensions seem to collapse in one master curve, except the suspensions at the highest particle volume fraction ($\varphi = 0.34$). This is not surprising as the abrasive silica suspensions exhibit shear thinning response at both temperatures indicating the presence of frictional contacts at all experimental conditions studied. Thus, small changes in the response might not be captured by the μ_P estimates. Similar behaviour can be observed for the filler silica suspensions (Figure 3.19f). However, unlike in abrasive silicas, an asymptotic value is not reached for the filler silicas even at the lower end of normalised shear rates (I_v) possibly due to their weak shear thinning response. The absence of frictional contacts between the filler silicas further supports the idea that their shear thinning and thickening rheology is dominated by the particle-solvent interactions (i.e. presence of short-range repulsive forces) and not interparticle friction.

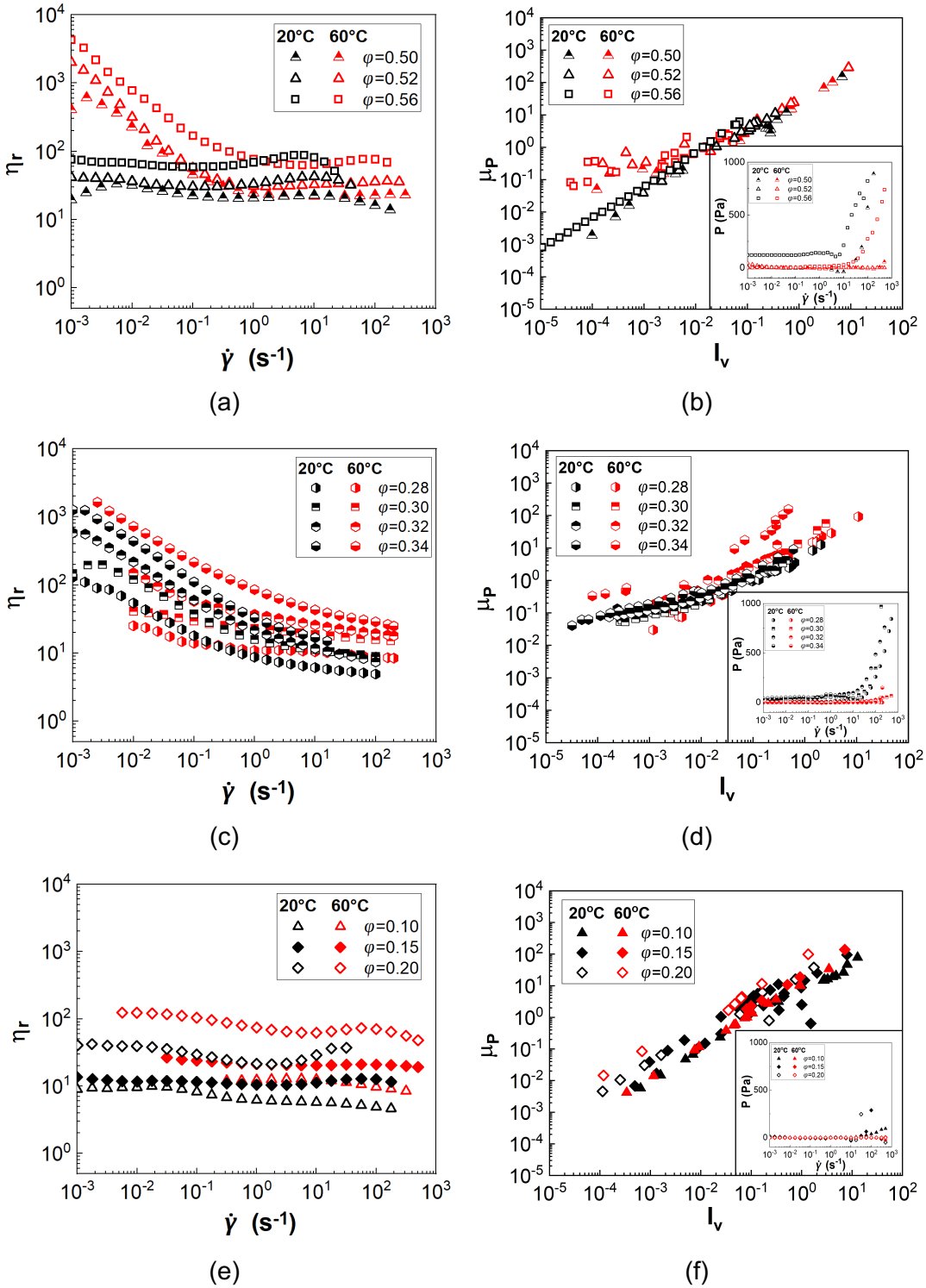

Figure 3.19: Relative viscosity values (η_r) as a function of shear rate ($\dot{\gamma}$) (left column) and macroscopic friction coefficients as a function of the viscous number (I_v) (right column) at 60°C. The corresponding data at 20°C are also presented for comparison. a) & b) glass spheres; c) & d) abrasive silicas and e) & f) filler silicas. The insets in b), d) and f) show indicative plots of the particle pressure (measured normal stress) to the shear rate.

Plotting the μ_P values for all suspensions together in Figure 3.20 shows that a universal master curve cannot be obtained due to the different experimental

conditions (temperature), the particle characteristics and volume fractions employed. The latter affect interparticle frictional contacts and subsequently, the values of the macroscopic friction coefficients. Two regimes can be observed in the low I_v region, which seem to be related to the extent of shear thinning in each case. The suspensions showing strong shear thinning and yield stress, i.e. glass spheres at 60°C, abrasive silicas at 20°C and 60°C, tend towards a higher macroscopic friction coefficient, compared to those showing weaker shear thinning, i.e. glass spheres at 20°C and filler silica suspensions at 20°C and 60°C. The deviations of μ_P from a single master curve have also been observed in numerical studies with varying dynamic friction coefficients, highlighting the strong effects of friction to suspension rheology (Gallier et al., 2014).

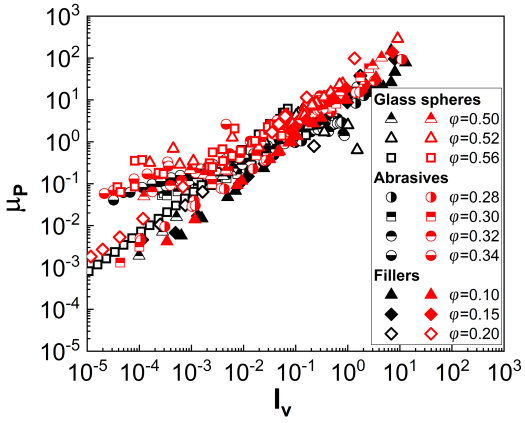

Figure 3.20: Master curve of the macroscopic friction coefficient of all non-Newtonian suspensions in glycerol at 20°C and 60°C as a function of the normalised shear rate.

In addition to the parameters discussed above influencing suspension shear thinning, Brownian motion-if present- comprises another factor promoting shear thinning. In the present study, the particles are highly polydisperse with some being in the submicron regime and inducing Brownian effects. are expected due to the particles being highly polydisperse. Table 3.9 shows the percentages of the particle that can induce Brownian effects estimated based on the size distribution of each particle type and assuming $Pe = 10$; the critical particle diameter below which Brownian effects can occur are $D \approx 2.3\ \mu m$ at 20°C and $D \approx 6.2\ \mu m$ at 60°C. It can be seen that the amount of particles to the total particle number being in the colloidal regime is at least two times higher at 60°C compared to room temperature (20°C) due to mainly the significantly lower viscosity of glycerol, i.e. 1.3 Pa at 20°C to 0.08 Pa at 60°C. Therefore, the shear thinning response of the suspensions at the elevated temperature can be partially attributed to the contribution of Brownian effects in

addition to the frictional contacts between the particles. However, these effects are limited to the low shear rate regime, as also discussed in Table 2.6, hence being restricted to only high particle volume fractions, where these low $\dot{\gamma}$ values are accessible without any sedimentation effects.

Table 3.9: Percentage % of the particles which can induce Brownian motion at the lowest shear rate of $\dot{\gamma} = 0.001s^{-1}$ based on the particle size distribution and assuming $Pe = 10$.

Particles	20°C	60°C
Glass spheres	9.5	27.4
Abrasive silicas	5.7	29.6
Filler silicas	N/A	11.9

The effect of temperature on the maximum packing fraction (φ_m) and the intrinsic viscosity (B) of the suspensions is shown in Figure 3.21. The φ_m values (Figure 3.21c) were estimated by fitting the Quemada equation (eq. (2.11)) to the $\eta_{r,0}$ and $\eta_{r,\infty}$ data for various particle volume fractions (Figure 3.21b). The corresponding relative viscosities obtained at 20°C are presented in Figure 3.21a for comparison. The B values (Figure 3.21d), on the other hand, were obtained by fitting the Mooney equation in each dataset given by (eq. (3.16)):

$$\eta_r = e^{\left(B*\frac{\varphi}{1-k\varphi}\right)} \tag{3.16}$$

where k is a fitting parameter. The latter was found to provide a better fit for all cases compared to the Krieger-Dougherty equation (eq. (2.9)). It should also be noted that the $\eta_{r,\infty}$ values were taken in the shear thinning region, i.e. before the onset of shear thickening for the glass spheres and filler silica suspensions.

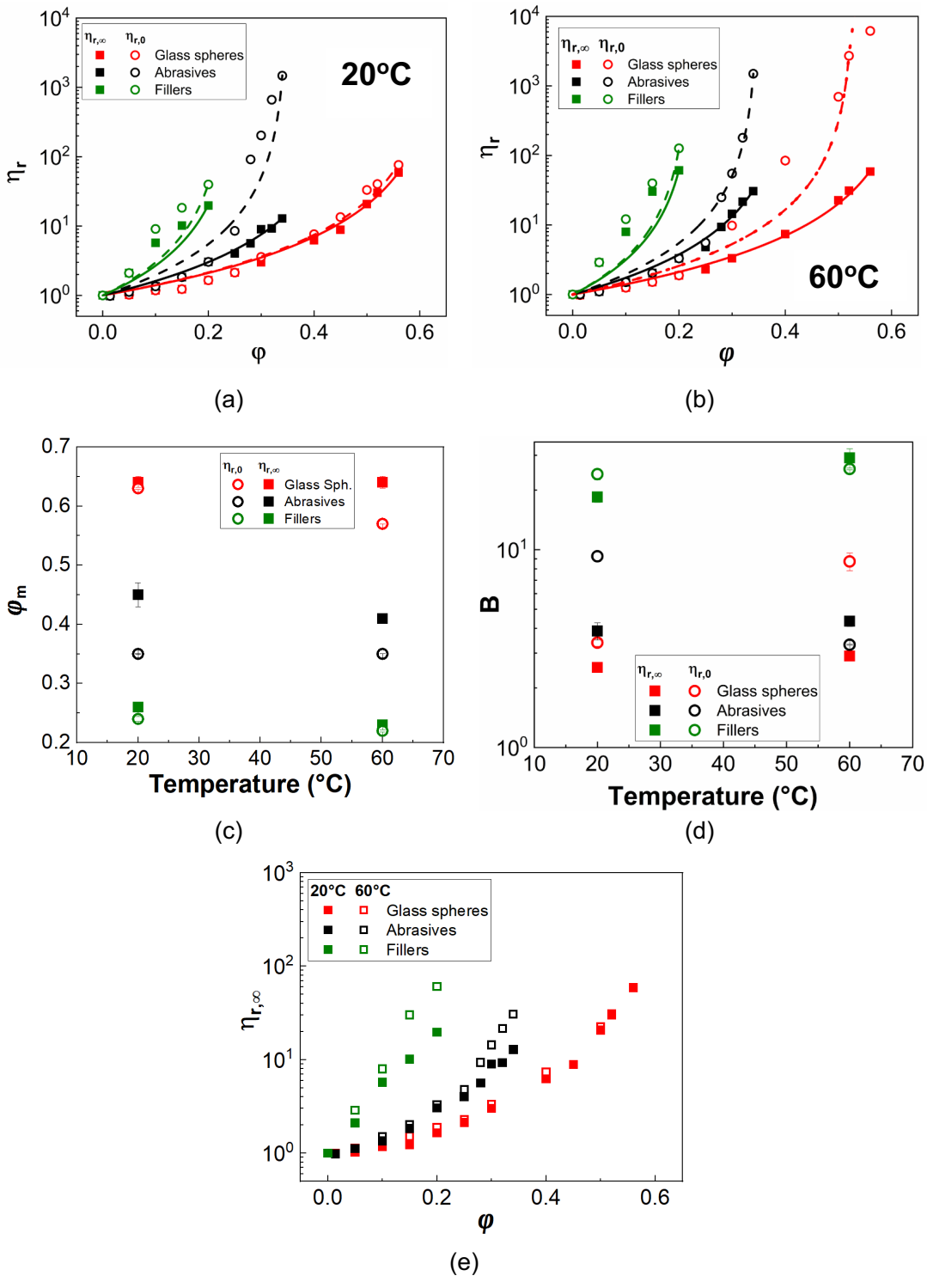

Figure 3.21: Zero shear rate relative viscosity ($\eta_{r,0}$) and infinite shear rate relative viscosity values ($\eta_{r,\infty}$) as a function of particle volume fraction (φ) at a) 20°C and b) 60°C. Continuous and dashed lines correspond to the Quemada equation fitting; c) Maximum packing fraction for all three types of suspensions as a function of temperature as derived from fitting the Quemada equation (eq. (2.11)) to the data in a and b; d) Intrinsic viscosity values derived from fitting the Mooney equation (eq. (3.16)) to the relative viscosities; e) Summary of the effect of temperature on the infinite shear relative viscosity values ($\eta_{r,\infty}$) as a function of particle volume fraction (φ).

Increasing the temperature to 60°C leads to higher relative viscosities (Figure 3.21b) compared to the 20°C (Figure 3.21a) and more pronounced differences between the zero (open symbols) and infinite shear rate (filled symbols) η_r values for the glass sphere suspensions due to stronger shear thinning. The effect of temperature on the rheology of the suspensions are better illustrated in Figure 3.21c and d. In particular, the maximum packing fraction (φ_m) (Figure 3.21c) is lower at the zero shear rate limit and at 60°C for all cases reported in this study. On the contrary, the intrinsic viscosity, B (Figure 3.21d) shows the opposite trend with higher values being observed at low shear rates and higher temperatures. The dependence of both parameters, i.e. φ_m and B, on temperature agrees with the presence of stronger interparticle interactions at 60°C, promoted due to a weakening in the thickness of the solvation layer.

Figure 3.21e highlights the effect of temperature on the infinite shear rate relative viscosity values ($\eta_{r,\infty}$). Although, the estimated $\eta_{r,\infty}$ values of the glass spheres suspensions overlap at all φ values for the two temperatures, deviations are observed for abrasive and filler silica suspensions, especially at $\varphi \geq 0.30$ for the abrasives and $\varphi \geq 0.15$, for the fillers respectively. The latter highlights that both particle characteristics and the solvent viscosity play a crucial role to suspension rheology.

Figure 3.22 plots the high shear rate limiting relative viscosities, $\eta_{r,\infty}$ of the highly concentrated suspensions in comparison to the frequency relative viscosity, $\eta'_{r,\infty}$, derived from the G'' values as $\lim_{\omega\to\infty} G''(\omega)/\omega$ at 60°C. A comparison with the corresponding data at 20°C is also included. $\eta'_{r,\infty}$ values represent the pure hydrodynamic component contribution to the total relative viscosity and is thus, independent of interparticle interactions, either repulsive or attractive (Blanc et al., 2018; Gao et al., 2017; Mewis and Wagner, 2012).

It can be seen that the $\eta'_{r,\infty}$ values are always lower than $\eta_{r,\infty}$ and show lower sensitivity to φ and temperature variations. The difference between $\eta'_{r,\infty}$ and $\eta_{r,\infty}$ provides an indication of the contact viscosity ($\eta_{r,c}$) assuming that $\eta_{r,\infty}$ is the result of hydrodynamic and contact forces. It can be seen that $\eta_{r,c}$ values increase with surface roughness and porosity as well as with temperature. Interestingly, this is not always proportionally related to the shear thinning response of the suspensions, especially at 60°C; one could expect that increased particle contacts will lead to more pronounced shear thinning through stronger frictional contacts and elastic deformation of the surface asperities. However, the shear thinning response of the abrasive silicas is suppressed at 60°C, which could be attributed to faster particle collisions, arising from

the extra heat energy offered to the system through heating, not allowing sufficient time for the asperities to deform.

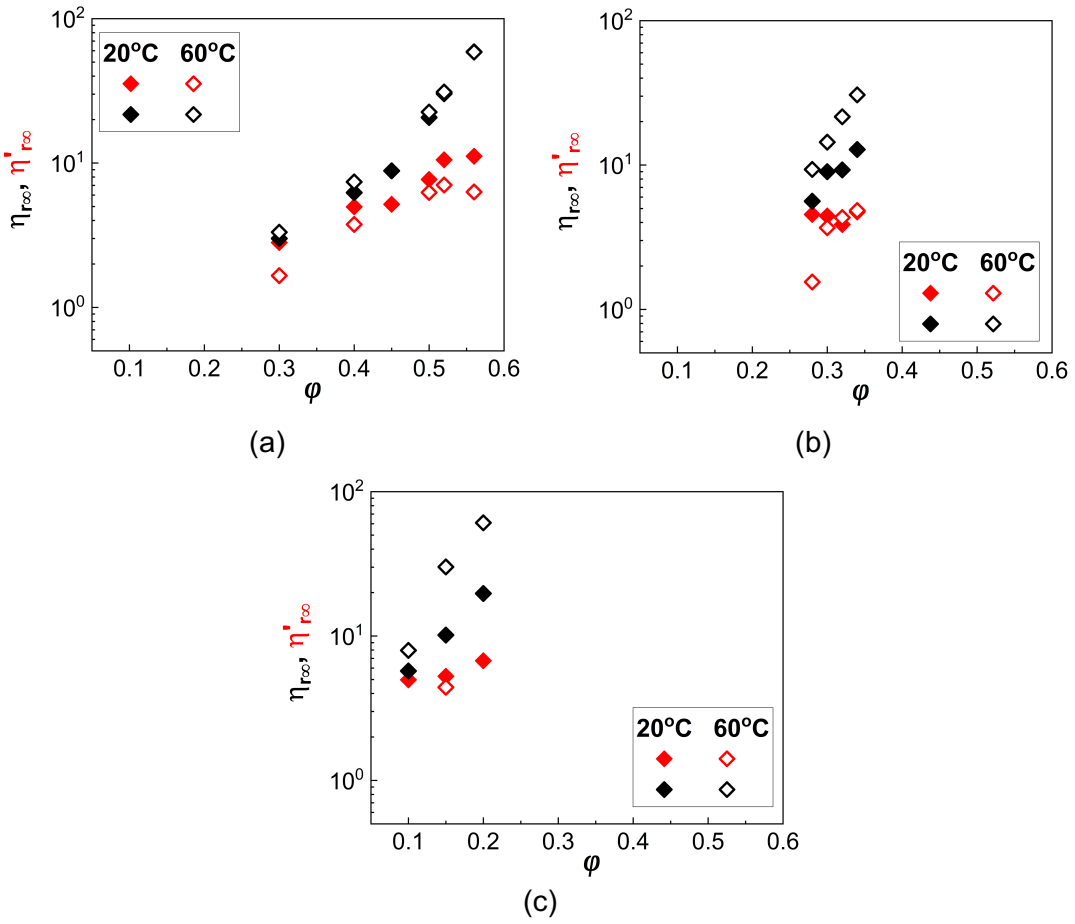

Figure 3.22: Comparison of the infinite shear rate relative viscosity ($\eta_{r,\infty}$) with the high frequency relative viscosity ($\eta'_{r,\infty}$) for all cases exhibiting non-Newtonian behaviour. a) Glass spheres; b) Abrasive silicas and c) Filler silicas at 60°C in comparison to 20°C.

3.2.6.2 Effect of particle specific surface area

The effect of temperature is also considered in relation to the particle specific surface area (S_p) for selected suspensions. In section 3.2.3, it was shown that increasing the particle specific surface area, increases the viscosity values and induces non-Newtonian behaviour at lower apparent particle volume fraction: this was found to stem from the increase in the effective particle volume fraction and the density of the free surface silanol groups.

Figure 3.23 displays the $\eta_{r,\infty}$ values for selected suspensions with φ varying from 0.05 to 0.20, as a function of the particle specific surface area at 20°C and 60°C. Increasing S_p leads to an exponential increase of the relative viscosity values in a semi-logarithmic plot. Most importantly, the dependence of $\eta_{r,\infty}$ on S_p intensifies with

the particle volume fraction and temperature due to stronger interparticle interactions. This behaviour is illustrated in Figure 3.23c plotting the exponents derived through the exponential fits to the data in Figure 3.23a and b; the latter are shown to increase with φ and temperature. It should be noted that the exponential fits should be treated with caution as only three points are available in each φ. The maximum packing fraction (φ_m) decreases almost three times by increasing S_p from $1.6\,m^2/g$ to $226.2\,m^2/g$, but it is less sensitive to temperature variations.

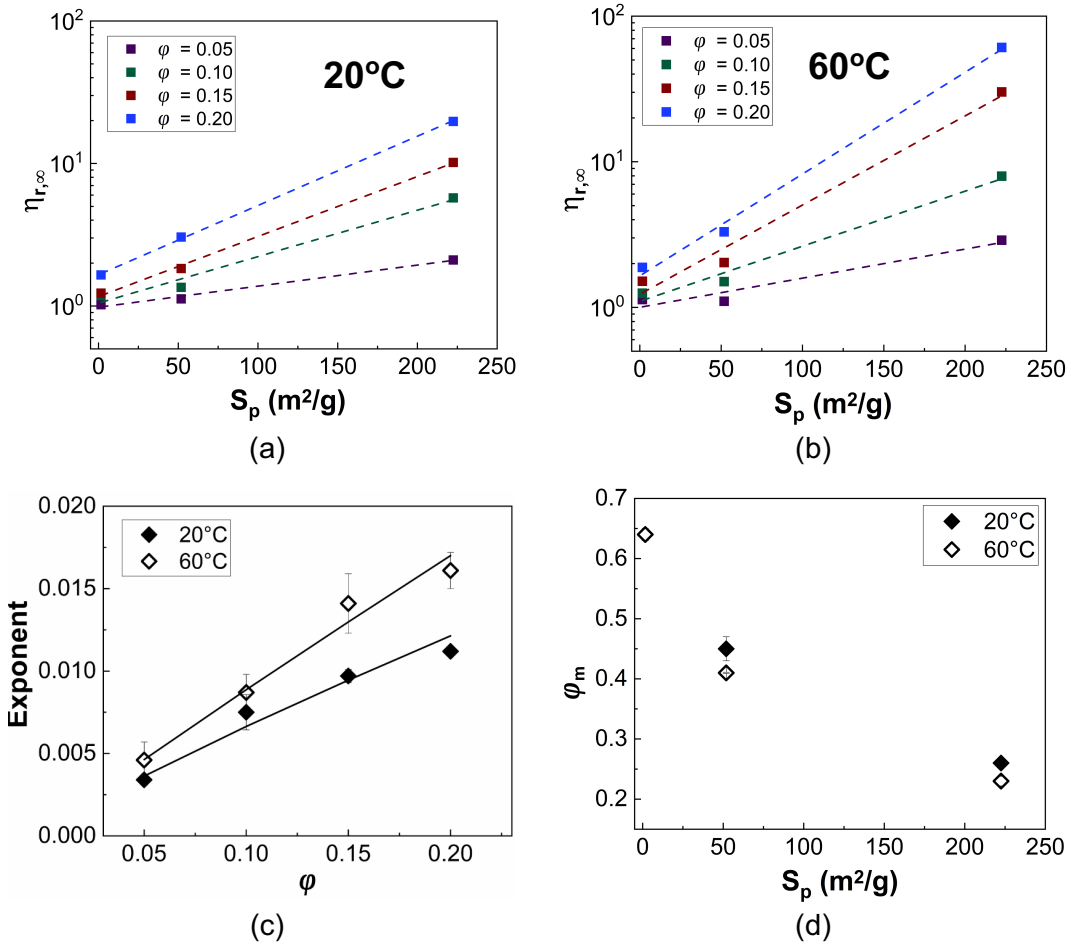

Figure 3.23: Effect of particle specific surface area on infinite shear relative viscosity ($\eta_{r,\infty}$) for low to intermediate particle volume fractions at a) 20°C and b) 60°C. Dashed lines correspond to the exponential fits of the data in Figure 3.23 a and b and the estimated exponents are presented in plot (c) as a function of particle volume fraction and temperature. Continuous lines were drawn to guide the eye. d) Maximum packing fraction (φ_m) derived from the $\eta_{r,\infty}$ values as a function of the particle specific surface area.

3.2.6.3 Oscillatory shear rheology

The rheological properties of selected highly concentrated suspensions were investigated under dynamic oscillatory shear at 60°C, similar to the measurements at

20°C. The acquired G', G'' and phase angle (δ) values are presented in Figure 3.24 as a function of the angular frequency (ω).

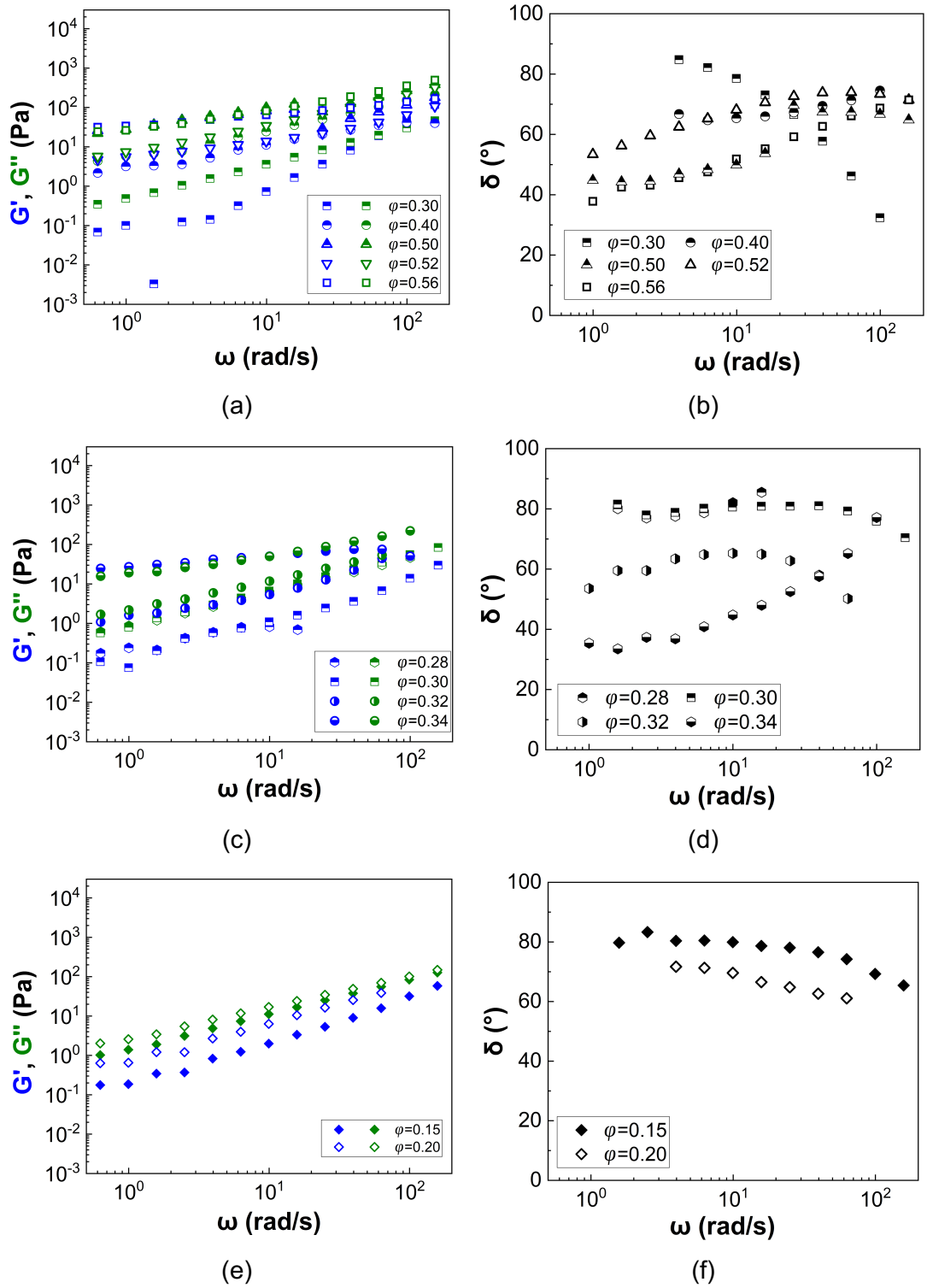

Figure 3.24: Storage (G') and loss moduli (G'') (left column) as well as the phase angle (δ) (right column) as a function of angular frequency (ω) generated from experimental frequency sweeps in the LVR of all highly concentrated suspensions in glycerol at 60°C. a) & b) glass spheres; c) & d) abrasive silicas and e) & f) filler silicas.

Both the G' and G'' values of all suspensions increase with particle volume fraction and angular frequency; similar to the behaviour of the suspension at 20°C. A viscous dominated response ($G'' > G'$) is mainly observed at low ω and a transition to a solid like behaviour (i.e. $G' > G''$) occurs at higher angular frequencies. This behaviour is also reflected in the measured phase angles (δ) (Figure 3.24b, c and f), which vary from $\delta = 80^o$ to $\delta = 30^o$ depending on the value of ω and the particle type. The viscoelastic nature of the suspensions can be attributed to the increased interparticle interactions arising from the solvation layer losing its lubrication effectiveness at such high temperature conditions.

Figure 3.25 illustrates the effect of temperature on the viscoelastic properties of indicative suspensions of the three particle types at a fixed volume fraction of $\varphi = 0.30$. The data used for the filler silicas were taken at a nominal volume fraction of $\varphi = 0.20$ which is equivalent to $\varphi = 0.30$ if estimated using the experimentally derived particle density ($\rho = 1.24\ g/ml$). Both the storage and loss modulus increase with increasing the particle specific surface area and decreasing the temperature. The measured phase angles for the glass spheres and filler silica suspensions are lower at 60°C, indicating an increase in suspension viscoelasticity which is in agreement with the increase in the shear thinning response under steady state. In contrast, the opposite trend is observed for the abrasive silicas reflecting the variations in the frictional contacts between particles leading to a decrease in the shear thinning behaviour as well.

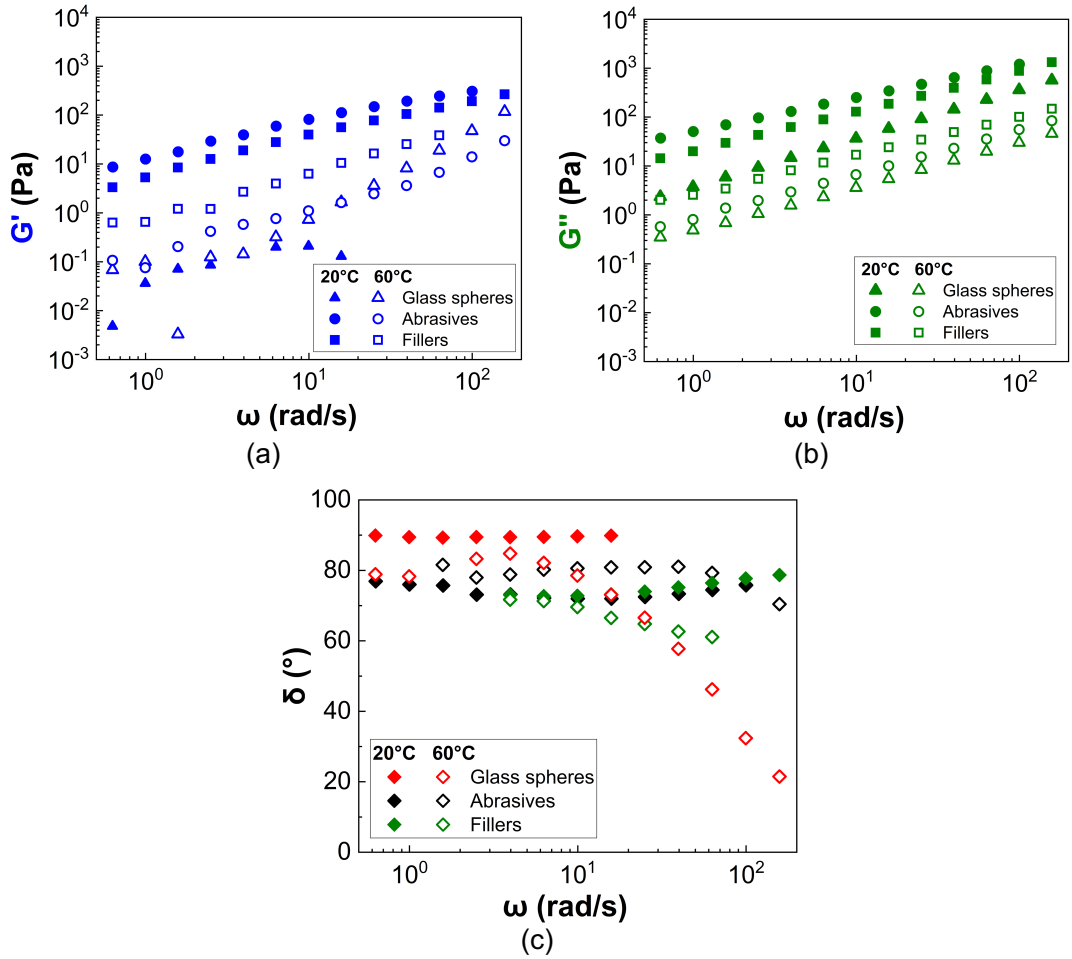

Figure 3.25: Indicative a) storage modulus (G') and b) loss modulus (G'') for the three suspensions in glycerol at 20°C and 60°C. The glass sphere and abrasive silica suspensions correspond to a particle volume fraction $\varphi = 0.30$, while the data for the filler particle suspensions correspond to $\varphi = 0.20$. c) Phase angles (δ) for the corresponding suspensions in a and b at the two temperatures.

3.3 Discussion

In this chapter the rheological properties of three types of non-Brownian silica particles suspended in glycerol were investigated to probe the friction-driven shear thinning mechanism. Suspension rheology and the onset of non-Newtonian rheological phenomena highly depend on interparticle and particle-fluid interactions. These interactions are governed by several parameters such as particle volume fraction, particle surface morphology, size and size distribution and the solvent physical properties. The influence of these will be discussed below in relation to shear thinning, yield stress and shear thickening rheology.

A particle subjected to a shear rheometric flow experiences various forces that can be repulsive or attractive. The balance between these two distinct force

categories is expressed in a simplified form as follows (eq. (3.17)) (Amiri et al., 2012; Warren et al., 2015):

$$F_{solvation} + F_{el} + F_{Brownian} = F_{hydrodynamic} + F_{friction} \quad (3.17)$$

$F_{solvation}$ describes the force arising from the solvation layer formed around the particles from glycerol through hydrogen bonding between the hydroxyl groups on the glycerol molecule and the free silanol groups present on silicas. F_{el} represents the electrostatic repulsive forces between the particles mainly arising from the weakly negatively charged silica surface. F_{el} has been found to scale with $1/e^{D_{pp}}$ (De Kretser and Scales, 2008) where D_{PP} is the particle-particle distance. $F_{Brownian}$ refers to the contribution of Brownian motion to suspension rheology. The Brownian force scales with the thermal energy in the system ($k_B\theta$, k_B is the Boltzmann constant, θ is the temperature) and the particle radius (α) as $F_{Brownian} = k_B\theta/\alpha$.

On the other hand, the attractive forces comprise two components: $F_{hydrodynamic}$ which refers to the hydrodynamic lubrication force arising when two particles approach each other, such that the suspending medium is squeezed out from the interparticle gap (Amiri et al., 2012), and expressed as:

$$F_{hydrodynamic} \sim 6\pi\eta_0\alpha^3\dot{\gamma}/D_{pp} \quad (3.18)$$

where η_0 is the viscosity of the suspending medium, α is the particle radius, $\dot{\gamma}$ is the shear rate, and $F_{friction}$ which results from direct particle-particle contacts and depends on particle surface characteristics (Warren et al., 2015).

In the present study, glycerol is used as a non-aqueous Newtonian suspending medium. As already discussed, both glycerol and silicas are highly hydrophilic with a copious amount of hydroxyl groups (-OH), leading to the formation of a solvation layer around the particles which prevents the interparticle contacts. The thickness and strength of the solvation layer is mainly dependent on the solvent viscosity and its physical properties, e.g. the content of water in glycerol (Amiri et al., 2012; Gao et al., 2017; Raghavan et al., 2000). In particular, at low temperatures ca 20°C, the viscosity of glycerol is high, producing a more stable layer around the particles, governing thus suspension rheology (Amiri et al., 2012). The stability of this lubrication film is also expected to increase with the specific surface area of the particles due to the increase in the surface silanol group density. The presence of the solvation layer suppresses the shear thinning behaviour of the glass sphere suspensions at 20°C through

hindering direct interparticle contacts, while weak shear thickening is observed at $\varphi \geq 0.50$.

Particle surface roughness seems to compete with the interparticle interaction screening induced by the glycerol layer as abrasive silica suspensions show pronounced shear thinning at $\varphi \geq 0.25$ under the same experimental conditions. Chatté et al. (2018) and Lobry et al. (2019) stated that the shear thinning behaviour stems from a reduction in the microscopic friction coefficient under increasing normal load due to the elastic deformation of the surface asperities. This theory appears to explain the shear thinning of the abrasive silicas sufficiently well enabling also the estimation of the critical load able to initiate this non-Newtonian response. However, the latter requires frictional contacts between the particles to occur, which are expected to be hindered by the solvation layer. Therefore, it is likely that surface roughness in combination with the high effective volume fraction due to porosity render possible the deformation and further rupture of this layer, enabling the frictional contacts between the abrasive silicas at increasing shear rate. A simplified representation of the mechanism proposed for the shear thinning behaviour of the highly concentrated abrasive silica suspensions is shown in Figure 3.26.

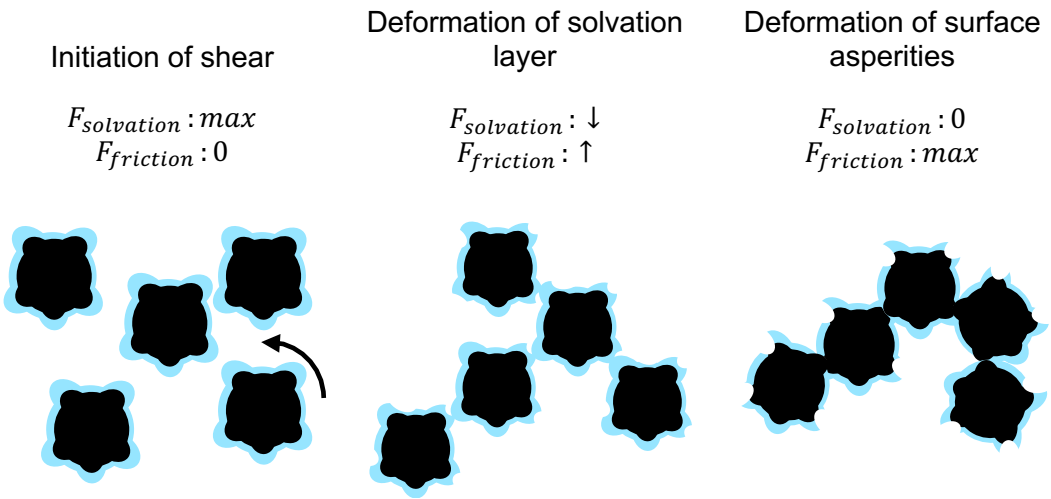

Figure 3.26: Schematic representation of the shear thinning mechanism for the abrasive silica suspensions at 20°C.

A non-monotonic effect of the particle specific surface area was observed in the steady state shear rheology of the suspensions with the filler silica suspensions exhibiting a rheological behaviour between that observed for the glass spheres and abrasive silica suspensions. The accurate explanation of the rheological behaviour of the filler silica suspensions is challenging and cannot be simply explained through the particle surface roughness or friction alone. The observed rheology of the filler silica

suspensions is likely to arise from the competition between the high effective volume fraction due to particle porosity and their increased specific surface area leading to a higher density of surface silanol groups thus, strengthening the solvation layer formed by glycerol. The two types of commercial silicas also differ in shape as shown in Chapter 2 with the abrasive silicas appearing slightly rougher that the filler silicas. Therefore, the surface asperities in the case of filler silicas might not be able to penetrate the formed solvation layer leading to a reduced shear thinning response.

Increasing the temperature from 20°C to 60°C distorts the balance of the forces presented in eq. (3.17), altering thus, the rheology of the suspensions. Heating transfers the system of the particles and the suspending medium to a higher kinetic energy state and thus, weakens the hydrogen bonding and consequently, the strength of the formed solvation layer around the particles. This reduces the $F_{solvation}$ but also the $F_{hydrodynamics}$, since both are highly dependent on glycerol viscosity which dramatically reduces from $\eta_{f,20°C} = 1.3\ Pa.s$ at 20°C to $\eta_{f,20°C} = 0.08\ Pa.s$ at 60°C. On the other hand, a decrease in $F_{solvation}$ allows particles to move closer to each other, which subsequently increases F_{el}. Brownian effects will also be favoured at higher temperatures since they are linearly related to temperature, thus increasing the term $F_{Brownian}$.

The particles used in the present study are highly polydisperse also spanning in the submicron regime where Brownian effects can affect the rheology of the suspensions. As discussed in Table 3.9 the ratio of the Brownian particles to the total number of particles in the suspension estimated at $Pe \geq 10$ (Foss and Brady, 2000) is relatively low at 20°C and $\dot{\gamma} = 0.001s^{-1}$, i.e. 9.5% for the glass spheres, 5.7% for the abrasive silicas and 0.3% for the filler silicas. However, this percentage seems to significantly increase at 60°C due to the decrease in glycerol viscosity. In particular, the corresponding ratio of the particles in the colloidal regimes increases above 20% for the glass sphere and abrasive silica suspensions, while it reaches a value of *ca* 12% for the filler silicas. Although Brownian motion might have an effect on suspension rheology, mainly increasing shear thinning behaviour, this is limited to the low shear rate range ($0.001s^{-1} \leq \dot{\gamma} \leq 0.1s^{-1}$) at both temperatures beyond which the ratio of the particles in the colloidal regime drop below 1%.

Heating the suspensions at 60°C enhances the shear thinning response of the glass sphere suspensions, whereas the opposite effect is observed for the porous and irregular abrasive silicas. The shear thinning response of the filler silica suspensions exhibits a lower sensitivity to temperature variations. The increase in the shear thinning for the glass spheres suspensions can be attributed to the system

moving from a state of very weak almost negligible frictional contacts at 20°C and low shear rates to a state of stronger interparticle contacts at 60°C, mainly due to the decrease in $F_{solvation}$ (Gao et al., 2017; Konijn et al., 2014; Warren et al., 2015) in combination with a higher contribution of Brownian effects, which also tend to elevate the zero shear rate viscosities.

Unlike the glass sphere suspensions, the shear thinning rheological behaviour of both types of commercial silicas was weakly suppressed by increasing the temperature from 20°C to 60°C. This behaviour contradicts the stronger interparticle interactions enabled in the less viscous fluid at higher temperature. However, these two suspensions, and especially the abrasive silicas, already experience shear thinning at 20°C due to frictional asperities. It is likely, thus, that heating the suspension and increasing the mobility of both the solvent molecules and that of the solid particles, due to the extra thermal energy offered to the system transforming to kinetic energy, reduces the contact time between the particle surfaces due to faster collisions. The latter leads to a decrease in $F_{friction}$ which leads to the shear thinning response according to Lobry et al. (2019).

In addition, the particle porosity and subsequently, the amount of solvent absorbed into the pores, might play a crucial role to suspension rheology by increasing the effective volume fraction (φ_{eff}), as discussed previously. It should be noted that the φ_{eff} values are expected to be the same between 20°C and 60°C as the particle and glycerol densities do not change with temperature. Although, low viscous fluids are expected to flow easier into the pores leaving less solvent in suspension, the higher motility of the glycerol molecules at elevated temperatures appears to counteract this phenomenon. In fact, the observed decrease in the extent of shear thinning for silicas might indicate that at 60°C, the concentration of the suspending medium in relation to the solids is higher compared to the 20°C, resulting in a lower effective volume fractions and thus, less pronounced non-Newtonian rheology.

Another parameter that seems to be sensitive to particle surface morphology and temperature is the apparent yield stress (τ_y). In general, yield stress values increase with particle volume fraction, due to a decrease in the particle-particle distance; the same effect is induced by increasing the particle surface roughness, due to the rough particles offering more areas of contact compared to spheres (Ancey and Lè Ne Jorrot, 2001; Blanc et al., 2018). In the present study, the yield stress values are obtained by extrapolating the shear stress curves at the limiting low shear rate region.

Although, the rheology of yield stress fluids has been widely reported in the literature, the real effect of temperature on this variable is still subject to debate and

is found to be highly system-specific (De Kretser and Scales, 2008). Most importantly, the yield stress both increases and decreases with temperature depending on the material properties and the experimental conditions applied. A plausible explanation for the decrease in the yield stress values might arise from the loosening of the interparticle forces due to the more random motion of the particles at higher temperatures (De Kretser and Scales, 2008; He et al., 2006). However, a higher temperature implies less viscous fluids, enabling stronger interparticle contacts and a decrease in the interparticle distance, which in turn can increase the yield stress (De Kretser and Scales, 2008; Gao et al., 2017; Vryzas et al., 2017; Warren et al., 2015).

The present study is also a testament that the yield stress can both increase and decrease with temperature depending on the particle system under investigation. An increase in the yield stress is observed for the glass sphere suspensions arising from the increase in the interparticle interactions at low shear rates and 60^{o}C. On the contrary, the yield stress of the abrasive silica suspensions decreased at 60^{o}C, mainly due to the ability of the particles to move more freely in the low viscous glycerol. The filler silica suspensions showed no evidence of yield stress in any of the experimental conditions and particle volume fractions studied. The lower effect of Brownian forces for the third type of suspensions might be responsible for the lack of yield stress.

The glass sphere and filler silica suspensions also exhibit shear thickening response at $\varphi \geq 0.50$ and $\varphi \geq 0.15$ respectively, which can be attributed to either interparticle frictional contacts or shear induced hydroclustering occurring at relatively high particle loadings (Brown et al., 2011b, 2010; Clavaud et al., 2017; Lin et al., 2015; Maranzano and Wagner, 2001b; Mari et al., 2014; Townsend and Wilson, 2017). The abrasive silica suspensions show no evidence of shear thickening in any of the experimental conditions applied, possibly due to the pronounced shear thinning and yield stress values, which can screen the shear thickening response as evidenced by earlier studies in the literature (Brown et al., 2010).

Increasing the temperature to 60^{o}C significantly suppresses the shear thickening response of both the glass sphere and filler silica suspensions. Repulsive forces between the particles generally increase with temperature due to their higher kinetic energy upon heating, forcing them to perform a more random motion. On the other hand, hydrodynamic forces reduce due to the dramatic reduction in the solvent viscosity. Since shear thickening occurs when the hydrodynamic lubrication forces dominate the total repulsive forces acting on the particles leading to cluster formation, higher temperatures increase the barrier that needs to be overcome to induce shear thickening. Under these circumstances, higher shear rates are required to bring particles in close proximity and thus, the shear thickening rheological response is

suppressed (Amiri et al., 2012; Liu et al., 2019; Warren et al., 2015) at the elevated temperature employed in the present study.

3.4 Concluding remarks

In this chapter, three different types of non-Brownian particles with different surface morphologies and porosities but similar size distributions, were suspended in glycerol and their rheology was investigated under steady state and oscillatory shear and varying temperature. The main aim of the present work was to probe the frictional driven mechanism that governs the shear thinning response of the suspensions. The suspension rheology was found to depend highly on the particle volume fraction (φ), the particle surface characteristics, the magnitude of the shear rate ($\dot{\gamma}$) and the solvent viscosity (η_f) which was altered through the applied temperature conditions.

Increasing the particle volume fraction increased the relative viscosity values and induced non-Newtonian rheological response. The critical φ for the onset of shear thinning and shear thickening varied depending on the particle surface characteristics and specific surface area. In particular, the filler silicas which had the higher degree of porosity among the three types, accompanied by the higher specific surface area, exhibited the onset of shear thinning at $\varphi = 0.10$, while shear thickening was also observed at $\varphi = 0.15$. Accordingly, the filler silicas showed the lowest value for the maximum packing fraction (φ_m). This behaviour was generally attributed to the high effective volume fraction (φ_{eff}) of the porous particles due to the solvent absorption into the pores but also the higher silanol density at increasing the particle specific surface area, able to induce stronger particle-particle but also particle-solvent interactions.

The affinity between the glycerol molecules and the silica particles led to the formation of a solvation layer around the particles, which seemed to suppress the shear thinning response of the 'smooth' glass spheres at 20°C, where the glycerol viscosity was high. In contrast, pronounced shear thinning response was observed for the abrasive silicas. The shear thinning of the latter was attributed to a recently introduced theory based on the elastic deformation of the surface asperities and the reduction of the microscopic friction coefficient at increasing normal loads. The filler silicas showed an intermediate behaviour between that of the glass spheres and the abrasive silicas, most likely arising from the intermediate effective volume fractions estimated for this type of particles using the experimentally derived density.

Increasing the temperature reversed the non-Newtonian behaviour of the suspensions; the shear thinning of the glass spheres was enhanced while that of the rough silicas was weakly suppressed. The shear thickening was suppressed for both the glass spheres and the filler silicas, whereas the abrasive silica suspensions showed no evidence of shear thickening in any experimental condition applied. The above highlight the significance of various parameters and their contribution to suspension rheology, especially in the case of the irregularly shaped and porous particles that are commonly employed in industrial formulations. The findings in this chapter generally showed that the flowability of particulate formulations could be tuned through either varying the applied environmental/manufacturing conditions or the particle surface properties so as certain properties are given to the end products.

The next chapter examines the rheology of the same particles suspended in a different solvent (mineral oil) to probe an additional mechanism to shear thinning rheology based on particle agglomeration and disaggregation with increasing shear.

Chapter 4

Adhesive particle suspensions [2]

The previous chapter examined the rheological properties of the three types of particle suspensions in glycerol. The effect of key parameters, such as the shear rate, the particle volume fraction, the particle surface roughness and porosity as well as the physical properties of the suspending medium, on the rheology of the suspensions was investigated under steady state and dynamic oscillatory shear at different temperature conditions. The shear thinning behaviour of the abrasive silica suspensions was attributed to a friction driven mechanism and in particular, to the elastic deformation of the surface asperities upon particle frictional contacts which leads to a reduction in the microscopic friction coefficient. However, the latter mechanism competed with the lubrications effect induced by the solvation layer formed by glycerol resulting in a suppression of the shear thinning response in the suspensions of glass spheres and filler silicas. The suspension rheology was mediated by the particle surface characteristics and porosity as well as the physical (viscosity) and chemical (hydroxyl groups, -OH) properties of glycerol. Glycerol seemed to generally suppress the non-Newtonian rheological phenomena of the suspensions, compared to suspensions in aqueous solutions presented in the literature. This behaviour is mainly attributed to the presence of a solvation layer formed through hydrogen bonding between the free surface silanol groups on the silicas and the hydroxyl groups of the glycerol molecules.

[2] Part of this chapter has been published in the Journal of non-Newtonian Fluid Mechanics and Physical Review Fluids.

A. Papadopoulou, J.J.J. Gillissen, H.J. Wilson, M.K. Tiwari, S. Balabani, 2020.' On the shear thinning of non-Brownian suspensions: friction or adhesion?', *Journal of non-Newtonian fluid Mechanics*, 281, p.104298.

J.J.J. Gillissen, A. Papadopoulou, M.K. Tiwari, S. Balabani, H.J. Wilson, 2020. 'Suspension rheology of adhesive particles at high shear rates.' *Physical Review Fluids*, 5, p. 053302.

This chapter aims to elucidate another mechanism of shear thinning behaviour in non-aqueous media based on particle agglomeration. When particles are attractive or suspended in solvents that favor particle-particle interactions, particle agglomerates are likely to form at low shear rates giving rise to high viscosity values and yield stress behaviour. Increasing the magnitude of the applied deformation (e.g. the shear rate), results in the agglomerates breaking down to smaller entities, leading to more homogeneous dispersions and reduced suspension viscosity (Eberle et al., 2014; Kaliviotis and Yianneskis, 2007; Min Kim et al., 2014). The latter highlights the importance of suspension microstructure on the rheology of such complex systems. Blood provides a typical example of an adhesive shear thinning systems exhibiting rich microstructure. The proteins in the blood plasma result in erythrocyte aggregation at low shear and disaggregation at higher ones giving rise to the shear thinning rheology observed in blood.

The work presented in this chapter focuses primarily on the glass sphere and abrasive silica suspensions in mineral oil at particle volume fractions in the dilute to semi-dilute regime ($\varphi = 0.005\ to\ 0.15$ and $\varphi = 0.02\ to\ 0.10$ respectively). The filler silicas were investigated only for $\varphi = 0.10$ due to the extremely high viscosity values and edge fracture observed during shearing, making their sample preparation and characterization challenging. All the measurements were conducted at 20^{o}C as temperature variations were not expected to affect mineral oil viscosity remarkably.

The chapter is divided into four main sections; section 4.1 providing a brief introduction to the conditions leading to particle agglomeration and the previous studies investigating suspensions microstructure and section 4.2 presenting the measured rheological properties, i.e. the relative viscosity (η_r) and the shear stress (τ), as a function of shear rate and particle volume fraction at room temperature. Time effects, including transient response and aging, will also be discussed for selected cases. This will be followed by the dynamic response of the suspensions investigated under dynamic frequency sweeps in the linear regime and microstructure characterization of the suspensions under applied deformation. The latter is examined using two different methods, i.e. an optical shearing technique and image processing techniques for relatively dilute suspensions and large amplitude oscillatory shear (LAOS) measurements for the more concentrated cases. The results will be discussed in section 4.3 in the light of particle-particle interactions and the absence of particle-solvent interactions in the non-polar suspending medium. A closing summary is provided in section 4.4.

4.1 Introduction

Suspension rheology is highly dependent on interparticle and particle-solvent interactions, which are governed by the competition of the attractive and repulsive forces acting between the particles. Various parameters can influence the balance between the different forces including particle size and surface morphology, particle volume fraction as well as the affinity between the particles and the carrier medium (Amiri et al., 2012; Blanc et al., 2018; Eberle et al., 2014; Mewis and Wagner, 2012).

More specifically, when particles are suspended in solvents which promote particle attraction, adhesion forces are expected to dominate suspension rheology. In the presence of adhesive systems, suspension rheology and in particular, the shear thinning response, is governed by the formation of agglomerates which break down under increasing applied deformations. This leads to the large structures reducing to smaller units and thus, lowering the viscosity with increasing shear rate, as has been demonstrated in biological fluids such as blood and silica particle suspensions (Bounoua et al., 2016; Eberle et al., 2014; Kaliviotis and Yianneskis, 2007; Min Kim et al., 2014; Snabre and Mills, 1996). Snabre and Mills (1996) were among the first to study the rheology of aggregated suspensions of both rigid spheres and blood. In this study, they were able to estimate the adhesion forces between the particles through bulk rheological data and in particular, the yield stress.

The shear induced microstructural changes of suspensions of adhesive particles play a key role in the shear thinning of such particle systems; these are also highly dependent on particle size distribution, volume fraction and surface characteristics (Blanc et al., 2018; Mewis and Wagner, 2012). For example**,** when Brownian motion is significant, due to the presence of small, submicron particles, agglomeration is favoured by the larger available surface for particle contacts leading to more pronounced shear thinning rheology (Mewis and Wagner, 2012). Additionally, rough particles can favour particle adhesion at lower particle volume fractions compared to smooth spheres due to larger number of contact points and hence contact area (Blanc et al., 2018).

Various methods have been employed to probe suspension microstructure, including simulations, spectroscopic techniques and bulk rheology (Egres et al., 2006; Gadala-Maria and Acrivos, 1980; Kalman and Wagner, 2009; Khandavalli and Rothstein, 2015; Morris, 2009; Sierou and Brady, 2002). For example, Kalman and Wagner (2009) utilised a novel scattering technique named Ultra Small Angle Neutron Scattering (USANS), which enabled the monitoring of the shear induced hydroclustering and subsequent shear thickening response of submicron silica

dispersions in polyethylene glycol. Khandavalli and Rothstein (2015) studied the origins of shear thickening for three different particle dispersions, i.e. fumed silica in polyethylene oxide, fumed silica in polypropylene glycol and cornstarch in water, using large amplitude oscillatory shear (LAOS). The LAOS experiments revealed that these suspensions shear thicken by three different mechanisms, i.e. cluster formation at sufficiently high applied shear rates flocculated by polymer bridging, hydrocluster formation and jamming respectively. Techniques based on ultrasound (Norisuye, 2017) or X-Ray tomography (Saint-Michel et al., 2019) have also been employed to probe suspension microstructure.

Direct visualisation of the structural changes of the particles under different shearing conditions comprises another method to monitor the microstructure of the suspension *in situ*. However, visualisation of particle suspension microstructure is challenging, especially for the highly dense suspensions, and thus optical imaging and actual quantification of the shear-induced characteristics of such systems has been fairly limited; to date very few relevant studies exist mainly focusing on smooth or spherical particles and biological samples, such as blood (Gunes et al., 2008; Kaliviotis et al., 2016; Lin et al., 2018; Ma et al., 2008; Massaro et al., 2020; Tanner, 2015; Varga et al., 2019).

4.2 Results

4.2.1 Steady state shear rheology

The rheological properties of dilute and semi-dilute glass sphere and abrasive silica suspensions in mineral oil under steady state shear are presented in Figure 4.1 in terms of the relative viscosity (η_r) and the shear stress (τ) as a function of the shear rate ($\dot{\gamma}$). These suspensions exhibit higher viscosity values compared to the corresponding suspensions in glycerol and a typical yield stress behaviour, while the onset of non-Newtonian response (shear thinning) occurs at concentrations as low as 2% v/v, which are much lower than the ones observed for the suspensions in glycerol.

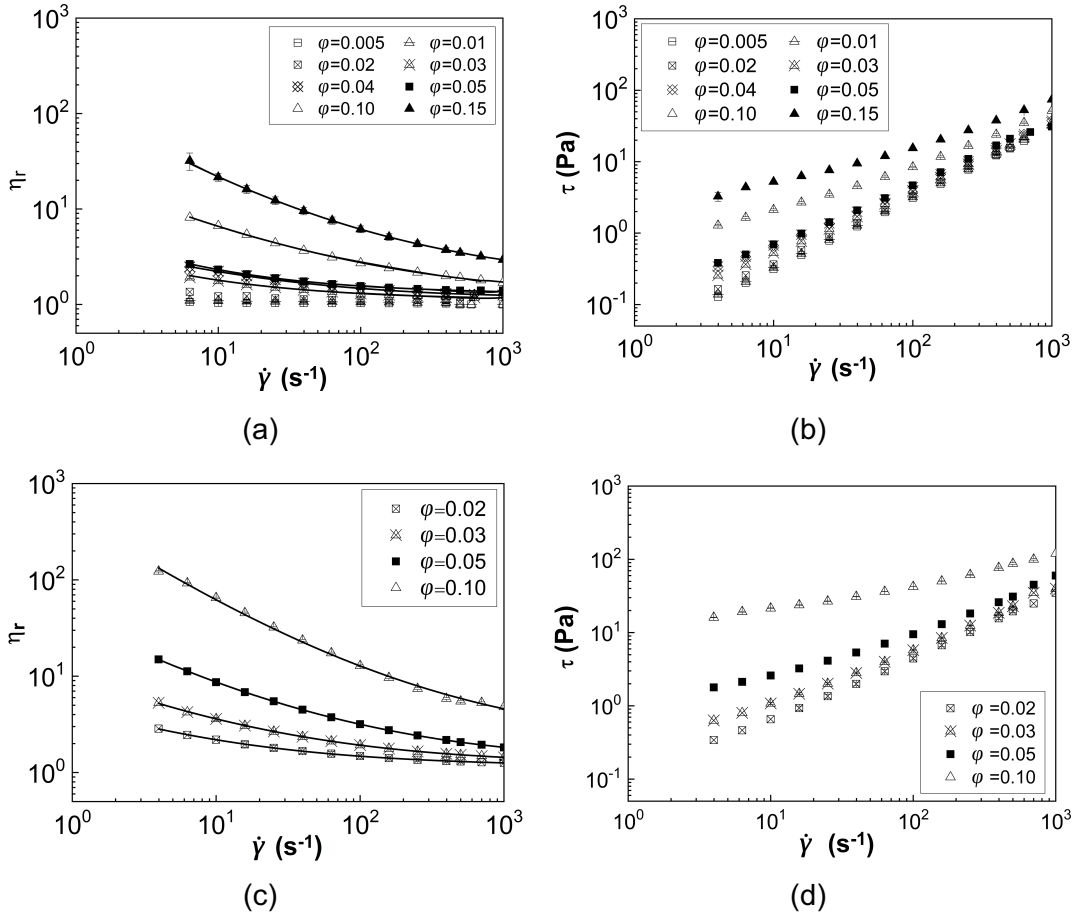

Figure 4.1: a) and c) Relative viscosity (η_r) and b) and d) shear stress (τ) of the different types of suspensions in mineral oil at 20°C as a function of shear rate ($\dot{\gamma}$) and particle volume fraction (φ). The data below the particle sedimentation limit have been excluded based on the Shields number. a) and b) refer to the glass sphere suspensions; c) and d) show the data of the abrasive silicas.

Mineral oil is non-polar; it consists of a mixture of alkanes and thus, no interactions with the free silanol groups on the silica particle surface are expected. Instead, large particle agglomerates and a gel network are likely to form originating from long range attractive forces (i.e. hydrogen bonding) between the free silanol groups on the surface of the non-Brownian silicas, giving rise to the flow curves in Figure 4.1a and c. These are characterised by pronounced shear thinning even at low particle concentrations (Chen et al., 2007; Nicodemo et al., 1974; Selimovic et al., 2007). The viscosity curves (Figure 4.1a and c) also reach an asymptotic Newtonian plateau at sufficiently high shear rates ($\dot{\gamma}$ ≥500 s^{-1}), indicating agglomerate disaggregation under these high shearing conditions.

The yield stress behaviour of these adhesive particle suspensions is well captured by the Herschel-Bulkley model. Fitting the experimental data shown in Figure 4.1a and c with the Herschel-Bulkley equation, modified to represent the shear viscosity

($\eta = \eta_\infty + (\tau_y/\dot{\gamma})(1 + (\lambda\dot{\gamma})^n)$) (eq. (2.5)), yields the infinite shear rate viscosity ($\eta_{r,\infty}$), the yield stress (τ_y) and the relaxation time (λ) values, summarized in Table 4.1 and Table 4.2 for the glass spheres and abrasive silica particle suspensions, respectively. The flow index (n) is kept constant at 0.5 for all particle concentrations, obtained through regression analysis.

Table 4.1: Relaxation times (λ), infinite shear rate relative viscosity ($\eta_{r,\infty}$) and yield stress values (τ_y) for the glass spheres suspensions in mineral oil as derived from fitting eq. (2.5) to the experimental data in Figure 4.1a.

φ	**0.03**	**0.04**	**0.05**	**0.10**	**0.15**
$\boldsymbol{\lambda}$ $(\boldsymbol{s})$	2.6	6.4	1.3	1.1	0.1
$\boldsymbol{\eta_{r,\infty}}$	1.1	1.2	1.3	1.3	1.2
$\boldsymbol{\tau_y}$ $(\boldsymbol{Pa})$	0.06	0.04	0.07	0.4	2.7

Table 4.2: : Relaxation times (λ), infinite shear rate relative viscosity ($\eta_{r,\infty}$) and yield stress values (τ_y) for the silica suspensions in mineral oil as derived from fitting eq. (2.5) to the experimental data in Figure 4.1c.

φ	**0.02**	**0.03**	**0.05**	**0.10**
$\boldsymbol{\lambda}$ $(\boldsymbol{s})$	44.5	8.9	0.7	0.1
$\boldsymbol{\eta_{r,\infty}}$	1.2	1.2	1.3	2.0
$\boldsymbol{\tau_y}$ $(\boldsymbol{Pa})$	0.01	0.1	0.6	11.4

The yield stress values (τ_y) for both suspensions in mineral oil are presented in Figure 4.2 as a function of particle volume fraction and a power law relation between τ_y and φ can be observed. The yield stress of the glass sphere suspensions is found to scale as $\tau_y \sim \varphi^3$, in agreement with Snabre and Mills (1996), who reported an exponent of 3 in the presence of rigid particle agglomerates. On the contrary, the yield stress for the abrasive silica suspensions in mineral oil scales with φ^4, implying a stronger effect of the volume fraction on suspension rheology compared, for example, to colloidal particle dispersions in which the yield stress scales with φ^2 (Eberle et al., 2014; Min Kim et al., 2014). This can be attributed to the fact that the silica particles in these experiments comprise clusters of colloidal particles which should have greater (fractal) surface area, thereby featuring a stronger dependence on volume fraction. It should be noted that the lowest concentration showing yield stress behaviour (φ=0.03) in the glass sphere suspensions does not follow the power law,

most likely due to the agglomerates being much smaller at such low particle volume fraction compared to the agglomerates formed at higher concentrations.

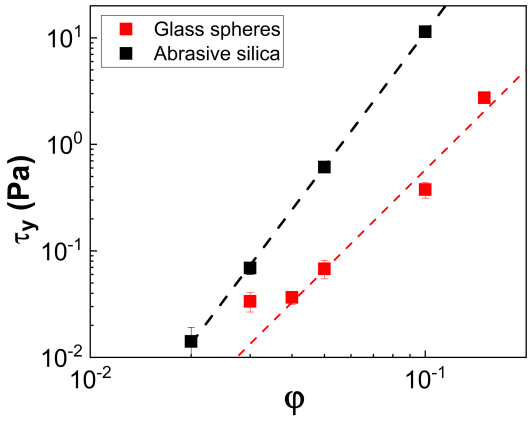

Figure 4.2: Yield stress (τ_y) values as a function of particle volume fraction (φ) estimated by fitting the Herschel-Bulkley equation to the data presented in Figure 4.1a and c.

Due to the weak interaction of the particles with mineral oil, as mentioned above, it is reasonable to expect that shear thinning stems from an adhesion driven mechanism, whereby particles form agglomerates at low shear rates, which break down at increasing applied deformations leading to a reduction in suspension viscosity and thus, shear thinning. Using dimensional analysis arguments, it can be postulated that the adhesion forces (F) for the two types of particles studied, will relate to the yield stress as $\tau_y \sim (F_A/a^2)\varphi^n$, where α corresponds to the single particle radius and not that of the agglomerates. The resulting estimated adhesion force for the glass spheres was found equal to 0.03 μN, while for the abrasive silicas 7 μN. The higher F_A values estimated for the abrasives is to be expected on the basis of a higher specific surface area, which enhances interparticle interactions in the non-polar solvent. A recent study, which utilized selected cases of the data presented above showed that a proxy for the adhesion force (F') between particles in adhesive suspensions can be estimated from the asymptotic approach of the suspension viscosity in the limit of infinite shear rate, where particle agglomerates are supposed to have completely broken down. It was found that the silica particles in the present study showed 10 times higher F' values compared to the smooth spheres, highlighting the importance of particle surface morphology on the interparticle interactions even under extreme shear rate conditions (Gillissen et al., 2020).

The infinite shear relative viscosity values, $\eta_{r,\infty}$, estimated by fitting eq. (2.5) to the viscosity data, are summarised in Figure 4.3a. The data of the corresponding suspensions in glycerol are also included in the same figure for comparison. It can be

clearly seen that the suspensions in mineral oil exhibit much higher viscosity values compared to the suspensions in glycerol even at the limiting high shear rates, where the particle agglomerates are expected to have completely broken down or have sizes comparable to the single units; this indicates the significant difference of the particle dynamics in the two solvents. The abrasive silicas exhibit higher relative viscosity values compared to the glass spheres due to the surface roughness (Genovese, 2012; Moon et al., 2015) in agreement with the corresponding suspensions in glycerol, where an increase in the relative viscosity with surface roughness was observed.

The maximum particle concentration to achieve a homogeneous dispersion of the particles in mineral oil (based on visual observations) was $\varphi = 0.15$ in contrast to the suspensions in glycerol where particle concentrations up to $\varphi = 0.62$ were achieved. Therefore, although suspending the particles in mineral oil limited the range of φ values to achieve a homogeneous suspension, the onset of non-Newtonian rheological behaviour (shear thinning) was shifted to much lower φ compared to suspensions in glycerol. This allowed insights into adhesive suspension behaviour to be drawn for dilute and semi-dilute systems. It should be noted that the φ values reported above should not be confused with the maximum packing fraction (φ_m) of the suspensions estimated through fitting the empirical models, (eq. (2.6) to (2.8)). The estimated φ_m values from the Krieger-Dougherty fittings to the $\eta_{r,\infty}$ values are presented in Figure 4.3b for the two types of particle suspensions in mineral oil. The corresponding data of the suspensions in glycerol are presented for comparison. The glass sphere suspensions show higher φ_m compared to the abrasive silicas at both suspending media, while there is almost a 50% reduction in the maximum packing for the suspensions in mineral oil compared to the glycerol case. This can be attributed to the particle agglomeration taking place in mineral oil.

Figure 4.3c shows the $\eta_{r,\infty}$ values of the suspensions in mineral oil as a function of the particle volume fraction normalised with the maximum packing estimated from the Krieger-Dougherty fitting (eq. (2.9)), to facilitate a comparison between the glass spheres and abrasive silicas but also with experimental data from literature. A good agreement is observed between the results of the glass sphere suspensions used in the present study and literature data for two sets of nearly monodisperse glass beads with $d = 20\ \mu m$ and $d = 40\ \mu m$ in mineral oil (Chen et al., 2007). On the contrary, the abrasive silicas show higher $\eta_{r,\infty}$ values despite scaling φ with φ_m highlighting the importance of particle surface morphology on suspension rheology, which cannot be fully captured by a single parameter, i.e. the φ_m.

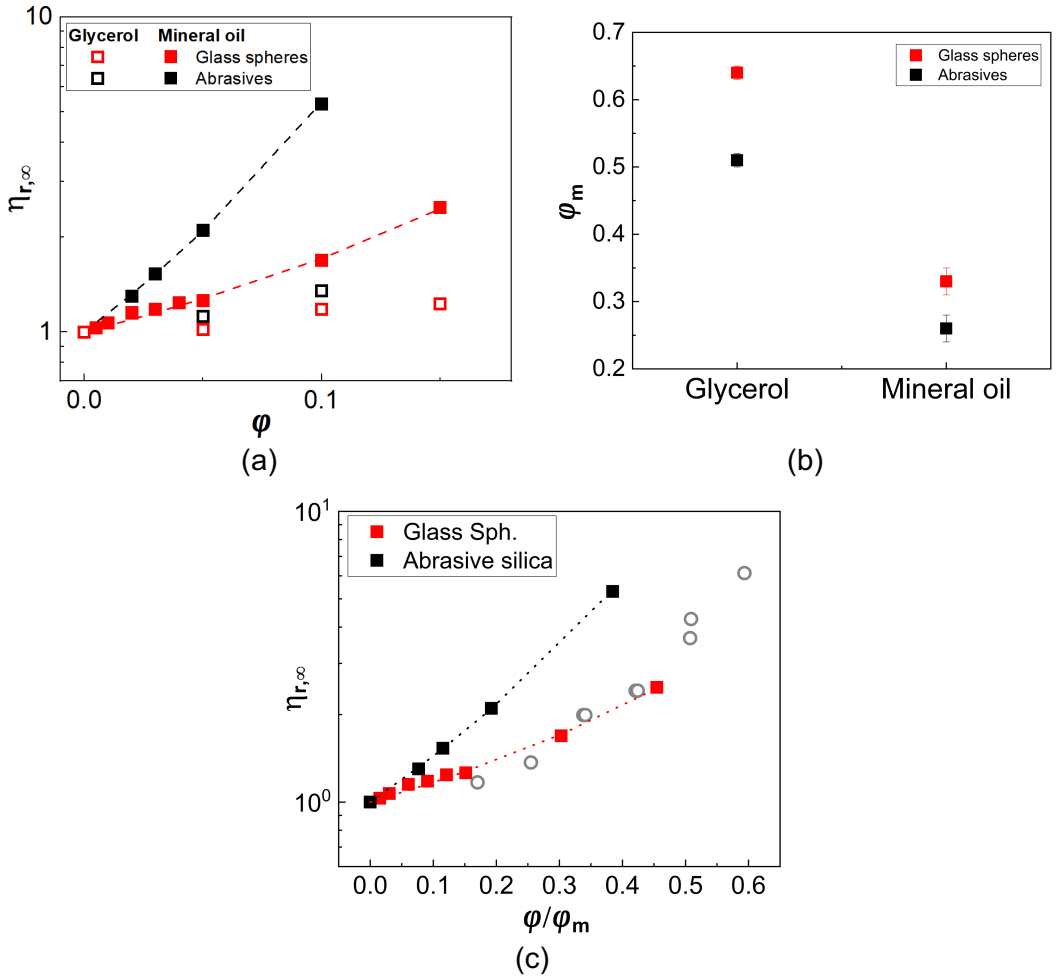

Figure 4.3: Infinite shear rate ($\eta_{r,\infty}$) relative viscosity as a function of particle volume fraction (φ) of the glass sphere and abrasive silica suspensions in mineral oil at 20°C. Dashed lines correspond to the Krieger-Dougherty fittings. The corresponding $\eta_{r,\infty}$ values of the suspensions in glycerol are included for comparison.; b) Maximum packing fraction of the suspensions of glass spheres and abrasive silicas in mineral oil in comparison to the glycerol case; c) Infinite shear rate ($\eta_{r,\infty}$) relative viscosity as a function of the normalized particle volume fraction (φ/φ_m) alongside experimental data from literature, ○: Chen et al. (2005). Dotted lines represent the Krieger-Dougherty fittings to the experimental data.

The estimated parameters from all fittings to the $\eta_{r,\infty}$ values are summarised in Table 4.3. The rough abrasive particles show lower maximum packing fractions for all cases and higher intrinsic viscosities (B) than the glass spheres implying a higher degree of agglomeration due to the surface roughness offering larger available contact areas between the particles (Blanc et al., 2018).

Table 4.3: Summary of the estimated parameters derived from fitting various empirical equations to the data presented in Figure 4.3a.

Sample	Krieger-Dougherty (eq. 2.7)		Servais et al. (2002) (eq. 2.9)		Quemada (eq. 2.8)
	B	φ_m	b	φ_m	φ_m
Glass Spheres	4.5	0.33	5.25	0.27	0.41
Silicas	13.3	0.26	-	-	0.18

In general, the estimated maximum packing fraction for these suspensions was much lower than the theoretically expected one for polydisperse randomly closed packed spheres ($\varphi_m \geq 0.64$) and rough crystals $\varphi_m \geq 0.44$ (Genovese, 2012). Deviations of the estimated φ_m values from the theory but also between the different fitted equations might occur due to the polydispersity and surface irregularity of the particles used in this study; parameters not accounted in all the existing empirical models but also the different degrees of freedom between the different empirical models, i.e. Krieger Dougherty has two (B and φ_m) in contrast to Quemada, which has one (φ_m).

The thixotropic behaviour of the suspensions in mineral oil was determined through upward (increasing the $\dot{\gamma}$) and subsequent downward (decreasing the $\dot{\gamma}$) steps with a resting period of 5 mins in between the steps; this is applied to allow particles to restructure and form agglomerates, following their disaggregation during the high shear rates reached in the upward step. No evidence of thixotropic behaviour (Figure 4.4) is observed for both types of suspensions since the relative viscosities obtained from the upward and downward steps overlap sufficiently well; small deviations occur only for the highest concentration of the glass sphere suspensions, i.e. $\varphi = 0.15$. The absence of thixotropy indicates that the agglomerates have short relaxation times and thus, the time allowed between the upward and downward steps is sufficient for the agglomerates to reach their initial structure before the application of shear.

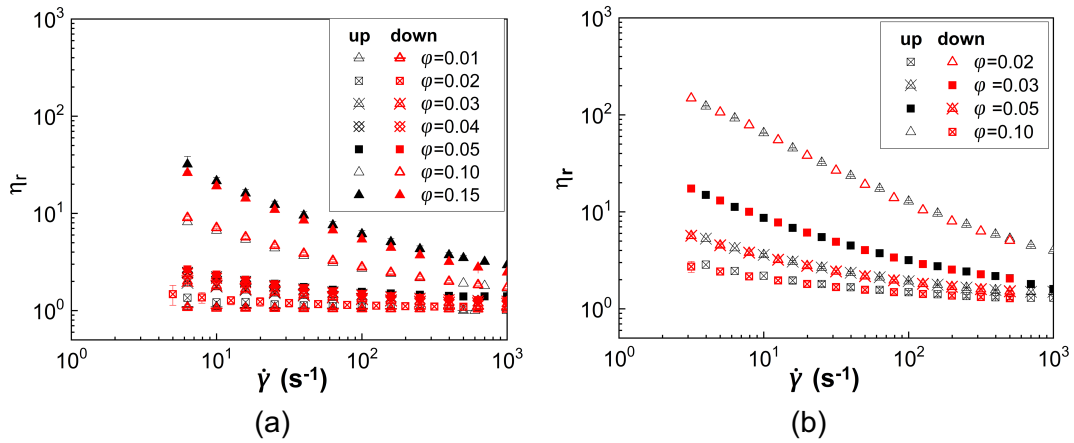

Figure 4.4: Thixotropic behaviour derived through ascending shear rate ramps (up) and descending shear rate ramps (down) under steady state for a) the glass sphere suspensions and b) the abrasive silica suspensions in mineral oil at 20°C.

The sensitivity of the agglomerates to the pre-shearing conditions applied and the gap between the parallel plates was also investigated for selected glass spheres suspensions. A comparison between the protocol used by Chen et al. (2005) and the one used in the present study is presented in Figure 4.5a. Chen et al. (2005) applied a pre-shearing step with $\dot{\gamma} = 50\ s^{-1}$ for 2 min followed by a rest period of 2 min, while in the present study all suspensions were subjected to a pre-shear of $\dot{\gamma} = 200\ s^{-1}$ for 5 min followed by a rest period of 5 min. Interestingly, the data obtained from the two different protocols are identical (Figure 4.5a). Therefore, it can be concluded that the formation of the agglomerates is insensitive to pre-shear, at least in the glass sphere case, given that the resting period is sufficient for the agglomerates to reform.

The effect of gap (h) was also examined, and the acquired data are summarised in Figure 4.5b for three particle volume fractions, i.e. $\varphi = 0.04$ (crossed diamonds), $\varphi = 0.05$ (squares) and $\varphi = 0.15$ (triangles). At first sight, increasing the gap from $h = 250\ \mu m$ to $h = 1000\ \mu m$ has a very low impact on the acquired rheology, especially for the lower concentrations of $\varphi = 0.04$ and $\varphi = 0.05$. However, higher deviations are observed for the glass sphere suspension at $\varphi = 0.15$ and the lower gap applied. More specifically, at $h = 250\ \mu m$, the suspension at $\varphi = 0.15$ exhibits lower viscosity values mainly at $\dot{\gamma}$ ranging from $6\ s^{-1}$ to $25\ s^{-1}$. It is likely that smaller gaps result in smaller agglomerates due to confinement, which lower the viscosity values and subsequently, require higher stresses to overcome sedimentation. Therefore, the data obtained at low shear rate and low h for the suspensions at $\varphi = 0.15$ might be subject to particle sedimentation. The same trend can also be observed in Table 4.4, which summarises the relative viscosity values of the suspensions presented in Figure 4.5b, at $\dot{\gamma} = 1000\ s^{-1}$ as a function of φ and h. Increasing the gap leads to a slight increase

of the η_r values at the limiting high shear rate region, which could be attributed to the formation of larger and possibly 3D structures enabled by the larger available space offered to the system under shear.

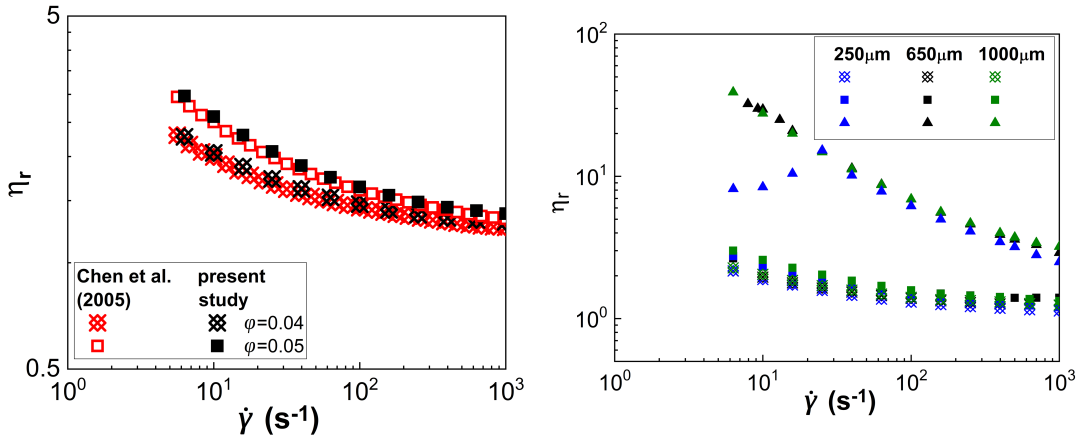

(a) (b)

Figure 4.5: a) Effect of the applied shear rate during the pre-shearing step for two indicative glass sphere suspensions in mineral oil; b) effect of gap for selected glass sphere suspensions in mineral oil, i.e. $\varphi = 0.04$ (crossed diamonds), $\varphi = 0.05$ (squares) and $\varphi = 0.15$ (triangles).

Table 4.4: Effect of the gap between the two parallel plates on the relative viscosity values at $\dot{\gamma} = 1000\ s^{-1}$ for the suspensions presented in Figure 4.5b.

φ	η_r		
	250 μm	650 μm	1000 μm
0.04	1.1	1.2	1.3
0.05	1.2	1.3	1.3
0.15	2.5	2.9	3.2

4.2.2 Oscillatory shear rheology – frequency sweeps in the LVR

The viscoelastic properties of both types of suspensions were investigated under dynamic frequency sweeps in the LVR and the acquired rheological response is presented in Figure 4.6. The storage (G') and loss (G'') moduli of the glass spheres (Figure 4.6a) and the abrasive silica (Figure 4.6c) suspensions are plotted as a function of the angular frequency (ω) and particle volume fraction (φ), while the corresponding phase angles are presented in Figure 4.6b and d respectively.

A transition from a liquid-like system (i.e. $G'' > G'$) is observed for the glass sphere suspensions at a particle volume fraction of $\varphi = 0.03$. At the lower particle concentrations, the G'' is higher than G', while both moduli increase almost linearly

with ω. Increasing the solids fraction (φ) leads to an increase in elasticity as both moduli become less frequency dependent, especially at $\varphi \geq 0.05$. The same trend is also reflected in the δ values (Figure 4.6b), which significantly decrease with increasing φ, approaching the elastic regime. In particular, the ω-dependence of the phase angle shows two different regions. At low ω the δ values increase with the applied frequency. However, beyond the crossover point where G' exceeds G'', the phase angles decrease with φ as the suspension becomes more elastic. This phenomenon diminishes at the higher particle volume fractions, where G' and G'' become almost independent of the angular frequency. The scatter in the δ values at $\varphi \leq 0.02$ can be related to the weak viscoelastic behaviour of these relatively dilute cases and an unstable state of the formed agglomerates.

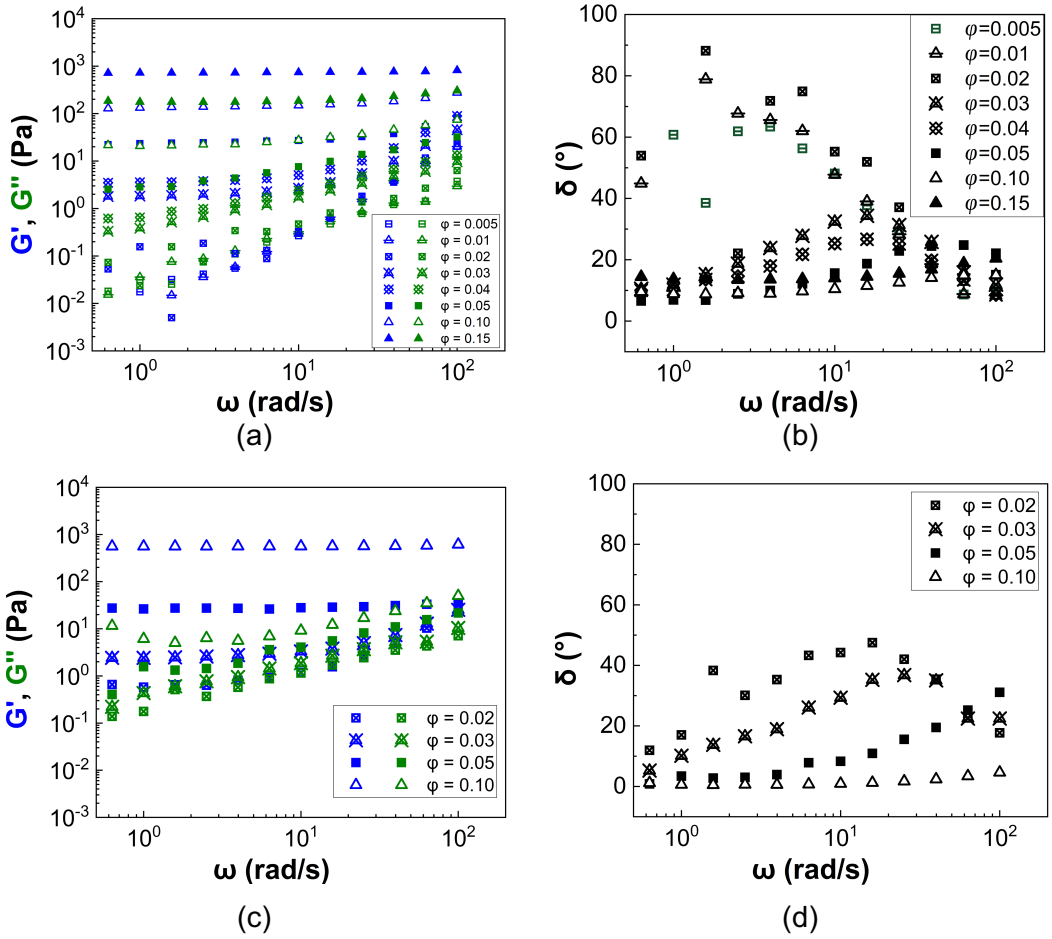

Figure 4.6: Storage (G') and loss moduli (G'') and the corresponding phase angles (δ) as a function of angular frequency (ω) generated from experimental frequency sweeps in the LVR of the suspensions in mineral oil. a) & b) glass spheres; c) & d) abrasive silicas.

The abrasive silica suspensions (Figure 4.6c) exhibit pronounced viscoelastic behaviour, while the transition to a solid-like material ($G' > G''$) occurs at particle

volume fractions lower than these investigated in the present study, i.e. $\varphi < 0.02$. The phase angles for the abrasive silicas (Figure 4.6d) are also lower compared to these of the glass sphere suspensions (Figure 4.6d). Similar behaviour has also been observed by several researchers for fumed silica particles suspended in non-polar and/or hydrophobic solvents (Chen et al., 2007; Hayashi and Kawaguchi, 2017a; Ma et al., 2017; Marunaka and Kawaguchi, 2017; Sugino and Kawaguchi, 2017). For example, Sugino and Kawaguchi (2017) investigated the rheology of fumed and precipitated silica in mineral oil and showed that both suspensions exhibited viscoelastic response (i.e. $G' > G''$) at particle volume fractions as low as $\varphi = 0.02$. This behaviour was attributed to gelation effects due to particle agglomeration (Sugino and Kawaguchi, 2017).

Suspending both the glass spheres and abrasive silicas in a non-polar solvent (mineral oil) enables the formation of particle agglomerates giving rise to strong viscoelastic behaviour. Increasing the particle volume fraction leads to stronger particle networks as indicated by the increase in the elastic behaviour and the decrease of the phase angles towards the zero value (purely elastic material). Increasing the particle surface roughness and porosity yields similar behaviour with φ as evidenced by the abrasive silicas showing the transition from a liquid-like to a solid-like material at lower φ compared to the glass spheres. The rheological response of the suspensions in mineral oil contrasts that of the suspensions in glycerol. The latter showed pure liquid like behaviour (i.e. $G' < G''$) irrespective of particle volume fraction, particle surface characteristics and applied experimental conditions due to the presence of a thick solvation layer around the particles formed by glycerol, which inhibited particle contact especially at room temperature (20^{o}C).

4.2.3 Transient suspension behaviour-Stress growth experiments

In section 4.2.1 the rheological properties of the glass sphere and abrasive silica suspensions were presented under steady state. To investigate the presence of particle sedimentation at the initiation of shearing, stress growth experiments were conducted at different shear rates ($\dot{\gamma}$) below and above the critical shear rate for sedimentation based on the Shields number for 120 secs. The suspensions were sheared at a fixed shear rate for 120 secs and the shear stress was monitored as a function of time. Figure 4.7 summarises the rheological response of selected glass sphere suspensions in mineral oil under stress growth measurements. The response of the instrument to the imposed shear rate ($\dot{\gamma}$) (Figure 4.7a) reached steady state at

the requested $\dot{\gamma}$ value, in a very short time in the order of 150 milliseconds, even at the lower values of shear rate, which could be more susceptible to noise effects arising from the instrument inertia; the red line illustrates the time when steady state was reached. Figure 4.7b and c represent the shear stress response of the glass sphere suspensions at indicative particle volume fractions of $\varphi = 0.02$ and $\varphi = 0.10$ respectively.

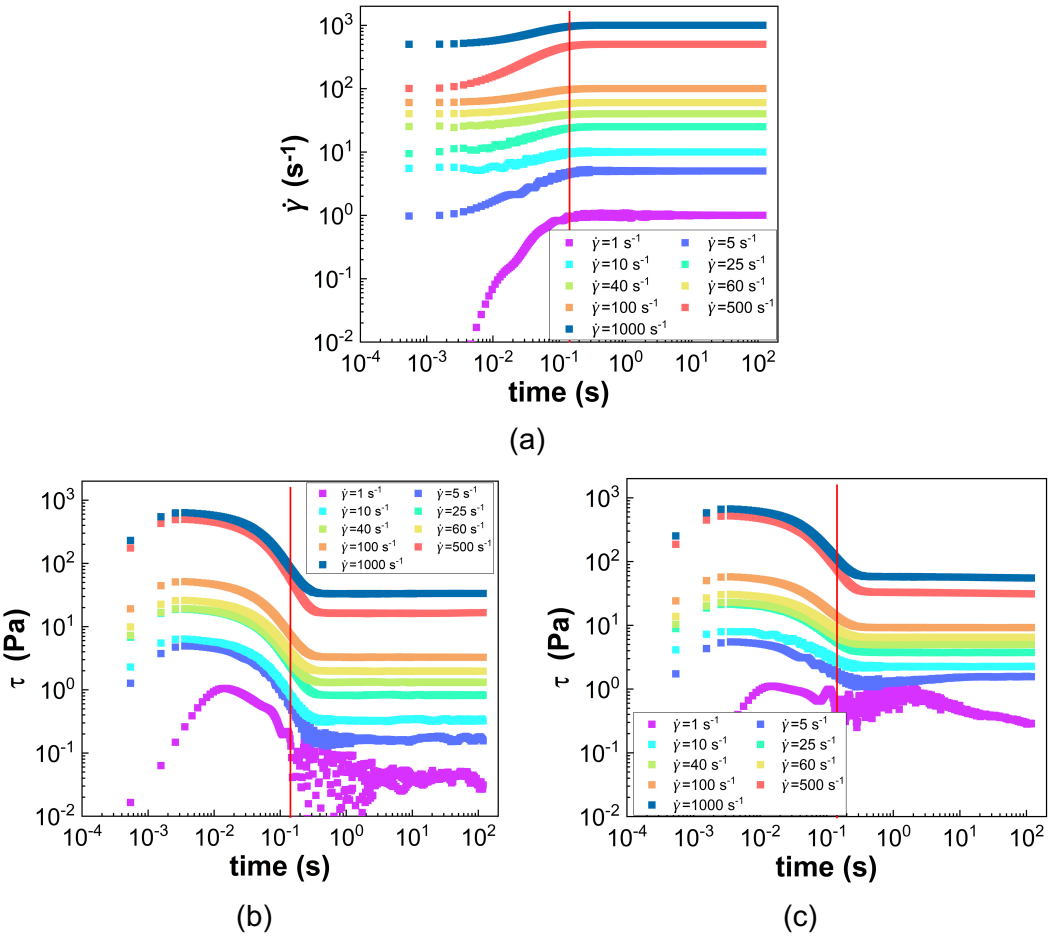

Figure 4.7: Response of selected glass sphere suspensions under stress growth: a) evolution of the different shear rates as a function of time; stress response of the glass sphere suspensions in mineral oil at b) $\varphi = 0.02$ and c) $\varphi = 0.10$. The solid red line corresponds to the time that the applied shear rate ($\dot{\gamma}$) reaches the required value.

All suspensions irrespective of the particle volume fraction (φ) and the imposed $\dot{\gamma}$ reached a constant shear stress value in a very short time frame in the range of milliseconds following the trend of the instrument response at the different $\dot{\gamma}$ values. However, a small delay, where the shear stress continues to decrease before reaching the steady state plateau, is observed for a short time in the order of 100 ms, for both suspensions and all the $\dot{\gamma}$ values. The delay time as well as the degree of the stress reduction decreases with increasing the particle volume fraction. This

behaviour might be associated with the shear thinning rheology and changes in the microstructure of the particle agglomerates as they are subjected to sufficiently high shear deformations till a steady state condition is achieved. At the steady state condition, the rate of breakage and reformation of the agglomerates are equal and thus, a constant stress response can be maintained. At the lowest shear rate applied ($\dot{\gamma} = 1\ s^{-1}$) some scattering in the acquired data and a decrease in the stress values are observed during the whole time of measuring. These deviations can be attributed to sedimentation effects as estimated through the Shields number ($Sh \leq 1$).

4.2.4 Ageing

Although the transient response of the suspensions is important in understanding their rheology, the stability of the suspension over a longer period of time plays an important role in the overall quality of the end formulation, especially its stability upon storage (Ma et al., 2017; Selimovic et al., 2007). Therefore, the rheology of selected abrasive and filler silica suspensions in mineral oil was monitored over a period of one week due to their high relevance in industrial applications. A fixed particle volume fraction of $\varphi = 0.10$ was studied at room temperature, under both steady state and oscillatory shear. The time frame of the measurements was selected based on previous studies on similar systems, which observed that suspensions reached equilibrium after 7 days (Selimovic and Hu, 2014). The samples were mixed each day before measurement to avoid particle sedimentation. The corresponding suspensions in glycerol were also tested under the same conditions and the data obtained are presented alongside those of the suspensions in mineral oil for comparison. The glass spheres are not included here as they did not show any ageing effects even in the glycerol case possibly due to the very low density of silanol groups.

Figure 4.8a and c summarize the rheological properties of the abrasive silica suspension in mineral oil at $\varphi = 0.10$ as obtained from the steady state and oscillatory frequency sweeps in the LVR. More specifically, the viscosity values are reported at a constant shear rate of $\dot{\gamma} = 10\ s^{-1}$, while the viscoelastic moduli are taken at a frequency of $f = 1\ Hz$ and a strain amplitude of $\gamma = 0.1\%$. All the data is normalized with the corresponding values measured on the day of sample preparation to better evaluate the evolution of the suspension rheology over the period of one week (7 days). The results obtained for the corresponding suspension in glycerol are also presented in Figure 4.8b and d for comparison.

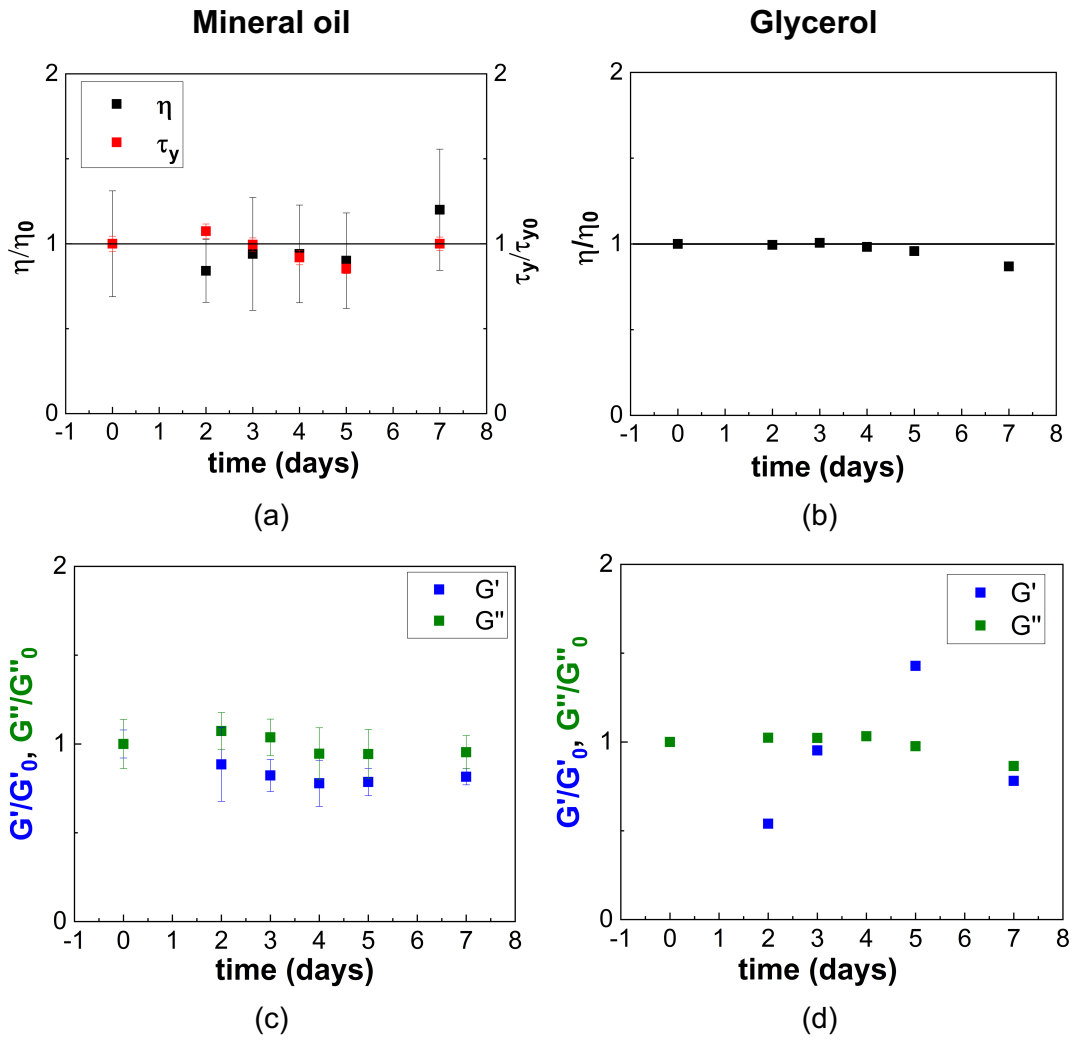

Figure 4.8: Rheological properties of a 10% v/v abrasive silica suspension in mineral oil for a period of 7 days at 20ºC. All the data have been normalised with their correspond values measured on the day of sample preparation (i.e. day 0, η_0, τ_{y0}, G'_0, G''_0). a) Normalised viscosity at $\dot{\gamma} = 10\ s^{-1}$ and c) normalised viscoelastic moduli at $f = 1\ Hz$ and $\gamma = 0.1\%$; b) and d) show the normalised viscosity and viscoelastic moduli respectively for the corresponding suspensions in glycerol.

Since mineral oil is a non-polar solvent, no interference with the hydrogen bonding between the particles is expected (Selimovic et al., 2007; Selimovic and Hu, 2014) and particle agglomeration is favoured in this type of suspensions. The presence of large particle agglomerates leads to stable suspensions and strongly elastic response ($G' > G''$) as shown in Figure 4.6c, which are less sensitive to ageing effects (Figure 4.8a and c). The viscosity and the yield stress values, as well as the viscoelastic moduli remain almost constant over time. Although deviations of the normalised variables from unity occur, these are within the measurement errors.

On the contrary, the suspension in glycerol shows a quite stable response over time with the normalized viscosity (Figure 4.8d) values remaining equal to one till the

5th day, and a slight decrease is only observed on the 7th day. The loss modulus, G'', (Figure 4.8d) follows the same trend with the viscosity since these variables are closely related. Furthermore, this suspension shows a viscous dominant response ($G' < G''$) over the whole testing period and thus, no systematic data could be obtained for the weak G' response. As discussed in the previous chapter, glycerol is a polar solvent with three hydroxyl groups (-OH) on its molecule. This enables the formation of a solvation layer around the particles preventing interparticle contacts and leading to Newtonian rheological response at these relatively dilute conditions. The stability of the suspensions induced by the presence of the solvation layer might be responsible for the absence of ageing effects for this type of suspension, while the drop of both the viscosity and the G'' on day 7 might be related to partial particle sedimentation upon storage due to the density mismatch between the solvent (glycerol, $\rho_f = 1.25\ g/ml$) and the particles (abrasive silicas, $\rho_p = 2\ g/ml$).

The ageing effect on the filler silica suspensions in mineral oil is presented in Figure 4.9a and c. The filler silicas in mineral oil exhibit an elastic dominated behaviour ($G' > G''$) and the variations of the average viscosity values are within the measurement errors. In contrast, pronounced ageing is observed for the filler silica suspension in glycerol (Figure 4.9b and d) through a decrease of both the viscosity and the viscoelastic moduli over time. It is likely that on the day of preparation, the filler silicas are partially agglomerated in glycerol, as not all the agglomerates formed upon storage were broken down during sample preparation under high shear mixing. This gives rise to high viscosity values at day zero (Figure 4.9b). However, the ability of glycerol to interfere with the hydrogen bonds between the silanol groups on the silica surface breaking the initially formed particle agglomerates leads to smaller units in the suspensions and thus, reduces the normalised viscosity over time, indicative of ageing response.

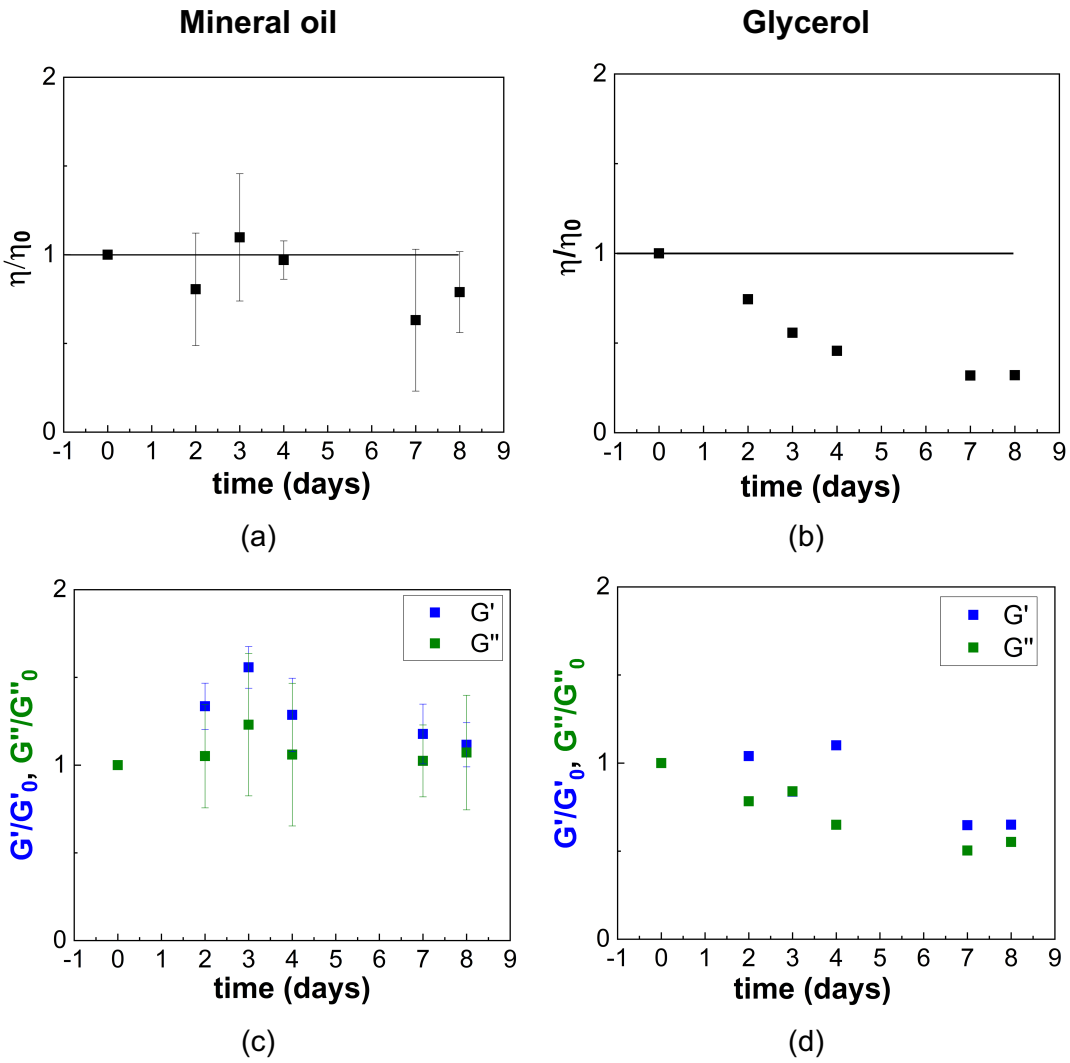

Figure 4.9: Rheological properties of a 10% v/v abrasive silica suspension in mineral oil for a period of 7 days at 20ºC. All the data have been normalised with their correspond values measured on the day of sample preparation (i.e. day 0, η_0, τ_{y0}, G'_0, G''_0). a) Normalised viscosity at $\dot{\gamma} = 1\ s^{-1}$ and c) normalised viscoelastic moduli at $f = 1\ Hz$ and $\gamma = 0.1\%$; b) and d) show the normalised viscosity and viscoelastic moduli respectively for the corresponding suspensions in glycerol.

Overall, the suspensions in mineral oil show higher stability and stronger viscoelastic behaviour in contrast to the ones in glycerol over the time period of investigation. Such stability experiments enable first, to appreciate the type of particle-particle and particle-solvent bonds and secondly, to propose suitable solvents and/or modifications on the silica surface characteristics in order to achieve the required rheology and stability to the end product.

4.2.5 Suspension microstructure

4.2.5.1 Optical shearing

To further elucidate the adhesive particle interactions and their role in the observed shear thinning behaviour, the suspension microstructure was visualized by means of an optical shearing method. This method allowed the direct quantification of the agglomeration process and the subsequent break down of aggregated structures of the sheared suspensions *in situ*. Optical methods are limited by the opacity of the sample and thus, successful visualization of suspension microstructure can only be achieved under relatively dilute conditions; the method is thus amenable to the suspensions in mineral oil since they are relatively dilute.

Figure 4.10 presents sample microstructure images acquired for a 5% v/v glass sphere suspension (left column) and a 3% v/v abrasive silica suspension (right column) in mineral oil. Filler silicas could not be visualized under the microscope due to the refractive index matching with the solvent (mineral oil). The glass sphere and abrasive silica suspensions in mineral oil exhibit rich microstructure which highly depends on the shear rate and particle surface morphology; this contrasts the behaviour of the suspensions in glycerol where no microstructure changes were observed under optical shearing (Figure 3.9).

At $\dot{\gamma} = 1\ s^{-1}$ glass spheres form large randomly shaped agglomerates (Figure 4.10a), while abrasive silicas elongated clusters extending to the whole image (Figure 4.10b). These structures can explain the differences in the estimated values of the adhesion force values between the glass spheres and the abrasives reported in section 4.2.1. Increasing the shear rate by one order of magnitude (from $\dot{\gamma} = 1\ s^{-1}$ to $\dot{\gamma} = 10\ s^{-1}$), particle agglomerates start breaking down and reducing in size (Figure 4.10c and d); this helps explain the observed shear thinning behaviour of the suspensions in mineral oil under steady state shear, as illustrated in Figure 4.1a and c. Further increase in the shear rate ($\dot{\gamma} = 100\ s^{-1}$) results in agglomerates breaking down to single units as indicated by the images of dispersed particles seen in Figure 4.10e and f.

It should be noted that at low shear rates, the particle agglomerates are likely to also evolve in the third (depth) dimension, which although not visible in the 2D images can induce a further reduction in the area occupied by the particles.

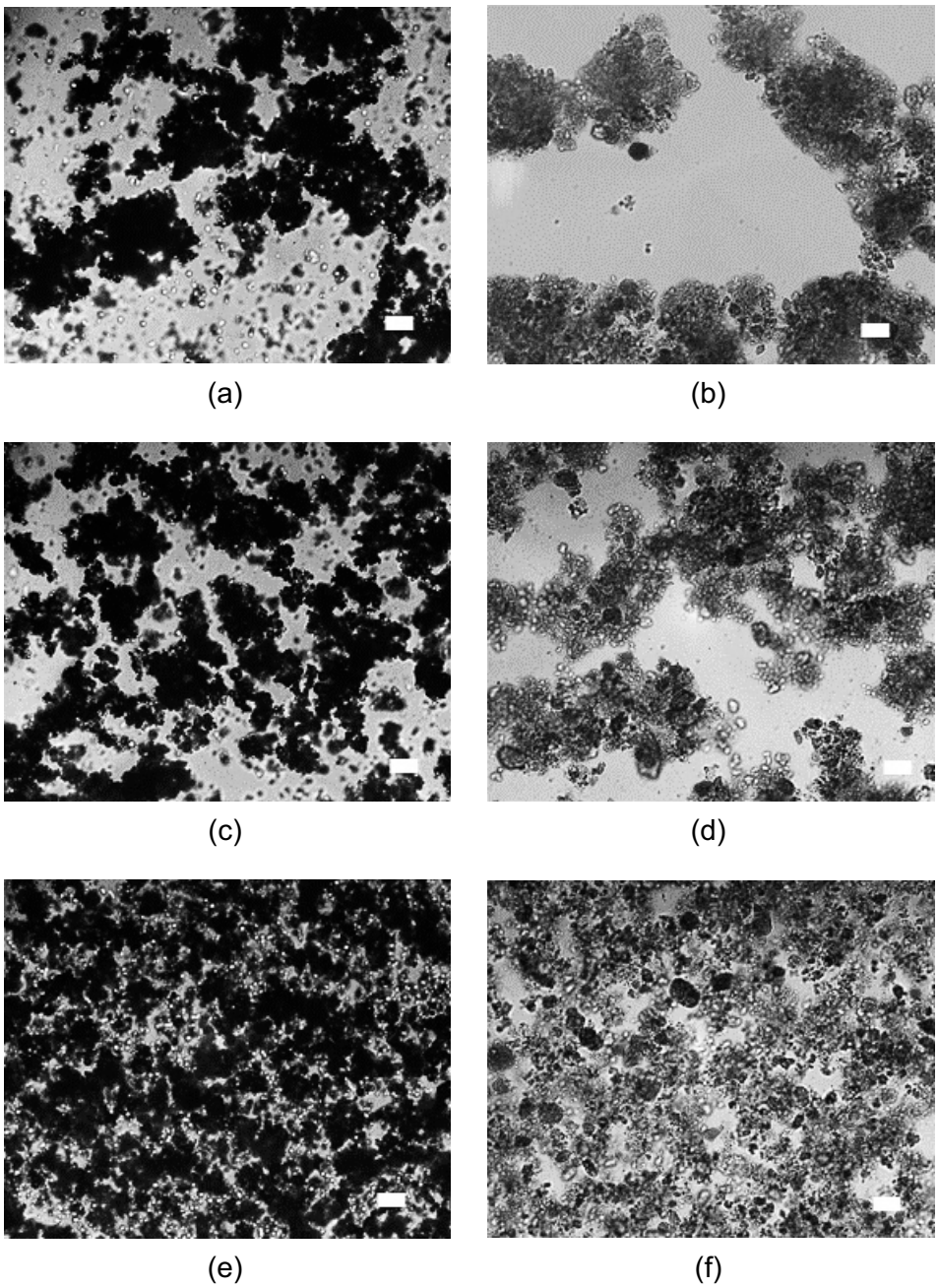

Figure 4.10: Sample images of the microstructure obtained for the 5% v/v glass sphere (left) and the 3% v/v silica (right) suspensions in mineral oil at shear rates: 1 s^{-1} (a, b); 10 s^{-1} (c, d) & 100 s^{-1} (e, f) and at room temperature. The scale bars (▬) correspond to 40 μm length.

In order to quantify suspension microstructure and characterise the extent of particle agglomeration, sets of 2000 images were obtained at different shear rates and analysed in MATLAB so as to calculate the aggregation index, A, introduced by Kaliviotis et al. (2016) and described in Chapter 2 (eq. (2.12)). The estimated A values, were normalised with the index value obtained at the highest shear rate employed in each case to facilitate the comparison. The normalised aggregation indices (A_N) are plotted in Figure 3.10 for the 5% v/v glass spheres (Figure 4.11a) and 3% v/v silica

particles (Figure 4.11b) in mineral oil. The corresponding values for the non-adhesive suspensions in glycerol are also included to highlight the difference between the different shear thinning mechanisms. A progressive decrease of the aggregation index, A_N, with shear rate can be observed for the adhesive suspensions in mineral oil and this trend is also reflected in the corresponding relative viscosity curves – shown as inset figures for the same range of shear rates – especially for the abrasive silicas (Figure 4.11b). The latter further confirms that the shear thinning behaviour of these suspensions is driven by adhesion between the particles.

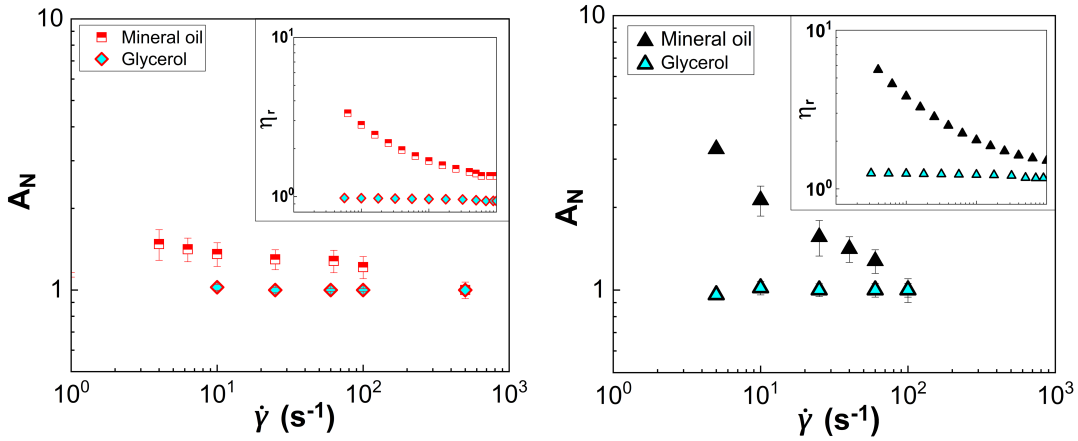

Figure 4.11: Normalised aggregation indices (A_N) for the suspensions presented in Figure 4.10 as a function of shear rate. a) 5% v/v glass spheres and b) 3% v/v abrasive silicas in mineral oil. The A_N values for the corresponding suspensions in glycerol are included for comparison. The insets in (a) and (b) represent the relative viscosity values vs shear rate for the corresponding suspensions in mineral oil and glycerol at 20°C.

To verify the reliability of the above used aggregation index, other measures of aggregation were also utilised, including image intensity correlation (eq. (2.13)) (Dusting et al., 2009), mean standard deviation of the image intensity (Kaliviotis et al., 2016) and the ratios of the particle free areas in the image (void) to either corresponding areas covered with particles (solid) (eq. (2.14)) or to the total image area (total) (eq. (2.15)). The image intensity correlation is a measure of the difference in mean intensity between successive images for a given shear rate and is expected to vary as shear increases. Estimates of all these parameters were produced, normalised with the corresponding values at maximum shear rate, similar to A_N and plotted in Figure 4.12 along with the data presented in Figure 4.11. It can be seen that all the measures exhibit similar trends to A_N for both the glass sphere (Figure 4.12a) and the abrasive silica (Figure 4.12b) suspensions in mineral oil, demonstrating the

validity of the aggregation index and its ability to directly monitor particle agglomeration and dispersion.

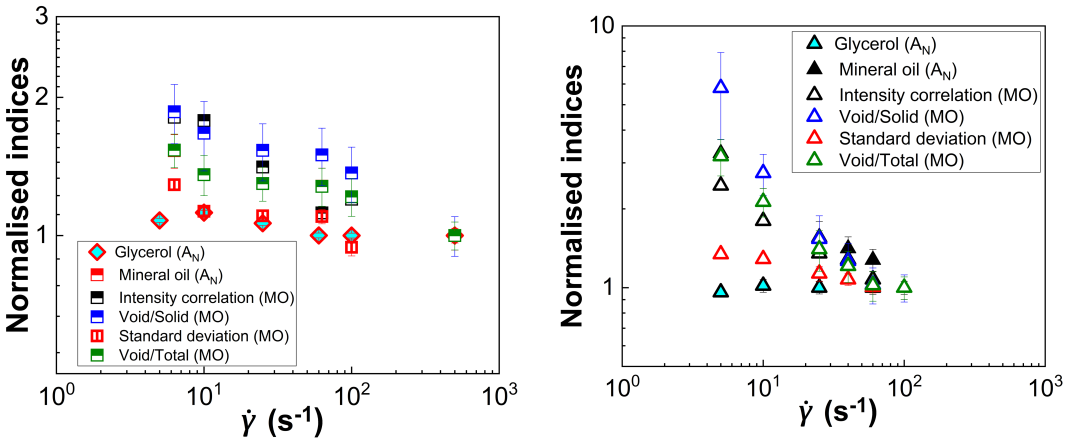

Figure 4.12: Comparison between the different measures of aggregation for the a) 5% v/v glass spheres and b) 3% v/v of abrasive silica suspensions in mineral oil.

4.2.5.2 Large Amplitude Oscillatory shear (LAOS)

LAOS experiments were further conducted as a means to probe the microstructure of denser suspensions difficult to be visualized under the microscope due to optical limitations. The three particle suspensions in mineral oil were tested under LAOS at a fixed φ of 0.10. The response of the corresponding suspensions in glycerol are also presented for comparison. The raw viscoelastic moduli (G' and G'') are illustrated in Figure 4.13 as a function of % strain amplitude (γ) at 20°C and frequency of $f = 1\ Hz$.

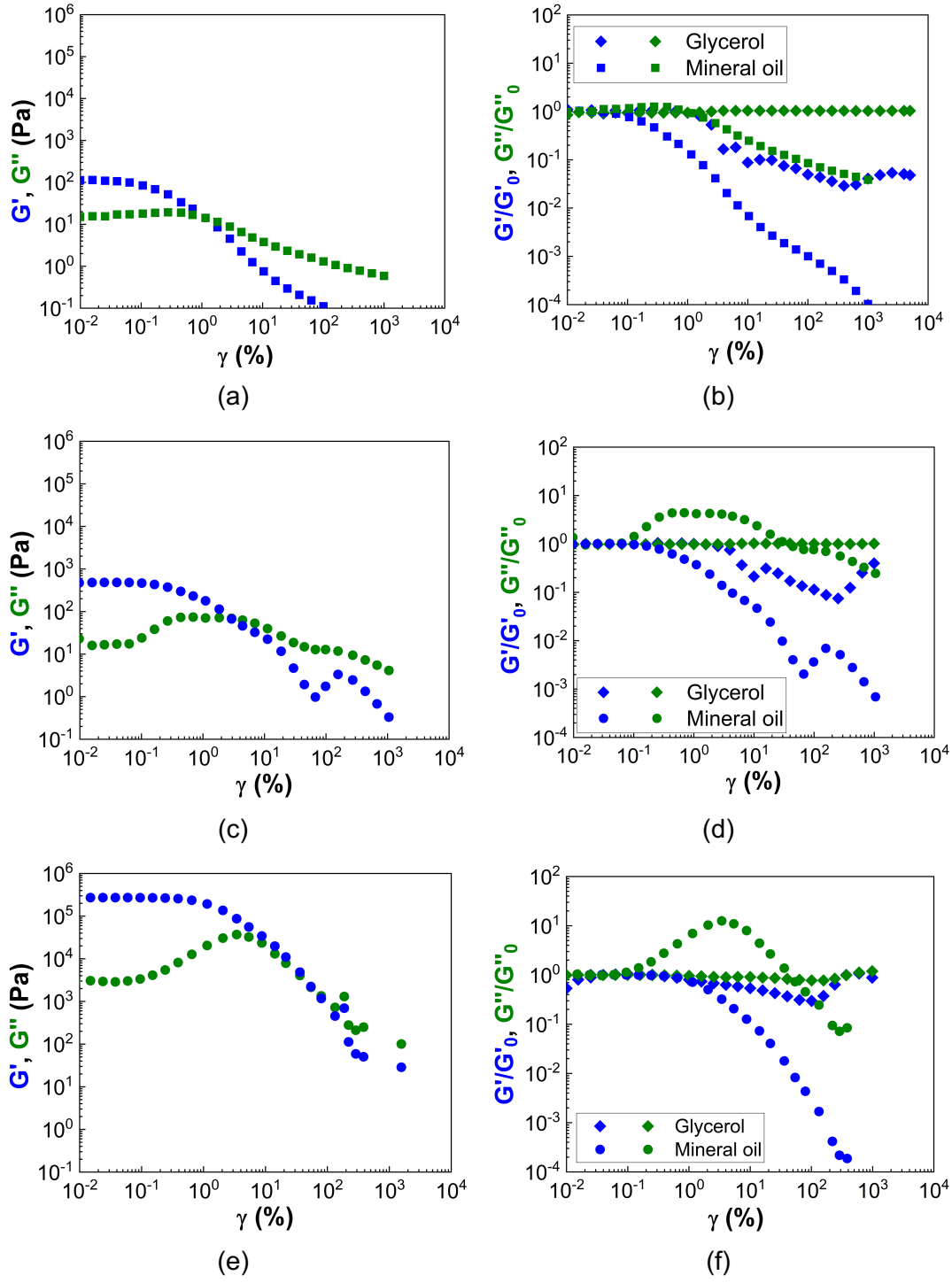

Figure 4.13: Raw storage (G') and loss (G'') moduli (left column) of the three particle suspension in mineral oil as a function of % strain amplitude at $\varphi = 0.10$, 20°C and $f = 1Hz$; right column- G' and G'' of the suspensions in mineral oil normalised with the corresponding values of the viscoelastic moduli in the LVR (G'_0, G''_0). The data for the corresponding suspensions in glycerol are included for comparison. a) and b) glass spheres; c) and d) abrasives silicas; e) and f) filler silicas.

All suspensions in mineral oil exhibit elastic dominated response in the linear viscoelastic region (G'>G''), while a crossover between the two moduli is observed at sufficiently high strain amplitudes making the suspensions viscous dominated ($G' <$

G''). The crossover point between the G' and G'' can be used as an alternative way to estimate the dynamic yield stress ($\tau_{y,d}$) of the suspensions. $\tau_{y,d}$ values estimated from the LAOS experiments are summarised in Table 4.5 along with the τ_y estimated under steady state in section 4.2.1. Although, the yield stress values obtained from the two different measurement types are comparable in the case of the glass sphere suspension, a higher deviation between τ_y and $\tau_{y,d}$ is observed for the abrasive silicas. In particular, the $\tau_{y,d}$ of the abrasive silica suspension is nearly four times lower than that estimated under steady state (τ_y), suggesting that the suspension microstructure also depends on the deformation type the suspension is subjected to (Galindo-Rosales and Rubio-Hernandez, 2009).

The $\tau_{y,d}$ value of the filler silica suspension is two orders of magnitude higher than that of the other two types of suspensions (glass spheres and abrasives). Stronger interparticle interactions at low shear due to the high specific surface area and density of the free surface silanol groups of the filler silicas might be responsible for this behaviour. It should be noted that due to the extremely high viscosity of this suspension, the τ_y value under steady state could not be obtained. Increasing particle specific surface area, S_p, also increases the extent of the linear viscoelastic region for the suspensions in mineral oil (Figure 4.13a, c and e) in agreement with the suspensions in glycerol; this highlights the important role of particle surface characteristics and porosity in suspension rheology.

Table 4.5: Comparison between the yield stress values of the three suspensions in mineral oil at $\varphi = 0.10$ and 20°C estimated from steady state (τ_y) and LAOS measurements ($\tau_{y,d}$).

Particle type	τ_y – steady state	$\tau_{y,d}$ – LAOS
Glass spheres	0.4	0.2
Abrasive silicas	11.4	2.8
Filler silicas	N/A	1680

The raw viscoelastic moduli of the glass sphere suspension (Figure 4.13a) exhibit strain thinning with increasing % γ which is typical of type I response under LAOS and can be well associated with the observed shear thinning behaviour of this suspension under steady state due to the particle agglomerates breaking down under increasing deformation rates. The abrasive (Figure 4.13a) and filler (Figure 4.13e) silica suspensions exhibit a more complex response under LAOS with the G' showing strain thinning and the G'' strain overshoot; this is typical of type III response under LAOS

(Hyun et al., 2011). It should be noted that the G'' of the abrasive silicas (Figure 4.13a) does not exhibit a clear peak but a plateau at intermediate strain amplitudes ($\gamma \approx 0.1\%$ to $\gamma \approx 10\%$). It is likely that within this γ range the agglomeration rate equates to the cluster break down rate leading to the observed plateau. On the other hand, the filler silica suspension (Figure 4.13e) exhibits a peak value of the G'' at a strain amplitude of $\gamma \approx 3\%$.

The viscoelastic moduli of all the suspensions were further normalised with the corresponding values of G' and G'' in the LVR to facilitate the comparison with the corresponding suspensions in glycerol and the estimated data of the glass sphere, the abrasive silica and the filler silica suspensions are presented in Figure 4.13b, d and f respectively. A higher dependence of both moduli on the applied strain amplitude can be observed for the suspensions in mineral oil with pronounced strain thinning and/or strain overshoot of the G''. In contrast, the suspensions in glycerol exhibit G'' values that are almost constant with the strain amplitude, especially for the glass sphere (Figure 4.13d) and abrasive silica suspensions (Figure 4.13d). The G' of the suspensions in glycerol also exhibits some non-linear effects (i.e. strain thinning (Figure 4.13b) and strain thickening (Figure 4.13d and f), which are much weaker than those observed for the corresponding suspensions in mineral oil; this can be related to the weak viscoelasticity of the suspensions in glycerol due to the presence of the solvation layer.

Under LAOS measurements the non-linear response arises from the contribution of the higher order odd harmonics and in particular, the third order harmonic, which is the next harmonic after the 1st with the highest intensity, to the stress signals. This effect can be reflected in the intracycle raw stress signals as a function of the strain amplitude obtained at each γ value; this type of plots is known as the elastic Lissajous plots and are widely used to identify the origins of the non-linear response. In particular, in the LVR the elastic Lissajous plots have a symmetric and elliptical shape, while deviations from this behaviour indicate the non-linear response. The elastic Lissajous plots of the abrasive and filler silica suspensions in mineral oil generated from the raw LAOS data are illustrated in Figure 4.14 at different strain amplitudes in the non-linear regime. The corresponding data of the glass sphere suspensions were omitted from the graph due to the raw stress signals being noisy. It can be seen that for the abrasive silicas a non-symmetric curve is only observed for the lower strain amplitude plotted in Figure 4.14, which is close to the crossover point. In contrast, pronounced asymmetry is observed in the elastic Lissajous plots of the filler silicas;

edge fracture inhibited the collection of data at the highest γ values, i.e. $\gamma = 6.7$ and $\gamma = 11.3$.

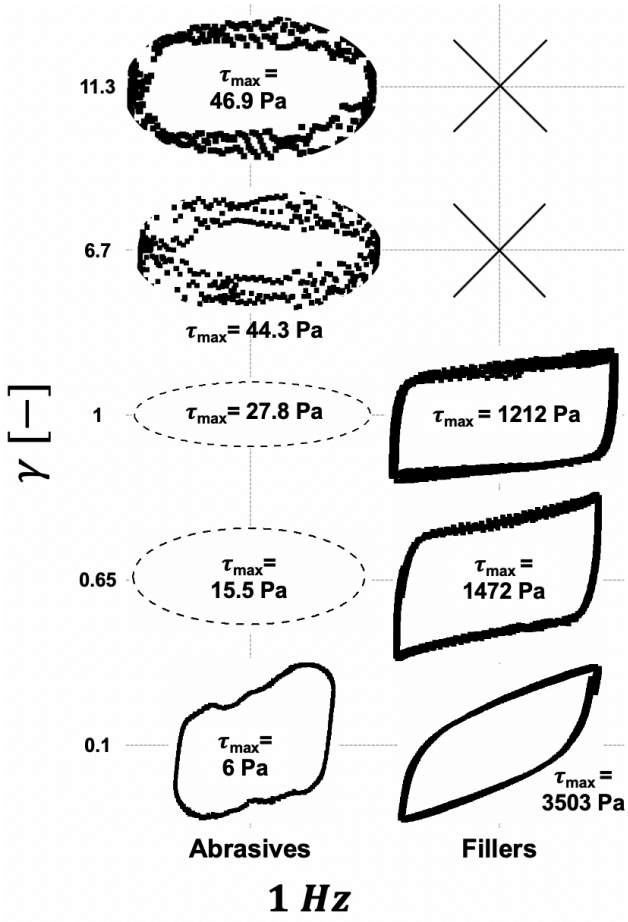

Figure 4.14: Raw LAOS data of the abrasive and filler silica suspensions in mineral oil at $\varphi = 0.10$ and 20°C, generated from experimental oscillatory tests shown as elastic Lissajous curves of total stress vs strain, according to the values of strain amplitude (γ) and frequency f = 1Hz. Dashed lines correspond to the elliptical fitting to the data to smoothen the noise occurring at the maximum stress areas, while insets represent the raw data. The x signs in the case of the filler silicas indicate that no data could be acquired at these high γ values due to edge fracture. The Lissajous curves for the glass spheres suspension were omitted from the graph due to the raw stress signals been noisy.

The Lissajous curves can be further utilized to estimate the non-linear parameters of the suspensions following the method described in section 2.5.2. The estimated variables, i.e. the dynamic minimum strain (G'_M) (blue hollow symbols) and large strain (G'_L) (blue filled symbols) moduli and the dynamic minimum (η_M) (green hollow symbols) and large strain rate viscosity (η_L) (green filled symbols) of all suspensions in glycerol are summarized in Figure 4.15 as a function of the % strain amplitude at 20°C and a frequency of $f = 1Hz$. The corresponding estimates of the non-linear variables for the suspensions in glycerol are also included for comparison.

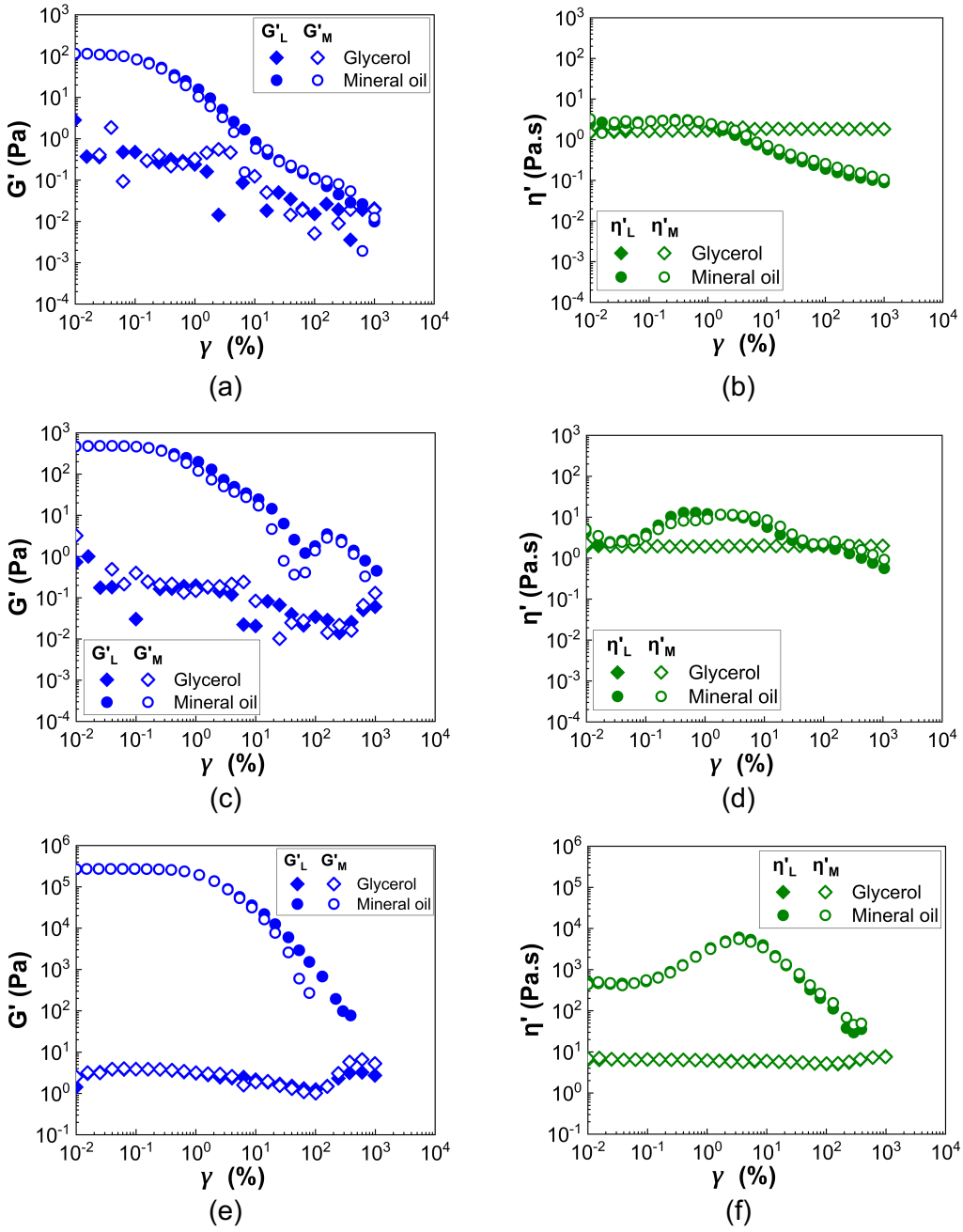

Figure 4.15: Non-linear viscoelastic moduli obtained through the Fast Fourier Transform of the raw stress signals (dynamic minimum strain (G'_M) (blue hollow symbols) and large strain (G'_L) (blue filled symbols) moduli (left column), dynamic minimum strain rate viscosity (η_M) (green hollow symbols) and large strain rate viscosity (η_L) (green filled symbols) (right column)) as a function of % strain amplitude for the three particle suspensions in mineral oil at $\varphi = 0.10$, $f = 1Hz$ and 20°C. a) and b) glass spheres; c) and d) abrasive silicas; e) and f) filler silicas. The data for the corresponding suspensions in glycerol are also included for comparison.

The non-linear variables of the suspensions in mineral oil presented in Figure 4.15 follow the same trend with the raw viscoelastic moduli (Figure 4.13a, c and e). The suspensions in mineral oil exhibit much higher G' compared to the suspensions in glycerol due to the particle agglomeration giving rise to suspension elasticity. The

difference between the G'_M and G'_L and η'_M and η'_L can be used to further estimate the stiffening (S) and thickening (T) ratios respectively, which can give a better insight on the origins of the non-linear response (Figure 4.16). It should be noted that it is the sign and not the actual value of the S and T variables that is meaningful in describing suspension behaviour under LAOS. For example, if $S > 0$ and $T < 0$ the suspension non-linearities are strain rate driven (i.e. the viscous component dominates), while if $S < 0$ and $T > 0$ the suspension exhibits strain driven instabilities, i.e. the elastic component dominates.

Figure 4.16a illustrates the stiffening and thickening ratio of the 10% v/v glass sphere suspension in mineral oil. Both ratios are equal to zero in the LVR, indicating a non-linear response, while beyond the LVR the T values become negative and the S values remain mainly positive and close to zero; this behaviour is indicative of strain rate driven instabilities. The abrasive silicas in mineral oil (Figure 4.16c) exhibit richer non-linear response with large deviations especially in the thickening ratio, T. In particular, at strain amplitudes below the crossover point the elastic component governs the instabilities, i.e. strain driven non-linearities ($S > 0$, $T > 0$) due to the presence of large particle agglomerates. Beyond the yield point the thickening ratio becomes negative giving rise to strain rate driven non-linear response ($S > 0$, $T < 0$) as the agglomerates break down and the viscous component dominates over the elasticity. The non-linear response of the filler silica suspension (Figure 4.16e) seems to also be strain rate driven ($S > 0$, $T < 0$) beyond the LVR in agreement with the observations made for the glass sphere and abrasive silica suspensions. A weaker non-linear response is observed for the suspensions in glycerol compared to that of the suspensions in mineral oil with the T values remaining close to zero for the whole range of strain amplitudes investigated. Weak instabilities arise from the elastic component as S values become negative at strain amplitudes $\gamma \geq 100\%$.

The degree of non-linear response under LAOS can be also assessed by monitoring the relative intensity of the third harmonic ($I_{3/1}$) as a function of the applied strain amplitude. The $I_{3/1}$ values of the three suspensions in mineral oil are plotted in Figure 4.16b, d and f, while the corresponding values of the suspensions in glycerol are also included for comparison. The estimated intensities of all suspensions in mineral oil are mostly higher than these of the suspensions in glycerol, indicative of the pronounced non-linear response of these suspensions. The $I_{3/1}$ values increase with γ till they reach a plateau at sufficiently high strain amplitudes; this behaviour has been mainly observed for hard elastic gels (Hyun et al., 2011). Correspondingly, the $I_{3/1}$ values of the suspensions in glycerol reach a maximum at $\gamma \approx 4\%$, independently

of the particle type and then drop again with a further increase in strain amplitude; this behaviour is indicative of soft gels with a viscous dominated response ($G' < G''$) (Hyun et al., 2011).

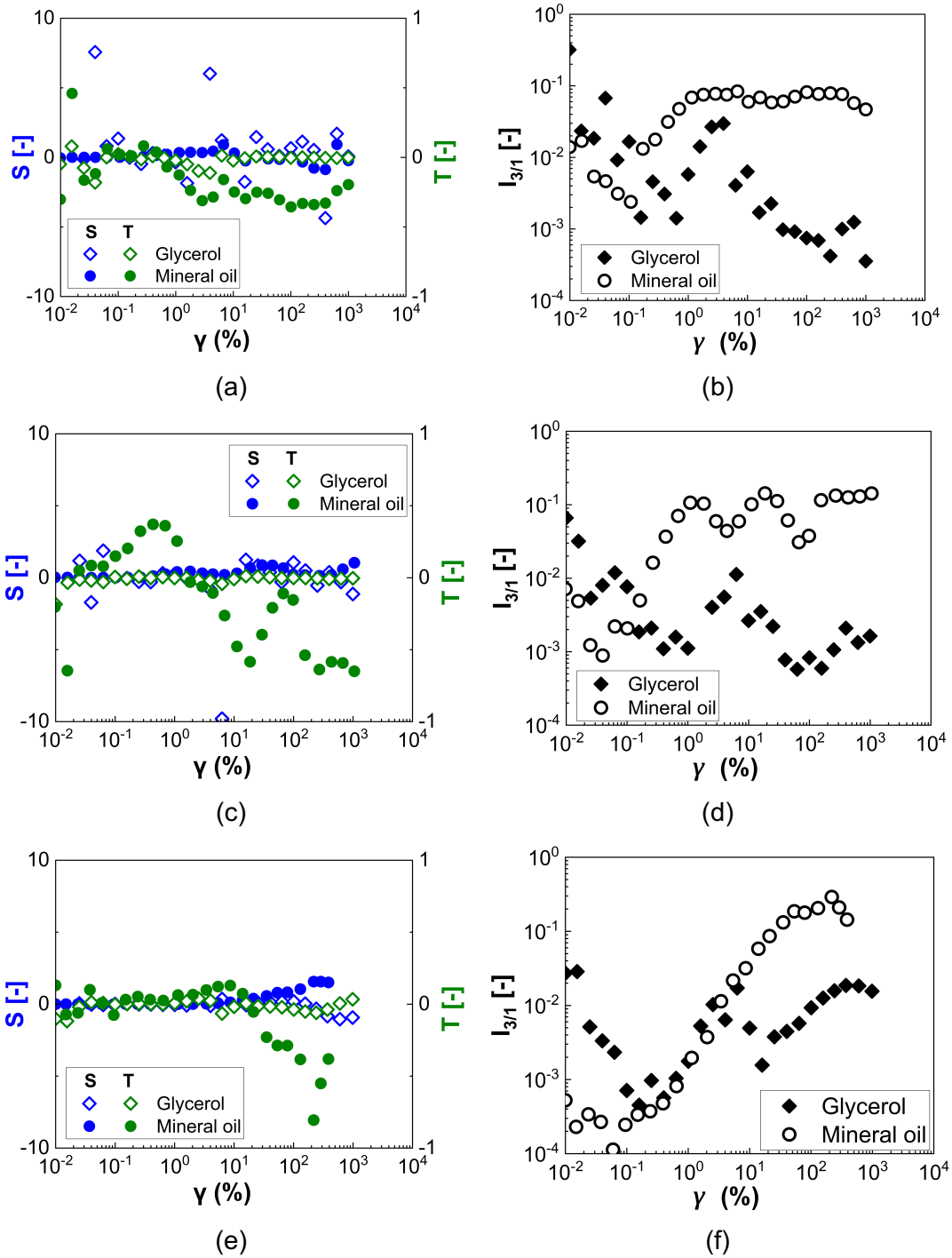

Figure 4.16: Stiffening (S) and thickening ratios (T) (left column) and Fourier spectra of the relative intensity of the third harmonic estimated from the data presented in Figure 4.15, as a function of % strain amplitude for the three particle suspensions in mineral oil at $\varphi = 0.10$, $f = 1Hz$ and 20°C. a) and b) glass spheres; c) and d) abrasive silicas; e) and f) filler silicas. The data for the corresponding suspensions in glycerol are also included for comparison.

In summary, the LAOS measurements of all suspensions in mineral oil at $\varphi = 0.10$ illustrate that the non-linear behaviour of these suspensions is mainly strain rate driven, indicating that the viscous component dominates suspension rheology under LAOS independent of the strongly elastic behaviour; this is in contrast to the finding for the corresponding suspensions in glycerol, which showed weak strain driven instabilities. These observations highlight the ability of LAOS to capture the microstructure differences of the suspensions arising from varying the physical and chemical properties of the suspending medium.

4.2.6 Rheology tuning via particle surface chemistry modifications

The previous sections highlighted the role of interparticle interactions on suspension rheology and in particular, the adhesion mechanism leading to shear thinning behaviour. The latter is desirable in many industrial applications; in fact, the ability to predict and control interparticle interactions can enable designing formulations with required rheological properties, which would ultimately lead to optimising manufacturing processes. Modifying particle surface chemistry provides such a tuning mechanism and it can also be exploited to enhance the particle dispersion capacity in different solvents (Hayashi and Kawaguchi, 2017b; Işçi et al., 2007; Marunaka and Kawaguchi, 2017, 2014; Zhang et al., 2017). Better dispersion also means that particle functionalisation can help tune the maximum packing fraction (Hayashi and Kawaguchi, 2017b).

In the present work, particle surface functionalisation was employed to improve the dispersion of particles in mineral oil and enable particle-solvent interactions to dominate over the particle-particle adhesion forces and hence, alter the shear thinning behaviour of suspensions. The glass sphere surface chemistry was modified with the addition of hydrophobic groups to improve their dispersion in mineral oil. Glass spheres were treated with two agents, i.e. palmitic acid and perfluorooctyltriethoxysilane, which are known to bind on the free silanol groups of glass spheres, weakening interparticle interactions (Chen et al., 2007; Go et al., 2017; Song et al., 2014; Yao Lu et al., 2015). The bonding mechanisms for the two agents are illustrated in Figure 4.17. The fluorosilane forms a siloxane bond between its silicon element and the free oxygens on the silica surface. On the other hand, in the case of palmitic acid an ester bond is created between its carboxyl group and the free silanol groups on silicas. These two molecules have chain lengths that are three

orders of magnitude smaller than the particle average diameter and thus, they are not expected to affect particle original diameter.

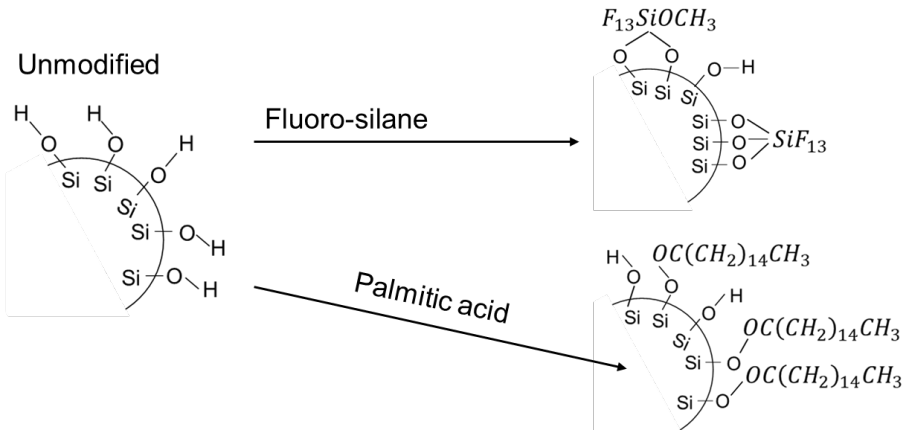

Figure 4.17: Schematic representation of the glass sphere surface chemistry modification. In the case of fluorosilane, a siloxane bond is created between the free hydroxyl group on silica and the silicon, whereas in the palmitic acid case, an ester bond is created between the hydroxyl group on silica and the carboxylic end of the reagent.

Figure 4.18a and b compare the relative viscosity and the shear stress values versus shear rate for a 5% v/v suspension of untreated and treated glass spheres in mineral oil, while Figure 4.18c presents the corresponding yield stress values and equivalent adhesion forces for the same suspensions. Two different concentrations of palmitic acid (PA36 and PA60) with differing concentration of hydrophobic groups were employed. The adhesion forces for the treated particle suspensions were estimated using the relation $\tau_y \propto (F/a^2)\varphi^n$ where n was taken equal to 3, as found from the rheology of the untreated particles.

It can be seen that as the concentration of the palmitic acid increases, the viscosity and yield stress values significantly decrease indicating a reduction in interparticle interactions as well as a better affinity between the particles and the solvent. Interestingly, at relatively high shear rates, all suspensions of treated glass spheres reach an asymptotic Newtonian plateau with a relative viscosity close to unity (i.e. $\eta_s = \eta_{fMO}$), while the untreated particles show higher relative viscosity values. The behaviour of the former implies that treated particles form weaker agglomerates compared to the untreated case, which completely disaggregate to individual units at $\dot{\gamma} > 100\ s^{-1}$ and can no longer affect solvent viscosity at such low concentrations, in agreement with the data obtained for the glycerol case. The adhesion forces decrease proportionally to the yield stress, as shown in Figure 4.18c. Therefore, controlling interparticle interactions through particle surface chemistry introduces new insights in

suspension rheology and can be exploited to tune rheology and enable the manufacturing of complex formulations.

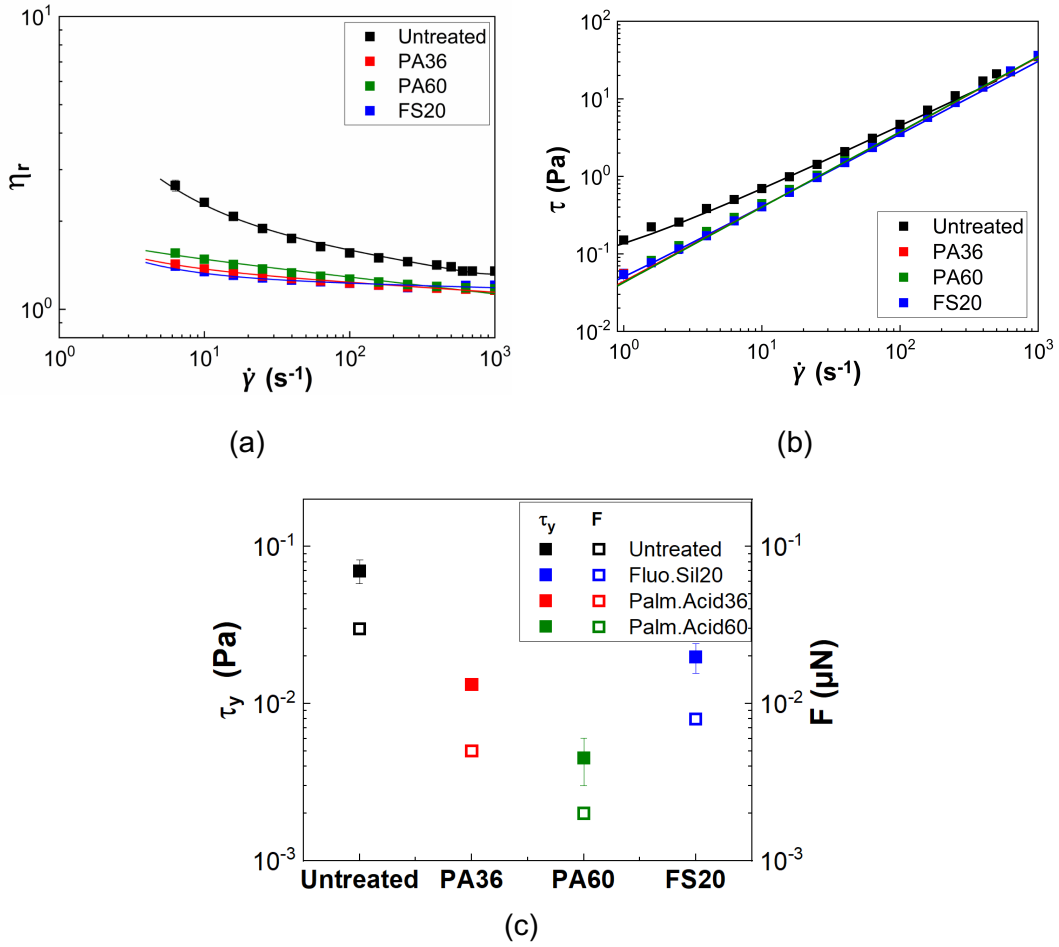

Figure 4.18: a) Relative viscosity values (η_r) as a function of shear rate for selected untreated and treated glass spheres in mineral oil at a concentration of 5% v/v and 20°C; b) ; c) Yield stress (τ_y) and equivalent adhesion force (F) for the treated and untreated glass sphere suspensions shown in (a). The numbers in the legend next to the hydrophobic agents represent the % w/w concentration of the reagent in relation to particle mass.

To further evaluate the reduction in size of the particle agglomerates after modifying the particle surface chemistry, images of the suspensions were taken right after sample preparation under no shearing conditions-except the mixing applied during sample preparation. Figure 4.19 shows indicative image examples of the untreated glass spheres (Figure 4.19a) and the glass spheres treated with fluorosilane (Figure 4.19b) in mineral oil at a concentration of $\varphi = 0.01$. The acquired images were analysed in MATLAB and the maximum particle equivalent diameter was estimated for each case. A clear reduction in the particle agglomerate size when the particle surface chemistry was altered with the introduction of the hydrophobic groups

is observed. The d_{95}, i.e. the particle diameter at which 95% of the measured particles have a size below this number, of the untreated glass spheres in water is also included in Figure 4.19c for comparison. The latter further confirms that particle attraction was hindered through particle surface chemistry functionalisation.

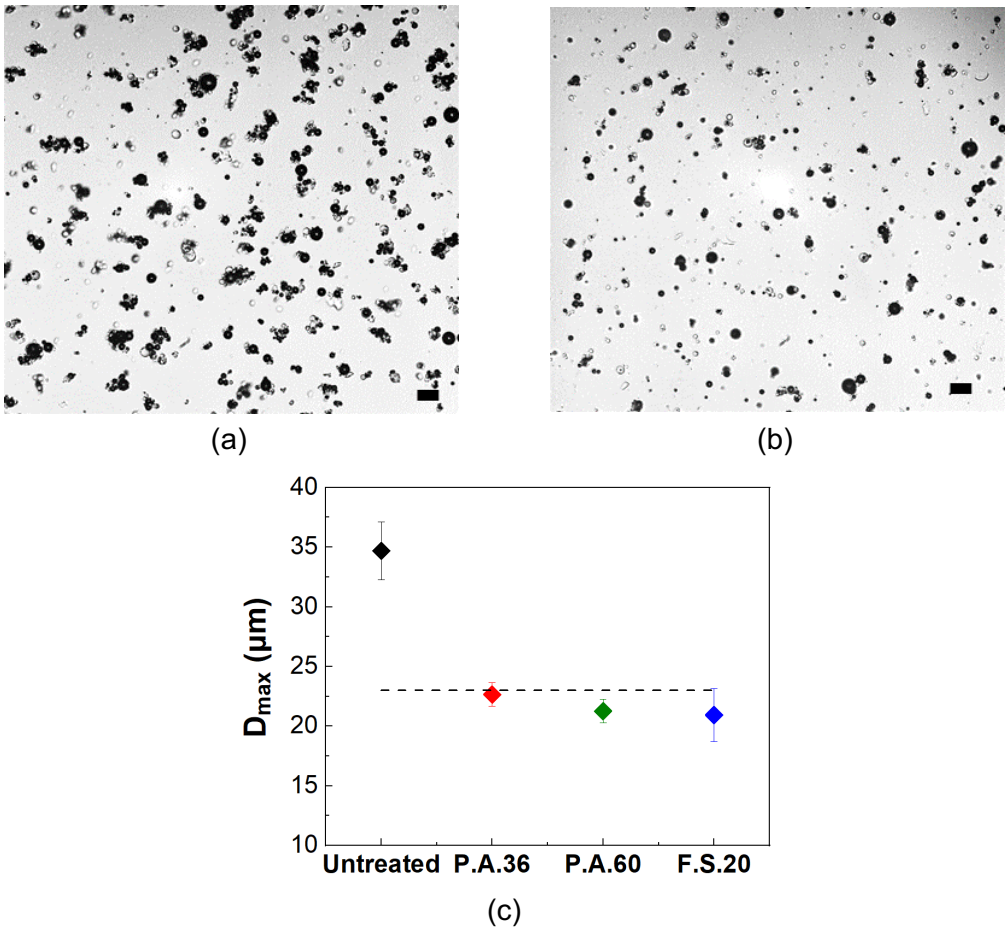

Figure 4.19: Indicative images of the untreated glass spheres (a) and glass spheres threated with fluorosilane (b) in mineral oil at $\varphi = 0.01$ under static conditions. The scale bars (▬) correspond to a length of 40 µm; c) Comparison of the maximum diameter for each suspension between the treated and untreated particles as observed under the microscope. The dashed line represents the d_{95} of the untreated glass spheres in water, i.e. the diameter at which 95% of the measured particles have sizes below this number.

4.2.7 Extent of shear thinning behaviour and effect of yield stress

The extent of shear thinning ($\eta_{r,e}$) as a function of particle volume fraction is summarised in Figure 4.20a for all suspensions in mineral oil. $\eta_{r,e}$ (Figure 4.20a) is defined as $\left(\eta_{r,6} - \eta_{r,\infty}\right)/\eta_{r,\infty}$, i.e. the ratio between the difference of the low shear relative viscosity, $\eta_{r,6}$ (taken at $\dot{\gamma}$=6.3 s^{-1} for all the shear thinning suspensions in mineral oil to avoid sedimentation effects, while the corresponding relative viscosity at the same shear rate was also considered for the glycerol case) and infinite shear relative viscosity to the infinite shear rate relative viscosity ($\eta_{r,\infty}$) values. The latter was derived from the Herschel-Bulkley fittings to the viscosity curves. The values for the suspensions in glycerol are also included for comparison with the $\eta_{r,e}$ estimated at the same low and high shear rate limits with these of the suspensions in mineral oil to facilitate the comparison. It should be recalled that the $\eta_{r,e}$ values in the previous chapter defined in eq. (3.12) used the zero shear rate viscosity ($\eta_{r,0}$) since most suspensions were fitted with the Carreau equation.

It can be seen (Figure 4.20a) that the suspensions in mineral oil start to shear thin at particle volume fractions as low as $\varphi = 0.02$ due to the formation of large particle agglomerates that break down with applied shear. This is in contrast to the behaviour of the suspensions in glycerol, which show an onset of shear thinning at a much higher particle concentration ($\varphi = 0.25$) attributed to the frictional contacts between neighbouring particles at sufficiently high normal loads. By modifying the glass sphere surface chemistry through the introduction of different hydrophobic groups, a suppression of the shear thinning response is achieved as indicated by a reduction in the $\eta_{r,e}$ values.

The yield stress of the glass sphere and abrasive silica suspensions in mineral oil are presented in Figure 4.20b alongside the critical stress values of the abrasive silica suspensions in glycerol responsible for the onset of shear thinning. Adhesive systems show typical yield stress behaviour and the estimated values highly depend on the particle volume fraction and particle surface characteristics (Eberle et al., 2014). In contrast, in the case of frictional suspensions (abrasives in glycerol) the estimated critical stress for the onset is φ-independent in agreement with the theory of Lobry et al. (2019).

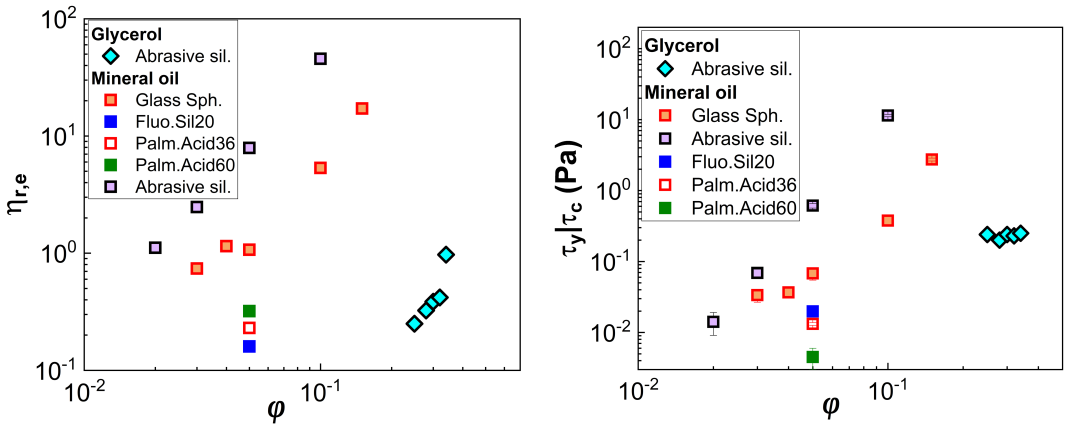

Figure 4.20: Summary of a) the extent of shear thinning as a function of particle volume fraction for all the shear thinning suspensions in mineral oil. The corresponding data in glycerol are presented for comparison; b) the estimated yield stress (τ_y) values for both suspensions in mineral oil. The critical stresses (τ_c), giving rise to the shear thinning of the abrasive suspensions in glycerol (discussed in the previous chapter) are included for comparison.

4.3 Discussion

In this chapter, an adhesion driven shear thinning mechanism was probed by suspending the three types of particles in mineral oil. The non-polar nature of the mineral oil leads to strong interparticle interactions and particle agglomeration between the hydrophilic silicas, which significantly influence suspension rheology. The degree of particle agglomeration is found to be dependent on particle surface roughness and porosity; these features are reflected in the particle specific surface area. An increase in particle surface roughness increases the available contact areas leading to the formation of larger agglomerates compared to the smooth glass spheres, as depicted in the microstructure images (Figure 4.10).

Unlike frictional suspensions in glycerol, the suspensions in mineral oil showed yield stress behaviour and pronounced shear thinning due to the agglomerates breaking down at increasing the shear rate at particle volume fractions as low as $\varphi = 0.02$. Similar phenomena were observed for suspensions of hydrophobic fumed silicas modified with hexadecyl chains in three alkanes, i.e. octane, dodecane and hexadecane (Marunaka and Kawaguchi, 2014). The suspensions in octane and dodecane exhibited more pronounced shear thinning compared to these in hexadecane and this behaviour was attributed to the affinity between the solvent and the particles. Hexadecane molecules were more likely to interfere with the hexadecyl groups on the particle surface compared to the other two solvents.

The extent of the shear thinning as well as the estimated yield stress values from the Herschel-Bulkley fits were dependent on the particle surface morphology as depicted by both phenomena being more pronounced for the abrasive silicas. The estimation of the yield stress enabled the quantification of an equivalent adhesion force for the two particle systems from the bulk rheology; its values were found to be two orders of magnitude higher for the abrasive silicas compared to the glass spheres. This can be related to the higher specific surface area of the former increasing the density of the surface silanol groups and promoting the hydrogen bonds between the abrasive silicas.

Analyzing the infinite shear rate relative viscosities for all suspensions as a function of particle volume fraction ($\eta_{r,\infty}$), revealed a significant reduction in the maximum packing for the suspensions in mineral oil, compared to those obtained for the suspensions in glycerol but also with increasing the particle specific surface area. Such low maximum packing fractions at a high shear rate ($\dot{\gamma} = 96\ s^{-1}$) have also been observed for hydrophobic fumed silicas (AEROSIL R8200) in mineral oil (Chen et al., 2007). It should also be noted that although Brownian effects slightly influenced the rheology of the suspensions in glycerol, such effects are expected to be negligible in mineral oil suspensions. This is due to, firstly the particle agglomerates increasing the average size of the solids in the suspension, and secondly, the shear rates able to overcome the sedimentation limit been sufficiently high to eliminate any effects of Brownian motion.

Ageing effects were investigated for the two types of commercial silicas (abrasives and fillers) in mineral oil at a fixed particle volume fraction of $\varphi = 0.10$ and a period of time 7-8 days. The formation of strong particle networks in suspensions in mineral oil was found to enhance suspension stability over time, unlike the frictional suspensions in glycerol that exhibit strong ageing effects. Selimovic et al. (2007) investigated the ageing of precipitated silica suspensions in different silicone oils (methyl-terminated and hydroxyl terminated) at particle volume fractions of $\varphi = 0.05$ and $\varphi = 0.08$ and a time period of 25 days. All suspensions exhibited an exponential decay of the viscoelastic moduli with time with the ageing effect being more pronounced for the suspensions in the hydroxyl-terminated silicone oil, as its hydroxyl groups can easily interfere with the hydrogen bonding between the silanol groups on the silica surface, similar to glycerol.

Particle agglomeration in the mineral oil suspensions gave rise to a solid-like behaviour at relatively low particle volume fractions ($\varphi \geq 0.05$). This was investigated through frequency sweeps in the LVR, where the G' was higher than the G'' and almost

independent from the angular frequency, ω. In contrast, the suspensions in glycerol had shown viscous dominant response ($G'' > G'$) for all the range of particle volume fractions and particle surface morphology investigated. Strongly elastic behaviour has also been observed for precipitated silica nanoparticles modified with poly-dimethyl siloxane (PDMS) and suspended in benzyl alcohol (Hayashi and Kawaguchi, 2017a). In that case suspension gelation occurred through the particle solvent interactions and thus, an increase in particle surface hydrophobicity delayed suspension gelation to higher particle volume fractions.

To verify the shear thinning and yield stress behaviour of the adhesive suspensions surface chemistry modification- through the introduction of hydrophobic groups- was employed to tune particle interactions and hence adhesion. Two different self-assembled monolayers, i.e. palmitic acid and fluorosilane, with varying concentrations of hydrophobic groups were employed to treat glass spheres. This inhibited interparticle interactions between the inherently hydrophilic glass spheres in mineral oil, as demonstrated by a decrease in the yield stress and adhesion force values, leading to reduced shear thinning behaviour. Chen et al (2007) also compared the rheology of hydrophilic fumed silicas in mineral oil with that of hydrophobic ones. It was observed that hydrophilic silicas exhibited much higher relative viscosity values at $\dot{\gamma} = 96s^{-1}$ compared to hydrophobic, due to the stronger particle agglomeration enabled through hydrogen bonding of the former.

4.4 Concluding remarks

The chapter elucidated a second mechanism inducing suspension shear thinning, based on the adhesive forces between particles when suspended in a non-polar solvent. In mineral oil, the particle-particle interactions were found to dominate the particle-solvent interactions and the suspensions showed pronounced shear thinning and yield stress behaviour at concentrations as low as 2% v/v for both glass spheres and abrasive silicas. This was attributed to the particles forming large agglomerates at low shear rates, which break down at increasing applied deformations leading to shear thinning. Particle agglomeration and disaggregation was reinforced by means of an optical shearing method, which enabled the visualization and quantification of aggregation characteristics *in situ,* through estimating an aggregation index. The transient behaviour of the particle agglomerates was monitored through stress growth measurements. The suspensions seemed to be reaching equilibrium within milliseconds after the application of shear in transient experiments indicating a short relaxation time of the agglomerates.

LAOS experiments were also conducted for suspensions in the semi-dilute concentration regime ($\varphi = 0.10$) and revealed mainly strain rate driven instabilities. Suspension rheology was further tuned through particle surface chemistry modification of the glass spheres using hydrophobic agents. The results presented in this chapter elucidated the importance of being able to control interparticle interactions and provided a framework for silica suspension rheology. The latter could serve as a significant tool for the design and optimisation of formulations with required rheological properties tailored to specific applications.

Industrial processes often involve high solid contents suspended in complex non-Newtonian suspending media. In the next chapter, the rheological properties of the glass spheres and the two types of silica particles (abrasives and fillers) will be investigated in two different non-Newtonian media, i.e. a purely elastic Boger fluid with constant viscosity and a shear thinning and viscoelastic matrix including Xanthan gum in a water/glycerol mixture. This will elucidate the competition between the non-Newtonian behaviour induced by the particles and that originating from the suspending medium, providing a better understanding on the rheology of complex industrial formulations.

Chapter 5

Suspensions in non-Newtonian suspending media

In Chapters 3 and 4 two different mechanisms of shear thinning were discussed: friction driven and adhesion driven, respectively. The former was studied by suspending the three types of particles, glass spheres, abrasive and filler silicas, in a polar solvent, glycerol. The latter was considered using a non-polar solvent, mineral oil. The physical and chemical properties of the two Newtonian suspending media significantly affected interparticle interactions and thus, suspension rheology, in parallel to other parameters, such as shear rate, particle volume fraction and particle surface roughness and porosity. Suspensions in glycerol showed shear thinning at $\varphi \geq 0.25$ due to the particle surface roughness enabling frictional contacts between them. In contrast, the suspensions in mineral oil exhibited pronounced shear thinning and yield stress behaviour attributed to the formation of large agglomerates, which break down at increasing shear reducing suspension viscosity.

However, in many industrial applications the suspending media are often complex and non-Newtonian, providing the appropriate integrity and stability to the end product. This gives rise to even more complicated particle dynamics, especially when polymer compounds interfere with interparticle interactions. This needs to be well understood for the design and successful manufacturing of formulations with specific properties. The work presented in this chapter aims to highlight the impact of non-Newtonian media to the rheology of selected particle suspensions in the highly concentrated regime, where particles themselves induce non-Newtonian phenomena. In particular, two different categories of non-Newtonian suspending media will be employed, i.e. an elastic solvent with constant viscosity (Boger fluid) and a shear thinning and weakly viscoelastic solvent (Xanthan gum solution).

This chapter will begin with a brief introduction (section 5.1) of the key findings reported in the literature for particle suspensions in non-Newtonian suspending media. The rheology of the suspensions in a Boger fluid will firstly be examined (section 5.2) under steady state and oscillatory shear at 20^{o}C, followed by the rheology of the suspensions in a shear thinning and weakly viscoelastic Xanthan gum solution under the same experimental conditions. The rheological properties of the suspensions in the two non-Newtonian suspending media at 60^{o}C are presented in section 5.4. The results obtained will be discussed and compared for all suspensions in section 5.5. followed by a closing summary in section 5.6. Appendix II also includes

more data on the rheology of the suspensions in the Xanthan gum solutions prepared with pure glycerol.

5.1 Introduction

Suspension rheology has been widely studied in the literature and complex phenomena have been observed by several researchers even for the simplest cases of spherical particles in Newtonian fluids (Denn and Morris, 2014); these involve shear thinning, shear thickening and yield stress. It is reasonable thus, to expect that adding a polymer into an already complex system can significantly influence suspension rheology by affecting particle-particle and particle-solvent interactions.

Polymers reinforced with particles are very commonly employed in industrial formulations to provide specific properties, such as improve solubility and stability of a product over time and controlled drug release applications (Bonacucina et al., 2004; Potanin, 2019; Young et al., 2005). Several experimental and computational studies aiming to resolve the rheological properties of particle suspensions in non-Newtonian media have been conducted by various researchers (Aliabadian et al., 2018; Bossis et al., 2017; Liard et al., 2014; Ma et al., 2017; Massaro et al., 2020; Tanner, 2019b; Vázquez-Quesada et al., 2019, 2017, 2016; Yang and Shaqfeh, 2018b, 2018a).

The key observations from rheological studies of suspensions in non-Newtonian media are summarized in the reviews of Tanner (2019), Yang and Shaqfeh (2018) and Shaqfeh (2019). Suspensions in shear thinning fluids show shear thinning that follows the behaviour of the suspending medium. On the contrary, in purely viscoelastic media, i.e. in the absence of non-Newtonian phenomena, suspensions can show shear thickening attributed to the strain hardening of the polymer chains under elongational flow around particles. The molecular weight of the polymer chains, the viscoelastic nature of the suspending medium, the particle volume fraction and the magnitude of applied shear rate are among the main factors affecting the driving mechanisms (e.g. polymer bridging, gelation, steric stabilization) behind the rheology of particles suspended in non-Newtonian carrier media.

Despite their high relevance in industrial and natural applications, experimental work on dense particle suspensions in non-Newtonian media, involving particles with complex surface morphology and porosity has been fairly limited in the literature. Recent work by Yang and Shaqfeh (2018) and Tanner (2019) focuses on numerical studies of suspensions of spherical particles in the dilute and semi-dilute concentration regimes. Therefore, more studies are needed to elucidate the mechanisms governing the rheology of more industrially relevant mixtures.

5.2 Particle suspensions in Boger fluid

Boger fluids are commonly used to isolate the effects of elasticity from non-Newtonian shear rheology, as they normally show strong elastic behaviour but constant viscosity. In the present study, the Boger fluid consists of 200 ppm polyacrylamide (PAA, $M_w = 5.5 \cdot 10^6\ g/mol$) in a 1% wt. water and 99% wt. glycerol solvent. The rheological properties of this solution under steady state and oscillatory shear are presented in Figure 5.1a and b respectively. It can be seen that the viscosity remains constant (Figure 5.1a) around the value of $\eta = 1\ Pa.s$ for at least three decades of shear rate ($\dot{\gamma}$). Also, both viscoelastic moduli increase with angular frequency. The contribution of the base fluid viscosity (1% wt. water/99% wt. glycerol) has been subtracted from the G'' values to better reflect the effect of polyacrylamide addition to the base fluid (Figure 5.1b). The measured phase angles (δ) for the Boger fluid at 20°C are also included in the same figure.

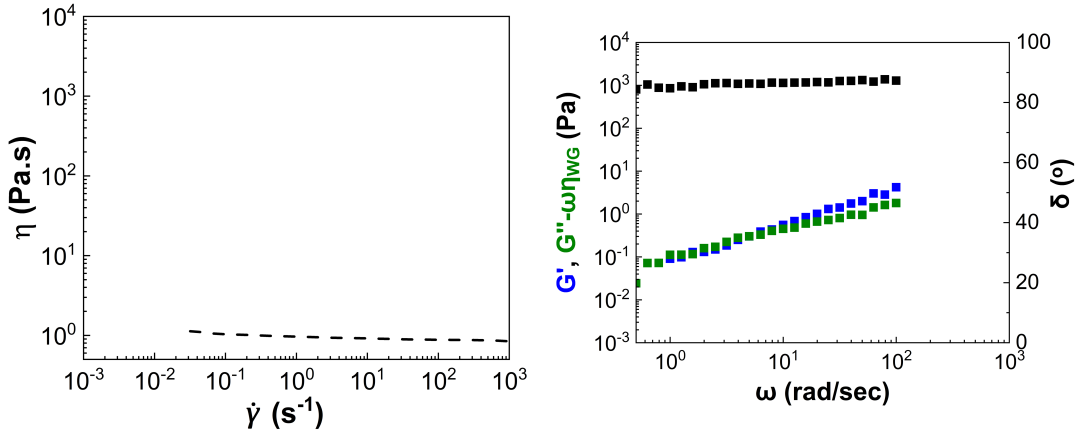

(a) (b)

Figure 5.1: a) Steady state viscosity of the Boger fluid at 20°C as a function of shear rate ($\dot{\gamma}$); b) viscoelastic moduli (storage, G', loss, G'', modulus) and phase angle (δ) of the Boger fluid at 20°C and $\gamma = 0.1\%$ as a function of angular frequency (ω). The contribution of the base fluid viscosity (water/glycerol) has been subtracted from the G'' values to isolate the effect of the polymer.

To evaluate the degree of elasticity of the Boger fluid the dimensionless elastic number (El, eq. (5.1)) is used which is expressed as follows.

$$El = \frac{t_e \eta_f}{\rho_f h^2} \tag{5.1}$$

where t_e is the elastic relaxation time and h is the gap height in the rheometer.

This number compares the elastic effects (numerator) to the viscous effects (denominator): the higher the elastic number is, the more likely elastic instabilities or flow features are to develop (Rothstein and McKinley, 2001).

The elastic relaxation time (t_e) of the Boger fluid is defined at the crossover point of the G' and G'' after subtracting the solvent's viscosity. It should be noted that polymer solutions are normally characterised by a range of relaxation times due to variations in the polymer chain length and interchain bonds (Rothstein and McKinley, 2001). This is also evidenced by the overlap between the G' and G'' values at angular frequencies $\omega \leq 10\ rad/sec$. However, using a single relaxation time at the crossover of the two moduli is still indicative of an average time scale and includes useful information about polymer dynamics. Thus, this method will be employed in all polymer solutions used in this chapter. The estimated t_e value along with the El number are presented in Table 5.1.

Table 5.1: Elastic relaxation time (t_e) estimated from the crossover point in the frequency sweep and elastic number (El) of the Boger fluid at 20°C.

Boger fluid at 20°C	
t_e (s)	1.25
El	$39 \cdot 10^4$

Sections 5.2.1 and 5.2.2 will present the rheological properties of selected suspensions in the highly concentrated regime of each particle type in the Boger fluid at room temperature (~20°C) under steady state and oscillatory shear measurements.

5.2.1 Steady state shear rheology

Figure 5.2 plots the viscosity and the shear stress values of all suspensions in the Boger fluid at room temperature as a function of shear rate and varying particle volume fractions (φ), while the insets in Figure 5.2 a, c and e show the corresponding relative viscosities of the suspensions. The volume fractions have been selected to be in the highly concentrated regime for each particle type, i.e. the ones inducing non-Newtonian rheology in the corresponding Newtonian solvent (Chapter 3). The ability to produce a homogeneous sample based on visual observations is also considered in the process of selecting φ. It should be recalled that the filler silicas could only be dispersed up to $\varphi = 0.20$ in the pure glycerol case and thus, the maximum φ value used in this case is 0.15. Hence this φ should be considered as dense, although it might appear as falling into the semi-dilute regime. Both the viscosity (η) and shear

stress (τ) values increase with particle volume for all suspensions, as the presence of solids induces a higher resistance of the fluid to the applied flow field.

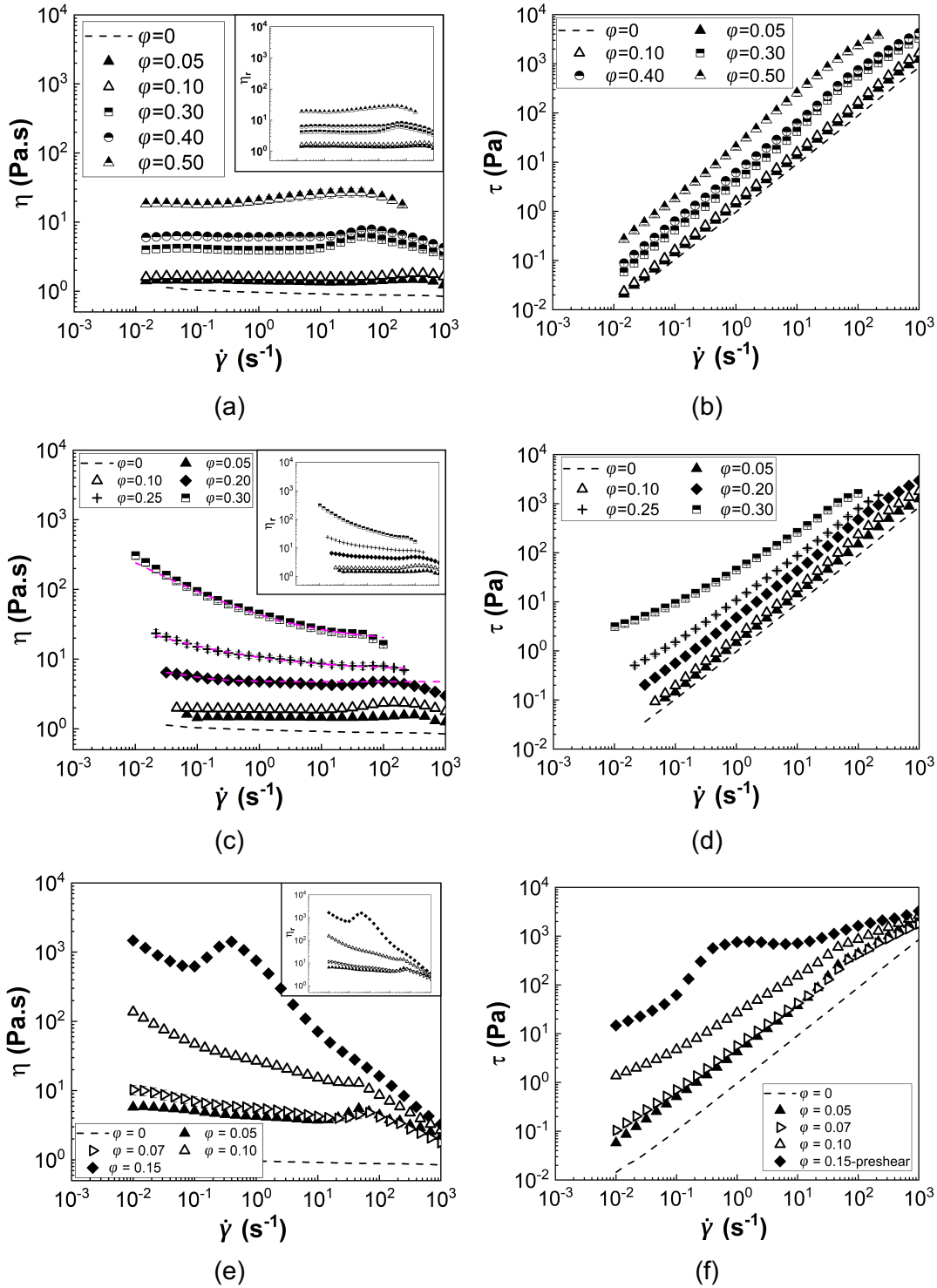

Figure 5.2: Viscosity (η) (left column)-insets show the corresponding relative viscosities (η_r)- and shear stress (τ) (right column) values of the three types of suspensions in the Boger fluid at ~20°C as a function of shear rate ($\dot{\gamma}$) and particle volume fraction (φ). a) and b) glass spheres; c) and d) abrasive silicas (Dashed lines correspond to the Carreau fittings); e) and f) filler silicas.

The glass sphere suspensions (Figure 5.2a) exhibit constant viscosity at low shear rate followed by mild shear thickening at particle volume fractions as low as $\varphi = 0.05$, which becomes more pronounced at higher φ. No yield stress can be identified through the shear stress curves (Figure 5.2b) of these suspensions. The abrasive silica suspensions (Figure 5.2c) exhibit weak shear thickening at $\varphi \leq 0.20$, which seems to diminish at the higher particle volume fraction. The abrasive silica suspensions at $\varphi = 0.25$ and $\varphi = 0.30$ show pronounced shear thinning, while yield stress behaviour, with a yield stress value of $\tau_y \approx 2\ Pa$ (Figure 5.2d), is also observed for the suspensions at the highest particle volume fraction. Shear thickening is also observed in the viscosity curves of the filler silica suspensions (Figure 5.2e) in addition to shear thinning and yield stress; the shear stress goes towards an asymptotic value at low shear rate as depicted in Figure 5.2f, especially at the higher particle volume fractions of $\varphi = 0.10$ ($\tau_y \approx 1\ Pa$) and $\varphi = 0.15$ ($\tau_y \approx 10\ Pa$). Unlike the glass sphere, the shear thickening reduces with φ, while it resumes at $\varphi = 0.15$.

Figure 5.3 illustrates the zero shear rate ($\eta_{r,0}$) and the infinite shear rate ($\eta_{r,\infty}$) relative viscosities of all suspensions in the Boger fluid as a function of particle volume fraction (φ). Since the base solvent includes only a low fraction of water (1% wt.) in glycerol, the estimated relative viscosity values can be compared with those obtained for the corresponding suspensions in pure glycerol (Chapter 3). The $\eta_{r,\infty}$ of the suspensions showing shear thickening response refers to the viscosity values at the plateau area before the onset of shear thickening. As already observed in Chapters 3 and 4, increasing the particle surface roughness and porosity increases the relative viscosity of the suspensions at both zero and infinite shear rate.

The glass sphere suspensions in the Boger fluid exhibit almost the same $\eta_{r,0}$ (Figure 5.3a) and $\eta_{r,\infty}$ (Figure 5.3b) values with those of suspensions in glycerol. In contrast, the addition of 200 ppm of polyacrylamide increases the relative viscosity values at zero (Figure 5.3a) and infinite shear rate (Figure 5.3b) of both the abrasive and filler silica suspensions compared to those of the suspensions in glycerol (Figure 5.3a).

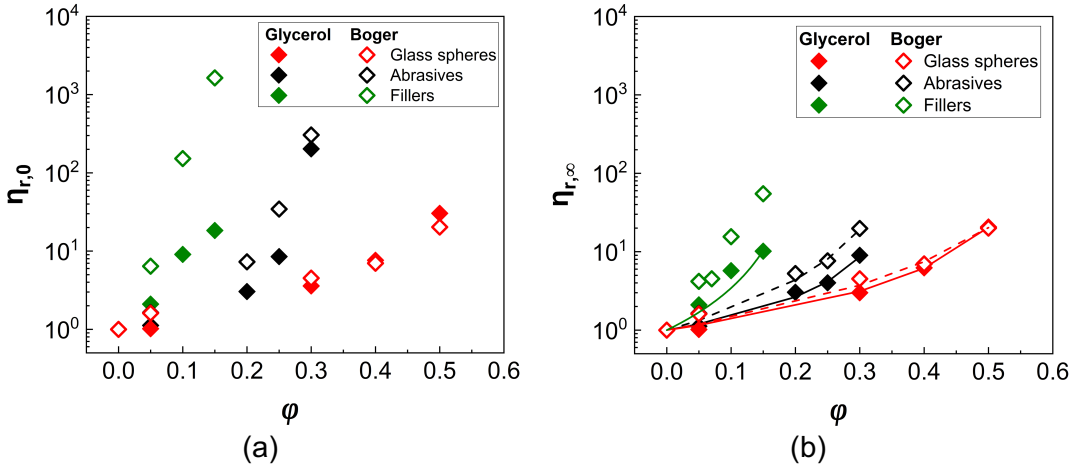

Figure 5.3: a) Zero shear rate ($\eta_{r,0}$) and infinite shear rate ($\eta_{r,\infty}$) relative viscosity of all the suspensions in the Boger fluid investigated in the present study at 20°C as a function of particle volume fraction (φ). The $\eta_{r,\infty}$ for the highly concentrated filler silica suspensions ($\varphi = 0.10$ & $\varphi = 0.15$) in the Boger fluid refer to the viscosity values at $\dot{\gamma} = 10^3 s^{-1}$. Continuous and dashed lines in (b) represent the Krieger-Dougherty fittings (eq. (2.9)) to the glass sphere and abrasive silica suspensions, while the filler silica suspensions were fitted with the Quemada equation (eq.(2.10)). Comparisons with the corresponding data in the pure glycerol at 20°C are also included.

The $\eta_{r,\infty}$ values (Figure 5.3b) of the glass sphere and abrasive silica suspensions in the Boger fluid are well described by the Krieger-Dougherty equation (eq. (2.7)). In contrast, eqs. (2.9) to (2.11) fail to describe the filler silica suspensions. The fittings are represented by continuous and dashed lines in Figure 5.3b, while the estimated variables, i.e. intrinsic viscosity (B) and maximum packing fraction (φ_m) are summarized in Table 5.2; the corresponding data for the suspensions in glycerol are also presented for comparison. It can be seen that both B and φ_m values increase in the presence of the polymer. The B values in the polymer solution are likely to represent not only the particle but also the polymer interactions and thus, are higher than those of the suspensions in the pure Newtonian solvent. On the other hand, the increase of the φ_m values in the presence of polymer might also be associated with the ability of the polyacrylamide molecules to keep the particles separate, possibly due to the polymer chains restricting the particles in certain positions within the solvent. The latter is likely to allow higher particle loadings to be achieved before the maximum packing and eventually, jamming phenomena occur.

Table 5.2: Intrinsic viscosity (B) and maximum particle packing (φ_m) obtained from the Krieger-Dougherty fittings to the glass sphere and abrasive silica suspensions $\eta_{r,\infty}$ data in Figure 5.3b. The data of the filler silicas in glycerol were fitted with the Quemada equation and thus, only the φ_m value is reported.

Solvents / **Particle type**	**glycerol**		**Boger fluid**	
	$\boldsymbol{B}$	$\boldsymbol{\varphi_m}$	$\boldsymbol{B}$	$\boldsymbol{\varphi_m}$
Glass spheres	2.72	0.59	3.33	0.68
Abrasive silicas	3.35	0.36	5.32	0.40
Filler silicas	-	0.26	-	-

The extent of shear thinning ($\eta_{r,e}$, eq. (3.12)) and shear thickening ($\eta_{r,t}$, eq. (3.13)) of the suspensions in the Boger fluid are plotted in Figure 5.4a and b respectively as a function of particle volume fraction (φ). The estimates for the corresponding suspensions in glycerol are included for comparison to better evaluate the effect of polyacrylamide on their rheology.

The Boger fluid appears to suppress the shear thinning behaviour of the glass sphere suspensions compared to that of the suspensions in pure glycerol, while promoting it for the two commercial silicas (abrasives and fillers) (Figure 5.4a). The pronounced shear thinning response of the abrasive silicas in glycerol was attributed to the strong frictional contacts between the rough particles upon shear (Chapter 3). Adding 200 ppm of polyacrylamide to the suspension does not seem to significantly alter its shear thinning response (black open diamonds in Figure 5.4a). It is likely that the polymer chains absorb on the silica surface leading to sterically stabilized suspensions at low shear rates. Increasing the applied deformation, the polymer chains extend which might lead to them detaching from the particle surface allowing frictional contacts to occur and induce shear thinning rheology.

The filler silica suspensions show more pronounced shear thinning compared to the counterpart suspensions in pure glycerol but also to the other two types of suspensions in the Boger fluid. Similar to the abrasive silicas, at high shear rates the enabled frictional contacts in conjunction with the high effective volume fraction due to particle porosity might explain this behaviour. It should be noted that the effective volume fractions for the commercial silicas are assumed to follow similar trends with those presented in Chapter 3, as the solvent and particle densities are not significantly altered with the addition of 1% wt. water in glycerol or the presence of polymer molecules. However, other factors such as the shape of the pores or entrapped air bubbles unable to be removed under vacuum during sample preparation might be

affecting the rheology of the filler silica suspensions making the interpretation of their shear thinning behaviour challenging (Figure 5.4a).

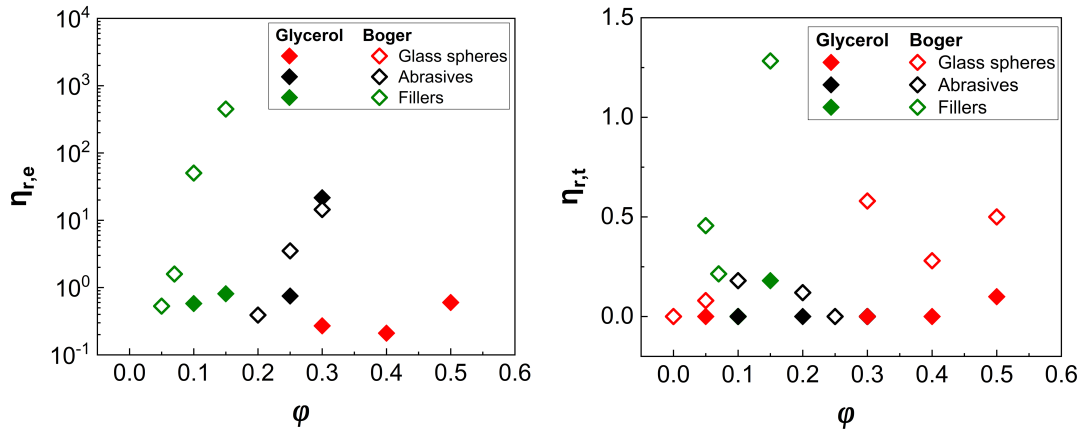

Figure 5.4: a) Extent of shear thinning and b) extent of shear thickening of all the suspensions in the Boger fluid at 20°C as a function of particle volume fraction (φ). Corresponding data for the suspensions in glycerol at 20°C are also included.

Interestingly, the glass sphere suspensions in the Boger fluid exhibit a pronounced shear thickening response under steady state (Figure 5.4b). This is in agreement with previous studies of nearly monodisperse polystyrene spheres in a Boger fluid (Scirocco et al., 2005) and numerical studies of particles in elastic media in the dilute and semi-dilute concentration regimes (Yang and Shaqfeh, 2018a, 2018b). Shear thickening of suspensions involving this type of suspending media has been mainly attributed to the strain hardening of the polymer chains under the elongational flow generated at the narrow interparticle gaps; this phenomenon is known as elastic thickening.

The abrasive silica suspensions also show shear thickening response at $\varphi \leq 0.20$; these suspensions showed Newtonian response in glycerol. However, this behaviour diminishes at higher particle volume fractions ($\varphi = 0.25$ and $\varphi = 0.30$) giving rise to strong shear thinning, which can screen shear thickening. Partial attachment of the polyacrylamide chains on the silica surface might limit the polymer chain elongation induced by the presence of extensional stresses responsible for suspension shear thickening in the Boger fluid resulting in a suppression of this non-Newtonian feature.

It should be noted that edge fracture was also observed for the abrasive silica suspensions at $\varphi = 0.25$ and $\varphi = 0.30$ (Figure 5.2c) at shear rates $\dot{\gamma} \leq 100\ s^{-1}$, i.e. similar to the $\dot{\gamma}$ values at which shear thickening occurred for the suspensions at lower φ. This phenomenon might comprise an additional factor responsible for masking the

shear thickening response of the denser abrasive silica suspensions. Such problems can be overcome by using Couette cell geometries that prevent edge fracture but due to requiring a high volume of sample they were not used in the present study.

Interestingly, the filler silica suspensions exhibit pronounced shear thickening, especially at $\varphi = 0.15$ (Figure 5.4b) in parallel to the strong shear thinning response (Figure 5.4a) compared to the corresponding suspensions in glycerol. The pronounced shear thickening response of the filler silica suspensions in the Boger fluid might arise from the synergetic effect of two mechanisms; first the presence of PAA molecules increase the viscosity and thus, the strength of the solvation layer inducing stronger repulsive forces between the particles and second, the elastic thickening induced by the polymer at sufficiently high shear rates.

5.2.2 Oscillatory shear rheology

The viscoelastic properties of the suspensions as well as the effect of particle addition on the elasticity of the Boger fluid was investigated through oscillatory frequency sweeps in the linear viscoelastic region (LVR, $\gamma = 0.1\%$). Figure 5.5 illustrates the viscoelastic moduli (storage, G', and loss, G'' modulus) and the phase angles of the three types of particles as a function of angular frequency (ω) at 20°C and selected particle volume fractions (φ).

All suspensions exhibit viscous dominated response in the LVR with G'' being always higher than G' values, while both moduli increase with both φ and ω. Increasing the particle volume fraction also increases the values of G' and G'' in a similar manner. The strong liquid like response of the glass sphere suspensions is also reflected in the measured phase angles (δ) (Figure 5.5b), which remain independent of ω and close to 90° at all φ values. The absence of viscoelasticity highlights the strong effect of the solvation layer formed by glycerol that prevents interparticle attraction, which might also have been reinforced by the presence of a highly elastic polymer solution.

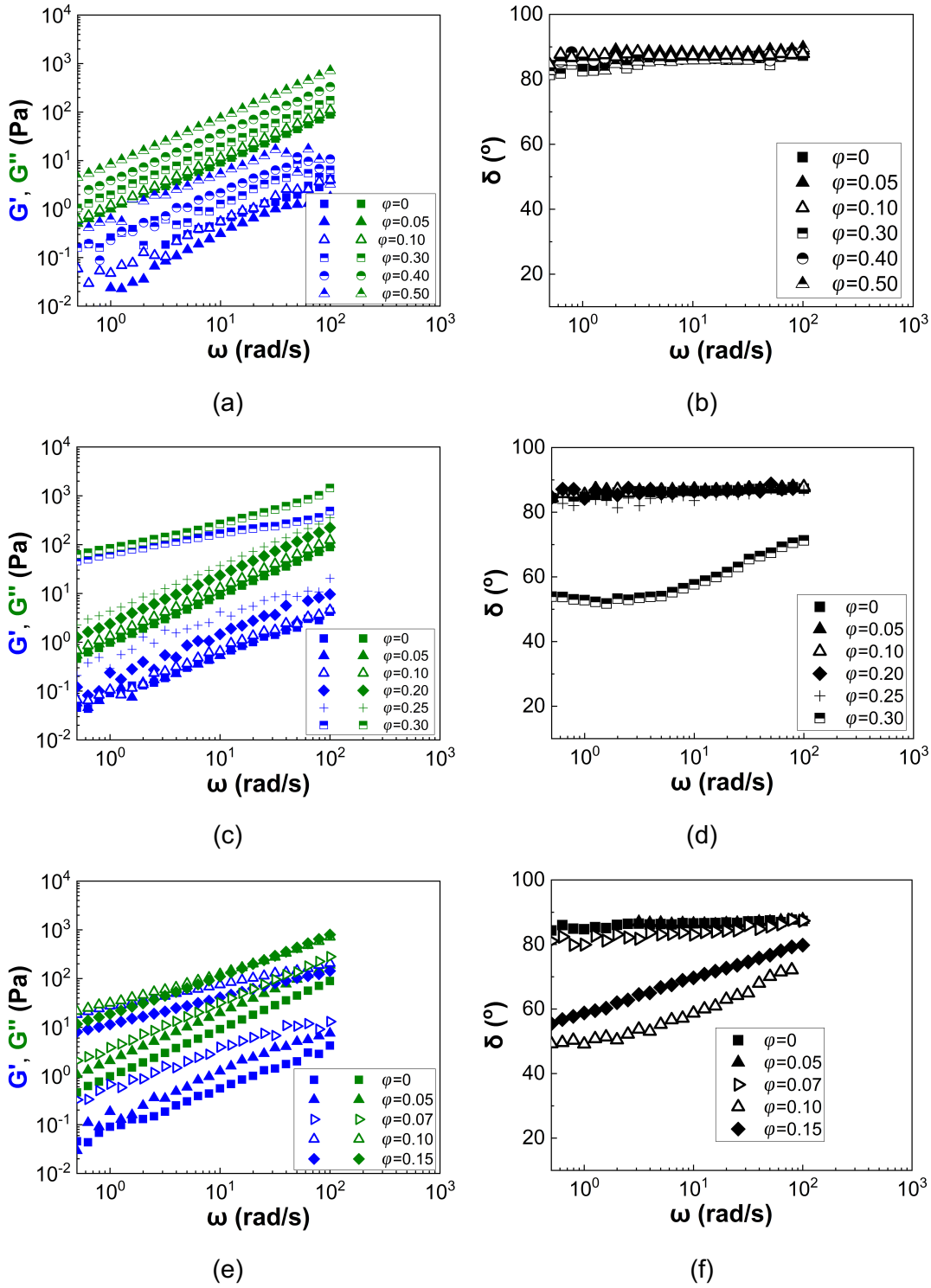

Figure 5.5: Viscoelastic moduli (G', G'') (left column) and phase angles (δ) (right column) of the selected suspensions in the Boger fluid as a function of angular frequency (ω) at ~20°C and $\gamma = 0.1\%$. a) and b) glass spheres; c) and d) abrasive silicas; e) and f) filler silicas.

Similar to the glass spheres, the abrasive silicas in the Boger fluid exhibit liquid like behaviour ($G'' < G'$) (Figure 5.5c) and phase angles of $\delta \approx 90^o$ (Figure 5.5d) at $\varphi \leq 0.25$. Interestingly, the suspension at the highest particle volume fraction ($\varphi = 0.30$) shows a more complex behaviour. Although the G'' values remain higher than G', the

values of the latter closely approach G'' at $\omega \leq 10\, rad/sec$ giving rise to more pronounced viscoelasticity, which is also manifested by a decrease in the values of the phase angles (Figure 5.5c) varying from $\delta = 50^o$ at $\omega = 5\, rad/sec$ to $\delta = 70^o$ at $\omega = 100\, rad/sec$. The partial attachment of the polyacrylamide chains on the abrasive silica surface can lead to entangled particle-polymer networks giving rise to suspension viscoelasticity at low deformation rates such as those investigated here under oscillatory shear. The density of the absorbed polymer chains also increases with an increase in the particle concentration as there are more available areas of contacts and thus, viscoelastic phenomena can be more pronounced for the suspension at the highest φ values (Saito et al., 2011).

The viscoelastic properties of the filler silica suspensions in the Boger fluid are described in Figure 5.5e and f as a function of angular frequency. The suspensions at $\varphi \leq 0.07$ act as viscous fluids, as seen by G'' being higher than G' (Figure 5.5e) and the phase angles (δ) being close to 90° (Figure 5.5f). Weak viscoelasticity arises at the higher particle volume fractions of $\varphi = 0.10$ and $\varphi = 0.15$, although $G'' > G'$ at the investigated ω range. As with the abrasive silicas, the observed response of the highly concentrated filler silica suspensions under oscillatory shear can be related to the formation of an entangled network between particles and polymer chains at low angular frequencies (Figure 5.2e and f).

5.2.3 Large amplitude oscillatory shear (LAOS) - microstructure

As discussed in previous chapters, the use of optical methods to monitor the microstructure of particle suspensions under shear is limited to the dilute particle volume fraction regime; higher particle concentrations lead to opaque samples rendering the visualization of single particles and microstructure patterns inaccessible. Since this chapter involved only suspensions in the dense regime for each particle type, the optical shearing technique was not applied. In contrast, Large Amplitude Oscillatory Shear (LAOS) measurements were conducted for selected suspensions in Boger fluid. The measured G' and G'' of all suspensions are plotted in Figure 5.6 as a function of % strain amplitude and particle volume fraction at 20°C and $f = 1Hz$ alongside the tan(δ) values defined as the ratio of the G'' to G' at each γ value (tan(δ)= G''/G').

The Boger fluid ($\varphi = 0$) shows viscous dominated response, with the G'' values remaining constant and independent of the applied strain amplitude; this behaviour aligns with the Newtonian response of these fluids under steady state. The G', on the

other hand, exhibits weak strain thinning at $\gamma \geq 50\%$, which can be attributed to alignment of the polymer chains with the applied flow field. All suspensions exhibit viscous dominated response under LAOS in agreement with the frequency sweeps, and this behaviour is also reflected in the tan(δ) values which are above 1 in all cases. Therefore, based on the findings in Chapter 4 and the liquid-like response of the suspensions in the Boger fluid, no particle agglomeration is expected to occur. However, a weak viscoelasticity is observed for the highly concentrated abrasive ($\varphi = 0.30$) (Figure 5.6c) and filler ($\varphi = 0.10$, $\varphi = 0.15$) (Figure 5.6e) silica suspensions at the low strain amplitude area (linear viscoelastic region) as the G' values closely approach these of the G''; this is likely to arise from the frictional contacts between the rough particles.

Beyond the LVR, both moduli exhibit strain thinning at intermediate strain amplitudes which becomes more pronounced with increasing φ and depends on the particle type. For example, the abrasives silicas at $\varphi = 0.30$ (Figure 5.6c) exhibit stronger strain thinning compared to the glass spheres suspension at $\varphi = 0.50$ (Figure 5.6a). At sufficiently high particle volume fractions and strain amplitudes, strain hardening especially of the elastic modulus, G', also occurs, which can be associated with the strain hardening of the polymer chains attributed to the elongational flows generated within the interparticle gaps. The critical γ value for the onset of strain hardening decreases with increasing φ, probably indicating an increase in the elongational stresses generated in the interparticle gaps.

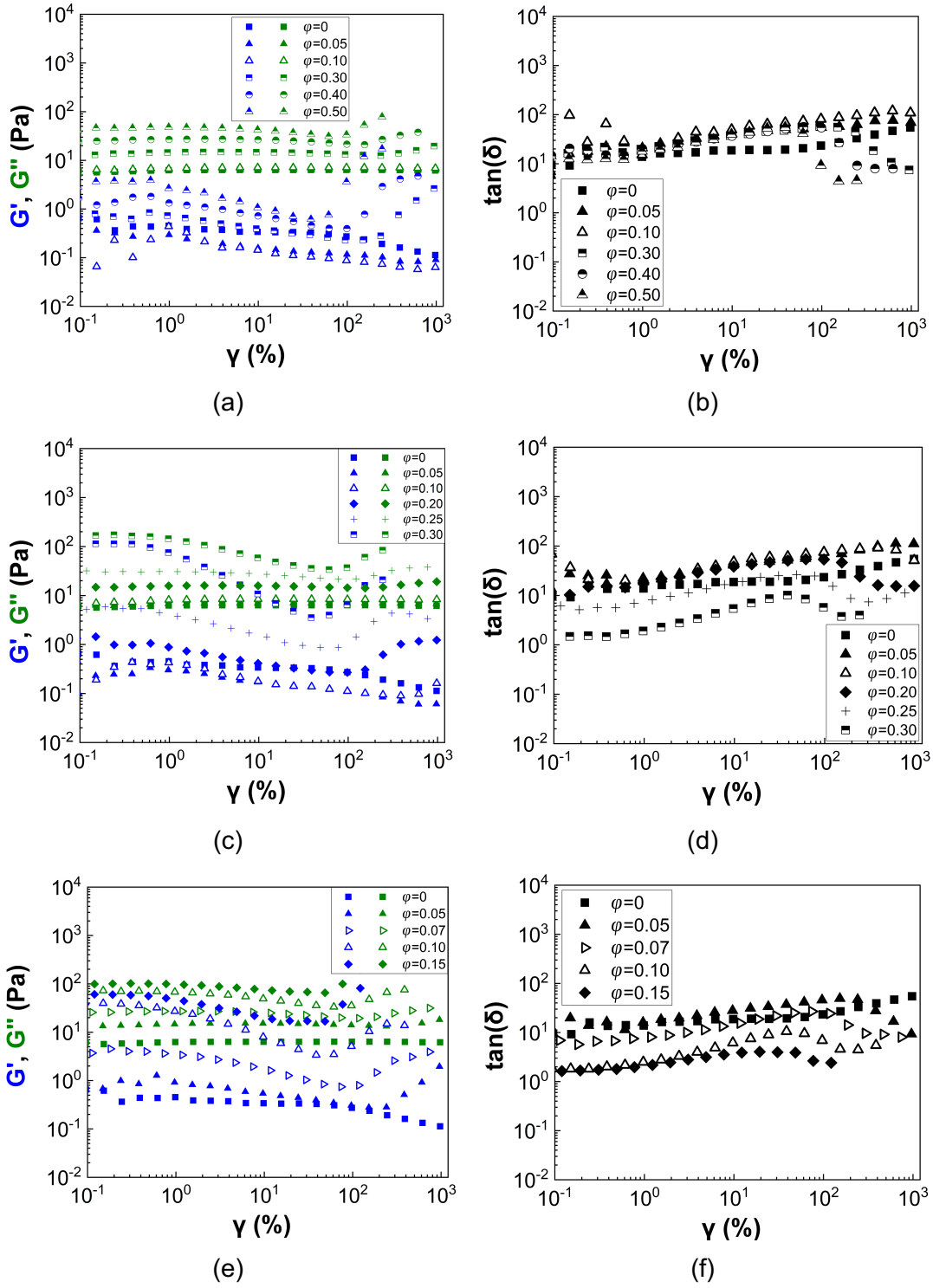

Figure 5.6: Viscoelastic moduli (G', G'') (left column) and tan(δ) (right column) values of the selected suspensions in the Boger fluid as a function of % strain amplitude (γ) and particle volume fraction (φ) at 20°C and $f = 1Hz$. a) and b) glass spheres; c) and d) abrasive silicas; e) and f) filler silicas.

5.3 Suspensions in a shear thinning fluid

Xanthan gum (Sigma Aldrich, $M_w = 1.76 \cdot 10^6\ g/mol$ measured by gel permeation chromatography) was used in the present study to prepare the shear thinning suspending media. The Xanthan gum concentration was kept constant at 0.1% w/v while the base fluid was a water/glycerol mixture (10/90 per volume) The water was added to facilitate the dissolution of the Xanthan gum powder in the solvent. It should be noted that two Xanthan gum solutions were also prepared using pure glycerol. However, due to deviations in the rheology of the different batches, only selected suspensions were investigated in these solvents and the corresponding data are shown in Appendix II. The viscosity (η) values of the Xanthan gum solutions used here at 20°C are presented in Figure 5.7a, while the corresponding viscoelastic moduli under oscillatory frequency sweeps in the linear viscoelastic region (LVR) in Figure 5.7b. In the latter, the contribution of the solvent's viscosity, i.e. water/glycerol ($\omega\eta_{WG}$) has been subtracted to isolate the effect of Xanthan gum in the solution. Although the Xanthan gum concentration as well as the composition of the base fluids were kept the same in all solvents, differences in the viscosity values can be observed (Figure 5.7a) especially at low shear rates; these originate from small changes in the preparation procedure required for the complete dissolution of the Xanthan gum powder in the fluids. Despite the differences in the viscosity values, the shear thinning degree of all solutions is similar with flow indices (n) varying from 0.4 to 0.5.

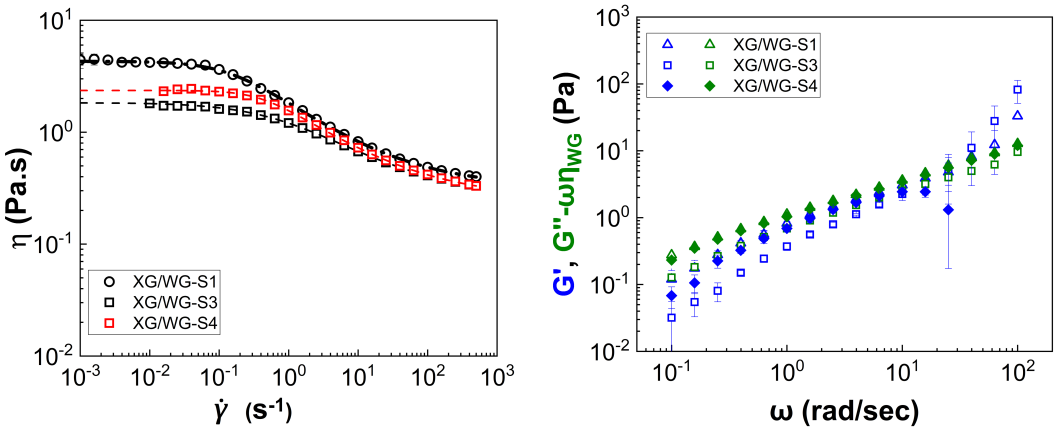

Figure 5.7: a) Viscosity (η) values as a function of shear rate ($\dot{\gamma}$) for all the Xanthan gum solutions (XG) in glycerol and in water/glycerol at 20°C; b) viscoelastic moduli (storage, G', loss, G'', modulus) of all Xanthan gum solutions at 20°C and $\gamma = 0.1\%$ as a function of angular frequency. The contribution of the base fluid viscosity (pure glycerol or water/glycerol) has been subtracted from the G'' values to isolate the effect of the polymer.

The relaxation times of the Xanthan gum solutions estimated from the crossover point of the two moduli (Figure 5.7b) after subtracting the solvents viscosity and the corresponding elastic times (El) are shown in Table 5.3. The solutions in 100% glycerol exhibit longer relaxation times and higher elastic numbers compared to these in the water/glycerol mixture due to probably the higher viscosity of the base solvent. It should also be noted that the El numbers of all Xanthan gum solutions are lower than that of the Boger fluid ($El = 39 \cdot 10^4$).

Table 5.3: Elastic relaxation times (t_e) estimated from the crossover point in the frequency sweep and elastic number (El) of all Xanthan gum solutions at 20°C.

No.	Solvents	t_e (s)	El
1	XG/G-S1	3.96	$2.5 \cdot 10^4$
2	XG/G-S2	9.96	$4.5 \cdot 10^4$
3	XG/WG-S1	0.16	526
4	XG/WG-S2	1.58	$5.4 \cdot 10^3$
5	XG/WG-S3	0.4	586
6	XG/WG-S4	0.63	$1.1 \cdot 10^3$

In the following sections (5.3.1 and 5.3.2), the rheological properties of the three types of particle suspensions in the Xanthan gum solutions in the water glycerol (1/9) mixture will be presented under steady state and oscillatory shear at 20°C. The selected volume fractions correspond to the highly concentrated regime for each particle type, as described in section 5.2 for the suspensions in the Boger fluid. The Xanthan gum solutions used to prepare the suspensions were the ones with no. 3, 5 and 6 in Table 5.3, since they show similar elastic numbers. In particular, the glass spheres were suspended in solution no. 5, the abrasive silicas in no. 3 and the filler silicas in no. 6. Selected suspensions using the Xanthan gum solution in pure glycerol were also investigated under steady state and oscillatory shear and the obtained results are presented in Appendix II.

5.3.1 Steady state shear rheology

The viscosity (η) values of the three types of particle suspensions, i.e. glass spheres, abrasive silicas and filler silicas, in the Xanthan gum solutions under steady state are shown in Figure 5.8 as a function of shear rate ($\dot{\gamma}$) and varying particle volume fractions (φ). Figure 5.9 shows the corresponding shear stress (τ) values for

all suspensions. The corresponding flow curves for the suspensions in the Newtonian base fluid, i.e. water/glycerol (1/9) are presented alongside for comparison.

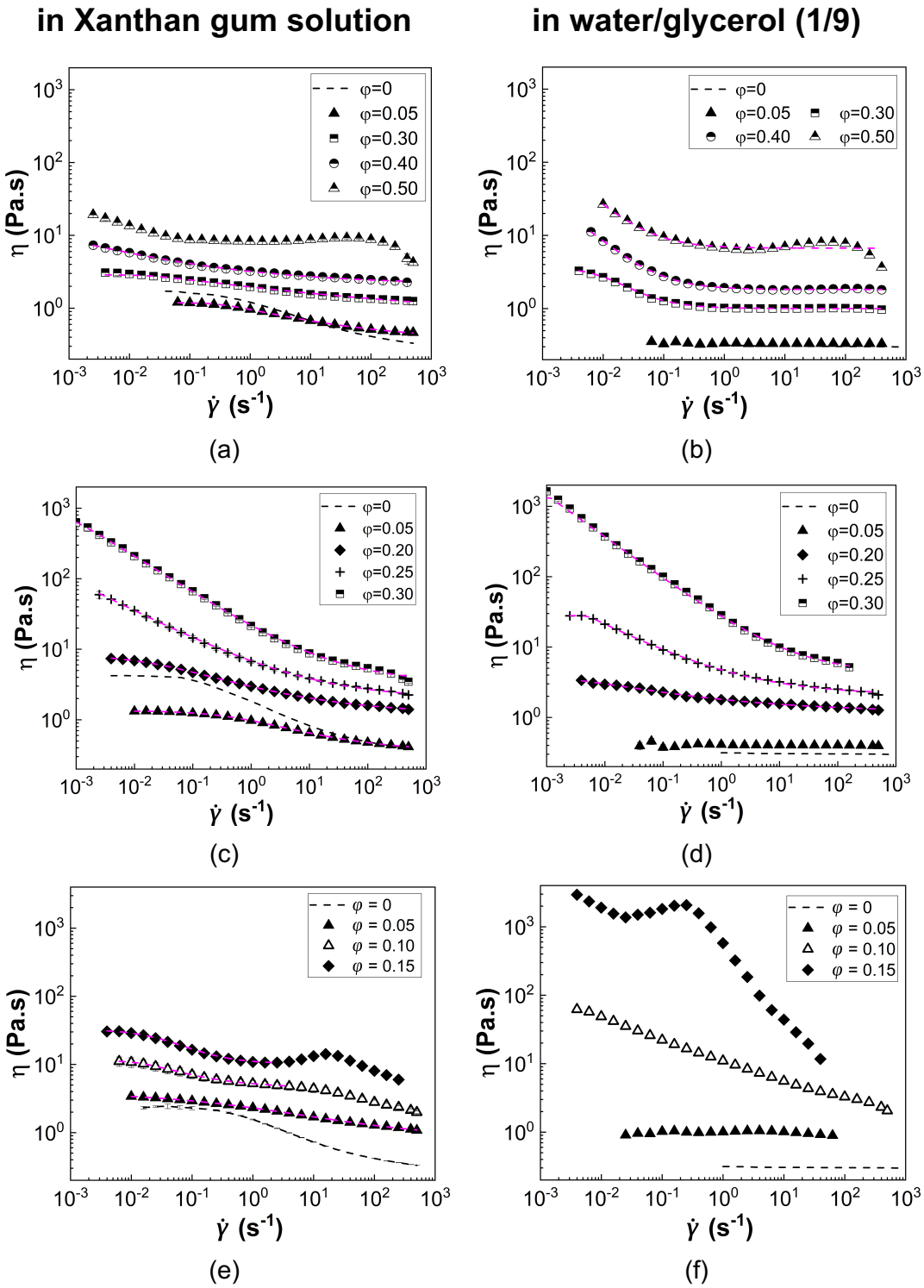

Figure 5.8: Viscosity (η) of selected suspensions in the 0.1% wt. Xanthan gum solution in water glycerol (1/9) (left column) as a function of shear rate ($\dot{\gamma}$) at 20°C. The corresponding data in the Newtonian water/glycerol (1/9) mixture are presented (left column) for comparison. Dashed lines correspond to the Carreau fittings to the shear thinning curves. a) and b) glass spheres; c) and d) abrasive silicas; e) and f) filler silicas.

Increasing the particle volume fraction leads to an increase in the viscosity of the suspending medium, both in the Xanthan gum solution and the pure water/glycerol mixture. The glass sphere suspensions (Figure 5.8a) in the Xanthan gum solution exhibit shear thinning response at all particle volume fractions investigated following the trend of the suspending medium A slightly different behaviour is observed for the same suspensions in the Newtonian water/glycerol mixture (Figure 5.8b), which show the onset of shear thinning at $\varphi \geq 0.30$. Shear thickening response is also observed at $\varphi = 0.50$ independently of the solvent used, i.e. Xanthan gum solution (Figure 5.8a) and water/glycerol (1/9) (Figure 5.8b). The latter is likely to arise from interparticle interactions at sufficiently high shear rate values rather than elastic thickening of the polymer chains, in contrast to the Boger fluid case.

The abrasive silica suspensions (Figure 5.8c) also exhibit a pronounced shear thinning response and the absence of shear thickening. Interestingly, the suspension at the lower φ of 0.05 shows lower viscosity values compared to that of the Xanthan gum solution at shear rates $\dot{\gamma} \leq 10\ s^{-1}$. It is likely that the shear rate at the close proximity of the particles is higher compared to the applied one due to the stresses generated in the interparticle gaps are a combination of shear and extensional flows. Therefore, a local increase of the shear rate can lead to a more pronounced reduction in the viscosity of the Xanthan gum solution at these areas leading to an overall decrease in suspension viscosity values. At such low particle volume fractions, especially, this reduction in viscosity due to the higher shear rates experienced by the Xanthan gum chains cannot be overcome by the presence of particles. On the other hand, at sufficiently high shear rates, the complete disentanglement of Xanthan gum combined with the higher particle motility equates the viscosity of the suspension with that of the suspending medium. Another explanation could also be that the particles interfere with the Xanthan gum molecules leading to their disaggregation and alignment to the direction of the applied flow field at lower apparent shear rates.

Comparing the rheology of the suspensions in the Xanthan gum solution to that of the suspensions in the water/glycerol (1/9) mixture (Figure 5.8d) shows an increase in the suspension shear thinning in the presence of a shear thinning fluid at $\varphi \leq 0.25$, while this weakly reduces at $\varphi = 0.30$. On one hand, the shear thinning behaviour of the suspensions in the dilute and semi-dilute regime (Figure 5.8c) stems from the shear thinning nature of the suspending medium. The denser suspensions in the Xanthan gum solution ($\varphi \geq 0.20$) exhibit the same behaviour as in the pure Newtonian solvent (Figure 5.8d); the shear thinning response in this case can result from the

competition between the interparticle and polymer dynamics. In particular, the presence of polymer chains can increase the strength of the solvation layer and further prevent interparticle contacts.

The filler silica suspensions in the Xanthan gum solution (Figure 5.8e) also exhibit shear thinning response at all φ values, while shear thickening is only observed for the highest particle volume fraction, $\varphi = 0.15$. It seems that the addition of Xanthan gum increases the low shear rate viscosity of the dilute suspension ($\varphi = 0.05$) compared to that in the Newtonian solvent (Figure 5.8f). The opposite behaviour is observed in the case of the suspensions at $\varphi = 0.10$ and $\varphi = 0.15$ in Xanthan gum (Figure 5.8e), where the shear viscosity is remarkably lower compared to the values obtained for the corresponding suspensions in the pure water/glycerol (1/9) mixture (Figure 5.8f) in the low shear rate region. The unexpectedly high viscosity values and extreme shear thinning observed for the higher concentrations of the water/glycerol suspensions in Figure 5.8f might be the result of two distinct parameters. First, interparticle interactions enabled through a thinner solvation layer due to the water presence and the high effective particle volume fraction due to particle porosity (as discussed in Chapter 3, section 3.2.2) and second, the effect of bubble entrapment during preparation, which could not be removed under vacuum. At low shear, bubbles can significantly increase suspension viscosity (Ducloué et al., 2015) acting as rigid particles. However, at increasing shear the soft bubbles can either break or elongate towards the direction of the applied flow field, which can lead to a reduction in the viscosity and thus, shear thinning rheology.

The shear stress (τ) of all suspensions in the Xanthan gum solution is illustrated in Figure 5.9a, c and e and the values increase both with shear rate ($\dot{\gamma}$) and particle volume fraction (φ). Yield stress behaviour, i.e. the shear stress reaching a plateau value at $\dot{\gamma}_{\to 0}$, is only observed for the highly concentrated abrasive silica suspensions (Figure 5.9c) at $\varphi = 0.25$ and 0.30; this behaviour probably arises from the frictional contacts between these particles and is also observed in the Newtonian water/glycerol mixture (1/9) (Figure 5.9d). In contrast, the glass sphere (Figure 5.9b) and filler silica (Figure 5.9f) suspensions show more pronounced yield stress behaviour in the Newtonian water/glycerol (1/9) mixture rather than when suspended in the Xanthan gum solution (Figure 5.9a and e respectively).

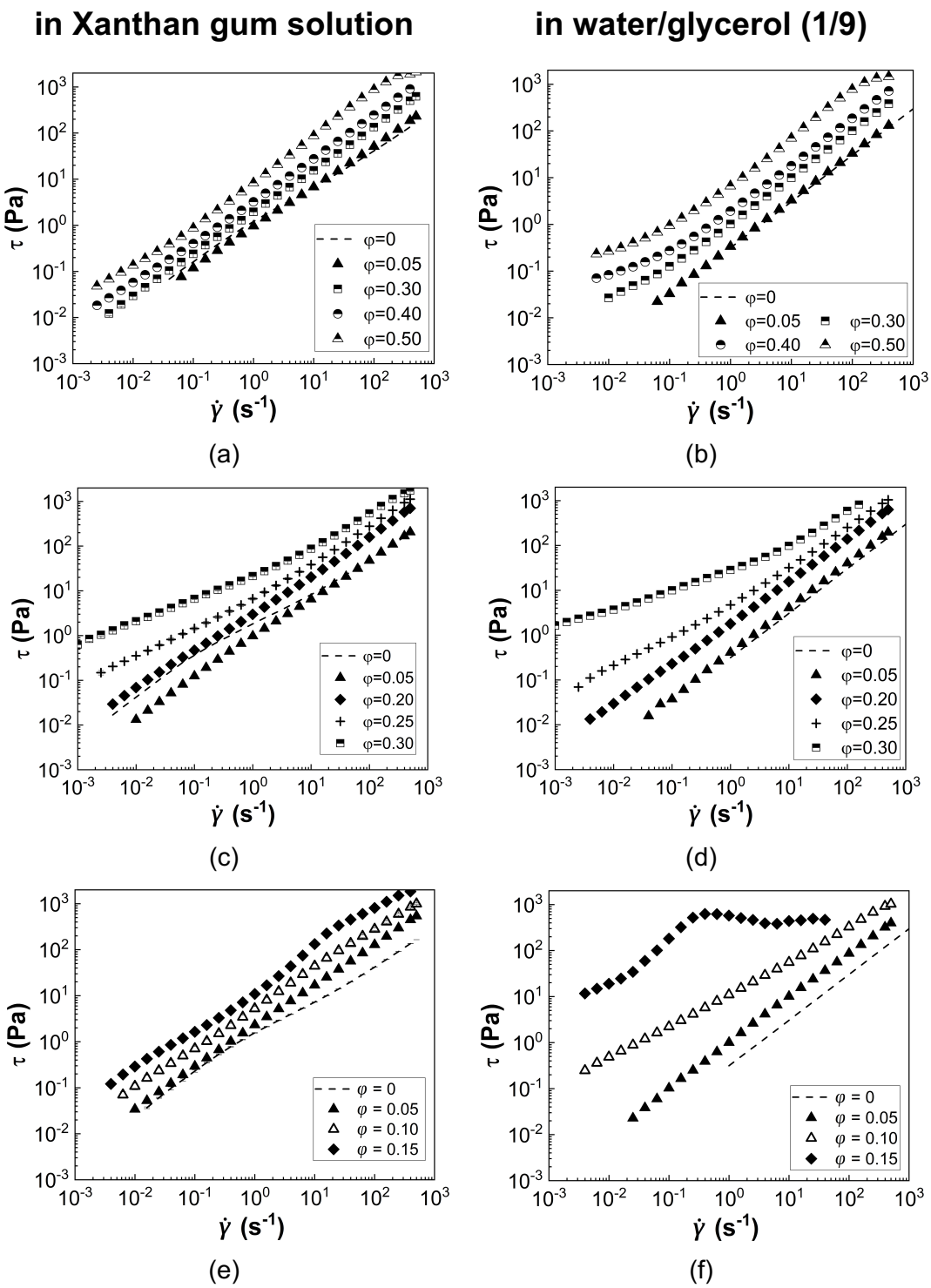

Figure 5.9: Shear stress (τ) of selected suspensions in the 0.1% wt. Xanthan gum solution in water glycerol (1/9) (left column) as a function of shear rate ($\dot{\gamma}$) at 20°C. The corresponding data in the Newtonian water/glycerol (1/9) mixture are presented (left column) for comparison. Dashed lines correspond to the Carreau fittings to the shear thinning curves. a) and b) glass spheres; c) and d) abrasive silicas; e) and f) filler silicas.

As also described in Chapter 3, glycerol is able to inhibit interparticle interactions through the formation of a thick solvation layer. A similar behaviour is expected to occur with the water/glycerol mixture since both solvents can bind on the silica surface through their hydroxyl groups (-OH). However, water molecules can offer only one -OH group compared to glycerol, which has three, and thus, a thinner solvation layer is expected in that case (Amiri et al., 2012; Gao et al., 2017). These conditions favour particle-particle interactions, which can induce yield stress behaviour and more pronounced non-Newtonian rheology in the corresponding suspensions. However, the Xanthan gum molecules seem to compete with particle contacts reducing their effectiveness, by strengthening the lubrication effect of the solvation layer, which results in suppressing the yield stress response under steady state.

Figure 5.10 plots the relative viscosity of all suspensions in the Xanthan gum solution at zero ($\eta_{r,0}$) (Figure 5.10a) and infinite ($\eta_{r,\infty}$) (Figure 5.10a) shear rates. The relative viscosity values are estimated using the $\eta_{r,\infty}$ of the Xanthan gum solution, which is close to that of the pure water/glycerol (1/9) solvent; this is thought to facilitate a better comparison against the values of the corresponding suspensions in the pure water/glycerol (1/9) mixture.

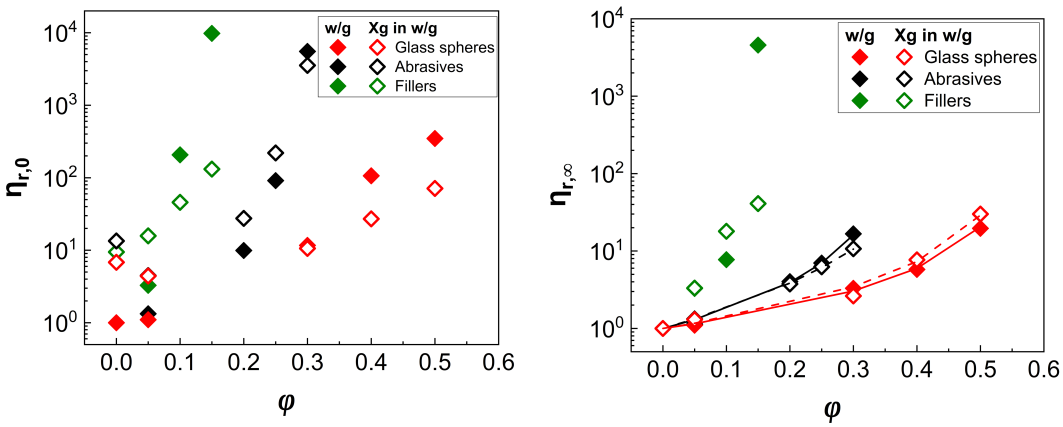

Figure 5.10: a) Zero shear rate ($\eta_{r,0}$) and b) infinite shear rate ($\eta_{r,\infty}$) relative viscosity values as a function of φ for all suspensions at 20°C. Continuous and dashed lines in (b) correspond to the Krieger-Dougherty fittings of the glass sphere and abrasive silica suspensions. The data of the filler silicas could not be described with the Krieger-Dougherty equation.

Interestingly, the addition of Xanthan gum to the suspension reduces the zero shear rate viscosity values of both the glass sphere and filler silica suspensions but increases those for the abrasive silica suspensions, in comparison to the suspensions in the equivalent Newtonian solvent. This is surprising as the presence of polymers in addition to the solid particles is expected to thicken the suspension; this effect should

also increase with particle porosity as the pores absorb part of the solvent increasing the effective volume fraction of both the particles and the polymer in the suspension. However, it seems that the Xanthan gum molecules strengthen the effectiveness of the solvation layer around the particles making them repel each other.

In contrast to the behaviour of the suspensions at low shear, the $\eta_{r,\infty}$ values (Figure 5.10b) of the suspensions are only weakly affected by the addition of Xanthan gum for almost all φ, independent of particle type. The data obtained for the glass sphere and abrasive silicas are well described by the Krieger-Dougherty equation and the estimated intrinsic viscosities (B) and maximum packing fractions (φ_m) obtained through the fittings are presented in Table 5.4. Neither the Krieger-Dougherty nor the Quemada models could fit the data of the filler silicas in both the Xanthan gum solution and the corresponding Newtonian solvent and thus, estimates of B and φ_m are not included in Table 5.4.

It can be seen that the addition of Xanthan gum increases the intrinsic viscosity of both the glass sphere and abrasive silica suspensions. The intrinsic viscosity is an inherent material property indicative of the degree of the solutes' contribution to the viscosity of the overall mixture. Therefore, in the presence of Xanthan gum, polymer-polymer and polymer-particle interactions contribute to the interparticle interactions leading to an increase in the B values. The φ_m values of the abrasive silica suspensions also increase in the polymer solution highlighting the effect of Xanthan gum on keeping the particles separate and enabling higher loading capacities before jamming occurs. It should be noted that similar to polyacrylamide, the Xanthan gum molecules can also bind on the silica surface though hydrogen bonding favouring particle repulsion.

Table 5.4: Intrinsic viscosity (B) and maximum particle packing (φ_m) obtained from the Krieger-Dougherty fittings to the glass sphere and abrasive silica suspensions $\eta_{r,\infty}$ data in Figure 5.10b. Neither the Krieger-Dougherty nor the Quemada models could fit the data of the filler silicas and thus, they are not presented in the table.

Solvents	**water/glycerol**		**Xanthan gum in water/glycerol**	
Particle type	$\boldsymbol{B}$	$\boldsymbol{\varphi_m}$	$\boldsymbol{B}$	$\boldsymbol{\varphi_m}$
Glass spheres	2.60	0.58	2.90	0.58
Abrasive silicas	4.90	0.39	5.40	0.54

The extent of shear thinning ($\eta_{r,e}$, eq. (3.12)) estimated from the flow curves of the suspensions in the Xanthan gum solution (Figure 5.8) is presented in Figure 5.11a, while the estimated $\eta_{r,t}$ (eq. (3.13)) values representing shear thickening are shown

in Figure 5.11b as a function of particle volume fraction (φ). The data for the corresponding suspensions in the Newtonian water/glycerol (1/9) mixture are also included for comparison.

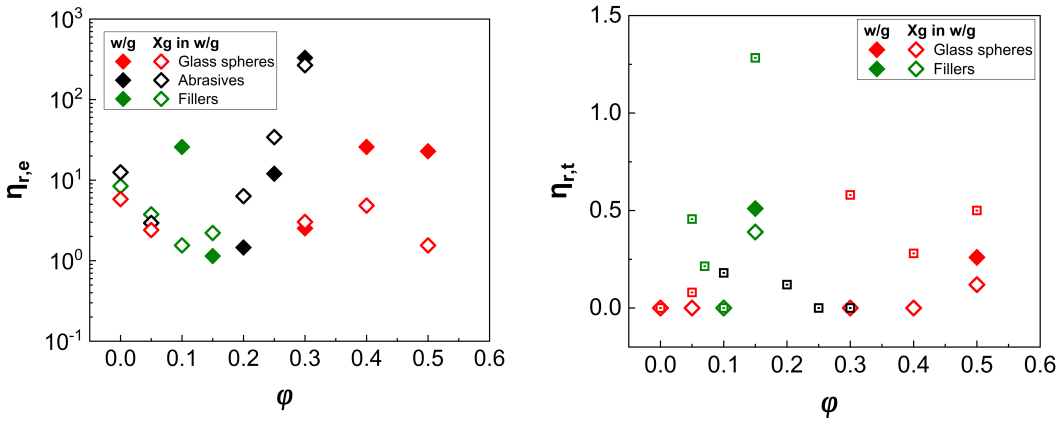

Figure 5.11: Extent of a) shear thinning ($\eta_{r,e}$) and b) shear thickening ($\eta_{r,t}$) as a function of φ for all suspensions in the Xanthan gum solution at 20°C. The data for the corresponding suspensions in the Newtonian water/glycerol (1/9) mixture are included for comparison along with the estimated $\eta_{r,t}$ for the Boger fluid.

Increasing the particle volume fraction generally enhances the non-Newtonian phenomena in suspension rheology, either shear thinning or shear thickening, regardless of particle type; this behaviour is observed in both the shear thinning suspending medium and the pure Newtonian base fluid. The addition of Xanthan gum leads to a reduction in the shear thinning (Figure 5.11a) response of the highly concentrated glass sphere suspensions compared to that in water/glycerol (1/9), possibly due to additional constraints on particle contacts compared to the ones caused by the solvation layer in the absence of polymer. The abrasive silicas exhibit a strong shear thinning response in the Xanthan gum solution, similar to that observed in the Newtonian base fluid, especially at $\varphi = 0.25$ and $\varphi = 0.30$, and thus this behaviour can be related to the frictional contracts between the rough abrasive silicas. In contrast, at lower φ ($\varphi \leq 0.20$), the $\eta_{r,e}$ of the suspensions increase in the presence of Xanthan gum; it is likely that this behaviour mainly originates from the shear thinning nature of the suspending medium as these suspensions showed no or negligible shear thinning in the Newtonian solvent. Interestingly, the shear thinning response of the filler silica suspensions decreases with increasing φ giving rise to shear thickening.

Overall, the addition of particles of any type seems to negatively influence the shear thinning response of the Xanthan gum solution (Figure 5.11a), especially at

dilute volume fractions ($\varphi = 0.05$), by decreasing its $\eta_{r,e}$ values. It is likely that the complete uncoiling of the Xanthan gum molecules under shear is partially prevented in the near vicinity of particles, leading to a reduction in its shear thinning response.

The shear thickening response of the glass sphere and filler silica suspensions observed in the water/glycerol mixture is also suppressed in the presence of Xanthan gum as indicated by a decrease in the $\eta_{r,t}$ values (Figure 5.11b). The latter might be due to the Xanthan gum chains interfering with particle-particle contacts at high shear inhibiting hydrocluster formation or the frictional contacts. The $\eta_{r,t}$ values estimated in the case of the Boger fluid are also included for comparison in Figure 5.11b. It can be seen that the suspensions in the Xanthan gum solution show much lower $\eta_{r,t}$ values, i.e. weaker shear thickening response, compared to that induced by the Boger fluid; this indicates that the shear thinning nature of the suspending medium might decrease the elastic thickening observed in the latter. Although, the Xanthan gum solution shows some elasticity with elastic numbers in the order of $El{\sim}10^3$, this is one order of magnitude lower than that estimated for the Boger fluid, thus, making it difficult to decouple the effects of elasticity and shear thinning on suspension shear thickening.

5.3.2 Oscillatory shear rheology

The effect of Xanthan gum viscoelasticity on suspension rheology is investigated through oscillatory frequency sweeps in the linear viscoelastic region (LVR, $\gamma = 0.1\%$). The measured storage (G') and loss (G'') moduli are presented in Figure 5.12 as a function of angular frequency (ω) at 20°C and varying particle volume fractions (φ). The data obtained for the same suspensions in the Newtonian water/glycerol (1/9) mixture are also included for comparison.

The storage and loss modulus of the suspensions in the Xanthan gum solution increase with increasing the angular frequency (ω) and particle volume fraction (φ) (Figure 5.12a, c and e). All suspensions show viscous dominated ($G' < G''$) response in the LVR in agreement to the behaviour of the suspending medium ($\varphi = 0$). An exception is the highly concentrated abrasive silica suspension at $\varphi = 0.30$ (Figure 5.12c), where the values of G' and G'' overlap for a wide range of angular frequencies. The latter indicates a broad range of relaxation times (Aliabadian et al., 2018; Marcovich et al., 2004) possibly originating from the competition between the interparticle interactions and the inhibition of those due to the presence of the solvation layer including polymer molecules.

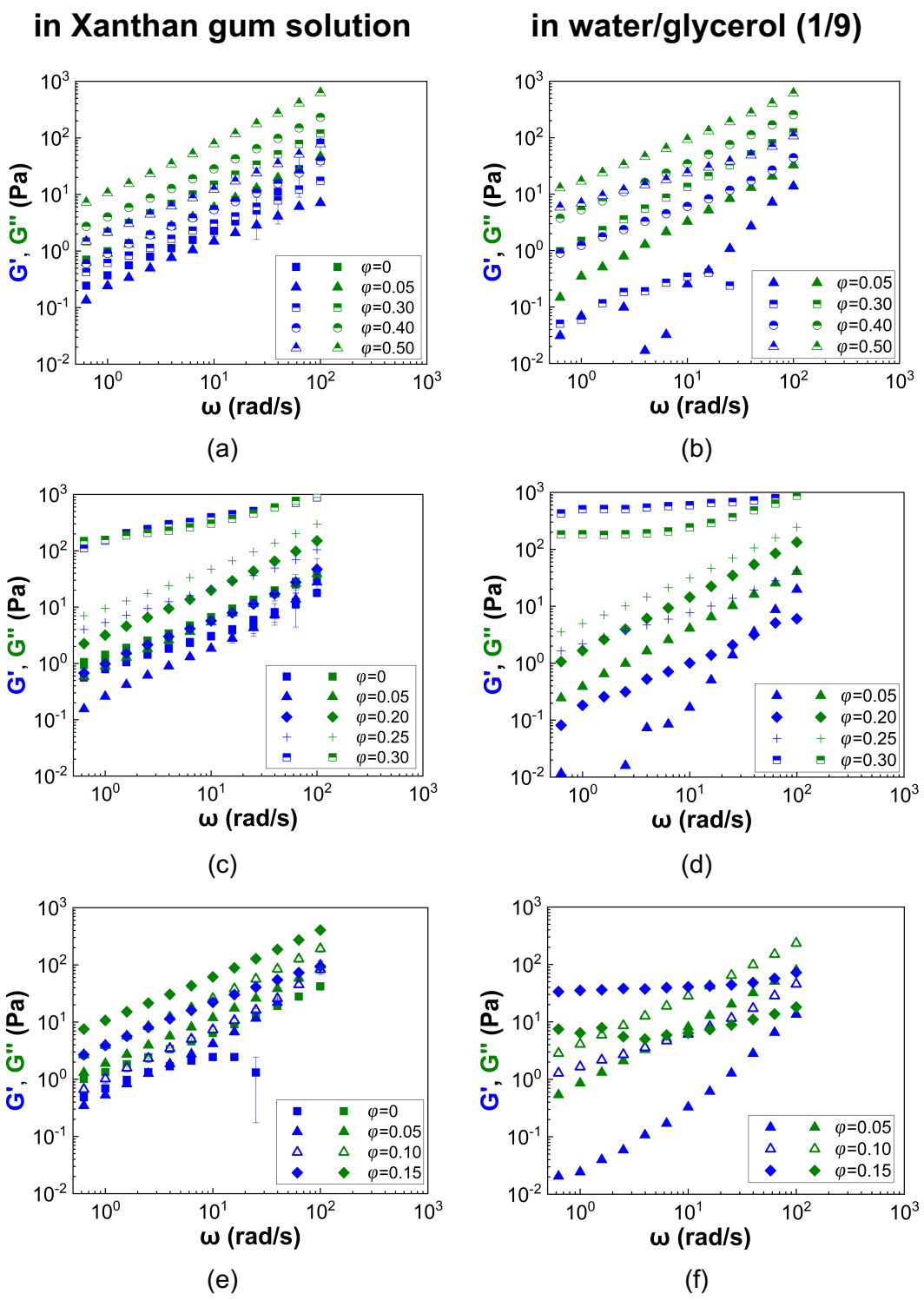

Figure 5.12: Viscoelastic moduli (storage, G' & loss, G'') of the three types of suspensions in the Xanthan gum solution in water/glycerol (1/9) (left column) as a function of particle volume fraction (φ) and angular frequency (ω). The measurements were conducted at 20°C and $\gamma = 0.1\%$. The corresponding data of the suspensions in the pure water/glycerol mixture (1/9) are included for comparison. a) and b) glass spheres; c) and d) abrasive silicas; e) and f) filler silicas.

The addition of Xanthan gum appears to strengthen the lubrication effect of the solvation layer and to suppress the elastic dominated response of these suspensions, as indicated by a decrease of the G' values below the G'' (Figure 5.12c and e) compared to the suspensions in the pure Newtonian solvent. The latter exhibit strongly viscous dominated response. An exception is the abrasive silica suspension at $\varphi = 0.30$ (Figure 5.12d) and the filler silicas at $\varphi = 0.15$ (Figure 5.12f), which show strong solid-like behaviour ($G' > G''$) for the whole range of ω values investigated. This behaviour is likely to arise from frictional contacts between the rough silicas, enabled due to the thinner solvation layer formed by the water/glycerol solution but also from the high effective particle volume fractions as the pores absorb a fraction of the solvent.

The viscoelasticity of the shear thinning Xanthan gum solution ($\varphi = 0$) and the corresponding particle suspensions is further evaluated by comparing the measured phase angles (δ). The δ values of all suspensions in the Xanthan gum solution are presented in Figure 5.13 alongside those of the suspensions in the pure water/glycerol (1/9) mixture. It can be seen that the addition of particles of any type, i.e. glass spheres, abrasive silicas, filler silicas, in the Xanthan gum solution decreases the viscoelastic response of the shear thinning solvent as described by an increase in its δ values (Figure 5.13a, c and e). Interestingly, the phase angles of the glass sphere (Figure 5.13a) and filler silica suspensions (Figure 5.13e) remain almost independent of φ, while those for the abrasive silicas (Figure 5.13c) increase with φ from $\delta \approx 60^o$ at $\varphi = 0$ to $\delta \approx 80^o$ at $\varphi = 0.30$. In contrast, the viscoelasticity of the suspensions in the water/glycerol (1/9) solution increases with φ, moving towards the elastic dominated region, which results in a gradual reduction of the phase angles to values $\delta < 20^o$ (Figure 5.13b, d and f). This behaviour agrees with the increased interparticle frictional contacts enabled through the disruption of the formed solvation layer, which are favoured with increasing φ.

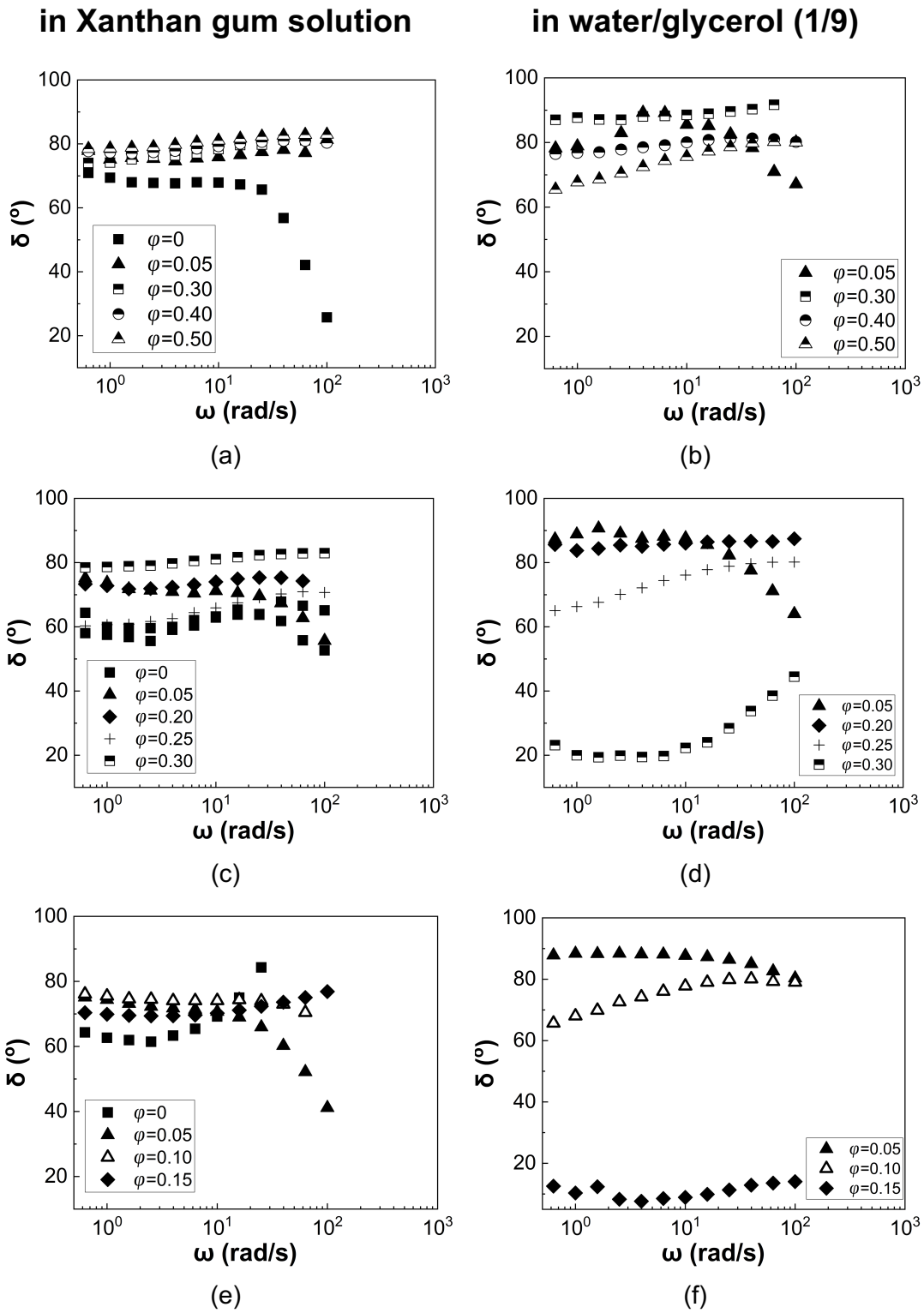

Figure 5.13: Phase angles (δ) of the three types of suspensions in the Xanthan gum solution in water/glycerol (1/9) (left column) as a function of particle volume fraction (φ) and angular frequency (ω). The measurements were conducted at 20°C and $\gamma = 0.1\%$. The corresponding data of the suspensions in the pure water/glycerol mixture (1/9) are included for comparison. a) and b) glass spheres; c) and d) abrasive silicas; e) and f) filler silicas.

It should be noted that microstructure data were not collected for all the suspensions in the Xanthan gum solutions. The high particle volume fractions used rendered the visualization of the suspensions under the optical shearing unfeasible. Large Amplitude Oscillatory Shear (LAOS) measurements were conducted only for selected suspensions due to their strongly viscous dominated response and the obtained data are presented in Appendix II. These data are presented overall in Appendix since no significant differences were observed in the presence of Xanthan gum compared to the rheology of the suspensions in pure glycerol.

5.4 Effect of temperature

In this section, the rheological properties of the selected suspensions will be presented at 60°C, under steady state and oscillatory shear extending the work presented in Chapter 3. The suspensions in the Boger fluid will be presented first followed by the Xanthan gum ones. The measured rheology at the elevated temperature will be compared between the different types of particles but also with the corresponding data at 20°C.

5.4.1 Suspensions in the Boger fluid

The rheological properties of the Boger fluid at 60°C, i.e. steady state viscosity and viscoelastic moduli are presented in Figure 5.14a and b respectively. The viscosity remains constant at a value of $\eta = 0.09\ Pa.s$ (Figure 5.14a) for the whole range of shear rates investigated, which is one order of magnitude lower than that at 20°C. The crossover point between the G' and G'' after subtracting the solvent viscosity from the G'' values is observed at an angular frequency of $\omega = 63\ rad/sec$ (Figure 5.14b) resulting in an elastic relaxation time of $0.1\ s$. The relaxation time and the estimated elastic number for the Boger fluid at 60°C are also summarised in Table 5.5. It can be seen that increasing the temperature significantly decreases the relaxation time and subsequently the elasticity of the polymer solution by an order of magnitude compared to 20°C, where an elastic number of El = 39·10^4 was observed. Experimental evidence has shown a slight increase in the toughness followed by a decrease of the compressibility of the polyacrylamide chains at high temperatures of ~ 60°C (Evingür and Pekcan, 2018).

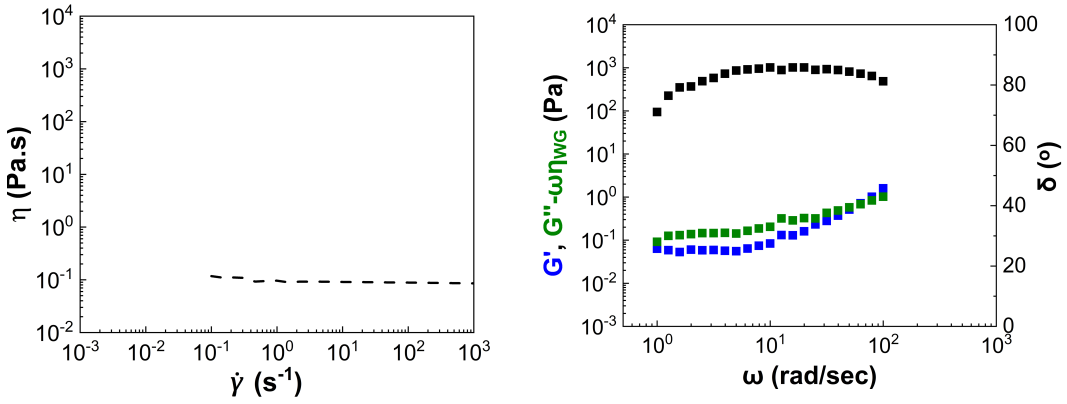

(a) (b)

Figure 5.14: a) Steady state viscosity of the Boger fluid at 60ºC as a function of shear rate ($\dot{\gamma}$); b) viscoelastic moduli (storage, G', loss, G'', modulus) and phase angles (δ) of the Boger fluid at 60ºC and $\gamma = 0.1\%$ as a function of angular frequency. The contribution of the base fluid viscosity (water/glycerol) has been subtracted from the G'' values to isolate the effect of the polymer.

Table 5.5: Elastic relaxation time (t_e) estimated from the crossover point in the frequency sweep and elastic number (El) of the Boger fluid at 60ºC. The values in brackets refer to the data estimated for the Boger fluid at 20ºC.

Boger fluid at 60°C	
t_e (s)	0.10 (1.25)
El	$36 \cdot 10^3$ ($39 \cdot 10^4$)

5.4.1.1 Steady state shear rheology

Figure 5.15 illustrates the viscosity (η) of the three types of particle suspensions in the Boger fluid, i.e. glass spheres, abrasive silicas and filler silicas, under steady state and at 60ºC. The viscosity versus shear rate curves of the same suspensions at 20ºC are also included as insets (Figure 5.15a, c and e) to ease the comparison between the two temperatures, while the dashed lines in the viscosity curves correspond to the Carreau fittings.

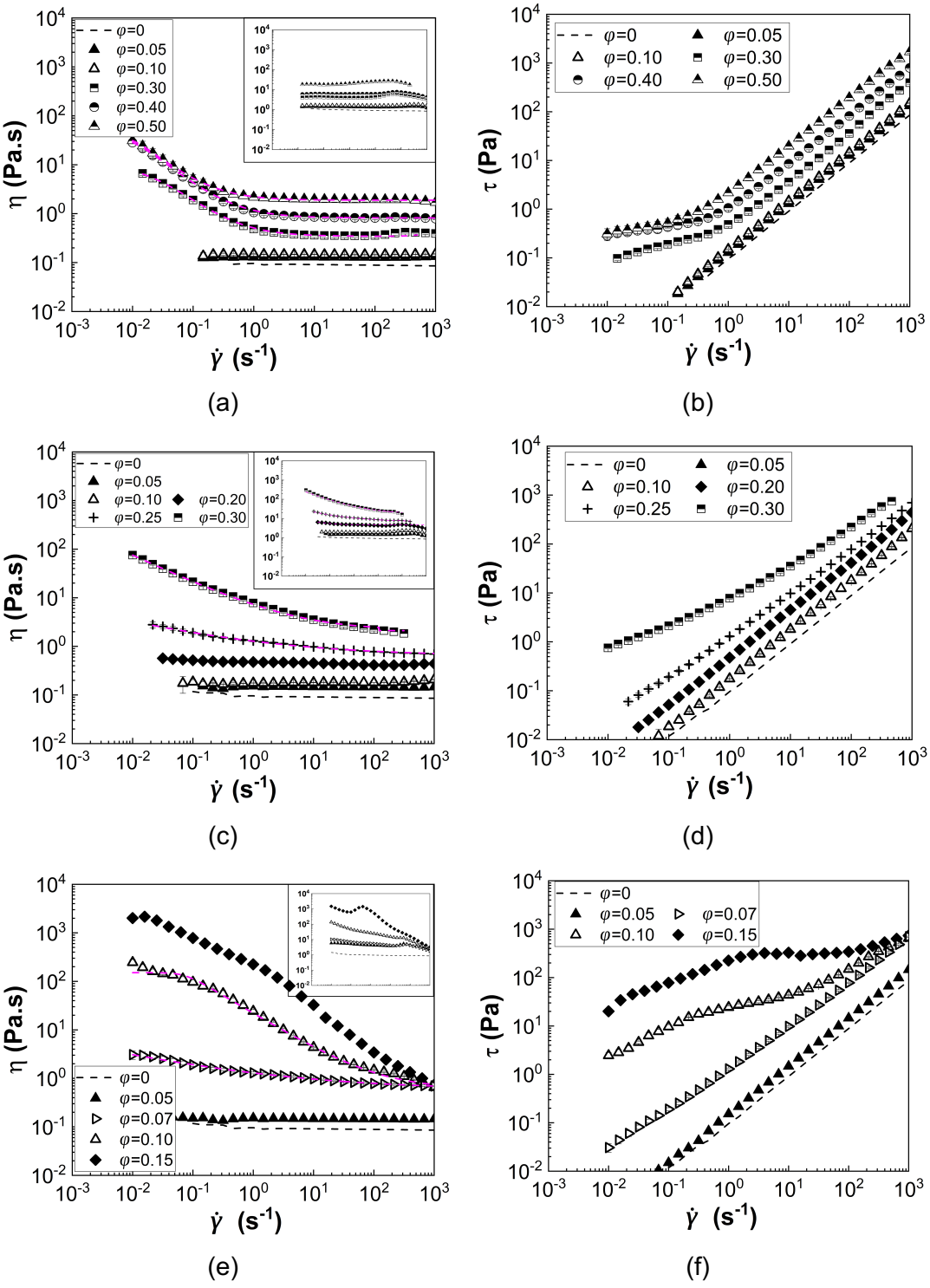

Figure 5.15: Viscosity (η) (left column) and shear stress (τ) (right column) values of selected suspensions in the Boger fluid at 60°C as a function of shear rate ($\dot{\gamma}$) and particle volume fraction (φ). The dashed lines in (a) represent the Carreau fittings. The insets in the viscosity plots represent the corresponding data at 20°C. a) and b) glass spheres; c) and d) abrasive silicas; e) and f) filler silicas.

The glass sphere suspensions (Figure 5.15a) exhibit Newtonian behaviour at the dilute regime, $\varphi \leq 0.10$, followed by yield stress (Figure 5.15b) and shear thinning

(Figure 5.15a) rheology at higher particle volume fractions ($\varphi \geq 0.30$). This behaviour is in agreement with the observations in pure glycerol attributed to a decrease in the thickness of the solvation layer due to a decrease in the viscosity of the water/glycerol mixture enabling interparticle contacts at low shear (Gao et al., 2017). The abrasive silica suspensions show (Figure 5.15c) similar shear thinning and yield stress behaviour (Figure 5.15d) at the higher particle volume fractions of $\varphi = 0.25$ and 0.30 to 20°C, while Newtonian behaviour is observed at $\varphi \leq 0.20$. Pronounced shear thinning is also observed for the filler silica suspensions at a lower particle volume fraction ($\varphi = 0.07$) (Figure 5.15e) compared to the response of the same suspensions under steady state at 20°C. High values of yield stress and jamming can also be observed for the filler silica suspensions at $\varphi = 0.10$ and 0.15, as the shear stress values reach a plateau at $\dot{\gamma}_{\to 0}$ (Figure 5.15f).

Unlike the shear thinning behaviour, which seems to be enhanced by increasing the temperature to 60°C, the opposite trend is observed for the shear thickening response, which is significantly reduced at 60°C. As discussed in section 5.2.1, the shear thickening in suspensions of particles in Boger fluids arises from the extensional thickening of the polymer chains under the effect of elongational stresses. Heating the suspensions to 60°C increases the toughness (i.e. decreases possibly the flexibility) of the polymer chains, reducing the relaxation time-scale and elastic number, thus higher stresses might be required to achieve the same degree of shear thickening as that obtained at lower temperatures.

The zero shear rate ($\eta_{r,0}$) and the infinite shear rate ($\eta_{r,\infty}$) relative viscosities of all suspensions in the Boger fluid at 60°C are illustrated in Figure 5.16a and b as a function of particle volume fraction (φ) in comparison to the data in pure glycerol; the corresponding data for the suspensions in the Boger fluid and pure glycerol at 20°C are also included as grey points, using the same symbols of each particle type for comparison. Increasing the particle surface roughness and porosity leads to an increase in the relative viscosity of the suspensions at both low and high shear rates, in agreement with the observations of the suspensions in pure glycerol and the data obtained at 20°C (section 5.2.1). The addition of 200 ppm of polyacrylamide in the suspension also thickens the suspensions, especially at low shear (Figure 5.16a), as indicated by the higher $\eta_{r,0}$ values compared to glycerol. On the contrary, at the high shear rate regime neither the presence of polyacrylamide nor the heating of the suspensions leads to significant variations in the relative viscosity values (Figure 5.16b).

The Krieger-Dougherty equation (eq. (2.9)) describes sufficiently well the $\eta_{r,\infty}$ values of the glass sphere and the abrasive silica suspensions in the Boger fluid, while it fails to predict those of the filler silica suspensions. The estimated variables from the fitting, i.e. the intrinsic viscosity (B) and the maximum packing fraction (φ_m), are presented in Table 5.6 alongside the corresponding variables of the suspensions in glycerol. The suspensions in the Boger fluid exhibit higher B and φ_m values compared to the inelastic Newtonian solvent. More importantly, the glass sphere suspensions in the Boger fluid show an unexpectedly high value of the maximum packing, $\varphi_m = 0.83$, even higher than the maximum reported value of $\varphi_m = 0.75$ for polydisperse systems. This might be related to the high polydispersity of these particles but also the effectiveness of the long polyacrylamide chains in keeping the particles well dispersed in the Boger fluid.

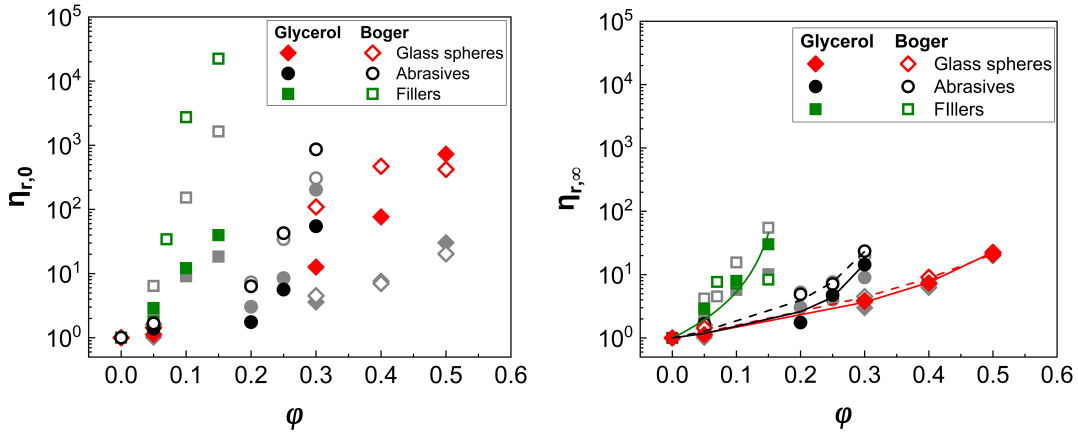

Figure 5.16: a) Zero ($\eta_{r,0}$) and infinite shear rate ($\eta_{r,\infty}$) relative viscosity of all the suspensions in the Boger fluid at 60°C as a function of particle volume fraction (φ). Continuous and dashed lines represent the Krieger-Dougherty fittings to the glass sphere and abrasive silica suspensions, while the filler silica suspensions were fitted with the Quemada equation. Comparisons with the corresponding data in the pure glycerol are included as closed colored points and the data obtained at 20°C are also included as grey points.

Table 5.6: Intrinsic viscosity (B) and maximum particle packing (φ_m) obtained from the Krieger-Dougherty fittings to the glass sphere and abrasive silica suspensions $\eta_{r,\infty}$ data in Figure 5.16b. The data of the filler silicas were fitted with the Quemada equation and thus, only the φ_m values are reported.

Solvents / **Particle type**	**glycerol**		**Boger fluid**	
	B	φ_m	B	φ_m
Glass spheres	3.21	0.64	3.98	0.83
Abrasive silicas	3.04	0.32	4.62	0.35
Filler silicas	-	0.24	-	-

Figure 5.17 illustrates the estimated $\eta_{r,e}$ and $\eta_{r,t}$ of all the suspensions in the Boger fluid as a function of the particle volume fraction. Comparisons with the corresponding data in pure glycerol and at 20°C are also included in the figures. It can be clearly seen that heating the suspension increases the shear thinning response of the glass sphere and filler silicas in the Boger fluid, while it weakly affects the abrasive silica suspensions (Figure 5.17a). More pronounced shear thinning rheology is also observed for all suspensions in the Boger compared to the corresponding suspensions in the pure glycerol at 60°C. Unlike the shear thinning response, increasing the temperature significantly suppresses or even eliminates the shear thickening response of the suspensions as indicated by a decrease in the $\eta_{r,t}$. The abrasive silicas are excluded from Figure 5.17b, since no shear thickening response is observed for these suspensions.

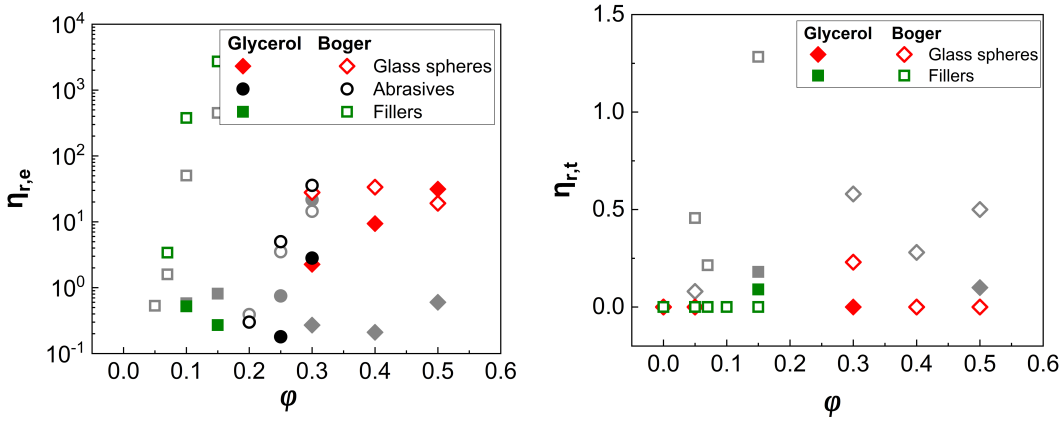

Figure 5.17: Extent of a) shear thinning ($\eta_{r,e}$) and b) shear thickening ($\eta_{r,t}$) of all the suspensions at 60°C as a function of particle volume fraction (φ). Grey points correspond to the values estimated for the same suspensions at 20°C in the two solvents, i.e. the Newtonian glycerol and the elastic Boger fluid. The $\eta_{r,t}$ values of the abrasive silica suspensions are omitted due to these suspensions exhibiting no shear thickening at 60°C.

As discussed in Chapter 3, Brownian effects are likely to affect the rheology of the suspensions due to particle polydispersity and in particular enhance their shear thinning response. The ratio of the particles able to induce such effects to the total number of particles was calculated at the lowest shear rate used ($\dot{\gamma} = 0.01\ s^{-1}$) in this case based on the particle size distributions and assuming $Pe = 10$. The critical particle size was $D = 1.2\ \mu m$ at 20°C and $D = 2.8\ \mu m$ at 60°C. It can be seen in Table 5.7 that the estimated % percentage of the particles in the colloidal regime is very low

almost negligible at 20°C, especially in the case of the abrasive and filler silica suspensions and thus, this was not discussed in section 5.2.1. A slight increase in the Brownian effects is observed at the higher temperature of 60°C, with the ratio being ~10% for the glass spheres and ~6% for the abrasive silicas. The increase in the shear thinning response of the suspensions at 60°C compared to the lower temperature can thus, be partially attributed to Brownian effects in addition to the disruption of the solvation layer enabling interparticle contacts. A reduction in the frictional contact time between the particles at 60°C might comprise another explanation for the decrease in suspension shear thinning compared to 20°C.

Table 5.7: Percentage (%) of the particles able to induce Brownian effects for all suspensions in the Boger fluid at 60°C in comparison to 20°C at $\dot{\gamma} = 0.01\ s^{-1}$, i.e. the lowest shear rate reached.

Particle type	20°C	60°C
Glass spheres	3.8	9.5
Abrasive silicas	0.4	5.7
Filler silicas	0.01	0.9

5.4.1.2 Oscillatory shear in the LVR

Figure 5.18 illustrates the viscoelastic moduli (storage modulus, G' and loss modulus, G'') and phases angles (δ) of all suspensions in the Boger fluid as a function of angular frequency, ω at 60°C; the data have been obtained from oscillatory shear frequency sweeps in the LVR. The δ values of the same suspensions at 20°C are included for comparison. The glass sphere suspensions mainly exhibit viscous dominated response at 60°C (Figure 5.18a) with G' showing lower values compared to G''. However, in contrast to 20°C, an increase in suspension viscoelasticity is observed at 60°C which depends both on φ and ω values. In particular, the phase angles (Figure 5.18b) decrease with increasing φ, especially at $\omega < 10\ rad/s$. This behaviour ca be attributed to the interparticle contacts enabled for the glass spheres at 60°C due to the decrease in the lubrication effect of the solvation layer, which also lead to shear thinning and yield stress behaviour under steady state shear.

Increasing the temperature does not significantly alter the rheology of the abrasive silica suspensions in the LVR (Figure 5.18c). The phase angles (Figure 5.18d) drop just below 80° for the suspensions at $\varphi = 0.25$, indicating a weak increase in viscoelasticity at the elevated temperature in agreement with the shear thinning response of this suspension under steady state. On the other hand, the obtained viscoelasticity for the suspension at $\varphi = 0.30$ is almost identical in the two

temperatures. In this case, interparticle frictional contacts already exist at 20°C and these are independent of temperature and the viscosity of the suspending medium.

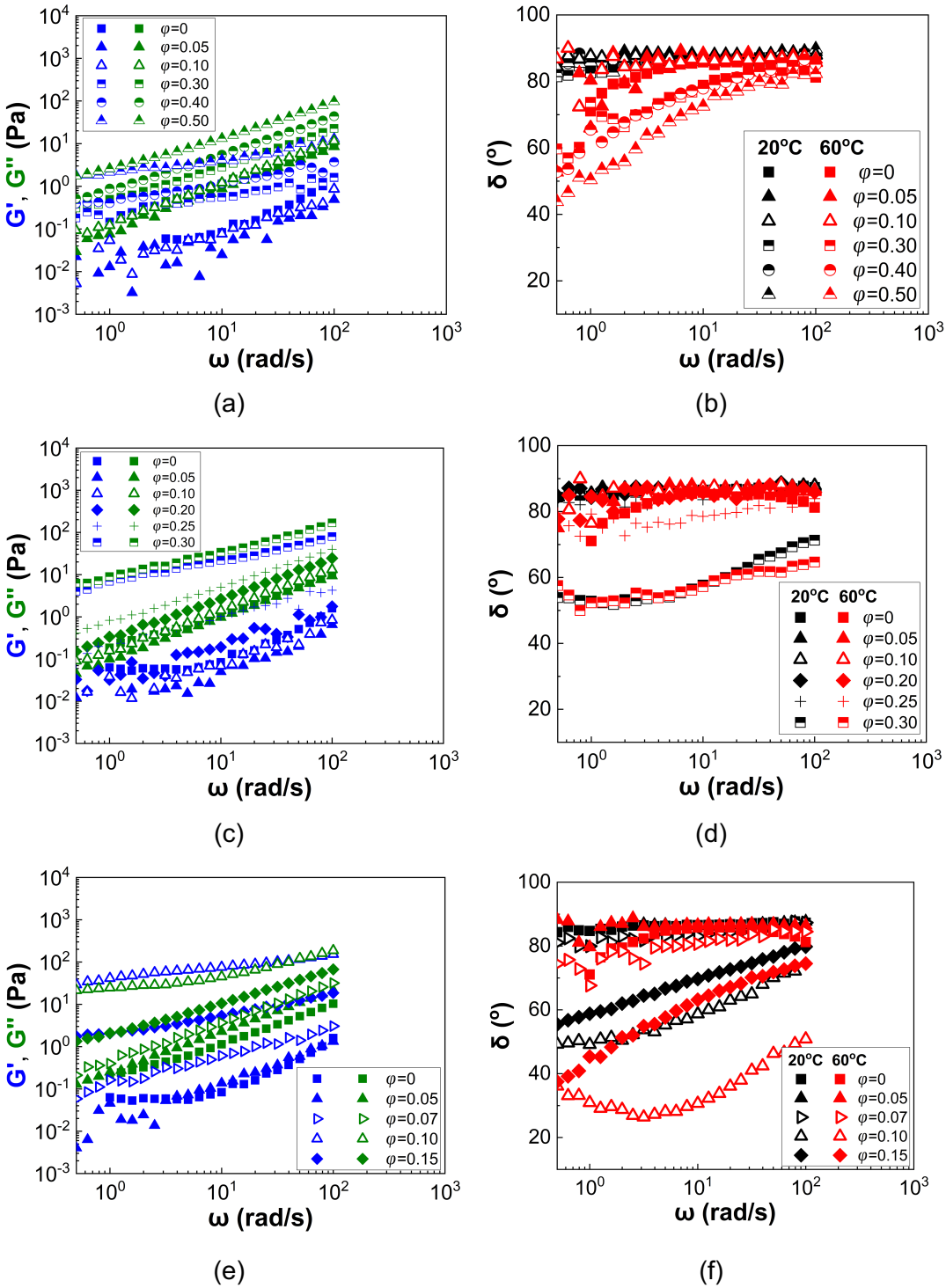

Figure 5.18: Viscoelastic moduli (G', G'') (left column) and phase angles (δ) (right column) of the selected suspensions in the Boger fluid as a function of angular frequency (ω) and particle volume fraction at 60°C (red points). The phase angles of the corresponding suspensions at 20°C are also included as black points for comparison. a) and b) glass spheres; c) and d) abrasive silicas; e) and f) filler silicas.

The filler silica suspensions exhibit rich viscoelastic phenomena at 60°C especially for the higher particle volume fractions of $\varphi = 0.10$ and 0.15. At the lower particle volume fractions ($\varphi \leq 0.07$), the suspensions are viscous dominated as $G' < G''$ (Figure 5.18e), while at higher φ they exhibit solid-like response at low ω, followed by a transition to a liquid-like response, i.e. $G' < G''$. Interestingly, the sample at $\varphi = 0.10$ shows a more pronounced viscoelasticity (Figure 5.18f) compared to that of $\varphi = 0.15$ indicated by lower δ values. It should be recalled that the same relation between the viscoelastic moduli of these two suspensions was also observed at 20°C. This behaviour might be attributed to the competitive interaction between the particles and the polymer dynamics.

5.4.2 Suspensions in Xanthan gum

The steady state viscosity and viscoelastic moduli of the Xanthan gum solutions at 60°C are presented in Figure 5.19a and b respectively. Although deviations of the viscosity values for the different Xanthan gum solutions were observed at 20°C (Figure 5.7a), these seem to significantly diminish at 60°C (Figure 5.19a) as the data of all solutions in the water/glycerol or pure glycerol solvents reduce to the respective viscosity of the base fluid, especially at higher shear rates ($\dot{\gamma}$).

An ordered-disordered transition of the Xanthan gum molecules has been reported in the literature at temperatures 50°C-60°C (Rochefort and Middleman, 1987). In other words, high temperatures disrupt the intermolecular structure of the Xanthan gum molecule leading to more single chains in solution independently of the shearing history applied during sample preparation. This further leads to a reduction in the shear thinning degree of the Xanthan gum solution at 60°C compared to 20°C and lower deviations between the different samples since the Xanthan gum concentration is kept constant. The elastic time scales estimated from the crossover point of the two moduli in the frequency sweep (after subtracting the solvent viscosity from the G'' values) (Figure 5.19b), and the corresponding elastic numbers (El) of all Xanthan gum solutions are summarized in Table 5.8. It can be seen that the temperature induced change in the structural conformation of the Xanthan gum molecules leads to a decrease in the El numbers of the solutions compared to those at 20°C (Table 5.3) and thus, a reduction in polymer elasticity.

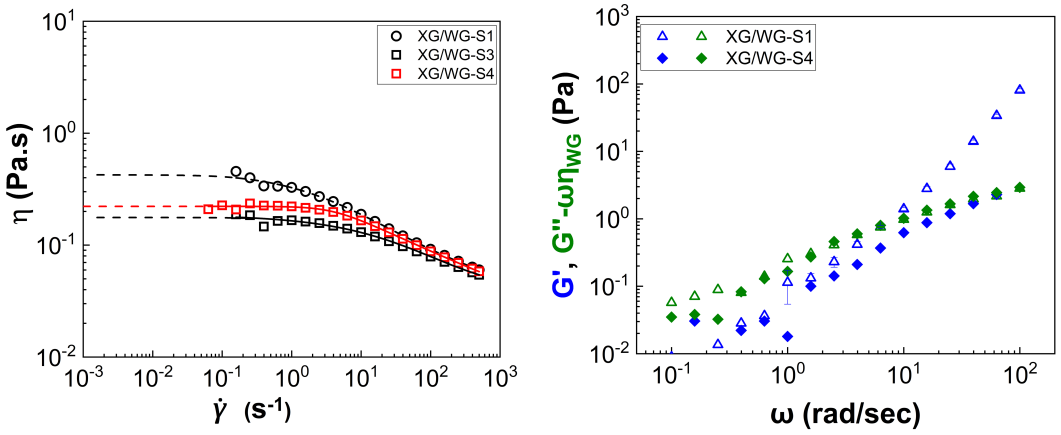

(a) (b)

Figure 5.19: a) Viscosity (η) values as a function of shear rate ($\dot{\gamma}$) for all the Xanthan gum (XG) solutions in glycerol and in water/glycerol at 60°C; b) viscoelastic moduli (storage, G', loss, G'', modulus) of all Xanthan gum solutions at 60°C and $\gamma = 0.1\%$ as a function of angular frequency. The contribution of the base fluid viscosity (pure glycerol or water/glycerol) has been subtracted from the G'' values to isolate the effect of the polymer.

Table 5.8: Elastic relaxation times (t_e) estimated from the crossover point in the frequency sweep and elastic number (El) of all Xanthan gum solutions at 60°C. (n/a indicates that no crossover point was observed in the frequency sweeps of these fluids). The fields highlighted with grey refer to the fluids used.

No.	Solvents	t_e (s)	El
1	XG/G-S1	0.16	73.5
2	XG/G-S2	n/a	n/a
3	XG/WG-S1	1	347
4	XG/WG-S2	1	373
5	XG/WG-S3	0.1	18
6	XG/WG-S4	0.1	23

5.4.2.1 Steady state shear rheology

Figure 5.20 shows the viscosity (η) values of all suspensions in the Xanthan gum solution alongside those in the pure Newtonian water glycerol mixture as a function of shear rate ($\dot{\gamma}$) and selected particle volume fractions (φ) at 60°C. The viscosity values of the corresponding suspensions at 20°C are also included as insets for comparison. The shear stress values (τ) of all suspensions as a function of $\dot{\gamma}$ are presented in Figure 5.21.

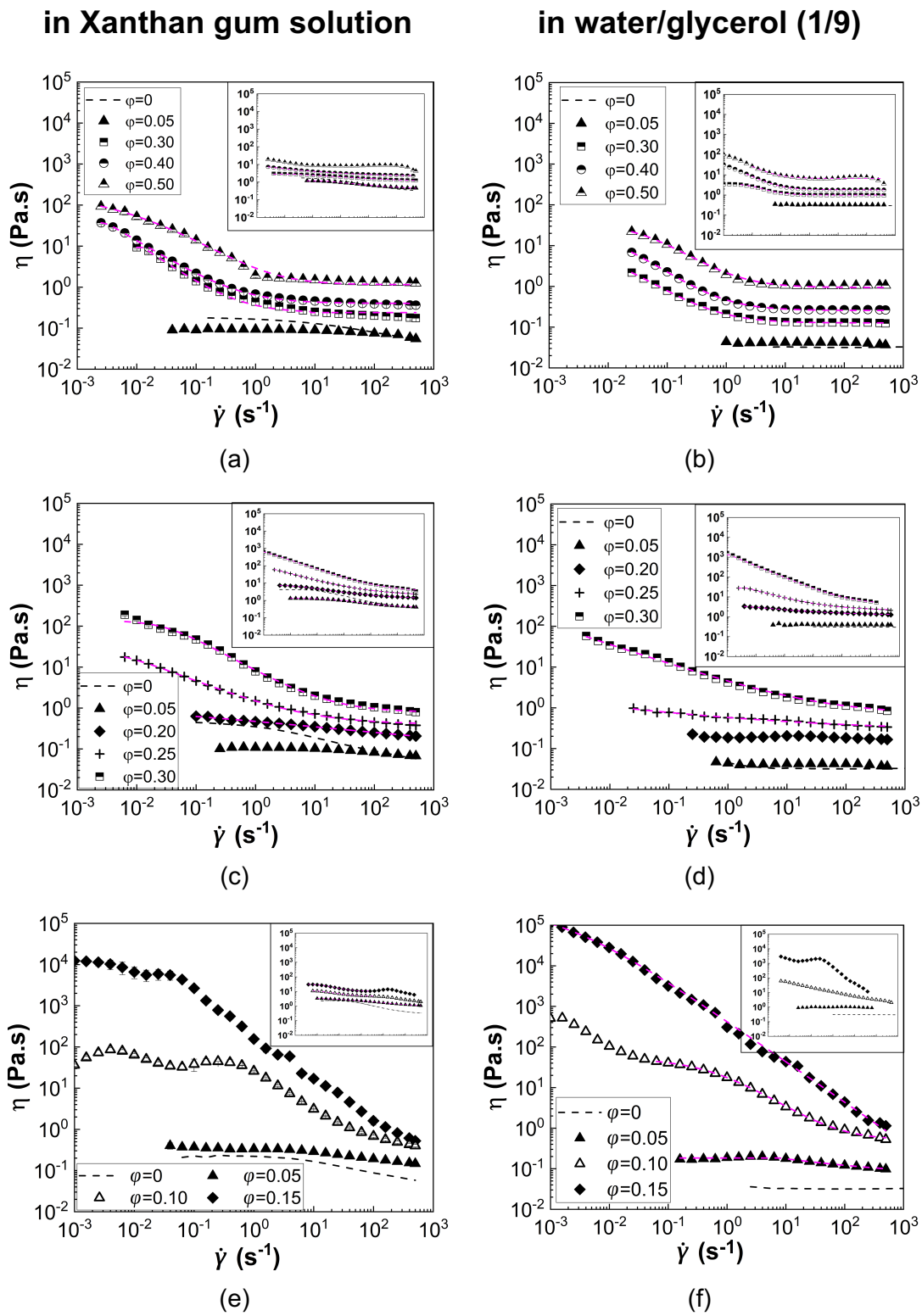

Figure 5.20: Viscosity (η) of selected suspensions in the 0.1% wt. Xanthan gum solution in water glycerol (1/9) (left column) as a function of shear rate ($\dot{\gamma}$) at 60°C. The corresponding data in the Newtonian water/glycerol (1/9) mixture are presented (left column) for comparison. Continuous lines correspond to the Carreau fittings to the shear thinning curves. a) and b) glass spheres; c) and d) abrasive silicas; e) and f) filler silicas.

Unlike the particle-free Xanthan gum solutions ($\varphi = 0$) for which the increase in temperature inhibits shear thinning, all suspensions in the shear thinning suspending medium exhibit a strong shear thinning response except at the lower particle volume fraction ($\varphi = 0.05$). Although, the increase in temperature lowers the viscosity of the Xanthan gum solution, the opposite trend is observed for the highly concentrated particle suspensions. At 60°C the low shear viscosity of the dense glass sphere suspensions at $\varphi \geq 0.30$ (Figure 5.20a) and filler suspensions (Figure 5.20e) at $\varphi = 0.10$ and 0.15 appear to increase with temperature. This behaviour is likely to arise from the disruption of the solvation layer due to the reduction of the base fluid viscosity (water/glycerol) enabling stronger interparticle interactions. In addition, the uncoiling of the Xanthan gum molecules at 60°C can increase the hydrodynamic volume of the polymer in solution and thus, increase suspension viscosity. A weaker increase of the low shear viscosity at 60°C compared to 20°C is observed for the abrasive silica suspensions in Xanthan gum solution at $\varphi \geq 0.20$ (Figure 5.20c).

Similarly, increasing the temperature also increases the viscosity of the suspensions in the Newtonian water/glycerol (1/9) solvent, especially at low shear (Figure 5.20b, d and f). The shear thinning response of all dense suspensions also increases with increasing temperature and particle surface roughness, from glass spheres (Figure 5.20b) to filler silicas (Figure 5.20f). A better comparison between the relative viscosities of the suspensions in the Xanthan gum solution and those in the water/glycerol (1/9) solvent is given in Figure 5.22 at zero and infinite shear rate.

Yield stress behaviour is observed for the highly concentrated suspensions of each particle type in the Xanthan gum solution as indicated by the shear stress curves reaching a plateau value at low/zero shear rate limit (Figure 5.21a, c and e). In particular, the glass sphere (Figure 5.21a) and abrasive silica (Figure 5.21c) suspensions seem to exhibit slightly higher shear stress values compared to these of the suspensions in the water/glycerol (1/9) (Figure 5.21b and d respectively). The filler silica suspensions in the Xanthan gum solution at $\varphi = 0.10$ and 0.15 show shear stress values that are independent of shear rate for $\dot{\gamma} \geq 0.1\ s^{-1}$, in agreement with their extreme shear thinning response in Figure 5.20e. Interestingly, this behaviour seems to worsen in the absence of Xanthan gum (Figure 5.21f) especially for the suspension at $\varphi = 0.15$, where τ remains constant for the whole range of $\dot{\gamma}$ values. This is indicative of a jamming state which is likely to stem from the massive reduction in the solvent viscosity at 60°C and the inability of the thin solvation layer to prevent particle-particle contact, especially in the case of the highly porous filler silicas. Entrapped air bubbles unable to be removed under vacuum during sample can deform

and elongate under high shear stresses and further enhance the shear thinning behaviour of these suspensions.

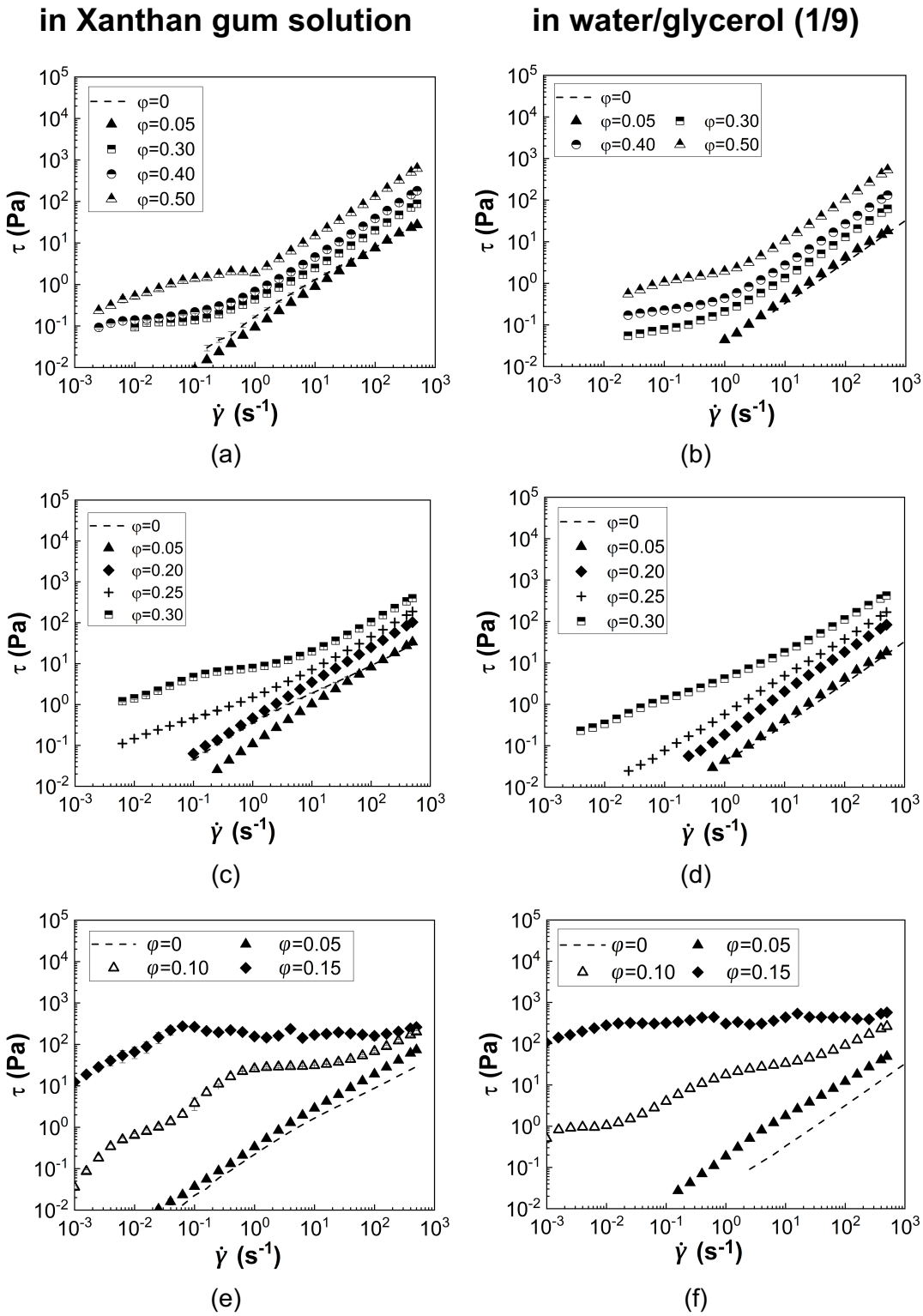

Figure 5.21: Shear stress (τ) values of selected suspensions in the 0.1% wt. Xanthan gum solution in water glycerol (1/9) (left column) as a function of shear rate ($\dot{\gamma}$) at 60°C. The corresponding data in the Newtonian water/glycerol (1/9) mixture are presented (left column) for comparison. a) and b) glass spheres; c) and d) abrasive silicas; e) and f) filler silicas.

Figure 5.22 illustrates the zero ($\eta_{r,0}$) (Figure 5.22a) and infinite shear rate relative viscosity ($\eta_{r,\infty}$) (Figure 5.22b) as well as the estimated $\eta_{r,e}$ values (Figure 5.22c), of all the suspensions in the Xanthan gum solution as a function of particle volume fraction (φ) at 60°C.

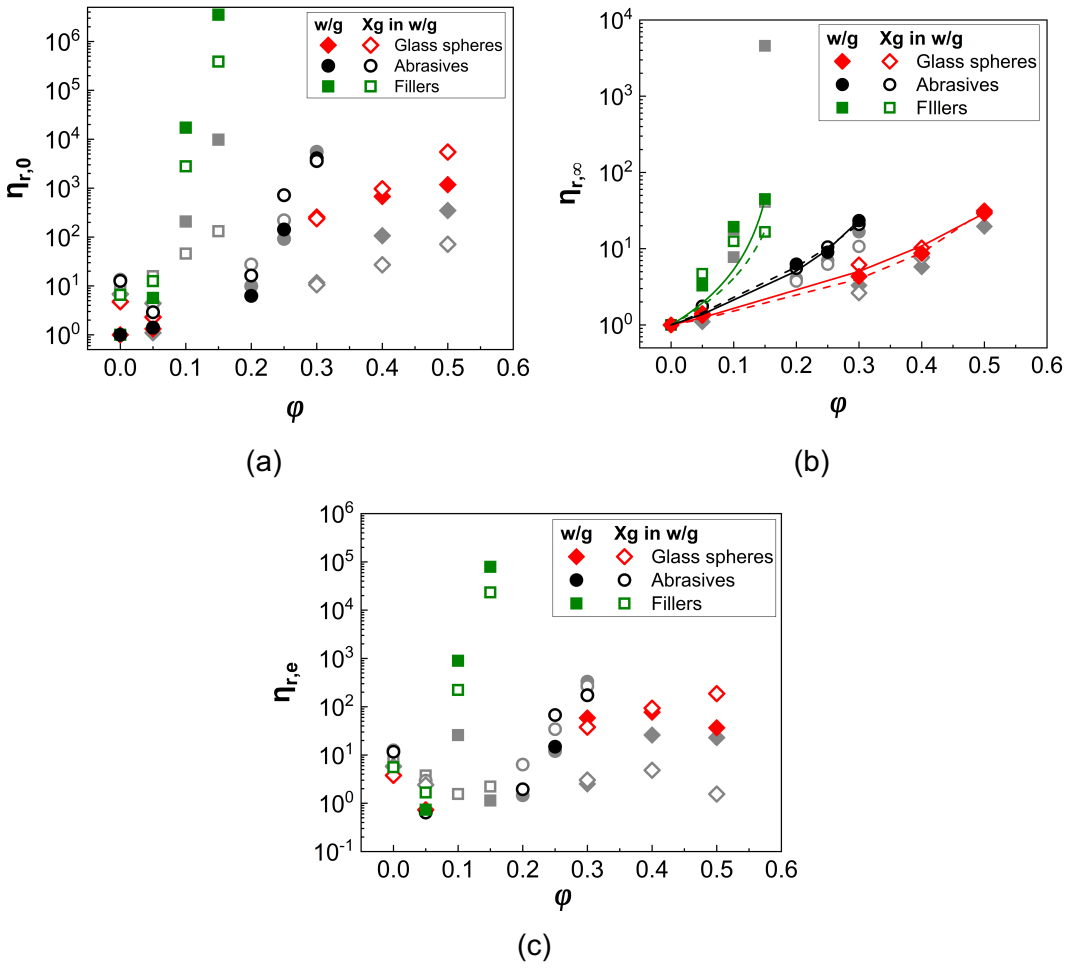

Figure 5.22: a) Zero shear rate ($\eta_{r,0}$) and b) infinite shear rate ($\eta_{r,\infty}$) relative viscosity values as a function of φ for all suspensions at 60°C. Continuous and dashed lines in (b) correspond to the Krieger-Dougherty fittings of the glass sphere and abrasive silica suspensions and the Quemada fittings to the filler silicas; c) Extent of shear thinning estimated from the zero shear rate and infinite shear rate suspensions viscosities. The grey points in all figures represent the corresponding values estimated for the suspensions at 20°C.

Heating the suspension to 60°C increases $\eta_{r,0}$ (Figure 5.22a) values in all cases of Xanthan gum suspensions; particle surface roughness and porosity has the same effect with temperature on $\eta_{r,0}$. The presence of Xanthan gum seems to increase the zero shear rate relative viscosity values of the glass sphere and abrasive silica suspensions, while the opposite effect is observed for the higher concentrations of

the filler silica suspensions ($\varphi = 0.10$ and 0.15). The uncoiling of the Xanthan gum molecules at 60°C can increase the hydrodynamic volume of the polymer in the solution leading to an increase in the viscosity values. However, in the case of the filler silicas, this phenomenon might not be sufficiently strong to dominate over the particle contacts and potential bubble effects on the rheology of these suspensions.

The effect of heating on the $\eta_{r,\infty}$ (Figure 5.22b) values is less pronounced compared to the $\eta_{r,0}$ ones. The relative viscosities of the suspensions in the Xanthan gum solution at high shear exhibit only a slight increase by increasing the temperature at 60°C compared to 20°C. At sufficiently high deformation rates the Xanthan gum molecules disentangle, and the single chains align with the direction of the applied flow field leading to a decrease in the viscosity values and shear thinning; this is independent of temperature. The conformation of the Xanthan gum network at such conditions might be similar to that obtained from the ordered-disordered transition at 60°C. The weak increase in the $\eta_{r,\infty}$ upon heating could possibly be explained either by an increase in the hydrodynamic volume of the Xanthan gum chains or the slightly stronger interparticle interactions promoted by the lower solvent viscosity. Interestingly, the values obtained for the suspensions in the shear thinning solvent are almost identical with those in the pure water/glycerol (1/9) mixture. The latter indicates that at infinite shear, the particle interactions are likely to dominate suspension rheology over the effect of Xanthan gum.

The $\eta_{r,\infty}$ (Figure 5.22b) values of the glass sphere and abrasive silica suspensions were fitted using the Krieger-Dougherty equation, while the Quemada equation offered a better fit for the filler silica suspensions. The estimated variables from the fittings, i.e. intrinsic viscosity (B) and maximum packing fraction (φ_m), are reported in Table 5.9. Increasing the particle surface roughness significantly decreases the maximum packing fraction. On the contrary, the intrinsic viscosity increases both with temperature and surface roughness indicating stronger interparticle and intermolecular interactions at such conditions. Similar to 20°C, φ_m increases with the addition of Xanthan gum possibly attributed to the uncoiled polymer chains interfering more easily with interparticle contacts, keeping the particles in certain positions within the suspension and hence, allowing more space to be filled before jamming.

Table 5.9: Intrinsic viscosity (B) and maximum particle packing (φ_m) obtained from the Krieger-Dougherty fittings to the glass sphere and abrasive silica suspensions $\eta_{r,\infty}$ data in Figure 5.22b at 60°C. The data of the filler silicas were fitted with the Quemada equation and thus, only the φ_m values are reported.

Solvents	**water/glycerol (1/9)**		**Xanthan gum in water/glycerol**	
Particle type	**B**	$\boldsymbol{\varphi_m}$	**B**	$\boldsymbol{\varphi_m}$
Glass spheres	3.40	0.62	4.30	0.80
Abrasive silicas	5.99	0.42	7.08	0.56
Filler silicas	-	0.18	-	0.20

The extent of shear thinning ($\eta_{r,e}$) estimated from eq. (3.12) is presented in Figure 5.22c. It can be seen that the shear thinning response increases with increasing the temperature in all suspensions ($\varphi \geq 0.05$) in a similar manner to $\eta_{r,0}$. The shear thinning response of the abrasive silica suspensions is the least affected by temperature variations. Particle addition also alters the shear thinning behaviour of the Xanthan gum solution and two observations can be made: at low φ, the presence of particles reduces the shear thinning of the polymeric solution, while at increasing φ, where shear thinning is also induced by the particles, the overall non-Newtonian response of the suspensions is enhanced, as indicated by an increase in the $\eta_{r,e}$ values.

In addition to interparticle and intermolecular interactions, Brownian motion is also likely to enhance suspension shear thinning. Table 5.10 summarises the percentage of particles being in the colloidal regime to the total number of particles in the suspension at $\dot{\gamma} = 0.001\ s^{-1}$. In the case of Xanthan gum suspensions, an average viscosity value of the shear thinning solvent was used in the Pe number to estimate the critical particle size able to induce Brownian effects. Similar to the Boger fluid suspensions, the effect of Brownian motion on suspension rheology significantly increases with temperature, while it reduces in the presence of Xanthan gum. Interestingly, 50% of the glass spheres in the water/glycerol solution at 60°C are able to induce Brownian effects, while this value reduces by half, ~20%, with the addition of Xanthan gum. This is attributed to the Xanthan gum molecules increasing the viscosity of the base solvents and thus, its effectiveness in overcoming Brownian effects by keeping the particles well dispersed in the suspension.

Table 5.10: Percentage (%) of the particles able to induce Brownian effects for all suspensions in the Newtonian water/glycerol mixture and the Xanthan gum solution at 60°C in comparison to 20°C at $\dot{\gamma} = 0.001\ s^{-1}$, i.e. the lowest shear rate reached.

Solvents	**water/glycerol (1/9)**		**Xanthan gum in water/glycerol**	
Particle type	**20°C**	**60°C**	**20°C**	**60°C**
Glass spheres	14.6	50	9.5	21.4
Abrasive silicas	13.3	40.7	1.2	18.6
Filler silicas	3.4	24.8	0.3	5.6

It should be noted that the extent of shear thickening is not presented here as none of the suspensions in the Xanthan gum solution exhibited this non-Newtonian feature. Although, weak shear thickening was observed for the glass sphere and filler silicas at 20°C, this behaviour seemed to diminish at 60°C; this agrees with the findings in Chapter 3 (section 3.2.5). Increasing the temperature to 60°C reduced the hydrodynamic forces responsible for hydrocluster formation and thus, hindered the shear thickening response of the suspensions at the elevated temperature.

5.4.2.2 Oscillatory shear in the LVR

The viscoelastic moduli (G', G'') of the suspensions in the Xanthan gum solution are illustrated in Figure 5.23 as a function of angular frequency (ω) and particle volume fraction at 60°C and a strain amplitude $\gamma = 0.1\%$. The response of the corresponding suspensions in the water/glycerol (1/9) solvent under oscillatory frequency sweeps are presented alongside for comparison.

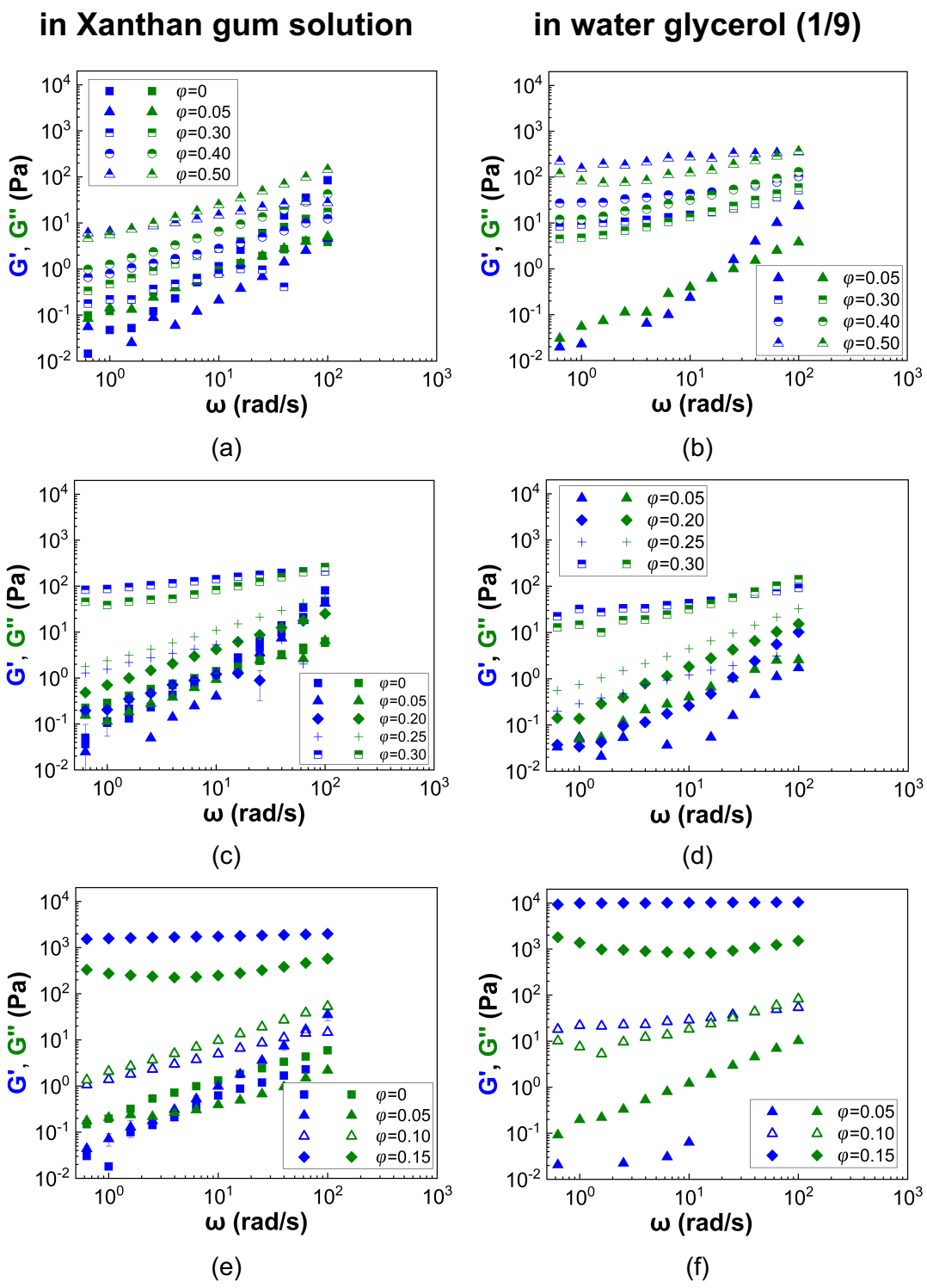

Figure 5.23: Viscoelastic moduli (storage, G' & loss, G'') of the three types of suspensions in the in the Xanthan gum solution in water/glycerol (1/9) (left column) as a function of particle volume fraction (φ) and angular frequency (ω). The measurements were conducted at 60°C and $\gamma = 0.1\%$. The data obtained for the suspensions in the pure water/glycerol mixture (1/9) are presented (right column) for comparison. a) and b) glass spheres; c) and d) abrasive silicas; e) and f) filler silicas.

The storage and loss moduli, both increase with increasing ω and φ values for almost all suspensions in the Xanthan gum solution at 60°C, which exhibit a viscous dominated response (Figure 5.23a, c and e), similar to the observations at 20°C. A strongly elastic dominated response can only be seen for the higher concentrations of the abrasive ($\varphi = 0.30$) (Figure 5.23c) and filler silica ($\varphi = 0.15$) (Figure 5.23e) suspensions. Interestingly, the suspensions in the Newtonian water/glycerol (1/9) (Figure 5.23b, d and f) show a higher degree of viscoelasticity compared to their counterparts in the Xanthan gum solution as described by an increase in the G' and G'' values. The onset of solid like response ($G' > G''$) is also observed at lower particle volume fractions. For example, the glass sphere suspensions (Figure 5.23b) exhibit solid like behaviour at low ω followed by a crossover point and a transition to a viscous dominated response at $\varphi \geq 0.30$, while this behaviour in the Xanthan gum solution is obtained at $\varphi = 0.50$ (Figure 5.23a). Therefore, it seems that interparticle interactions are favored in the Newtonian solvent giving rise to suspension elasticity, whereas the presence of Xanthan gum might interfere with interparticle contacts leading to a suppression of the viscoelastic response, as observed at 20°C.

The phase angles (δ) are shown in Figure 5.24 as a measure of the relative elasticity of the suspensions; the values of all suspensions at 20°C are included for comparison. The glass sphere suspensions in Xanthan gum solution (Figure 5.24a) show slightly lower δ values at 60°C and low ω indicating an increase in the suspension viscoelasticity compared to 20°C. In contrast, the viscous dominated suspensions of abrasive silicas ($\varphi \leq 0.25$ in Figure 5.24c) and filler silicas ($\varphi = 0.05$ and $\varphi = 0.10$ in Figure 5.24e) show very weak dependence on temperature, as the measured phase angles at 60°C have similar values with these at 20°C. A remarkable decrease in the δ values with increasing temperature is obtained for the abrasive silicas at $\varphi = 0.30$ and filler silicas at $\varphi = 0.15$, which can be attributed to the strong frictional contacts between the particles being favoured in a lower viscosity solvent.

Unlike the observations for the suspensions in the Xanthan gum solution, a 50% reduction in the measured phase angles is observed for the glass spheres in water/glycerol (Figure 5.24b) indicating an increase in suspension elasticity through enhanced interparticle interactions but also the high contribution of Brownian effects at low shear. On the contrary, the suspensions of the rough silicas in the Newtonian solvent (Figure 5.24d and f) are weakly affected by the temperature conditions. Particle dynamics are likely to govern the suspension viscoelastic response of the abrasive and filler silicas in water/glycerol and these are less susceptible to temperature variations.

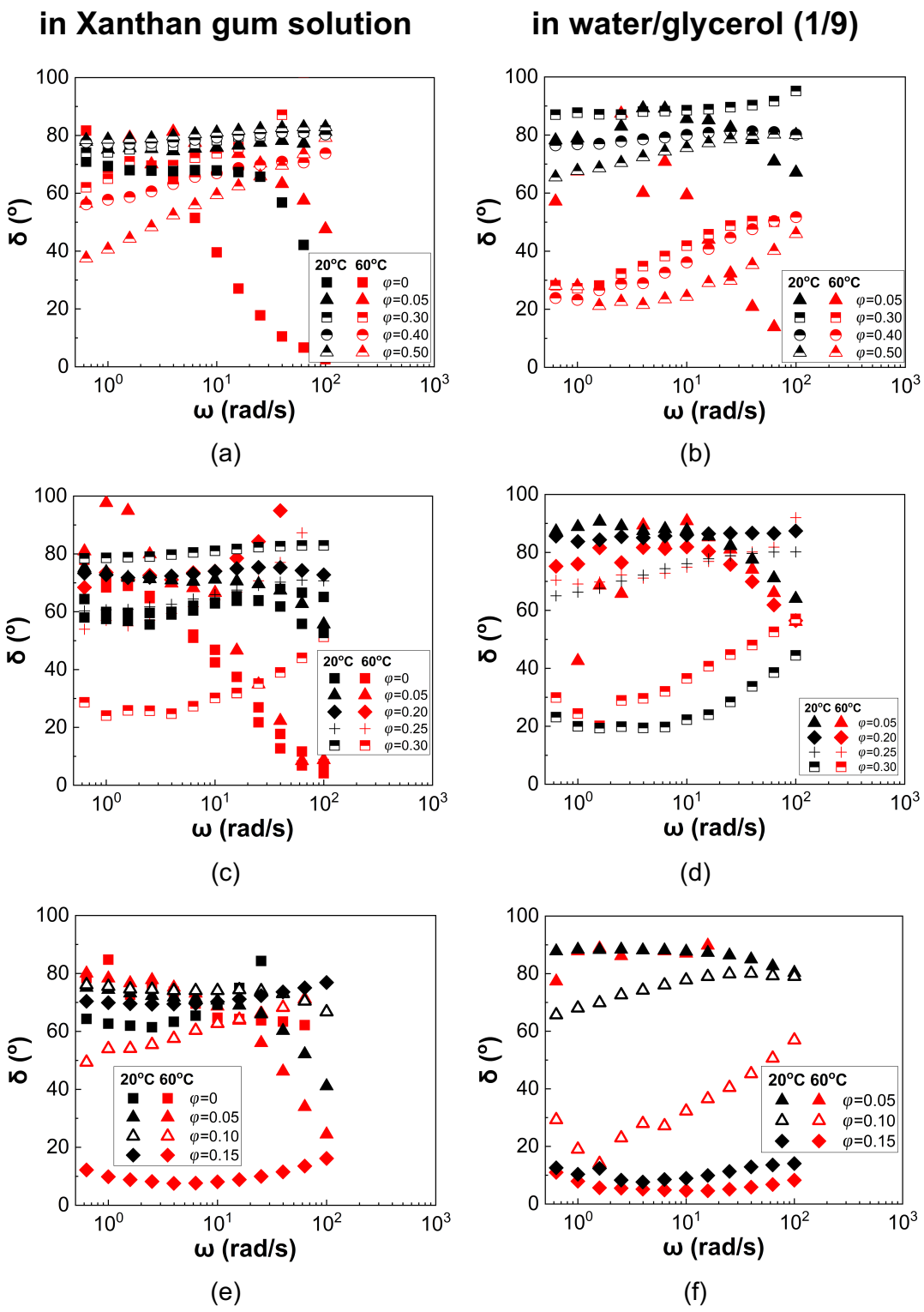

Figure 5.24: Phase angles (δ) of the three types of suspensions in the Xanthan gum solution in water/glycerol (1/9) (left column) as a function of particle volume fraction (φ) and angular frequency (ω). The measurements were conducted at 60°C (red points) and $\gamma = 0.1\%$, while the corresponding data at 20°C (black points) are also included for comparison, alongside the phase angles of the suspensions in the pure water/glycerol mixture (1/9) (right column). a) and b) glass spheres; c) and d) abrasive silicas; e) and f) filler silicas.

5.5 Discussion

Particles suspended in polymer solutions are ubiquitous in industrial applications. Suspension rheology even in the simplest cases of Newtonian suspending media can be highly complex, as also described in Chapter 3, while the different mechanisms governing these complex rheological phenomena are poorly understood. The presence of polymers in a suspension can further alter particle dynamics adding to the complexity of the observed rheology. Several factors have been reported in the literature to influence the rheology of particle suspensions in polymer and viscoelastic media, ranging from the properties of the polymer matrix (i.e. shear thinning, shear thickening, viscoelasticity) (Gunes et al., 2008; Pal, 2015; Potanin, 2019; Won and Kim, 2004; Yang and Shaqfeh, 2018a) and molecular weight to the particle surface characteristics and chemistry (Aliabadian et al., 2018; Ma et al., 2017; Ndong and Russel, 2012; Olanrewaju et al., 2013).

A particle subjected to shearing flows experiences various forces, which can be either repulsive or attractive. In the presence of polymers, molecules can be grafted on the particle surface or get entrapped in the narrow interparticle gaps inducing additional stresses and interfering with interparticle interactions. Therefore, extra terms should be added to the force balance (eq. (3.17)) in Chapter 3 to account for the polymer induced effects (Amiri et al., 2012; Mewis and Wagner, 2012; Warren et al., 2015) as follows:

$$F_{solvation} + F_{el} + F_{Brownian} + F_{steric} = F_{hydrodynamic} + F_{friction} + F_{depletion} \quad (5.2)$$

$F_{solvation}$ refers to the solvation layer formed by water and glycerol around the particles through hydrogen bonding. The electrostatic (F_{el}) force is assumed to be negligible as the particles are not expected to be charged in any of the suspensions and thus, its effect will not be discussed here. The contribution of Brownian effects to the observed rheology of all suspensions and experimental conditions applied has already been discussed in sections 5.4.1 and 5.4.2. F_{steric} arises from the polymer chains binding on the particle surface; this leads to an increase in the repulsive forces and helps in keeping the particles well dispersed in the suspending medium, i.e. preventing aggregation (Warren et al., 2015). Both Xanthan gum (Potanin, 2019) and polyacrylamide (Aliabadian et al., 2018) are able to bind on the silica surface and thus,

phenomena related to steric stabilisation are likely to occur. The steric force can be written as (Warren et al., 2015):

$$F_{steric} \sim \frac{\alpha k_B \theta \delta_{polymer} \varphi_{polymer} \rho_f}{M_w} g\left(\frac{D_{pp}}{\delta_{polymer}}\right) \quad (5.3)$$

where M_w is the polymer molecular weight, $\delta_{polymer}$ the thickness of the polymer layer on the silicas, $\varphi_{polymer}$ is the fraction of the polymer chains that bind on the silica to the total polymer concentration, D_{pp} the interparticle distance, α the particle radius and θ the temperature. The factor k_B is the Boltzmann constant ($1.38 \cdot 10^{-23}$ $m^2 \cdot kg \cdot s^{-2} \cdot K^{-1}$) and $g\ (D_{pp}/\delta_{polymer})$ is a dimensionless form of the interparticle distance.

On the other hand, the attractive forces comprise mainly three components: $F_{hydrodynamic}$ defined in Chapter 3 with eq. (3.18); $F_{friction}$, which results from direct particle-particle contacts and depends on particle surface characteristics; $F_{depletion}$, which refers to the depletion attraction between the particles as the polymer chains get squeezed out from the interparticle gaps.

In the present study, the non-Newtonian media were prepared adding an amount of water in glycerol to facilitate the dissolution of the polymers in the solution. Thus, a solvation layer is present around the particles preventing direct interparticle contact, especially at 20°C due to the higher viscosity of the base solvent. However, its thickness is expected to reduce with increasing the water content (Amiri et al., 2012) as the water molecules have only one hydroxyl group (-OH) to bind on the silica surface in contrast to glycerol, which has three.

The effect of the particle volume fraction, surface morphology and porosity on the rheology of the suspensions in the non-Newtonian solvents is similar to that in the corresponding Newtonian solvents, as also observed by Scirocco et al. (2005) for sufficiently large non-Brownian particles. Increasing the particle surface roughness and porosity increased suspension viscosity and promoted non-Newtonian rheology at lower particle volume fractions. These phenomena are generally associated with the increase in the effective volume fraction of the abrasive and filler silicas, as part of the solvent gets absorbed into the particle pores. It should be noted that the effective volume fraction of the particles in the non-Newtonian suspending media is expected to follow the same trends with those presented in Chapter 3 (section 3.2.3) since neither the presence of polymers or the addition of water significantly alters the solvent and particle densities. The particle specific surface area and the subsequent increase of the silanol group density on the silica surface (glass spheres: $\delta_{OH} =$

$0.012\ mmol\ OH/g\ SiO_2$, abrasive silicas: $\delta_{OH} = 0.40\ mmol\ OH/g\ SiO_2$, filler silicas: $\delta_{OH} = 1.70\ mmol\ OH/g\ SiO_2$), can also lead to enhanced interparticle and particle-solvent interactions.

The Krieger-Dougherty and the Quemada equations described sufficiently well the infinite shear rheology of the suspensions in the non-Newtonian solvents. An increase in the estimated variables, i.e. intrinsic viscosity (B) and maximum packing fraction (φ_m) was observed in the non-Newtonian solvents compared to those obtained for the suspensions in the corresponding Newtonian fluids. The increase in the estimated B values can be attributed to the presence of polymer-polymer and particle-polymer interactions imposing additional stresses to the hybrid composites, (particles suspended in a polymer solution). In contrast, for the suspensions in pure Newtonian solvents interparticle interactions mostly contribute to the values of B. The φ_m (maximum packing fraction) also increase in the presence of polymers; it is likely that the polymers strengthen the thickness of the solvation layer, i.e. increasing the $F_{solvation}$, which acts as a barrier to interparticle contacts and allows a higher loading capacity in the suspension before jamming. Partial absorption of the polymers on the silica surface through hydrogen bonding can also contribute to keeping the particles separate (i.e. F_{steric} increases) increasing thus, φ_m.

Particle porosity also plays a significant role to suspension rheology increasing not only the effective particle volume fraction but also the polymer concentration in the suspension compared to the apparent one (Olanrewaju et al., 2013). The latter influences both particle and polymer dynamics leading to increased suspension viscosities and enhanced non-Newtonian behaviour. At room temperature (~20°C), the suspensions in the Boger fluid exhibited higher relative viscosity values at both shear rate regimes (zero and infinite, Figure 5.3) compared to those in the corresponding Newtonian solvent, which agrees to the above statement.

On the contrary, the opposite effect is observed for the suspensions in the Xanthan gum solution at 20°C compared to the suspensions in the pure water/glycerol mixture (Figure 5.10). The addition of the Xanthan gum seemed to reduce the relative viscosity of the suspensions, especially for the glass sphere and filler silica suspensions. The observed trend might be attributed to the partial absorption of the Xanthan gum chains on the silica surface, which will decrease the hydrodynamic volume of the polymer in the suspension (Ndong and Russel, 2012) and reduce interparticle attraction through an increase in the F_{steric}. The possible strengthening of the solvation layer in the presence of Xanthan gum molecules might be another

reason for reducing suspension viscosity as interparticle interactions are inhibited more effectively.

The Boger fluid induces pronounced shear thickening to the suspensions at particle volume fractions as low as $\varphi = 0.05$ at 20°C; shear thickening in the pure glycerol was only observed for the highly concentrated glass sphere and filler silica suspensions ($\varphi \geq 0.50$ and $\varphi \geq 0.15$ respectively). This phenomenon is mainly associated with the hardening of the long polyacrylamide chains under the effect of high elongational stresses generated within the narrow interparticle gaps (Choi et al., 1999; Scirocco et al., 2005, 2004; Shaqfeh, 2019; Yang and Shaqfeh, 2018b; Zarraga et al., 2001). Interestingly, increasing the particle volume fraction of the abrasive silicas at $\varphi \geq 0.25$ reduced the shear thickening response of this type of suspensions giving rise to strong shear thinning. The frictional contacts between the abrasive silicas at sufficiently high particle concentrations responsible for shear thinning (Amiri et al., 2012; Chatté et al., 2018; Lobry et al., 2019) are likely to dominate over the polymer induced thickening and thus, leading to a decrease in the shear thickening of the overall suspension.

The Xanthan gum solutions also exhibit a degree of viscoelasticity, but this is much lower compared to that of the Boger as indicated by the lower elastic numbers of the former. The elastic thickening induced by the Boger fluid is not observed for the suspensions in Xanthan gum solutions. It is likely that the shear thinning nature of the suspending medium can suppress elastic thickening. However, due to the lower elasticity of the Xanthan gum solution compared to the Boger fluid, it is hard to distinguish between the effects of shear thinning and suspending medium elasticity on suspension shear thinning.

The Xanthan gum solution promotes the shear thinning behaviour of the suspensions at low particle volume fractions, $\varphi = 0.05$, which can be attributed to the shear thinning nature of the suspending medium. In contrast, the suspensions at higher particle volume fractions exhibit a decrease in their shear thinning response in the presence of Xanthan gum compared to the corresponding suspensions in the Newtonian solvent. It should be noted that shear thinning response is also induced by the particles in the Newtonian water/glycerol solvent at such high volume fractions, which is related to the interparticle frictional contacts followed by an increase in $F_{friciton}$. Therefore, a suppression in the shear thinning of the highly dense suspensions possibly arises from the Xanthan gum molecules limiting particle-particle frictional contacts.

Mild shear thickening is also observed for the glass sphere and filler silica suspensions in the Xanthan gum solutions showing a similar degree to that in the Newtonian water/glycerol solvent. Therefore, it is likely that the mechanism inducing shear thickening in these suspensions is the same independently of the suspending medium. Shear thickening in the glass sphere suspensions is induced when the hydrodynamic forces are able to overcome the sum of the repulsive forces leading to hydrocluster formation at sufficiently high particle volume fractions. In the case of filler silicas, on the other hand, this is likely to arise from an increase in the thickness of the solvation layer due to the high surface silanol group density, as discussed in Chapter 3, inducing short range repulsive forces.

Increasing the temperature to 60°C, leads to an increase of the relative viscosity values at zero and infinite shear for the suspensions in the Boger fluid compared to those at 20°C; this also agrees with the observations for the suspensions in the pure Newtonian solvent. The viscosity of the base fluid (water/glycerol) significantly decreases from 20°C to 60°C leading to a decrease in the strength and thickness of the solvation layer ($F_{solvation}$ decreases). These conditions favor the interactions between the particles in the polymeric fluid as also evidenced by an increase in the shear thinning response of all suspensions independent of particle type at 60°C. Unlike shear thinning, the shear thickening of the glass sphere and the abrasive silicas in the Boger fluid is suppressed with increasing the temperature. Experimental evidence in the literature suggests a decrease in the flexibility (increase in toughness) of the polyacrylamide chains at temperatures around 60°C (Evingür and Pekcan, 2018). The latter might lead to a suppression in suspension shear thickening since higher elongational stresses are required to induce hardening to the polymer chains in a similar extent to the lower temperatures.

The shear thinning response of the dilute suspensions ($\varphi = 0.05$) in the Xanthan gum solvent seems to weakly reduce at 60°C compared to their response at 20°C, following the trend of the suspending medium; the shear thinning response of the Xanthan gum solution is also suppressed by increasing the temperature to 60°C due to a change in the structural conformation of the Xanthan gum molecules, i.e. a transition from an ordered to a disordered state at elevated temperatures (Rochefort and Middleman, 1987). In contrast, the shear thinning response of the highly concentrated suspensions of all particle types is enhanced at 60°C, in a similar manner to the suspensions in the Newtonian water/glycerol (1/9) solvent. Friction-enabled shear thinning arising from interparticle contacts in the presence of a thinner solvation layer at 60°C is likely to dominate suspension rheology under such particle volume fraction and temperature conditions, even in the presence of polymers.

Brownian motion comprises another factor contributing to suspension shear thinning, especially in the case of the water/glycerol mixture.

The shear thickening behaviour of the suspensions in the Xanthan gum solution seems to be suppressed by increasing the temperature to 60°C for both the glass sphere and the filler silicas; shear thickening was speculated to arise either from hydrocluster formation for the glass spheres or solvation forces for the filler silica suspensions at 20°C (Clavaud et al., 2017; Lin et al., 2015; Maranzano and Wagner, 2001a; Raghavan and Khan, 1997; Townsend and Wilson, 2017). A decrease in the hydrodynamic force ($F_{hydrodynamic}$) due to the strong reduction of the solvent viscosity at 60°C renders it unable to overcome the sum of the repulsive forces ($F_{solvation}$, F_{steric}). The latter shifts the onset of shear thickening for the glass sphere suspensions to higher shear rate values, which might be difficult to reach due to edge fracture effects. In the case of the filler silicas, although the thickness of the solvation layer is likely to reduce at elevated temperatures, the higher thermal energy offered to the suspension upon heating leads to a more random movement of the particles and faster collisions between them, limiting the interparticle contact time and subsequently, reducing their effect on shear thickening rheology.

5.6 Concluding remarks

This chapter provided a thorough experimental study on the rheology of dense particle suspensions in two different polymer solutions: a high molecular weight polyacrylamide in 1% wt. water and 99% wt. glycerol mixture, namely Boger fluid and a Xanthan gum in water/glycerol (1/9) solution. Using commercial polydisperse particles with complex surface characteristics and uncontrolled surface roughness and porosity significantly extends the existing experimental studies in the literature, which focus on nearly monodisperse rigid spheres. The important effect of the suspending medium rheological properties on suspension rheology was investigated, to probe the complex particle and polymer dynamics involved in such suspensions, resembling formulations typically employed in industrial manufacturing.

The particle volume fraction (φ) was found to influence the rheology of the suspensions in the non-Newtonian suspending media in a similar manner to that in the corresponding Newtonian solvents. In particular, the filler silica suspensions showed higher viscosity values and more pronounced non-Newtonian rheological phenomena at lower φ compared to the glass sphere and abrasive silica suspensions as also observed for the suspensions in the corresponding Newtonian glycerol and

water/glycerol solvents. The Krieger-Dougherty and Quemada equations described sufficiently well the infinite shear rheology enabling the estimation of the intrinsic viscosities (B) and the maximum packing fraction (φ_m). The suspensions in the non-Newtonian solvents exhibited higher φ_m values compared to those in the Newtonian counterparts; this could indicate that the presence of polymers contribute to the effectiveness of the solvation layer, formed by glycerol and water, on keeping the particles separate allowing higher particle loading capacities till jamming occurs.

The nature of the non-Newtonian solvents also played a crucial role in suspension rheology. Pronounced shear thickening was observed for the suspensions in the Boger fluid at room temperature and low particle volume fractions of $\varphi = 0.05$; this behaviour was mainly attributed to the hardening of the polyacrylamide chains under high elongational stresses. On the other hand, the addition of Xanthan gum enhanced the shear thinning of the suspensions at low particle volume fraction, which was mainly attributed to the shear thinning nature of the suspending medium, as these suspensions exhibited Newtonian response in the pure water/glycerol (1/9) mixture. The opposite trend was observed for the shear thinning response of the highly dense suspensions, where the shear thinning behaviour was weakly suppressed in the presence of Xanthan gum indicating a competition between interparticle interactions and the strengthening of the solvation layer by the polymer chains.

Increasing the temperature to 60°C led to an increase in the relative viscosity of all suspensions independent of particle type and suspending medium followed by an increase in the shear thinning compared to that of the same suspensions at room temperature (~20°C). In contrast, the shear thickening response of all suspensions was suppressed at the higher temperature. In the case of the Boger fluid this was attributed to the decrease in the flexibility of the polymer chains requiring higher elongational stresses to induce elastic thickening. In the Xanthan gum solutions, particle interactions were found to govern the shear thickening of the suspensions either through hydrocluster formation or frictional contacts. The reduction in the hydrodynamic forces or in the contact time between the particles with increasing the temperature could explain the suppression of suspension shear thickening at 60°C.

The findings presented in this chapter open new insights on how to manipulate suspension rheology, increase or reduce their viscosity as well as tune shear thinning and shear thickening response through the addition of polymers with varying molecular weights and physical properties, especially these related to their response under different applied deformations.

Chapter 6

Conclusions and Future work

6.1 Main findings

The thesis involved an extensive characterisation of the rheological properties of three types of non-colloidal particle suspensions with high industrial relevance. Two types of commercial silicas, commonly used as abrasives and fillers/thickeners in oral healthcare applications, were suspended in non-aqueous solvents and their suspension rheology was studied under steady state and oscillatory shear. Relatively smooth glass spheres with similar size distribution with that of the commercial ones were also used as a model system to investigate how differently the non-idealised particles behave compared to spheres. The effect of temperature and the solvents physical and chemical properties on suspension rheology was investigated to probe the shear thinning mechanism governing the rheology of suspensions of highly rough and porous silica particles. The particles were also suspended in two non-Newtonian suspending media, i.e. a viscoelastic Boger fluid with constant viscosity and a shear thinning and weakly viscoelastic Xanthan gum solution in an attempt to decouple the effects of viscoelasticity and shear thinning of the suspending media on suspension rheology.

The bulk rheology measurements were conducted using a hybrid stress-controlled rheometer (DHR-3, TA Instruments) under steady state and oscillatory shear modes. Small amplitude oscillatory shear (SAOS) measurements and frequency sweeps were performed to investigate the viscoelastic properties of the suspensions in the linear viscoelastic region. Microstructure changes under shear were also studied *in situ* for dilute glass sphere and abrasive silica suspensions using an optical shearing cell (CSS-450, Linkam Scientific Ltd.) and a bespoke microscope. Large amplitude oscillatory shear (LAOS) measurements were performed for selected suspensions in the dense concentration regime to explore the non-linear rheology of the suspensions and also provide links with microstructure features.

Increasing the particle volume fraction led to an increase in suspension viscosity and induced non-Newtonian rheological phenomena even in the case of Newtonian suspending media. This was attributed to a decrease in the interparticle distance, which subsequently, enhanced interparticle interactions. The particle surface roughness and porosity also increased suspension viscosity and induced non-linear

rheology at lower particle volume fractions compared to the relatively smooth and non-porous glass spheres. The presence of surface asperities generally, offer a higher density of available contacts between the particles, while porosity increases the effective volume fraction of the particles in the suspension as the pores absorb part of the solvent. These characteristics can further enhance the non-Newtonian rheological phenomena in suspension rheology.

The shear thinning of the suspensions in glycerol was attributed to a friction-enabled mechanism. This is based on the elastic deformation of the surface asperities as the particles come into contact upon increasing the shear rate. The critical shear stress for the onset of shear thinning was estimated for the abrasive silica suspensions in glycerol, which exhibited the most pronounced shear thinning response. However, the presence of the solvation layer around the particles hindered the frictional contacts between the glass spheres and suppressed the shear thinning response at 20^{o}C. Both glycerol and silicas have copious amounts of hydroxyl groups and thus, hydrogen bonds can very easily be generated between them. This leads to the formation of a thick solvation layer around the particles, which can inhibit interparticle interactions and subsequently, suppress the non-Newtonian rheology, especially at low temperature conditions where glycerol's viscosity is high. In contrast in the case of the abrasive silicas, the particle surface roughness seems to be able to penetrate the solvation layer enabling frictional contacts between the particles leading to strong shear thinning response. Although frictional shear thinning seems a plausible explanation for the rheological response of the abrasive silicas, there might also be other mechanisms contributing to this response. For example, partial deformation of the solvation layer in such a way to enable a better lubrication between the particles or induce their alignment to the direction of the applied flow field might also contribute to enhancing suspension shear thinning.

Although the filler silicas exhibited the highest porosity and specific surface area out of the three particles studied and thus, one could expect the highest degree of shear thinning, a non-monotonic effect of S_p on suspension rheology was observed. The filler silica suspensions exhibited reduced shear thinning response close to that of the glass spheres and shear thickening at $\varphi \geq 0.15$. This non-monotonic response further highlights that more complex particle dynamics might be involved in the rheology of such suspensions, especially when the particles reach a surface porosity close to 90%. The high specific surface area leading to a high density of surface silanol groups on the filler silicas is postulated to enhance the strength of the formed solvation layer suppressing the shear thinning behaviour and giving rise to shear thickening through the short-range repulsive forces between the particles.

The oscillatory shear measurements in the linear viscoelastic region showed a viscous dominated response ($G' < G''$, $\delta \sim 90^o$) for most particle suspensions in glycerol possibly arising from the hindered interparticle contacts in the presence of the solvation layer. However, the abrasive silica suspensions at particle volume fractions of $\varphi \geq 0.30$ showed increased viscoelastic behaviour with $\delta \ll 90^o$ which is in agreement with the pronounced shear thinning behaviour of these suspensions under steady state shear and the related interparticle frictional contacts. The non-monotonic effect of the particle specific surface area for the filler silicas was also reflected in the oscillatory shear measurements which showed higher phase angles compared to the abrasive silicas at similar effective volume fractions.

Heating the suspensions from 20°C to 60°C led to remarkable changes of their rheology. For example, the glass sphere suspensions exhibited enhanced shear thinning and yield stress behaviour at 60°C, which were absent at the lower temperature conditions. On the contrary, the shear thinning response of the rough and porous silicas (both abrasives and fillers) was weakly suppressed with temperature. The increase in the shear thinning response of the glass sphere suspensions was related to the solvation layer becoming thinner at the elevated temperature enabling interparticle contact. Interparticle enabled frictional contacts between the glass spheres led to shear thinning rheological phenomena at low shear in conjunction with an increase in the effect of Brownian motion due to particle polydispersity. Remarkably, around 30% of the glass spheres were able to induce Brownian motion at 60°C and the lowest shear rate of $\dot{\gamma} = 0.001\ s^{-1}$. In contrast the suspensions of abrasive and filler silicas were already in the frictional regime at 20°C and thus, their rheology was weakly affected by the applied temperature conditions. The maximum packing fraction of all suspensions was slightly decreased with temperature indicating enhanced interparticle contacts at 60°C compared to 20°C.

An additional mechanism for shear thinning rheological behaviour was probed by suspending the glass spheres and abrasive silicas in a non-polar solvent, mineral oil. Mineral oil has no hydroxyl groups to interfere with the active silanol groups on the silica surface and thus, particle agglomeration is favoured. Shear thinning in these systems was induced at much lower particle volume fractions compared to the glycerol suspensions arising from the agglomerates breaking down upon increasing shear rate. Oscillatory shear experiments showed strong viscoelasticity compared to the suspensions in glycerol and a transition to a solid-like response ($G' > G''$) at particle volume fractions much lower compared to glycerol, i.e. $\varphi \sim 0.10$. The bulk rheology and the breakup of the agglomerates were further confirmed through direct visualisation of the sheared suspension microstructure *in situ* using an optical

shearing cell. An aggregation index based on image analysis was estimated to monitor particle agglomeration and disaggregation. This technique was limited to low particle volume fractions, i.e. $\varphi \leq 0.05$, while the study of suspension microstructure at higher particle volume fractions, was complemented by performing Large Amplitude Oscillatory Shear (LAOS) measurements. An attempt to tune suspension shear thinning was made through modifying the glass sphere surface chemistry and in particular, introducing hydrophobic groups to inhibit particle agglomeration. A reduction in both the shear thinning degree and the yield stress values was observed for the suspensions of the hydrophobic particles in mineral oil compared to these obtained for the inherently hydrophilic silica suspensions. This study highlighted the importance of hydrogen bonding in particle suspension rheology as well as that of the competing effects between particle-particle and particle-solvent interactions. Inhibiting interparticle hydrogen bonding can serve as a means to tune and control suspension non-Newtonian rheology and help in designing formulations with rheological properties tailored to specific applications.

Industrial formulations often involve suspending media with high degrees of viscoelasticity and shear thinning behaviour. To decouple the effects of these two non-linear phenomena on the rheology of dense suspensions consisting of particles with uncontrolled surface roughness and porosity, two different suspending media were used. The media were a viscoelastic Boger fluid with constant viscosity and a shear thinning and weakly viscoelastic Xanthan gum solution. The suspensions in the Boger fluid exhibited pronounced shear thickening at particle volume fractions as low as $\varphi = 0.05$. This was attributed to the hardening of the polymer chains originating from the high elongation stresses generated in the narrow interparticle gaps. This phenomenon is known as elastic thickening. The shear thinning nature of the Xanthan gum solution seemed to suppress suspension shear thickening, giving rise to shear thinning behaviour especially for suspensions in the dilute concentration regime. The suspensions in both non-Newtonian suspending media exhibited higher maximum packing fractions compared to the corresponding suspensions in their Newtonian counterpart solvents, revealing an ability of the polymer chains to keep particles away from each other, through possibly strengthening the effect of the solvation layer, and allowing higher particle loadings before jamming.

Heating the suspensions to 60^{o}C led to suppressing the shear thickening of the suspensions regardless of the particle type or the nature of the solvent. In the case of the Newtonian solvents, the decrease in the shear thickening behaviour was attributed to a decrease in the hydrodynamic forces responsible for hydroclustering and their inability to overcome the sum of the repulsive forces acting on the particles.

On the other hand, in the case of the suspensions in the non-Newtonian solvents, the suppression of the shear thickening by increasing the temperature could be associated with a decrease in the flexibility of the polymer chains requiring higher stresses to show hardening.

As a final note, particle suspensions are complex fluids and exhibit rich rheological phenomena under different experimental and manufacturing/processing conditions; these are closely related to changes in both the particle and suspending medium microstructure under shear. Gaining a deeper and more fundamental understanding on how these irregularly shaped particles, commonly employed in industrial manufacturing, respond under different applied deformations and flow fields will allow the more accurate prediction and control of their rheological behaviour. The present study elucidated the competing effects between a solvation layer formed by solvent molecules and interparticle frictional contacts and adhesion. Suspension shear thinning was tuned through introducing hydrophobic groups to inhibit particle agglomeration. The ultimate goal of this work is to aid manufacturers in understanding the complex rheology entailed in suspensions of highly irregular particles and further, the engineering of formulations with rheological properties tailored to specific applications.

6.2 Main contributions of the thesis

The main contributions of this work include:

- A fundamental understanding on the specific mechanisms governing the shear thinning rheology of non-Brownian silica particles with uncontrolled surface roughness and porosity, commonly employed in industrial formulations and suspended in non-aqueous polar and non-polar solvents (glycerol and mineral oil).
- Relationships between the microstructure and suspension rheology through direct visualisation of dilute systems and large amplitude oscillatory shear measurements (LAOS), applicable to the densely concentrated particle suspensions.
- Alternative design routes to control suspension rheology, whether to promote or suppress shear thinning through utilising the particle surface chemistry and solvent chemical properties and the applied temperature conditions. This can ultimately offer new insights into the manufacturing and manipulation of complex non-Brownian particle suspensions.

- An attempt to decouple the effects of suspending medium viscoelasticity and shear thinning on the rheology of complex non-Brownian particle suspensions. Altering particle dynamics through the addition of suitable polymer molecules can be beneficial in suppressing or enhancing suspension shear thickening rheology.

6.3 Suggestions for future work

The commercially available particles employed in this study are highly polydisperse, irregularly shaped, extremely rough and porous in contrast to the ideal spherical particles that have been widely studied in the literature. These complex particle characteristics present many challenges in the systematic investigation of the role of roughness and porosity on the measured rheology. Therefore, future work could aim on investigating the rheology of suspensions with a high degree but also controlled roughness and/or porosity to get a deeper understanding of the effect of these parameters on suspension rheology. Also, the effect of particle size and morphology could be another parameter to be investigated on the rheology of such highly rough and porous particles. This could be achieved by sieving the commercial silicas in the present study to narrow down their size distribution.

In Chapter 3, the rheological response of the suspensions is based on the competing effects between interparticle and particle-solvent interactions. A more thorough investigation of the solvation layer formed by glycerol under different experimental conditions, such as varying shear rate and temperature, could help in better understanding the rheology of the suspensions investigated in the present thesis. Small angle neutron scattering (SANS) or dynamic light scattering (DLS) comprise two useful techniques that could be applied in order to investigate the pattern/structure of the solvation layer or the hydrodynamic radius of the silica particles respectively. Quantifying the density of the silanol groups on the silica surface by utilising spectroscopic techniques (e.g. Fast Fourier Transform Infrared Spectroscopy (FTIR), Solid state Nuclear Magnetic Resonance (S-state NMR)) could further elucidate the non-monotonic effect of the particle specific surface area and its originating mechanics.

The frictional driven shear thinning mechanism seemed a plausible explanation for the shear thinning behaviour of the abrasive silicas suspended in glycerol. However, other mechanisms were also able to influence the observed suspension shear thinning behaviour. A more systematic investigation of the competing effects between particle-particle and particle-solvent interactions by systematically varying the particle

surface properties and/or the solvent is required to distinguish between the different shear thinning mechanisms more accurately. Applying Atomic Force Microscopy (AFM) techniques with a colloidal probe can provide information about the interparticle forces, either frictional or adhesive. Performing powder rheology and tribology measurements to the dry particle powder and the suspensions (i.e. lubricated particles) can provide valuable information about the frictional contacts between the particles and how these might be hindered in the presence of glycerol. For example, different types of interparticle frictional contacts (i.e. rolling, sliding friction, adhesion through hydrogen bonding) can significantly affect suspension rheology. Therefore, understanding the specific mechanisms of action in each system could ultimately lead to the development of predictive models for suspension rheology aiding in the manufacturing of formulations with specific rheological properties.

In Chapter 4, the rheological properties of selected suspensions in mineral oil were tuned through modifying the particle surface chemistry with two hydrophobic agents. However, only a few hydrophobic groups were used and also limited cases of the degree of surface modification. A systematic investigation of the effect of surface hydrophobicity on silica suspensions using different suspending media, hydrophobic agents and monitoring the time of surface treatment could open new insights on tuning suspension rheology more accurately. The adhesion force between the particles in the mineral oil was estimated through bulk rheology and the yield stress values. A more accurate quantification of interparticle interactions and the subsequent adhesion forces could be achieved using Atomic Force Microscopy (AFM) measurements.

Industrial formulations often involve more than one type of particles. Mixing the two types of commercial silicas or the irregular silicas with the glass spheres at varying ratios but keeping the overall particle volume fraction fixed will help in resembling systems that are close to real applications. This could contribute to a better understanding of how the rheology of complex real systems evolves by varying particle characteristics. The use of surfactants and/or sweeteners is typical in the toothpaste and overall food and pharmaceutical industry and comprises another interesting area to be investigated. Certain excipients might interact with the silicas and further influence suspension rheology in desired but also undesired ways.

During industrial manufacturing, shear and extensional flows are very often interconnected. The response of complex fluids under extensional flows can be significantly different from the shear response. Therefore, a complete characterization of the rheological behaviour of formulations relevant to industrial applications requires the study of the suspension rheology under extensional flows, in addition to shear flow experiments. This is particularly important in additive manufacturing applications.

The studies already available in the literature related to the rheology of particles suspended in non-Newtonian suspending media are limited to spherical and nearly monodisperse particles as well as in the dilute and semi-dilute concentration regime. The present research work mainly discussed the rheology of suspensions at the highly concentrated regime to investigate the combined effects of polymer and particle interactions. A more thorough and systematic investigation of such systems and their microstructure changes upon shear is needed to complement the currently available literature.

Varying the particle volume fraction with smaller steps will help in clearly identifying the critical particle concentration for the onset of the non-Newtonian rheological phenomena and understand particle and polymer dynamics in the hybrid composites. A remarkable observation in Chapter 5 is the reduction in the zero shear viscosity and the shear thinning degree of the Xanthan gum solution with the addition of glass spheres and abrasive silicas at $\varphi = 0.5$. A more thorough investigation of this phenomenon would elucidate the mechanisms driving it and provide further insights on how the presence of particle at low volume fraction affect the polymer dynamics.

Polymers with varying molecular weight and concentration in the suspension constitute another important factor influencing suspension rheology. The Xanthan gum solutions used in the present study showed lower elastic numbers compared to that of the Boger fluid. Tuning the Xanthan gum concentration so as to equate the elastic number of the Boger fluid will further aid in decoupling the combined effects of suspending medium viscoelasticity and shear thinning on suspension rheology. The use of different polymers with varying properties (i.e. molecular weight, extensibility, elasticity) could enable a better evaluation of the interactions between the silicas, the polymer chains and the suspending medium, opening new insights in tuning suspension rheology through that route. Varying the chemical properties of the polymers and thus, their ability of attaching on to the particle surface will significantly affect the suspension rheological behaviour though influencing the degree/presence of depletion, steric and bridging phenomena.

The present work utilised only viscometric flows to evaluate suspension rheology. However, conventional rheometers are sometimes limited in the shear rate range that can be achieved and thus, might not be able to describe processes where high shear rates are generated, such as spraying ($\dot{\gamma} > 10^5$) or high shear mixing. In such cases, capillary rheometers can be used to extend the shear rate range to higher values required in certain industrial applications. Another technique to study suspension rheology at high frequencies involved the use of a Piezo Axial Vibrator, which has a frequency range between 10 and 10^4 Hz. Non-viscometric flows using simple

geometries, such as pipe flow or straight channels could also be investigated to mimic typical industrial manufacturing conditions and thus, provide better links between academic research and industry.

Microstructure visualisation of the suspensions under shear proved a useful tool in explaining the observed bulk rheological phenomena, especially for the suspensions in mineral oil. However, this study was limited to the dilute concentration regime where single aggregates could be captured and analysed while the visualisation of densely packed suspensions proved challenging. Over the last years attention has been given in the design of perfectly refractive index matched suspensions and their use in Particle Image Velocimetry (PIV) and Laser Induced Fluorescent (LIF) techniques to enable microstructure visualisation of dense suspensions. PIV based techniques or specific fluorescent probes could also be employed as a means to gain valuable information about the local stresses generated within the narrow interparticle gaps as the typical rheological curve refers to the bulk suspension. PIV techniques can measure particle and solvent velocity, which can be used to investigate the deformation field within the suspensions. The latter can be further related to the distribution of the particles in the suspension under flow and provide information about local rheology and stresses.

Confocal microscopy is another technique able to provide microstructure measurements of suspensions at different depts of the sample. Non-optical scattering techniques (e.g. SANS) can also prove useful in understanding suspension microstructure under shear. Obtaining accurate data for suspension microstructure is of crucial importance as it can lead to the development and validation of microstructure-based suspension prediction models.

References

Aliabadian, E., Sadeghi, S., Kamkar, M., Chen, Z., Sundararaj, U., 2018. Rheology of fumed silica nanoparticles/partially hydrolyzed polyacrylamide aqueous solutions under small and large amplitude oscillatory shear deformations. J. Rheol. 62, 1197–1216.

Amiri, A., Øye, G., Sjöblom, J., 2012. Stability and Flow-Induced Flocculation of Fumed Silica Suspensions in Mixture of Water-Glycerol. J. Dispers. Sci. Technol. 338, 1247–1256.

Ancey, C., Lè Ne Jorrot, H., 2001. Yield stress for particle suspensions within a clay dispersion. J. Rheol. 45, 297–319.

Archard, J.F., 1957. Elastic deformation and the laws of friction. Proc. R. Soc. Lond. A 243, 190–205.

Ardakani, H.A., 2014. Rheology of Pastes: Effects of Fibrillation, Thixotropy and Structure. The University of British Columbia.

Asija, N., Chouhan, H., Bhatnagar, N., 2015. Effect of Specific Surface Area on the Shear Rheology of Fumed Silica Dispersions. Delhi.

Barnes, H.A., 2000. A handbook of elementary rheology, 1st ed. The University of Wales Institute of Non-Newtonian Fluid Mechanics, University of Wales.

Barnes, H.A., 1995. A review of the slip (wall depletion) of polymer solutions, emulsions and particle suspensions in viscometers: its cause, character, and cure. J. Non-Newtonian Fluid Mech 56, 221–251.

Barnes, H.A., 1989. Shear-Thickening in suspensions of non-aggregating solid particles dispersed in Newtonian liquids. J. Rheol. 33, 1205–10514.

Batchelor, G.K., Green, D.J.T., 1972. The determination of the bulk stress in a suspension of spherical particles to order c2. J. Fluid Mech 801, 401–427.

Blair, D.L., Mueggenburg, N.W., Marshall, A.H., Jaeger, H.M., Nagel, S.R., 2001. Force distributions in three-dimensional granular assemblies: Effects of packing order and interparticle friction. Phys. Rev. E 63.

Blanc, F., D'Ambrosio, E., Lobry, L., Peters, F., Lemaire, E., 2018. Universal scaling law in frictional non-Brownian suspensions. Phys. Rev. Fluids 3, 114303-1–12.

Blanc, F., Lemaire, E., Meunier, A., Peters, F., Ed Eric Blanc, F., 2013. Microstructure in sheared non-Brownian concentrated suspensions. J. Rheol. 57, 273–292.

Boersma, W.H., Laven, J., Stein, H.N., 1992. Viscoelastic properties of concentrated shear-thickening dispersions. J. Colloid Interface Sci. 149, 10–22.

Bonacucina, G., Martelli, S., Palmieri, G.F., 2004. Rheological, mucoadhesive and release properties of Carbopol gels in hydrophilic cosolvents. Int. J. Pharm. 282, 115-130.

Bossis, G., Boustingorry, P., Grasselli, Y., Meunier, A., Morini, R., Zubarev, A., Volkova, O., 2017. Discontinuous shear thickening in the presence of polymers adsorbed on the surface of calcium carbonate particles. Rheol. Acta 56, 415–430.

Bounoua, S., Lemaire, E., Férec, J., Ausias, G., Kuzhir, P., 2016. Shear-thinning in concentrated rigid fiber suspensions: Aggregation induced by adhesive interactions. J. Rheol. 60, 1279–1300.

Boyd, J., Buick, J.M., Green, S., 2007. Analysis of the Casson and Carreau-Yasuda non-Newtonian blood models in steady and oscillatory flows using the lattice Boltzmann method. Phys. Fluids 19, 093103-1–14.

Boyer, F., Guazzelli, É., Pouliquen, O., 2011. Unifying suspension and granular rheology. Phys. Rev. Lett. 107(18),188301(1-5)

Brown, E., Forman, N.A., Orellana, C.S., Zhang, H., Maynor, B.W., Betts, D.E., Desimone, J.M., Jaeger, H.M., 2010. Generality of shear thickening in dense suspensions. Nat. Mater. 9, 220–224.

Brown, E., Jaeger, H.M., 2014. Shear thickening in concentrated suspensions: phenomenology, mechanisms and relations to jamming. Reports Prog. Phys. Rep. Prog. Phys 77, 46602–23.

Brown, E., Zhang, H., Forman, N.A., Maynor, B.W., Betts, D.E., Desimone, J.M., Jaeger, H.M., 2011b. Shear thickening and jamming in densely packed suspensions of different particle shapes. Phys. Rev. E 84, 31408.

Burlawar, S., Klingenberg, D.J., Root, T.W., Schlafmann, K., Tim Scott, C., 2019. Effect of temperature on the rheology of concentrated fiber suspensions. J. Rheol. 63, 677–691.

Businesswire, 2019. Global $36+ Billion Toothpaste Market, 2024: Growth, Trends and Forecast Analysis from 2019 [WWW Document]. URL https://www.businesswire.com/news/home/20190509005698/en/Global-36-Billion-Toothpaste-Market-2024-Growth

Chang, C., Powell, R.L., 1994. Effect of particle size distributions on the rheology of concentrated bimodal suspensions. J. Rheol. 38, 85–98.

Chang, G.-S., Koo, J.-S., Song, K.-W., 2003. Wall slip of vaseline in steady shear rheometry. Korea-Australia Rheol. J. 15, 55–61.

Chatté, G., Comtet, J., Niguès, A., Bocquet, L., Siria, A., Ducouret, G., Lequeux, F., Lenoir, N., Ovarlez, G., Colin, A., 2018. Shear thinning in non-Brownian suspensions. Soft Matter 14, 865–1070.

Cheal, O., Ness, C., 2018. Rheology of dense granular suspensions under extensional flow. J. Rheol. 62, 501–512.

Chen, D.T.N., Wen, Q., Janmey, P.A., Crocker, J.C., Yodh, A.G., 2010. Rheology of Soft Materials. Annu. Rev. Condens. Matter Phys 1, 301–22.

Chen, S., Øye, G., Sjöblom, J., 2007. Rheological properties of silica particle suspensions in mineral oil. J. Dispers. Sci. Technol. 26, 791–798.

Chen, S., Øye, G., Sjöblom, J., 2005. Rheological Properties of Aqueous Silica Particle Suspensions. J. Dispers. Sci. Technol. 26, 495–501.

Chhabra, R.P., Richardson, J.F., 2008. Non-Newtonian Flow and Applied Rheology, 2nd ed. Butterworth-Heinemann.

Chinesta, F., Ausias, G., 2015. Rheology of Non-spherical Particle Suspensions, 1st ed. ISTE Press Ltd., London.

Choi, H.J., Vinay, S.J., Jhon, M.S., 1999. Rheological properties of particle suspensions in a polymeric liquid. Polymer (Guildf). 40, 2869–2872.

Chu, B., Brady, A.T., Mannhalter, B.D., Salem, D.R., 2014. Effect of silica particle surface chemistry on the shear thickening behaviour of concentrated colloidal suspensions. J. Phys. D Appl. Phys. 47, 7.

Citerne, G.P., Carreau, P.J., Moan, M., 2001. Rheological properties of peanut butter. Rheol. Acta 40, 86–89.

Clavaud, E., Erut, A., Metzger, B., El Forterre, Y., 2017. Revealing the frictional transition in shear-thickening suspensions. Proc. Natl. Acad. Sci. 114, 5147–5152.

Coussot, P., 2014. Yield stress fluid flows: A review of experimental data. J. Nonnewton. Fluid Mech. 211, 31–49.

Cwalina, C.D., Wagner, N.J., 2016. Rheology of non-Brownian particles suspended in concentrated colloidal dispersions at low particle Reynolds number. J. Rheol. 60, 47–59.

D'Avino, G., Greco, F., Maffettone, P.L., 2017. Particle Migration due to Viscoelasticity of the Suspending Liquid and Its Relevance in Microfluidic Devices. Annu. Rev. Fluid Mech 49, 341–60.

D'Avino, G., Greco, F., Maffettone, P.L., 2015. Rheology of a dilute viscoelastic suspension of spheroids in unconfined shear flow. Rheol Acta 54, 915–928.

D'Avino, G., Maffettone, P.L., 2015. Particle dynamics in viscoelastic liquids. J. Nonnewton. Fluid Mech. 215, 80-104.

Datt, C., Elfring, G.J., 2018. Dynamics and rheology of particles in shear-thinning fluids.

Daugan, S., Talini, L., Herzhaft, B., Peysson, Y., Allain, C., 2004. Sedimentation of Suspensions in Shear-Thinning Fluids. Oil Gas Sci. Technol. 59, 71–80.

Davis, R.H., Zhao, Y., Galvin, K.P., Wilson, H.J., 2003. Solid-solid contacts due to surface roughness and their effects on suspension behaviour. R. Soc. 361, 871–894.

De Kretser, R.G., Scales, P.J., 2008. The effect of temperature on the yield stress of mineral suspensions. J. Colloid Interface Sci. 328, 187–193.

De Kruif, C.G., Van Iersel, E.M.F., Vrij, A., Russel, W.B., 1985. Hard sphere colloidal dispersions: Viscosity as a function of shear rate and volume fraction. J. Chem. Phys. 83, 4717–4725.

Denn, M.M., Morris, J.F., 2014. Rheology of non-Brownian suspensions. Annu. Rev. Chem. Biomol. Eng. 5, 203–228.

Dinkgreve, M., Paredes, J., Denn, M.M., Bonn, D., 2016. On different ways of measuring "the" yield stress. J. Nonnewton. Fluid Mech. 238, 233–241.

Dishon, M., Zohar, O., Sivan, U., 2009. From repulsion to attraction and back to repulsion: The effect of NaCl, KCl, and CsCl on the force between silica surfaces in aqueous solution. Langmuir 25, 2831–2836.

Domenech, T., Velankar, S.S., 2017. Microstructure, phase inversion and yielding in immiscible polymer blends with selectively wetting silica particles. J. Rheol. 61, 363–377.

Ducloué, L., Pitois, O., Goyon, J., Chateau, X., Ovarlez, G., 2015. Rheological behaviour of suspensions of bubbles in yield stress fluids. J. Nonnewton. Fluid Mech. 215, 31–39.

Dusting, J., Kaliviotis, E., Balabani, S., Yianneskis, M., 2009. Coupled human erythrocyte velocity field and aggregation measurements at physiological haematocrit levels. J. Biomech. 42, 1438–1443.

Eberle, A.R., Martys, N., Porcar, L., Kline, S.R., George, W.L., Kim, J.M., Butler, P.D., Wagner, N.J., 2014. Shear viscosity and structural scalings in model adhesive hard-sphere gels. Phys. Rev. E 89, 050302-(1-5).

Egres, R.G., Nettesheim, F., Wagner, N.J., 2006. Rheo-SANS investigation of acicular-precipitated calcium carbonate colloidal suspensions through the shear thickening transition. J. Rheol. 50, 685–709.

Egres, R.G., Wagner, N.J., 2005. The rheology and microstructure of acicular precipitated calcium carbonate colloidal suspensions through the shear thickening transition. J. Rheol. 49, 719–746.

Elbishari, H., Satterthwaite, J., Silikas, N., 2011. Effect of filler size and temperature on packing stress and viscosity of resin-composites. Int. J. Mol. Sci. 12, 5330–5338.

Evingür, G.A., Pekcan, O., 2018. Temperature Effect on the Elasticity of Acrylamide-n-Isopropylacrylamide Copolymers. J. Macromol. Sci. Part BPhysics.

Ewoldt, R.H., Hosoi, A.E., Mckinley, G.H., 2008. New measures for characterizing nonlinear viscoelasticity in large amplitude oscillatory shear. J. Rheol. 52, 1427–1155.

Ewoldt, R.H., Hosoi, A.E., McKinley, G.H., 2007. Rheological Fingerprinting of Complex Fluids using Large Amplitude Oscillatory Shear (LAOS) Flow.

Foss, D.R., Brady, J.F., 2000. Structure, diffusion and rheology of Brownian suspensions by Stokesian Dynamics simulation. J. Fluid Mech 407, 167–200.

Frankei, N.A., Acrivos, A., 1967. On the viscosity of a concentrated suspension of solid spheres. Chem. Eng. Sci. 22, 847–853.

Fusier, J., Goyon, J., Chateau, X., Toussaint, F., 2018. Rheology signature of flocculated silica suspensions. J. Rheol. 62, 753–771.

Gadala-Maria, F., Acrivos, A., 1980. Shear-induced structure in a concentrated suspension of solid spheres. J. Rheol. 24, 799–1693.

Galindo-Rosales, F.J., Rubio-Hernandez, F.J., 2009. Static and Dynamic Yield Stresses of Aerosil® 200 Suspensions in Polypropylene Glycol. Appl. Rheol. 20, 22787-1–10.

Gallier, S., Lemaire, E., Peters, F., Lobry, L., 2014. Rheology of sheared suspensions of rough frictional particles. J. Fluid Mech. 757, 514–549.

Gamonpilas, C., Morris, J.F., Denn, M.M., 2016. Shear and normal stress measurements in non-Brownian monodisperse and bidisperse suspensions. J. Rheol. 60, 289–296.

Gao, J., Mwasame, P.M., Wagner, N.J., 2017. Thermal rheology and microstructure of shear thickening suspensions of silica nanoparticles dispersed in the ionic liquid [C 4 mim][BF 4]. J. Rheol. 61, 525–535.

Gaudio, P. Del, Ventura, G., Taddeucci, J., 2013. The effect of particle size on the rheology of liquid-solid mixtures with application to lava flows: Results from analogue experiments. Geochemistry Geophys. Geosystems 14, 2661–2669.

Genovese, D.B., 2012. Shear rheology of hard-sphere, dispersed, and aggregated suspensions, and filler-matrix composites. Adv. Colloid Interface Sci. 171–172, 1–16.

Gillissen, J.J.J., Papadopoulou, A., Tiwari, M.K., Balabani, S., Wilson, H.J., 2020. Suspension rheology of adhesive particles at high shear-rates. Phys. Rev. Fluids 5, 053302.

Giudice, F. Del, Sathish, S., D 'avino, G., Shen, A.Q., 2017. From the Edge to the Center: Viscoelastic Migration of Particles and Cells in a Strongly Shear-Thinning Liquid Flowing in a Microchannel. Anal. Chem. 89, 13146− 13159.

Go, M.-R., Bae, S.-H., Kim, H.-J., Yu, J., Choi, S.-J., 2017. Interactions between Food Additive Silica Nanoparticles and Food Matrices. Front. Microbiol. 8, 1–12.

Gunes, D.Z., Scirocco, R., Mewis, J., Vermant, J., 2008. Flow-induced orientation of non-spherical particles: Effect of aspect ratio and medium rheology. J. Nonnewton. Fluid Mech. 155, 39–50.

Guy, B.M., Hermes, M., Poon, W.C.K., 2015. Towards a Unified Description of the Rheology of Hard-Particle Suspensions. Phys. Rev. Lett. 115.

Hayashi, H., Kawaguchi, M., 2017a. Effects of the degree of surface modification on the rheological responses of precipitated silica suspensions in benzyl alcohol. J. Dispers. Sci. Technol. 38, 737–742.

Hayashi, H., Kawaguchi, M., 2017b. Effects of the degree of surface modification on the rheological responses of precipitated silica suspensions in benzyl alcohol. J. Dispers. Sci. Technol. 38, 737–742.

He, M., Wang, Y., Forssberg, E., 2006. Parameter studies on the rheology of limestone slurries. Int. J. Miner. Process. 78, 63–77.

Hermes, M., Guy, B.M., Poonguilhem, W.C.K., Catesmatthieu Wyart, P.E., Poon, W.C.K., Poy, G., Cates, M.E., Wyart, M., 2016. Unsteady flow and particle migration in dense, non-Brownian suspensions. J. Rheol. 60, 905–916.

Heussinger, C., 2013. Shear thickening in granular suspensions: inter-particle friction and dynamically correlated clusters. Phys. Rev. E 88.

Heymann, L., Peukert, S., Aksel, N., 2002. Investigation of the solid–liquid transition of highly concentrated suspensions in oscillatory amplitude sweeps. J. Rheol. 46, 93-112.

Hoyle, C., Dai, S., Tanner, R., Jabbarzadeh, A., 2020. Effect of particle roughness on the rheology of suspensions of hollow glass microsphere particles. J. Nonnewton. Fluid Mech. 276, 104235.

Hsiao, L.C., Jamali, S., Glynos, E., Green, P.F., Larson, R.G., Solomon, M.J., 2017. Rheological state diagrams for rough colloids in shear flow. Phys. Rev. Lett. 119, 158001(1–6).

Hsu, C.-P., Ramakrishna, S.N., Zanini, M., Spencer, N.D., Isa, L., 2018. Roughness-dependent tribology effects on discontinuous shear thickening. PNAS 115, 1–6.

Hyun, K., Wilhelm, M., Klein, C.O., Cho, K.S., Nam, J.G., Ahn, K.H., Lee, S.J., Ewoldt, R.H., Mckinley, G.H., 2011. A review of nonlinear oscillatory shear tests: Analysis and application of large amplitude oscillatory shear (LAOS). Prog. Polym. Sci. 36, 1697–1753.

Iordan, A., 2009. Rheological properties of biological materials: from cell suspensions to tissues. University Joseph Fourier.

Işçi, S., Güngör, N., Alemdar, A., Isik Ece, Ö., 2007. Influence of clay surface modification on morphology and rheology of polyethylene glycol/montmorillonite nanocomposites. J. Compos. Mater. 41, 1521–1533.

James, D.F., 2009. Boger Fluids. Annu. Rev. Fluid Mech 41, 129–42.

Jeffrey, D.J., Acrivos, A., 1976. The rheological properties of suspensions of rigid particles. AIChE J. 22, 417–432.

Jia, D., Hamilton, J., Zaman, L.M., Goonewardene, A., 2007. The time, size, viscosity, and temperature dependence of the Brownian motion of polystyrene microspheres. Am. J. Phys. Teach. 75, 111–115.

Jones, R., Pollock, H.M., Cleaver, J.A.S., Hodges, C.S., 2002. Adhesion forces between glass and silicon surfaces in air studied by AFM: Effects of relative humidity, particle size, roughness, and surface treatment. Langmuir 18, 8045–8055.

Kaliviotis, E., Dusting, J., Sherwood, J.M., Balabani, S., 2016. Quantifying local characteristics of velocity, aggregation and hematocrit of human erythrocytes in a microchannel flow. Clin. Hemorheol. Microcirc. 63, 123–148.

Kaliviotis, E., Yianneskis, M., 2007. On the effect of dynamic flow conditions on blood microstructure investigated with optical shearing microscopy and rheometry. Proc. Inst. Mech. Eng. Part H J. Eng. Med. 221, 887–897.

Kalman, D.P., Wagner, N.J., 2009. Microstructure of shear-thickening concentrated suspensions determined by flow-USANS. Rheol. Acta 48, 897–908.

Katepalli, H., John, V.T., Tripathi, A., Bose, Arijit, Bose, A, 2017. Microstructure and rheology of particle stabilized emulsions: Effects of particle shape and inter-particle interactions. J. Colloid Interface Sci. 485, 11–17.

Khandavalli, S., Rothstein, J.P., 2015. Large amplitude oscillatory shear rheology of three different shear-thickening particle dispersions. Rheol Acta 54, 601–618.

Ki-Won Song, Hoa-Youn Kuk, Gap-Shik Chang, 2006. Rheology of concentrated xanthan gum solutions: Oscillatory shear flow behavior. Korea-Australian Rheol. J. 18, 67–81.

Kim, C., 2001. Migration in concentrated suspension of spherical particles dispersed in polymer solution, Korea-Australia Rheology Journal. 13, 19-27.

Kitano, T., Kataoka, T., Shirota, T., 1981. An empirieal equation of the relative viscosity of polymer melts filled with various inorganic fillers. Rheol. Acta 20, 207–209.

Konijn, B.J., Sanderink, O.B.J., Kruyt, N.P., 2014. Experimental study of the viscosity of suspensions: Effect of solid fraction, particle size and suspending liquid. Powder Technol. 266, 61–69.

Krieger, Irvin M., Dougherty, T.J., 1959. A mechanism for non-Newtonian flow in suspensions of rigid spheres. Trans. Soc. Rheol. 3, 137–152.

Krieger, Irvin M, Dougherty, T.J., 1959. A Mechanism for Non-Newtonian Flow in Suspensions of Rigid Spheres. Trans. Soc. Rheol. 3, 137–152.

Lamer, T.F., Thomas, B.R., Curtis, D.J., Badiei, N., Williams, P.R., Hawkins, K., 2017. The application of large amplitude oscillatory stress in a study of fully formed fibrin clots. Phys. Fluids 29.

Lee, Y.-F., Luo, Y., Brown, S.C., Wagner, N.J., 2020. Experimental test of a frictional contact model for shear thickening in concentrated colloidal suspensions. J. Rheol. 64, 267–282.

Liard, M., Martys, N.S., George, W.L., Lootens, D., Hebraud, P., 2014. Scaling laws for the flow of generalized Newtonian suspensions. J. Rheol. 58, 1993–2015.

Lin, N.Y.C., Guy, B.M., Hermes, M., Ness, C., Sun, J., Poon, W.C.K., Cohen, I., 2015. Hydrodynamic and contact contributions to continuous shear thickening in colloidal suspensions. Phys. Rev. Lett. 115, 228304(1–6).

Lin, N.Y.C., Ness, C., Cates, M.E., Sun, J., Cohen, I., 2016. Tunable shear thickening in suspensions. PNAS 113, 10774–10778.

Lin, Y.-J., Barman, S., He, P., Zhang, Z., Christopher, G.F., Lisa Biswal, S., 2018. Combined interfacial shear rheology and microstructure visualization of asphaltenes at air-water and oil-water interfaces. J. Rheol. 62 (1), 1-10.

Liu, X.-Q., Bao, R.-Y., Wu, X.-J., Yang, W., Xie, B.-H., Yang, M.-B., 2019. Temperature induced gelation transition of fumed silica/PEG shear thickening fluid. R. Soc. Chem. Adv.

Liu, Z., Liu, L., Zhou, H., Wang, J., Deng, L., 2015. Toothpaste microstructure and rheological behaviors including aging and partial rejuvenation. Korea-Australia Rheol. J. 27, 207–212.

Lobry, L., Lemaire, E., Blanc, F., Gallier, S., Peters, F., 2019. Shear thinning in non-Brownian suspensions explained by variable friction between particles. J. Fluid Mech. 860, 682–710.

Luckham, P.F., Ukeje, M.A., 1999. Effect of particle size distribution on the rheology of dispersed systems. J. Colloid Interface Sci. 220, 347–356.

Ma, A.W.K., Mackley, M.R., Chinesta, F., 2008. The microstructure and rheology of carbon nanotube suspensions. Int. J. Mater. Form. 1, 75–81.

Ma, L., Xu, J., Coulombe, P.A., Wirtz, D., 1999. Keratin filament suspensions show unique micromechanical properties. J. Biol. Chem. 274, 19145–19151.

Ma, T., Yang, R., Zheng, Z., Song, Y., 2017. Rheology of fumed silica/polydimethylsiloxane suspensions. J. Rheol. 61, 205–215.

Macosko, C.W., 1994. Rheology: Principles, Measurements and Applications, 1st ed. Wiley-VCH, United States of America.

Mader, H.M., Llewellin, E.W., Mueller, S.P., 2013. The rheology of two-phase magmas: A review and analysis. J. Volcanol. Geotherm. Res. 257, 135–158.

Madraki, Y., Ovarlez, G., Hormozi, S., 2018. Transition from Continuous to Discontinuous Shear Thickening: An Excluded-Volume Effect. Phys. Rev. Lett. 121.

Malvern Instruments, 2012. Understanding yield stress measurements.

Maranzano, B.J., Wagner, N.J., 2001a. The effects of particle size on reversible shear thickening of concentrated colloidal dispersions. J. Chem. Phys. 114, 10514–10527.

Maranzano, B.J., Wagner, N.J., 2001b. The effects of interparticle interactions and particle size on reversible shear thickening: Hard-sphere colloidal dispersions. J. Rheol. 451, 1205–111.

Marcovich, N.E., Reboredo, M.M., Kenny, J., Aranguren, M.I., 2004. Rheology of particle suspensions in viscoelastic media. Wood flour-polypropylene melt. Rheol. Acta 43, 293–303.

Mari, R., Seto, R., Morris, J.F., Denn, M.M., 2015a. Nonmonotonic flow curves of shear thickening suspensions. Phys. Rev. E 91.

Mari, R., Seto, R., Morris, J.F., Denn, M.M., 2015b. Discontinuous shear thickening in Brownian suspensions by dynamic simulation. Proc. Natl. Acad. Sci. U. S. A. 112, 15326–30.

Mari, R., Seto, R., Morris, J.F., Denn, M.M., 2014. Shear thickening, frictionless and frictional rheologies in non- Brownian suspensions. J. Rheol. 58, 1693–1724.

Marunaka, R., Kawaguchi, M., 2017. Rheological behavior of hydrophobic fumed silica suspensions in aromatic dispersion media. J. Dispers. Sci. Technol. 38, 223–228.

Marunaka, R., Kawaguchi, M., 2014. Rheological behavior of hydrophobic fumed silica suspensions in different alkanes. Colloids Surfaces A Physicochem. Eng. Asp. 456, 75–82.

Massaro, R., Colombo, G., Puyvelde, P. Van, Vermant, J., 2020. Viscoelastic cluster densification in sheared colloidal gels. Soft Matter 16, 2437–2447.

Maurath, J., Bitsch, B., Schwegler, Y., Willenbacher, N., 2016. Influence of particle shape on the rheological behavior of three-phase non-brownian suspensions. Asp. Colloids Surfaces A Physicochem. Eng. Asp. 497, 316–326.

McKinley, G., 2012. Motivation for LAOS!, in: Int. Congress Rheology. Lisbon.

Mewis, J., Wagner, N.J., 2012. Colloidal Suspension Rheology, 1st ed. Cambridge University Press, New York.

Miller, R.R., Lee, E., Powell, R.L., 1991. Rheology of solid propellant dispersions. J. Rheol. 35, 901–919.

Min Kim, J., Eberle, A.P.R., Kate Gurnon, A., Porcar, L., Wagner, N.J., 2014. The microstructure and rheology of a model, thixotropic nanoparticle gel under steady shear and large amplitude oscillatory shear (LAOS). J. Rheol. 58, 1301–1328.

Moon, J.Y., Dai, S., Chang, L., Lee, J.S., Tanner, R.I., 2015. The effect of sphere roughness on the rheology of concentrated suspensions. J. Nonnewton. Fluid Mech. 223, 233–239.

Morris, J.F., 2009. A review of microstructure in concentrated suspensions and its implications for rheology and bulk flow. Rheol. Acta 48, 909–923.

Mueller, S., Llewellin, E.W., Mader, A.H.M., 2010. The rheology of suspensions of solid particles. Proc. R. Soc. A 466, 1201–1228.

Mueller, S., Llewellin, E.W., Mader, H.M., 2011. The effect of particle shape on suspension viscosity and implications for magmatic flows. Geophys. Res. Lett. 38, L13316(1-5).

Mwasame, P.M., Wagner, N.J., Beris, A.N., 2016. Modeling the effects of polydispersity on the viscosity of noncolloidal hard sphere suspensions. J. Rheol. 60, 225–240.

Narumi, T., See, H., Suzuki, A., Hasegawa, T., 2005. Response of concentrated suspensions under large amplitude oscillatory shear flow. J. Rheol. 49, 71–85.

Ndong, R.S., Russel, W.B., 2012. Rheology of surface-modified titania nanoparticles dispersed in PDMS melts: The significance of the power law. J. Rheol. 56, 27–43.

Ness, C., Sun, J., 2016a. Shear thickening regimes of dense non-Brownian suspensions. Soft Matter 12, 914–924.

Ness, C., Sun, J., 2016b. Two-scale evolution during shear reversal in dense suspensions. Phys. Rev. E 93.

Ness, C., Sun, J., 2015. Flow regime transitions in dense non-Brownian suspensions: Rheology, microstructural characterization, and constitutive modeling. Phys. Rev. E 91.

Nguyen, C.T., Desgranges, F., Roy, G., Galanis, N., Maré, T., Boucher, S., Mintsa, H.A., 2007. Temperature and particle-size dependent viscosity data for water-based nanofluids – Hysteresis phenomenon. Int. J. Heat Fluid Flow 28, 1492–1506.

Nicodemo, L., Nicolais, L., Landel, R.F., 1974. Shear rate dependent viscosity of suspensions in newtonian and non-newtonian liquids. Chem. Eng. Sci. 29, 729–735.

Niu, R., Gong, J., Xu, D.-H., Tang, T., Sun, Z.-Y., 2015. The effect of particle shape on the structure and rheological properties of carbon-based particle suspensions. Chinese J. Polym. Sci. 33, 1550–1561.

Norisuye, T., 2017. Structures and dynamics of microparticles in suspension studied using ultrasound scattering techniques. Polym. Int. 66, 175–186.

Olanrewaju, K.O., Bae, T.H., Nair, S., Breedveld, V., 2013. The rheology of suspensions of porous zeolite particles in polymer solutions. Rheol. Acta 53, 133–141.

Ovarlez, G., Mahaut, F., Deboeuf, S., Lenoir, N., Hormozi, S., Chateau, X., 2015. Flows of suspensions of particles in yield stress fluids. J. Rheol. 59, 1449–1486.

Pal, R., 2015. Rheology of Suspensions of Solid Particles in Power-Law Fluids. Can. J. Chem. Eng. 93, 166–173.

Pan, Z., De Cagny, H., Weber, B., Bonn, D., 2015. S-shaped flow curves of shear thickening suspensions: Direct observation of frictional rheology. Phys. Rev. E 92, 032202(1–5).

Papadopoulou, A., Gillissen, J.J., Wilson, H.J., Tiwari, M.K., Balabani, S., 2020. On the shear thinning of non-Brownian suspensions: Friction or adhesion? J. Nonnewton. Fluid Mech. 281, 104298.

Patankar, N.A., Hu, H.H., 2001. Rheology of a suspension of particles in viscoelastic fluids. J. Nonnewton. Fluid Mech. 96, 427–443.

Pavlik, M., 2009. The dependence of suspension viscosity on particle size, shear rate, and solvent viscosity. College of Liberal Arts and Sciences.

Peyla, P., Verdier, C., 2011. New confinement effects on the viscosity of suspensions. EPL 94.

Potanin, A., 2019. Rheology of silica dispersions stabilized by polymers. Colloids Surfaces A Physicochem. Eng. Asp. 562, 54–60.

Qin Xu, Sayantan Majumdar, EricBrown, Heinrich M. Jaeger, 2014. Shear thickening in highly viscous granular suspensions. EPL 107, 68004(1–6).

Quemada, D., 1978. Rheology of concentrated disperse systems II. A model for non-newtonian shear viscosity in steady flows. Rheol. Acta 17, 632–642.

Raghavan, S.R., Khan, S.A., 1997. Shear-thickening response of fumed silica suspensions under steady and oscillatory shear. J. Colloid Interface Sci. 185, 57–67.

Raghavan, S.R., Walls, H.J., Khan, S.A., 2000. Rheology of silica dispersions in organic liquids: New evidence for solvation forces dictated by hydrogen bonding. Langmuir 16, 7920–7930.

Rao, M.A., 2014. Flow and functional models for rheological properties of fluid foods, in: Rheology of Fluid, Semisolid, and Solid Foods. Springer, New York, pp. 27–36.

Rathee, V., Arora, S., Blair, D.L., Urbach, J.S., Sood, A.K., Ganapathy, R., 2019. Unraveling the Role of Frictional Contacts and Particle Orientational Order During Shear-thickening in Suspensions of Colloidal Rods.

Rochefort, W.E., Middleman, S., 1987. Rheology of Xanthan Gum: Salt, Temperature, and Strain Effects in Oscillatory and Steady Shear Experiments. J. Rheol. 31, 337–369.

Rothstein, J.P., McKinley, G.H., 2001. Non-isothermal modification of purely elastic flow instabilities in torsional flows of polymeric fluids. Phys. Fluids 13, 382–396.

Royer, J.R., Blair, D.L., Hudson, S.D., 2016. Rheological signature of frictional interactions in shear thickening suspensions. Phys. Rev. Lett. 116, 188301(1–5).

Rutgers, I.R., 1962. Relative viscosity of suspensions of rigid spheres in Newtonian liquids. Rheol. Acta. h

Saint-Michel, B., Manneville, S., Meeker, S., Ovarlez, G., Bodiguel, H., 2019. X-ray Radiography of Viscous Resuspension. Phys. Fluids 31, 103301-1–17.

Saito, Yu, Hirose, Yuji, Otsubo, Y., Saito, Y, Hirose, Y, Otsubo, · Y, 2011. Effect of poly(ethylene oxide) on the rheological behavior of silica suspensions. Rheol Acta 50, 291–301.

Sarkar, S., Shatoff, E., Ramola, K., Mari, R., Morris, J., Chakraborty, B., 2017. Shear-induced organization of forces in dense suspensions: signatures of discontinuous shear thickening. Powders & Grains 140, 09045(1–4).

Scirocco, R., Vermant, J., Mewis, J., 2005. Shear thickening in filled Boger fluids. J. Rheol. 49, 551–567.

Scirocco, R., Vermant, J., Mewis, J., 2004. Effect of the viscoelasticity of the suspending fluid on structure formation in suspensions. J. Non-Newtonian Fluid Mech 117, 183–192.

Selimovic, S., Hu, Y., 2014. Aging effects in suspensions of silica particles. Mat. Res. Soc. Symp. Proc. 790, 7.11(1–6).

Selimovic, S., Maynard, S.M., Hu, Y., 2007. Aging effects of precipitated silica in poly(dimethylsiloxane). J. Rheol. 51, 325–340.

Servais, C., Jones, R., Roberts, I., 2002. The influence of particle size distribution on the processing of food. J. Food Eng. 51, 201–208.

Seto, R., Mari, R., Morris, J.F., Denn, M.M., 2013. Discontinuous shear thickening of frictional hard-sphere suspensions. Phys. Rev. 111, 218301(1–5).

Shaqfeh, E.S.G., 2019. On the rheology of particle suspensions in viscoelastic fluids. AIChE J. 65, e16575.

Shenoy, A. V., 1999. Rheology of Filled Polymer Systems, First. ed. Kluwer Academic Publishers, Dordrecht, The Netherlands.

Sierou, A., Brady, J.F., 2002. Rheology and microstructure in concentrated noncolloidal suspensions. J. Rheol. 46, 1031–1056.

Singh, R., Sanchez, O., Ghosh, S., Kadimcherla, N., Sen, S., Balasubramanian, G., 2015. Viscosity of magnetite–toluene nanofluids: Dependence on temperature and nanoparticle concentration. Phys. Lett. A 379, 2641–2644.

Snabre, P., Mills, P., 1996. 1. Rheology of Weakly Flocculated Suspensions of Rigid Particles. J. Phys. III 6, 1811–1834.

Song, J., Huang, S., Lu, Y., Bu, X., Mates, J.E., Ghosh, A., Ganguly, R., Carmalt, C.J., Parkin, I.P., Xu, W., Megaridis, C.M., 2014. Self-Driven One-Step Oil Removal from Oil Spill on Water via Selective-Wettability Steel Mesh. Appl. Mater. interfaces 6, 19858−19865.

Sousa, P.C., Pinho, F.T., Alves, M.A., Oliveira, M.S.N., 2016. A review of hemorheology: Measuring techniques and recent advances. Korea Aust. Rheol. J. 28, 1–22.

Stamm, J.W., 2007. Multi-function toothpastes for better oral health: a behavioural perspective. Int. Dent. J. 57, 351–363.

Stickel, J.J., Powell, R.L., 2005. Fluid mechanics and rheology of dense suspensions. Annu. Rev. Fluid Mech 37, 129–49.

Sugino, Y., Kawaguchi, M., 2017. Fumed and precipitated hydrophilic silica suspension gels in mineral oil: stability and rheological properties. Gels 3, 1–12.

TA Instruments, 2014. Rheology Theory and Applications.

Tanner, R.I., 2019a. Rheology of noncolloidal suspensions with non-Newtonian matrices. J. Rheol. 63, 705.

Tanner, R.I., 2018. Aspects of non-colloidal suspension rheology. Phys. Fluids 30, 101301(1–13).

Tanner, R.I., 2015. Non-colloidal suspensions: Relations between theory and experiment in shearing flows. J. Nonnewton. Fluid Mech. 222, 18–23.

Tanner, R.I., Dai, S., 2016a. Particle roughness and rheology in noncolloidal suspensions. J. Rheol. 60, 809–818.

Tanner, R.I., Dai, S., 2016b. Rheology of non-colloidal suspensions with corn syrup matrices. Rheol. Acta 35, 739–747.

Tanner, R.I., Ness, C., Mahmud, A., Dai, S., Moon, J., 2018. A bootstrap mechanism for non-colloidal suspension viscosity. Rheol. Acta 57, 635–643.

Townsend, A.K., Wilson, H.J., 2017. Frictional shear thickening in suspensions: The effect of rigid asperities. Phys. Fluids 29, 121607–121607.

Trofa, M., D'Avino, G., 2020. Rheology of a Dilute Suspension of Aggregates in Shear-Thinning Fluids. Micromachines 11, 443.

Trofa, M., D'Avino, G., Hulsen, M.A., Maffettone, P.L., 2016. The effect of wall slip on the dynamics of a spherical particle in Newtonian and viscoelastic fluids subjected to shear and Poiseuille flows. J. Nonnewton. Fluid Mech. 236, 123–131.

Truby, J.M., Mueller, S.P., Llewellin, E.W., Mader, H.M., 2015. The rheology of three-phase suspensions at low bubble capillary number. Proc. R. Soc. A 471, 1–18.

Trulsson, M., Degiuli, E., Wyart, M., 2017. Effect of friction on dense suspension flows of hard particles. Phys. Rev. E 95, 012605(1–7).

Valmacco, V., Elzbieciak-Wodka, M., Besnard, C., Maroni, P., Trefalt, G., Borkovec, M., 2016. Dispersion forces acting between silica particles across water: Influence of nanoscale roughness. Nanoscale Horizons 1, 325–330.

Varga, Z., Grenard, V., Pecorario, S., Taberlet, N., Dolique, V., Manneville, S., Divoux, T., McKinley, G.H., Swan, J.W., 2019. Hydrodynamics control shear-induced pattern formation in attractive suspensions. Proc. Natl. Acad. Sci. 116, 12193–12198.

Vázquez-Quesada, A., Español, P., Tanner, R.I., Ellero, M., 2019. Shear thickening of a non-colloidal suspension with a viscoelastic matrix. J. Fluid Mech. 880, 1070–1094.

Vázquez-Quesada, A., Mahmud, A., Dai, S., Ellero, M., Tanner, R.I., 2017. Investigating the causes of shear-thinning in non-colloidal suspensions: Experiments and simulations. J. Nonnewton. Fluid Mech. 248, 1–7.
Vázquez-Quesada, A., Tanner, R.I., Ellero, M., 2016. Shear Thinning of Noncolloidal Suspensions. Phys. Rev. Lett. 117, 108001(1–5).

Vryzas, Z., Kelessidis, V.C., Nalbantian, L., Zaspalis, V., Gerogiorgis, D.I., Wubulikasimu, Y., 2017. Effect of temperature on the rheological properties of neat aqueous Wyoming sodium bentonite dispersions. Appl. Clay Sci.

Vryzas, Z., Wubulikasimu, Y., Gerogiorgis, D.I., Vassilios C. Kelessidis, 2016. Understanding the temperature effect on the rheology of water-bentonite suspensions, in: Annual Transactions of the Nordic Society of Rheology .

Warren, J., Offenberger, S., Toghiani, H., Pittman, C.U., Lacy, T.E., Kundu, S., 2015. Effect of temperature on the shear-thickening behavior of fumed silica suspensions. Appl. Mater. Interfaces 7, 18650–18661.

Won, D., Kim, C., 2004. Alignment and aggregation of spherical particles in viscoelastic fluid under shear flow. J. Nonnewton. Fluid Mech. 117, 141–146.

Yang, M., Shaqfeh, E.S.G., 2018a. Mechanism of shear thickening in suspensions of rigid spheres in Boger fluids. Part I: Dilute suspensions. J. Rheol. 62, 1363.

Yang, M., Shaqfeh, E.S.G., 2018b. Mechanism of shear thickening in suspensions of rigid spheres in Boger fluids. Part II: Suspensions at finite concentration. J. Rheol. 62, 1379.

Yao Lu, Sanjayan Sathasivam, Jinlong Song, Colin R. Crick, Claire J. Carmalt, Ivan P. Parkin, 2015. Robust self-cleaning surfaces that function when exposed to either air or oil. Repel. Mater. 347, 1132–1135.

Young, S., Wong, M., Tabata, Y., Mikos, A.G., 2005. Gelatin as a delivery vehicle for the controlled release of bioactive molecules, in: Journal of Controlled Release. pp. 256–274.

Yüce, C., Willenbacher, N., 2017. Challenges in rheological characterization of highly concentrated suspensions — A case study for screen-printing silver pastes. J. Vis. Exp 122, 55377(1–17).

Zarraga, I.E., Hill, D.A., Leighton, D.T., 2001. Normal stresses and free surface deformation in concentrated suspensions of noncolloidal spheres in a viscoelastic fluid. J. Rheol. 45, 1065–1084.

Zarraga, I.E., Hill, D.A., Leighton, D.T., 2000. The characterization of the total stress of concentrated suspensions of noncolloidal spheres in Newtonian fluids. J. Rheol. 44, 185–220.

Zenit, R., Feng, J.J., 2018. Hydrodynamic Interactions Among Bubbles, Drops, and Particles in Non-Newtonian Liquids. Annu. Rev. Fluid Mech 50, 505–34.

Zhang, S., Sha, N., Zhao, Z., 2017. Surface modification of α-Al2O3 with dicarboxylic acids for the preparation of UV-curable ceramic suspensions. J. Eur. Ceram. Soc. 37, 1607–1616.

Zhou, J.Z.Q., Tunan Fang, Guihua Luo, Peter HT Uhlherr, 1995. Yield stress and maximum packing fraction of concentrated suspensions. Rheol. Acta 34, 544–561.

Zhuravlev, L.T., 2000. The surface chemistry of amorphous silica. Zhuravlev model. Colloids Surfaces A Physicochem. Eng. Asp. 173, 1–38.

Zhuravlev, L.T., Potapov, V. V, 2006. Density of silanol groups on the surface of silica precipitated from a hydrothermal solution. Russ. J. Phys. Chem. 80, 1119–1128.

Appendices

Appendix I Frictional suspensions

I.1 Effect of the solvent viscosity on the viscoelastic moduli at 20°C

In an attempt to determine the contribution of the solvent viscosity to the loss/ viscous modulus of the suspensions and obtain an estimation of the apparent relaxation time of the suspension, the solvent viscosity multiplied by the angular frequency ($\omega\eta_f$) is subtracted from the G'' values. The estimated moduli, denoted as G''^*, are presented in Figure I.1 as a function of ω and φ. It can be seen that subtracting the solvent contribution from the G'' values does not influence the measured trends; the suspensions remain strongly viscous dominated ($G'' > G'$), while no crossover of the two moduli could be obtained. Therefore, the relaxation times of most suspensions are possibly low and cannot be estimated for the present frequency sweeps, as they lie outside the frequency limits applied.

The effect of the thick solvation layer around the glass and silica particles formed by the glycerol can be two-fold; on one hand, the viscosity and subsequently the loss modulus, G'', of the suspension increases due to the particle addition, while, on the other hand, the presence of the solvent layer inhibits the real interparticle contacts and minimises the possibility of particle adhesion-gelation. Therefore, in most cases the measured elastic component (G') of the suspension remains lower than the viscous one (G'') (Amiri et al., 2012; Boersma et al., 1992; Gao et al., 2017).

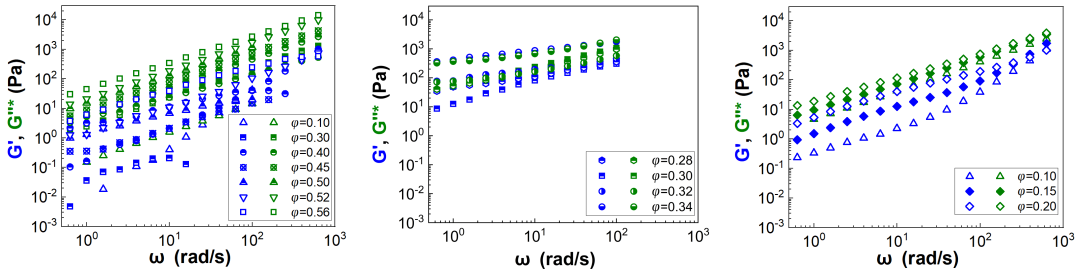

(a) (b) (c)

Figure I.1: Storage (G') and normalised loss moduli (G''^*) as a function of angular frequency (ω) for all suspensions in glycerol; a) glass spheres, b) abrasive silicas and c) filler silicas at 20°C. The G''^* represent the G'' after subtracting the solvent contribution to the values, i.e. $G''^* = G'' - \omega\eta_f$ ($\eta_f = 1.3\ Pa.s$).

I.2 Effect of temperature on the LVR

The effect of temperature on the linear viscoelastic region of the suspensions was also tested through small amplitude oscillatory shear experiments (SAOS) and an indicative example is presented in Figure I.2 for an abrasive silica suspension in glycerol at $\varphi = 0.30$ and at the two temperatures (20°C, 60°C). it can be seen that the extent of the LVR is not significantly affected by the temperature conditions applied and thus, the same strain amplitude of $\gamma = 10^{-1}$ % was applied to all frequency sweeps performed independent of the temperature and particle characteristics.

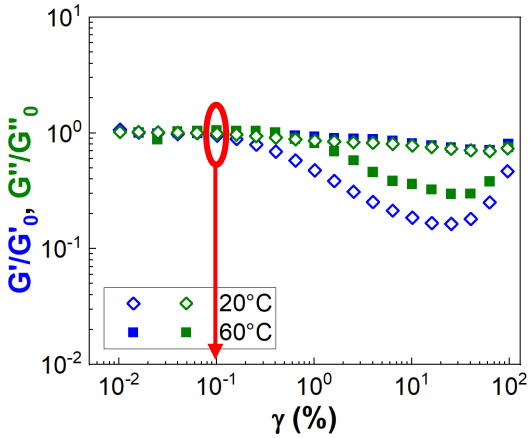

Figure I.2: Indicative small amplitude oscillatory shear measurements for defining the linear viscoelastic region (LVR) at a frequency of $f = 1Hz$. Comparison of the normalised G' and G'' for a 30% v/v abrasives suspension in glycerol between 20°C and 60°C.

I.3 Effect of temperature on the rheology of selected suspensions (at the onset of non-Newtonian response)

This section describes the changes in suspension rheology with a gradual increase in temperature from 20°C to 60°C in increments of 10°C.

I.3.1 Glass spheres, $\varphi = 0.50$

Figure I.3 summarizes the rheology of the 50% v/v glass sphere suspension under steady state shear, while the response of the suspension under dynamic oscillatory shear is presented in Figure I.4 and Figure I.5. The gradual evolution of the shear thinning behaviour and the subsequent suppression of the shear thickening monitored at increasing temperatures from 20°C to 60°C can be seen in Figure I.3a. Fitting the Carreau equation to the viscosity versus shear rate data in the shear thinning region

of the curve yields an exponential decrease of the flow indices (Figure I.3b) indicating the increase in shear thinning. The apparent yield stress (Figure I.3c) values derived by extrapolating the shear stress curves at $\dot{\gamma}_{\to 0}$ also show an exponential increase with temperature; this is attributed to a decrease in the strength of the solvation layer around the particles due to the higher kinetic energy of both the glycerol molecules and the solid phase (Gao et al., 2017) with increasing temperature. The latter enables stronger interparticle interactions between the particles resulting in pronounced shear thinning and yield stress.

Except the thickness of the solvation layer, other factors can also promote shear thinning behaviour such as the effect of Brownian motion. Brownian effects are expected to occur in this case due to the high polydispersity of the glass sphere. The ratio of the particles able to induce Brownian motion compared to the non-Brownian ones was estimated by looking at the size distribution of the particles and assuming $Pe = 10$. The ratio was found 4% at 20°C, while it increased to 15% at 60°C at a low shear rate of $\dot{\gamma} = 0.004\ s^{-1}$. The suppression of the shear thickening (Figure I.3a) with temperature can be attributed to a decrease in the hydrodynamic force and its inability to surpass the sum of the repulsive forces acting on the particles.

Additionally, Figure I.3d shows the variation of the zero shear rate ($\eta_{r,0}$) and infinite shear rate ($\eta_{r,\infty}$) relative viscosities with temperature. The $\eta_{r,\infty}$ values were estimated from the flow curve region before the onset of shear thickening. The rate of increase in these parameters with temperature illustrates the change in shear thinning behaviour, e.g. $\eta_{r,0}$ values increase much faster than $\eta_{r,\infty}$ leading to increased shear thinning with temperature. The high frequency relative viscosity $\eta'_{r,\infty}$ representing the hydrodynamic contribution to the suspension viscosity is also shown in the same figure. This parameter is always smaller than the total relative viscosity at infinite shear indicating that suspension rheology is governed not only by hydrodynamics but also particle contacts (Mewis and Wagner, 2012).

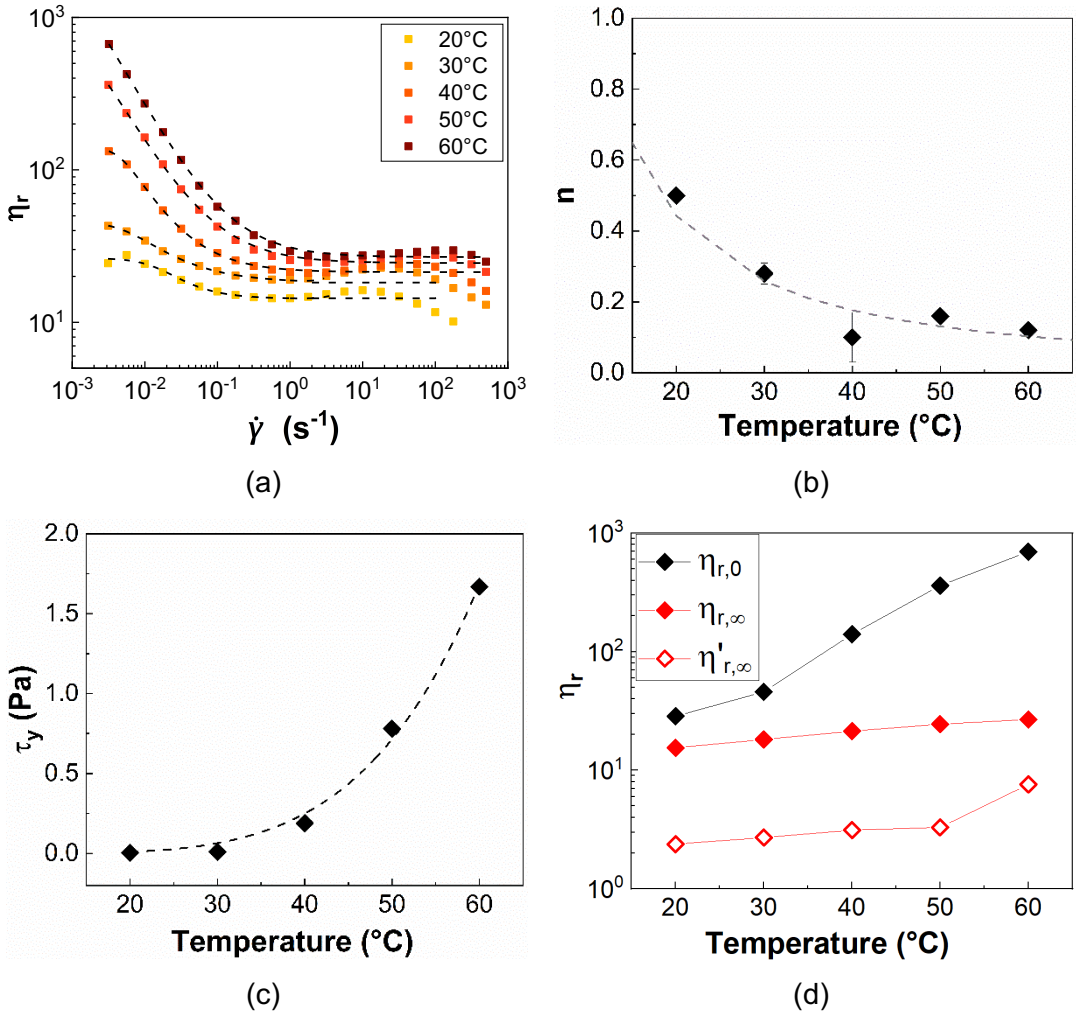

Figure I.3: a) Relative viscosity (η_r) as a function of shear rate ($\dot{\gamma}$) and temperature of the 50% v/v glass sphere suspension in glycerol; Dashes lines correspond to the Carreau-Yasuda equation fitting at the shear thinning area; b) flow index (n), c) zero-shear ($\eta_{r,0}$), infinite-shear ($\eta_{r,\infty}$) relative viscosity and high frequency relative viscosity ($\eta'_{r,\infty}$) and d) apparent yield stress values (τ_y) as a function of temperature.

The dependence of the viscoelastic properties of the glass sphere suspensions on temperature are illustrated in Figure I.4. Both moduli (G', G'') decrease with increasing temperature, with G'' showing a slightly higher sensitivity than G', for temperatures between 20ºC and 60ºC. The measured phase angles (Figure I.4b) also decrease with temperature indicating an increase in the viscoelasticity of the material, which is in accordance with the steady state shear results and the enhancement of the shear thinning rheology discussed in Chapter 3.

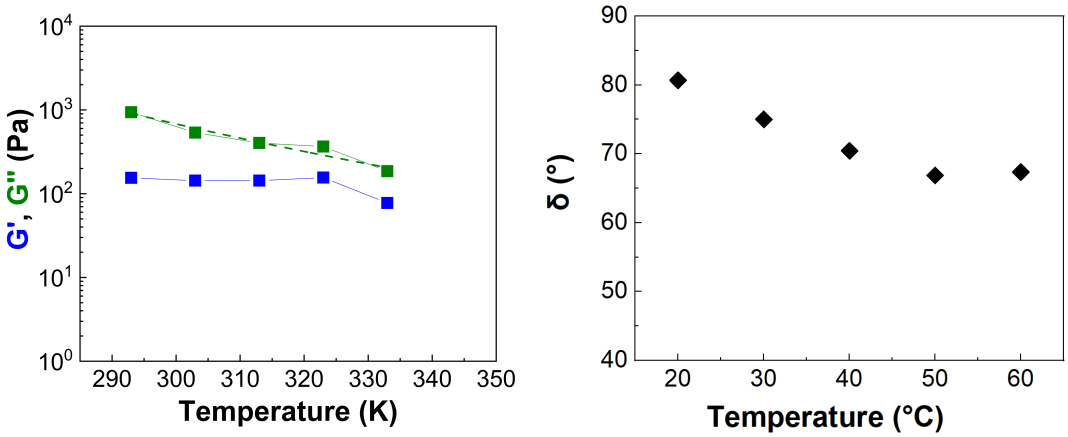

(a) (b)

Figure I.4: a) Storage (G') and loss moduli (G'') as a function of temperature (in Kelvin-K to enable the Arrhenius fitting) and b) phase angle as a function of temperature generated from frequency sweeps in the LVR at $f = 10Hz$ for the 50% v/v glass spheres suspension in glycerol.

Oscillatory temperature ramps were performed in the LVR ($\gamma = 0.2\%$, $f = 1\ Hz$) with temperatures varying from 20°C to 60°C. Figure I.5a, b and c summarise the results obtained after subsequent heating and cooling steps. The sample was first heated (Step 1) at a rate of 2°C/min and then cooled (Step 2) after a resting time of 3 mins using the same cooling rate. An additional heating step (Step 3) was performed to evaluate the reversibility of the different phenomena. The storage modulus (G') (Figure I.5a) increases by one order of magnitude with increasing the temperature (θ), while the G'' values show (Figure I.5b) a weaker increase. The latter is in contrast to what was observed in Figure I.4a where both moduli decrease with temperature.

During the temperature sweep longer heating times are applied and thus, the particle-particle interactions have more time to build up. The disruption of the solvation layer might also be more pronounced at longer heating times allowing a higher degree of particle-particle contacts. However, the solvation layer is never completely eliminated preventing the formation of a strongly elastic particle network. This is reflected through the viscous dominated response of the suspensions at all temperatures comparing the data presented in Figure I.5a and b, i.e. $G'' > G'$, and the measured phase angles (δ) (Figure I.5c) remain within the viscoelastic regime with values ranging from 90° to 40°.

Upon cooling (Step 2), the two moduli exhibit higher values compared to those obtained at Step 1, especially at $\theta \leq 40°C$. Successive heating of the suspension (Step 3) managed to recover G' to its initial values during step 1 only at relatively high temperatures. This behaviour indicates the lack of a complete reversibility during the

heating process (Step 1); this can be partially attributed to particle agglomeration in parallel to the frictional contacts between the particles at higher temperatures might be responsible for this behaviour (Liu et al., 2019). On the contrary, a better agreement between the two heating steps (Step 1 and Step 3) is observed for the G'' values with small deviations occurring at $\theta \leq 30°C$. The decrease of the measured phases angles (δ) in Figure I.5c further indicates the increase in the viscoelasticity of the suspensions with temperature and the irreversibility of the mechanisms involved upon heating the glass sphere suspension.

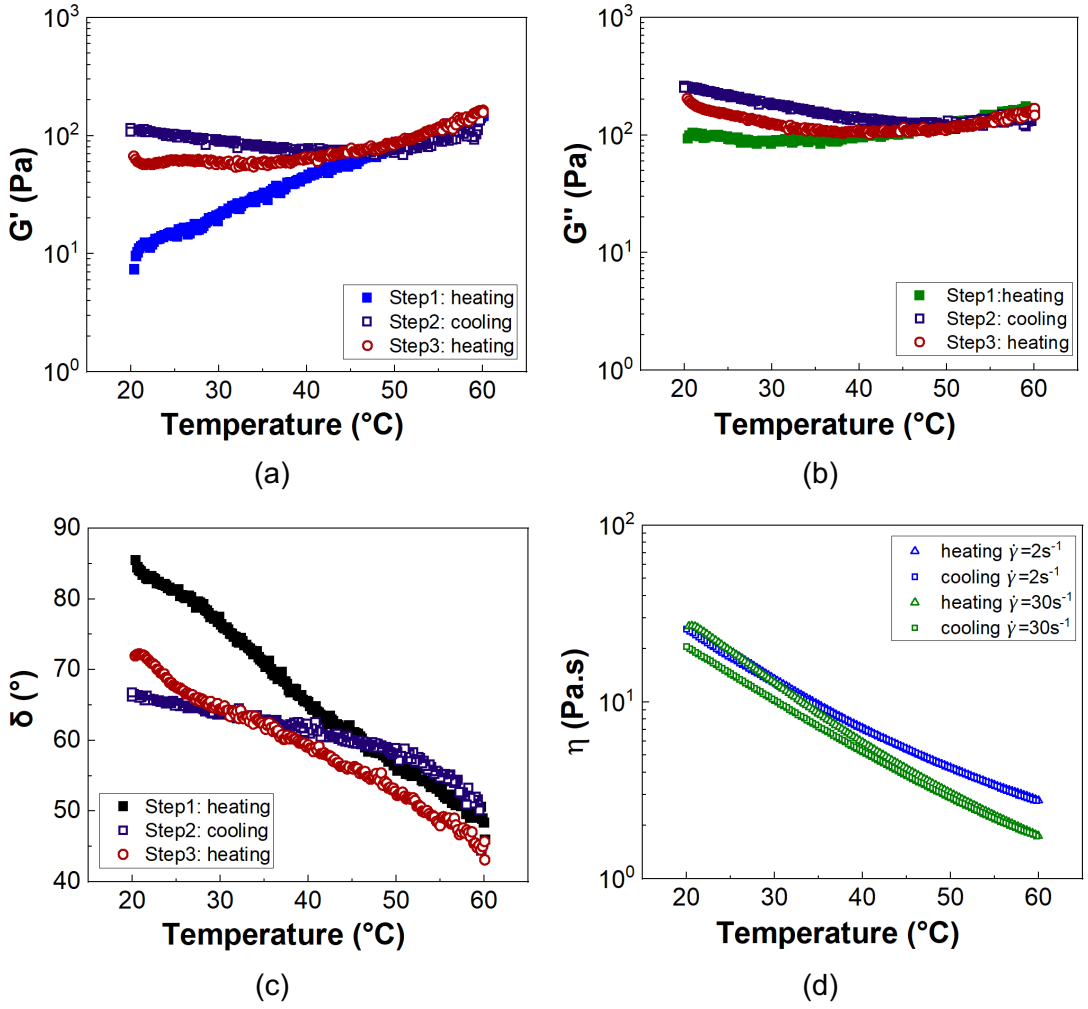

Figure I.5: a) Storage modulus (G'); b) loss modulus (G'') and c) phase angle (δ) of a 50% v/v glass sphere suspension in glycerol as a function of temperature under successive heating and cooling steps. The measurements were acquired under oscillatory shear mode at $\gamma = 0.2\%$ and $f = 1Hz$ with a resting period of 3 mins; d) Steady state viscosity (η) as a function of temperature for the same suspension at two different shear rates ($\dot{\gamma}$) under successive heating and cooling steps.

Indicative temperature sweeps at two different shear rates ($\dot{\gamma} = 2\ s^{-1}$ and $\dot{\gamma} = 30\ s^{-1}$) under steady state shear (Figure I.5d) show that the viscosity values decrease with increasing temperature in all cases, while different hysteretic phenomena depending on the shear rate are observed; no hysteresis between heating and cooling is observed at the low $\dot{\gamma}$, whereas at $\dot{\gamma} = 30\ s^{-1}$ lower viscosities are obtained during the cooling step and for $\theta \leq 40°C$. This behaviour can be described on the basis of the suspension rheology shown in Figure I.3a; at $\dot{\gamma} = 2\ s^{-1}$ the suspension is in the intermediate Newtonian plateau and therefore no microstructure changes are expected. On the other hand, at $\dot{\gamma} = 30\ s^{-1}$ the suspension shows weak shear thickening, which diminishes with increasing the temperature (Figure I.3a). Thus, the lower viscosity values observed during the cooling step might imply an inability of the suspension to recover its shear thickening response following heating in the time frame of the experiment.

I.3.2 Abrasives, $\boldsymbol{\varphi = 0.30}$

Figure I.6 and Figure I.7 present the rheology of a 30% v/v abrasive silica suspension under steady state shear and dynamic oscillatory shear respectively. It can be seen (Figure I.6a) that the shear thinning response of the abrasive silicas diminishes with increasing the temperature from 20°C to 60°C. This is better illustrated in the variation of the flow index with temperature (Figure I.6b), obtained by Carreau fits to the data, as well as the variation of $\eta_{r,0}$ (Figure I.6c). The high frequency relative viscosity ($\eta'_{r,\infty}$) values are offset by the same amount from $\eta_{r,\infty}$ implying that particle dynamics are not significantly affected by the temperature variations.

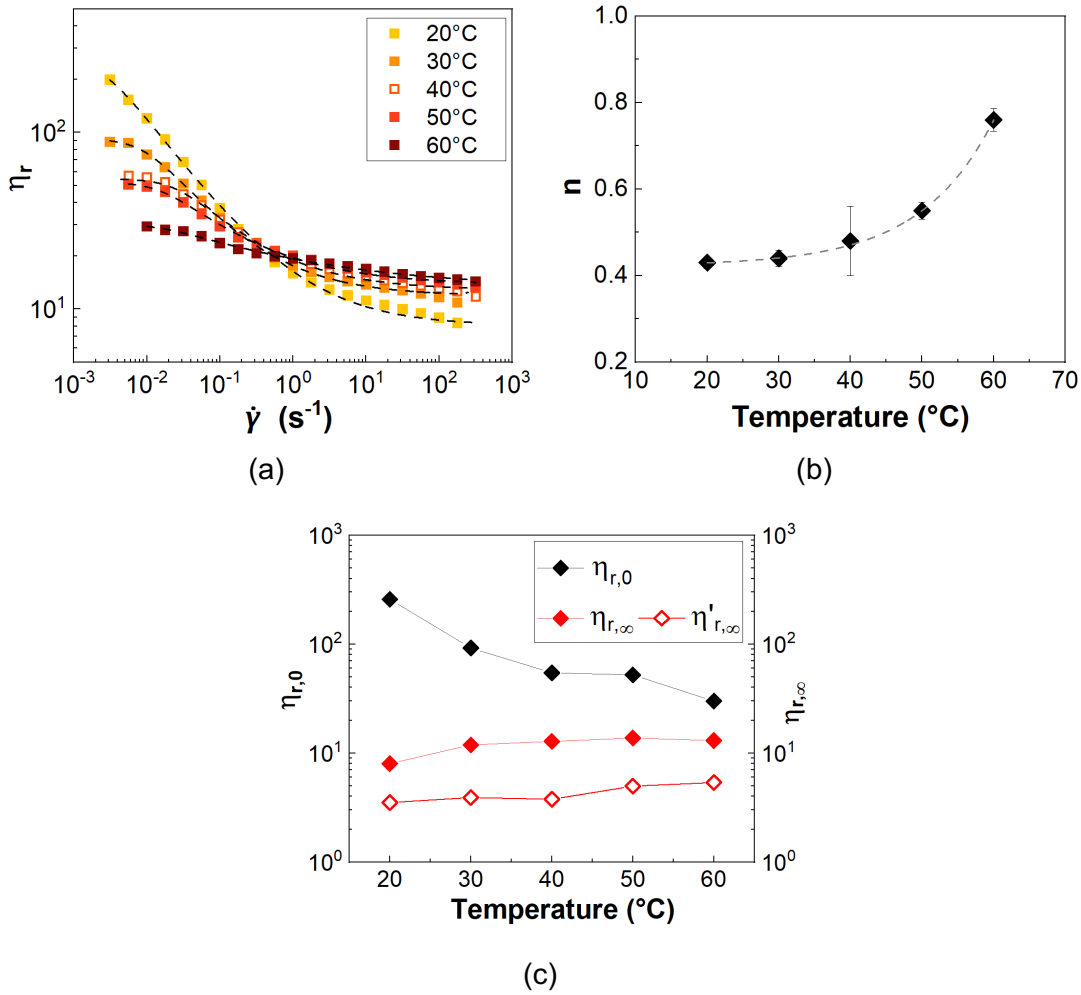

Figure I.6: a) Relative viscosity (η_r) as a function of shear rate ($\dot{\gamma}$) and temperature of the 30% v/v abrasive silica suspension in glycerol; Dashes lines correspond to the Carreau-Yasuda equation fitting at the shear thinning area; b) flow index (n), c) zero-shear ($\eta_{r,0}$), infinite-shear ($\eta_{r,\infty}$) relative viscosity and high-frequency relative viscosity ($\eta'_{r,\infty}$) as a function of temperature.

The viscoelastic moduli also decrease with increasing the temperature (Figure I.7a) similar to the glass sphere suspension. G' values show a slight variation with temperature and the phase angle (Figure I.7b) indicate a liquid like behaviour for $\theta \leq 50^oC$. The response of the abrasive silicas to increasing temperature is not consistent with that of the glass spheres. Unlike the glass spheres, the elasticity of the silica suspensions weakly increases at 60°C, while the shear thinning response is significantly suppressed with no evidence of apparent yield stress.

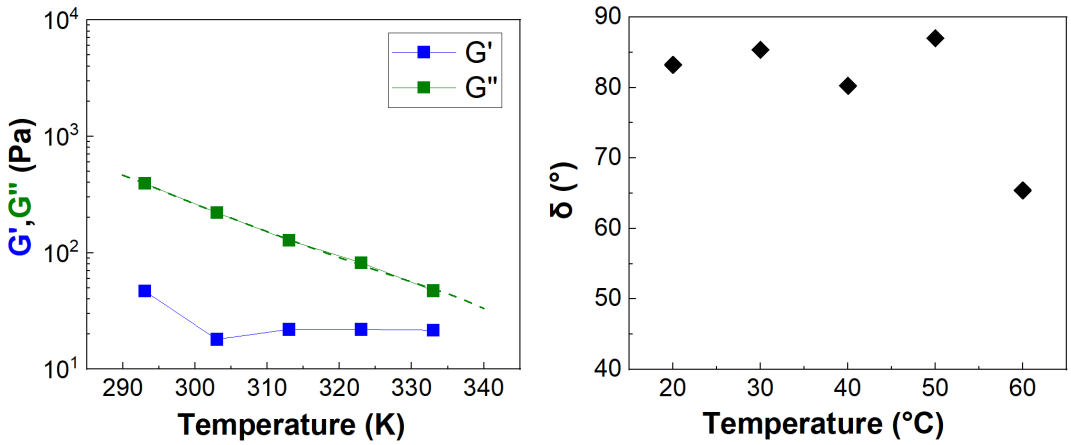

Figure I.7: a) Storage (G') and loss moduli (G'') as a function of temperature (in Kelvin-K to enable the Arrhenius fitting) and b) phase angle as a function of temperature generated from frequency sweeps in the LVR at $f = 10Hz$ for the 30% v/v abrasive silica suspension in glycerol.

It can be postulated that the particle surface roughness and porosity might compete with an increase in the Brownian effect due to the presence of submicron particles in the size distribution (5.7% at $\dot{\gamma} = 0.001\ s^{-1}$ being the ratio of particles in the colloidal regime in relation to the total number of particles in the suspension) in a different way that they do for the relatively smooth glass spheres. The abrasive silicas exhibit shear thinning behaviour at 20°C; attributed to frictional contacts; increasing the temperature and thus, the mobility of both the glycerol molecules and particles, leads to faster collisions, which might not allow sufficient time for the asperities to deform. Another factor that might be contributing to this rheological response is the porosity of the particles; as glycerol molecules become more mobile at higher temperatures, the possibility of them absorbing into the particle pores may decrease. Therefore, more solvent remains in suspension lubricating the particle surface but also decreasing the effective volume fractions of the solids in suspension.

I.3.3 Fillers, $\varphi = 0.15$

The filler suspensions at 15% v/v exhibit a similar shear thinning response to temperature changes as abrasive silicas (Figure I.8a). The weakening of the shear thinning behaviour with temperature is reflected in the flow indices rising towards unity (Newtonian behaviour) (Figure I.8b). Figure I.8c shows that the relative viscosities in both regions of the viscosity curve before the shear thickening area increase with temperature, while ${\eta'}_{r,\infty}$ values remain constant with temperature; the latter indicates

that the hydrodynamic contribution to the viscosity is not affected by temperature. Figure I.9a shows that both moduli decrease with temperature, with the G'' being more sensitive than G'. The phase angles (δ) (Figure I.9b) also remain independent of temperature at $\theta \leq 40^{o}C$, while their values decrease at higher temperatures.

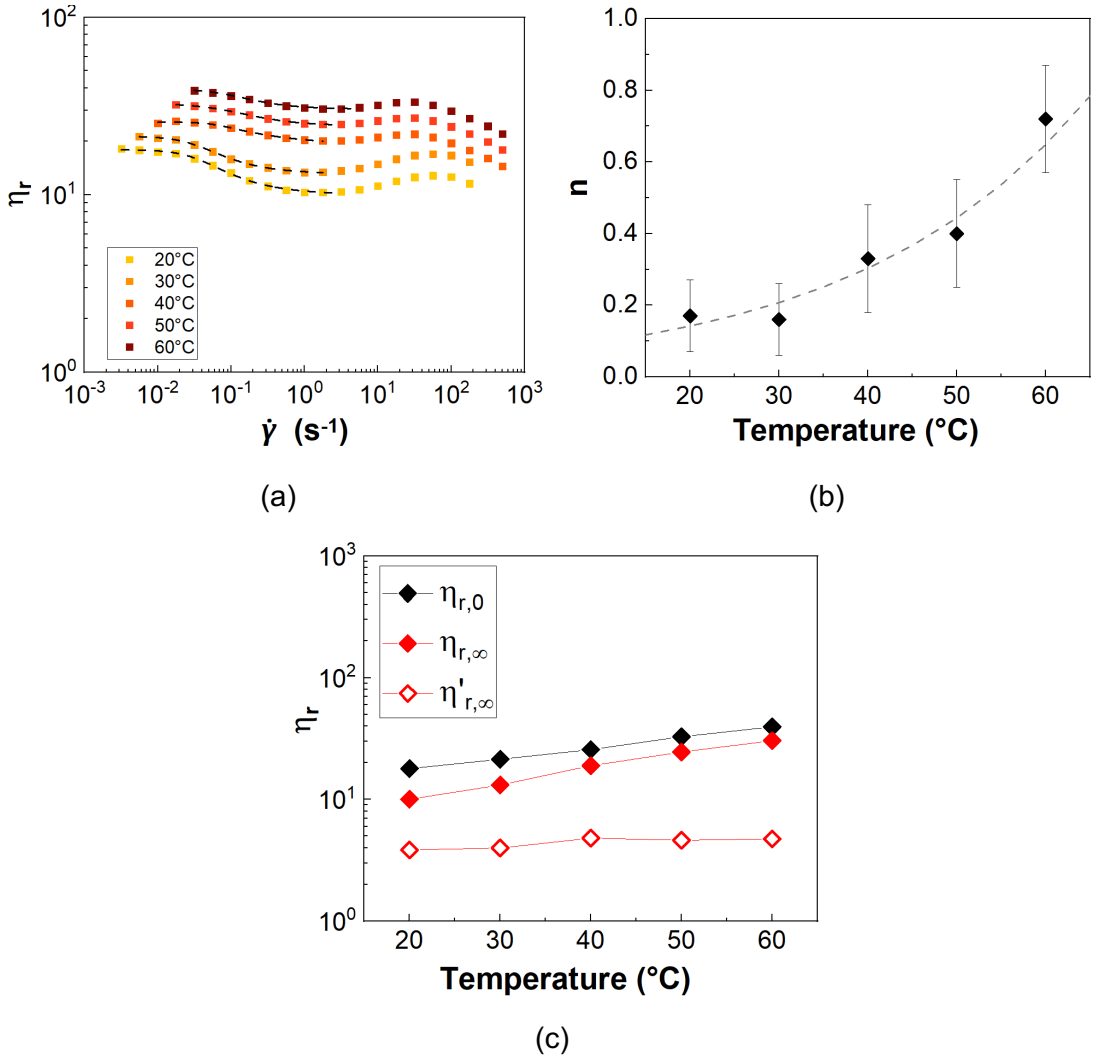

Figure I.8: a) Relative viscosity (η_r) as a function of shear rate ($\dot{\gamma}$) and temperature of the 15% v/v filler silica suspension in glycerol; Dashed lines correspond to the Carreau-Yasuda equation fitting at the shear thinning area; b) flow index (n), c) zero-shear ($\eta_{r,0}$), infinite-shear ($\eta_{r,\infty}$) relative viscosity and high-frequency relative viscosity ($\eta'_{r,\infty}$) as a function of temperature.

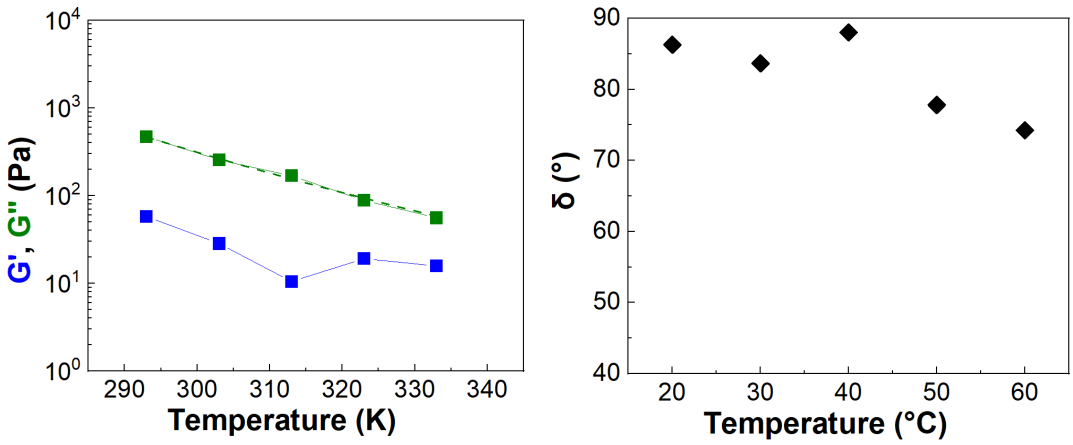

(a) (b)

Figure I.9: a) Storage (G') and loss moduli (G'') as a function of temperature (in Kelvin-K to enable the Arrhenius fitting) and b) phase angle as a function of temperature generated from frequency sweeps in the LVR at $f = 10Hz$ for the 15% v/v filler silica suspension in glycerol.

I.3.4 Arrhenius plot

The Arrhenius equation was also employed to evaluate the effect of temperature on suspension rheology. This is given by:

$$\eta_{\varphi,T}/\eta_{\varphi,T_r} = \exp\left(\frac{E_\varphi}{RT}\right) \quad \text{(I.1)}$$

where $\eta_{\varphi,T}$ is the viscosity of the suspension at a certain volume fraction (φ) and temperature (T), η_{φ,T_r} is the viscosity of the suspension at the same volume fraction (φ) and a reference temperature (T_r), E_φ is the activation energy of the suspension, R is the universal gas constant ($8.314\ J/(molK)$) and T is the temperature.

The calculations are performed using the two extreme regions in the viscosity curve, i.e. the zero shear rate ($\eta_{\dot{\gamma}=0}$) and the infinite shear rate ($\eta_{\dot{\gamma}=\infty}$) viscosity at a function of temperature and the loss modulus (G'') at the frequency of $f = 10\ Hz$. The data at 20°C are used as the reference and the corresponding viscosities and G'' are normalised accordingly. An exponential fit (eq. (I.1)) can be applied to the normalised values as a function of the inverse temperature in order to derive the activation energies of the suspensions under investigation; their values are summarised in Table I.1.

The data in Table I.1 show that the estimated activation energy for glycerol (E_0) is higher than the activation energies estimated using the suspension viscosity values $\eta_{\dot{\gamma}=0}$ and $\eta_{\dot{\gamma}=\infty}$. The latter implies that the viscosity of the suspensions is less susceptible to temperature variations compared to the sensitivity of the pure

suspending medium. This behaviour generally, arises from a reduction in the free volume available for molecular motion when solids are present in the solvent (Shenoy, 1999). Good agreement is also observed between the E_φ values estimated using the $\eta_{\dot{\gamma}=\infty}$ and the G''. The small deviations in the estimates of the activation energy from the two variables might be related to the different experimental conditions applied, i.e. steady state shear versus dynamic oscillatory shear. In contrast, using the zero shear viscosity values leads to a more complex behaviour. The estimated E_φ is lower than the E_0 for the glass sphere and the filler silica suspensions, while it is remarkably higher for the abrasive silica suspension. This can be attributed to several factors such as particle surface morphology, the volume fraction or crowding effects, which are more likely to influence suspension rheology at the low shear rate limit rather than the infinite shear.

Table I.1: Activation energy values estimated for the zero shear rate ($\eta_{\dot{\gamma}=0}$) and infinite shear rate ($\eta_{\dot{\gamma}=\infty}$) viscosities as well as the loss modulus (G'').

Particle type & φ	Activation energy (kJ/mol), E_φ		
	$\eta_{\dot{\gamma}=0}$	$\eta_{\dot{\gamma}=\infty}$	G'' $(f = 10\ Hz)$
Glycerol ($\varphi = 0$)	56.5		-
Glass spheres ($\varphi = 0.50$)	23.0	45.1	30.2±4.1
Abrasive silica ($\varphi = 0.30$)	82.3	49.1	42.3±0.6
Filler silica ($\varphi = 0.15$)	40.3	33.4	42.2±1.8

Appendix II

Suspensions in the Xanthan gum/glycerol solutions

Two different Xanthan gum solutions were used in the present study with constant Xanthan gum concentration (0.1% w/v) but varying the glycerol/water content of the solvent, i.e. 100% glycerol and 10% v/v distilled water and 90% v/v of glycerol. The water was added to facilitate the dissolution of the Xanthan gum powder in the solvent. A comparison between the rheology of the suspensions in the shear thinning fluids with the properties of the corresponding suspensions in the Newtonian aqueous and non-aqueous fluids will be presented in parallel.

This appendix will focus on the rheology of the suspensions using the two Xanthan gum solutions in pure glycerol. The particle volume fraction will be restricted at the highly concentrated regime, and more specifically, at the onset of non-Newtonian rheology as observed for the suspensions in glycerol. The particle volume fractions correspond to $\varphi = 0.50$ for the glass spheres, $\varphi = 0.30$ for the abrasive silicas and $\varphi = 0.10$ for the filler silicas.

II.1 Steady state shear rheology

Figure II.1 depicts the absolute viscosity values under steady state of the two xanthan gum solutions and the corresponding suspensions at the onset of non-Newtonian behaviour as observed in the glycerol case, i.e. glass spheres $\varphi = 0.50$, abrasive silicas $\varphi = 0.30$, filler silicas $\varphi = 0.10$, as a function of shear rate. It can be seen that the addition of xanthan gum (Figure II.1a) increases significantly, i.e. by one order of magnitude, the viscosity of glycerol at low shear while it has little effect at the high shear limit (Ki-Won Song et al., 2006). The second batch of the Xanthan gum solution (blue points) showed slightly lower viscosity values and weaker shear thinning response compared to the first batch (magenta circles). The latter might imply a poorer dissolution of the Xanthan gum powder in glycerol or a higher degree of moisture absorption during sample preparation. The sample preparation was also different with the second batch requiring a lower mixing time and lower temperatures for the Xanthan gum powder to be dissolved.

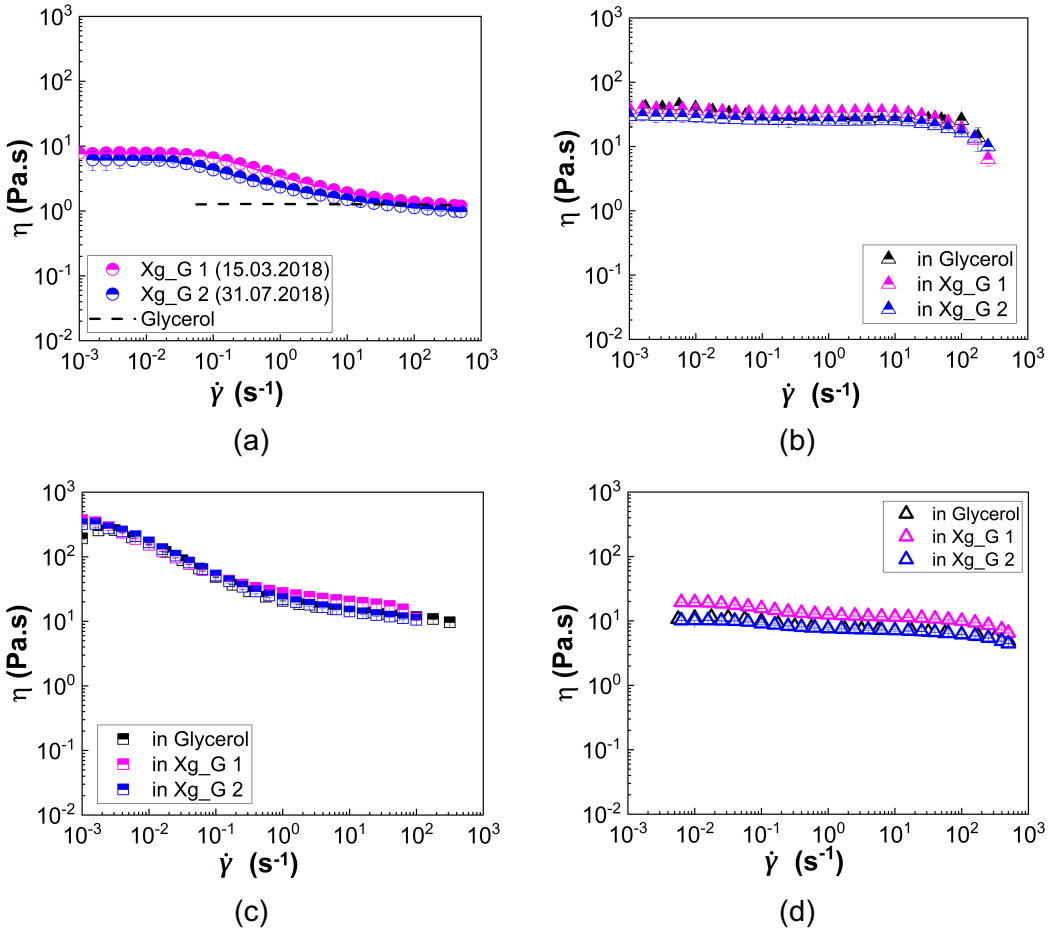

Figure II.1: Steady state viscosity (η) as a function of shear rate ($\dot{\gamma}$) of indicative suspensions in the two different batches of the 0.1% w/v Xanthan gum in glycerol solution at 20°C; a) Xanthan gum solutions; b) 50% v/v glass spheres; c) 30% v/v abrasive silicas & d) 10% v/v filler silicas. The data of the same suspensions in glycerol are included for comparison.

Figure II.1b, c and d show the absolute viscosity (η) values of the three types of particle suspensions in the two Xanthan gum solutions as a function of shear rate ($\dot{\gamma}$). It can be clearly seen that the addition of particles increases the viscosity of the Xanthan gum solvent in all cases, while it also alters their shear thinning response in different ways. The abrasive silicas (Figure II.1c) induce the higher increase in both the low and high shear rate viscosity of the suspending media as well as stronger shear thinning response. In contrast, a lower increase in the viscosity values is observed for the glass sphere (Figure II.1b) and filler silica suspensions (Figure II.1d) followed by a suppression in the shear thinning response of the Xanthan gum solution. The difference in the particle volume fraction (and effective volume fraction) also influences the response of the suspensions in the various solvents.

Interestingly, the suspensions in the two Xanthan gum solutions exhibit similar trends and almost identical viscosities with these of the suspensions in the Newtonian glycerol. This is surprising taking into account that Xanthan gum can bind on silica

surface through hydrogen bonding imparting pronounced yield stress and shear thinning rheology (Potanin, 2019). The observations from the present study seem to follow different polymer and particle dynamics. In the dense concentration regime, high shear and extensional stresses are likely to generate in the narrow interparticle gaps. Under these extreme conditions, the long Xanthan gum chains are prone to detach from the silica surface (Bossis et al., 2017; Ma et al., 2017), leaving the particles polymer free and thus, interparticle and particle-glycerol interactions are expected to dominate suspension rheology.

To mimic industrial environment, the rheology of all suspensions was also studied at 60°C. The absolute viscosity values of the two Xanthan gum solutions as well as the three types of particle suspensions at the onset of non-Newtonian response are presented in Figure II.2. The corresponding suspensions in glycerol are included for comparison.

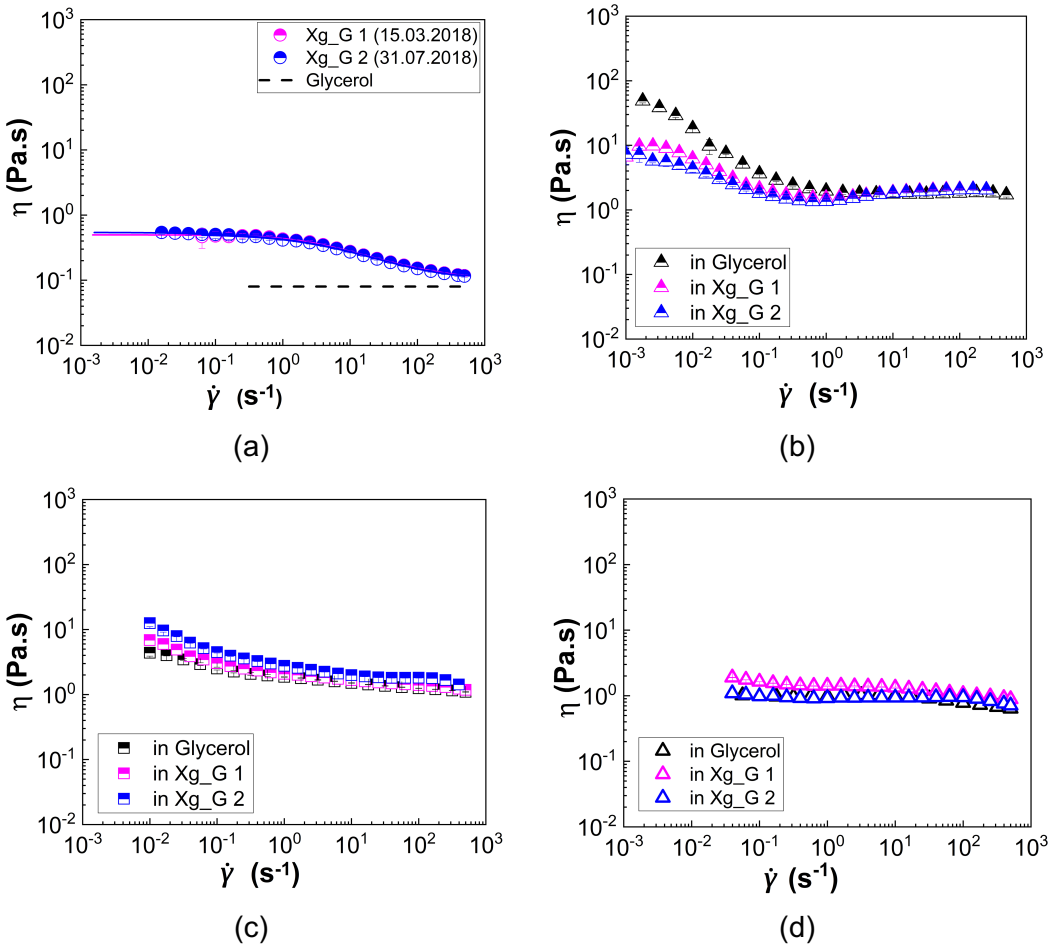

Figure II.2: Steady state viscosity (η) as a function of shear rate ($\dot{\gamma}$) of indicative suspensions in the two different batches of the 0.1% w/v Xanthan gum in glycerol solution at 60°C; a) Xanthan gum solutions; b) 50% v/v glass spheres; c) 30% v/v abrasive silicas & d) 10% v/v filler silicas. Comparisons with the corresponding suspensions in glycerol are also provided.

Although the two Xanthan gum solutions showed small differences in the viscosity values and the shear thinning degree at 20°C, these seem to eliminate at 60°C as the viscosity curves of the two solvents perfectly overlap (Figure II.2a). Experimental evidence in literature suggests that the Xanthan gum molecules undergo a structural conformation change, i.e. a transition from a helical structure to a random coil, at temperatures around 50°C to 60°C (Rochefort and Middleman, 1987). The shearing history and heating effects induced to the Xanthan gum molecules upon preparation seem to eliminate at 60°C as the polymer chains undertake a similar uncoiled structure in both solvents, while the concentration of Xanthan is kept constant. In parallel, the viscosity values significantly decrease by one order of magnitude with temperature following the trend of the base fluid (glycerol), while the shear thinning degree also reduces compared to 20°C (Figure II.1a) due to the order-disorder transition of the polymer network.

Increasing the temperature to 60°C induces shear thinning and yield stress behaviour to the glass sphere suspension in both Xanthan gum solutions (Figure II.2b). Although this behaviour is similar to the corresponding suspensions in pure glycerol, the addition of Xanthan gum seems to weakly reduces the viscosity of the suspension at low shear. Interparticle interactions enabled through the loss of strength in the solvation layer were responsible for the obtained rheological response of the suspension in pure glycerol at the elevated temperature. These dynamics seem to govern the rheology of the suspensions in the shear thinning fluids as well. However, the lower viscosity values at low shear might imply the ability of the long uncoiled Xanthan gum chains to thicken the solvation layer and partially regain its efficiency in preventing direct particle contacts. On the other hand, the rheology of the abrasive (Figure II.2c) and filler silica (Figure II.2d) suspensions is not significantly altered by increasing the temperature to 60°C. In these systems interparticle interactions are prominent and thus, the presence of a low concentration of Xanthan gum only slightly increases suspension viscosity, while having a negligible effect to particle dynamics.

The change in rheology of the suspensions in the Xanthan gum solutions upon heating are better reflected in Figure II.3, which illustrates the relative viscosity values (η_r) of all suspensions as a function of shear rate ($\dot{\gamma}$) at 20°C and 60°C. The infinite shear rate viscosity of the shear thinning fluids as obtained from the Carreau fittings was used to estimate the η_r of the suspensions to facilitate the comparison with the corresponding suspensions in glycerol; these are also included as black points in the figures.

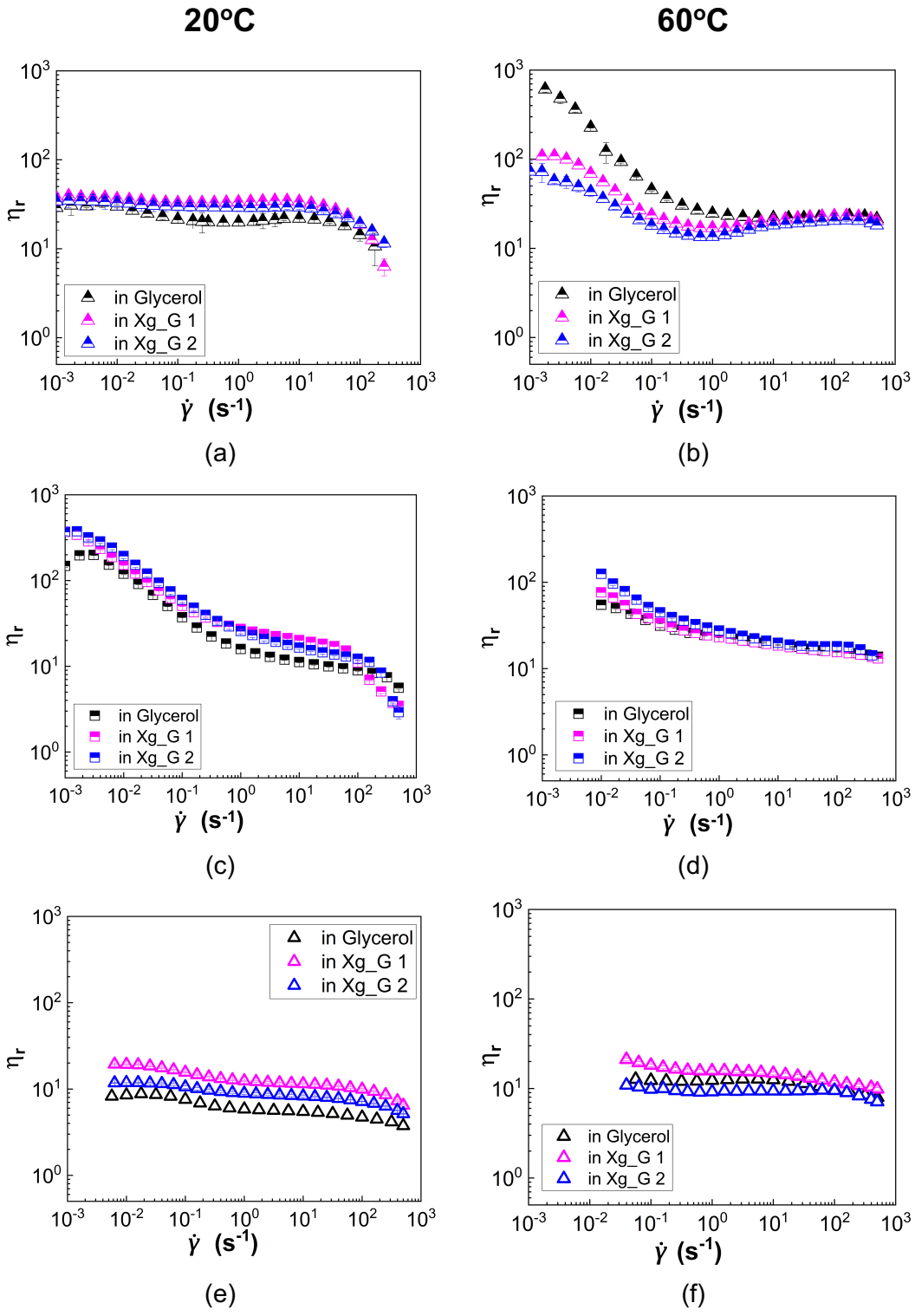

Figure II.3: Relative viscosity (η_r) as a function of shear rate ($\dot{\gamma}$) of indicative suspensions in the two different batches of the 0.1% w/v Xanthan gum in glycerol solution at 20°C (left column) 60°C (right column); a) and b) 50% v/v glass spheres; c) and d) 30% v/v abrasive silicas; e) and f) 10% v/v filler silicas. A comparison with the corresponding suspensions in glycerol are also provided. The relative viscosity of the suspensions in the shear thinning solvents is estimated using the infinite shear rate viscosity of the suspending medium as obtained from the Carreau fits.

The relative viscosity values increase in the presence of Xanthan gum for almost all suspensions at both temperatures (20°C and 60°C) compared to the corresponding suspensions in pure glycerol. This is understandable as the presence of polymer chains induces extra stresses in the suspension in addition to these induced by the particles leading to an overall increase in suspension viscosity. This phenomenon should be more pronounced in the case of the porous abrasive and filler silicas as the pores absorb part of the solvent leading to an increase in the effective volume fraction of both the polymers and the particles. An exception is the glass sphere suspensions at 60°C where the polymer chains are likely to strengthen the solvation layer acting as a barrier to particle attraction as discussed above. The weak shear thinning response of the glass spheres in glycerol at 20°C (Figure II.3a) seems to eliminate with the addition of Xanthan gum. In contrast, the presence of polymer molecules does not significantly influence the shear thinning nature of the abrasive (Figure II.3c) and filler silica (Figure II.3e) suspensions compared to their response in the simple Newtonian solvent.

Although increasing the temperature favors the shear thinning response of the glass sphere suspensions in the Xanthan gum solutions (Figure II.3b), the opposite trend is observed for the abrasive (Figure II.3d) and filler silica (Figure II.3f) suspensions. These suspensions already experience frictional contacts at 20°C through their surface roughness inducing shear thinning rheological behaviour. At 60°C, faster collisions and a reduction in the contact time and thus, the magnitude of frictional contacts between the particles are likely to occur due to the extra energy offered to the system through heating. The reduced shear thinning of the Xanthan gum solvent at 60°C in addition to the decrease in particle contacts are speculated to be responsible for the overall suppression in suspension shear thinning at the elevated temperature.

II.2 Linear oscillatory shear rheology

Oscillatory frequency sweeps in the linear viscoelastic region ($\gamma = 0.1\%$) were also conducted for the selected suspensions in the two Xanthan gum solutions to evaluate the effect of solvent viscoelasticity to suspension rheology. Figure II.4a and b illustrate the viscoelastic moduli (storage, G', and loss modulus, G'') and the measured phase angles (δ) of the two shear thinning fluids at 20°C as a function of angular frequency (ω). The contribution of the solvent's viscosity, i.e. glycerol, has been also subtracted from the G'' values to isolate the contribution of the pure polymer to the base fluid.

It can be seen that the first batch exhibits higher values of both moduli and stronger viscoelastic behaviour, i.e. lower phase angles, compared to the second batch. This behaviour also agrees with the higher viscosity values and the slightly stronger shear thinning behaviour of this Xanthan gum solution under steady state. The relaxation time of the two Xanthan gum solutions can also be estimated from the critical angular frequency at the crossover point of the two moduli. The Xg_G 1 solution exhibits a lower relaxation time ($\lambda = 3.96\ s$) compared to Xg_G 2 ($\lambda = 9.96\ s$). The difference in the λ values can be attributed to the Xg_G 1 having a higher density but with smaller length of chains due to the more rigorous mixing applied during sample preparation. This can be responsible for both the increase in the viscosity and viscoelasticity of the solution as well.

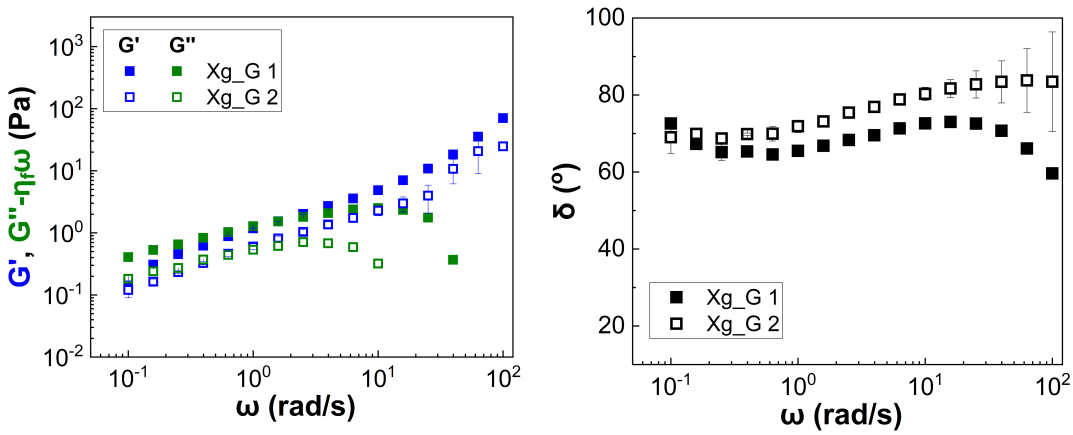

(a) (b)

Figure II.4: a) Viscoelastic moduli (storage, G' and loss, G'' modulus) of the two Xanthan gum solutions in glycerol as a function of angular frequency (ω) at 20°C. The effect of the solvent (glycerol) has been subtracted from the viscous component (G'') to evaluate the elastic relaxation times of the fluid; b) Corresponding phase angles as a function of angular frequency (ω).

The viscoelastic moduli (G', G'') of all suspensions in the Xanthan gum solutions are presented in Figure II.5 alongside the measured phase angles (δ) as a function of angular frequency (ω) at 20°C. The data of the corresponding suspensions are also presented for comparison.

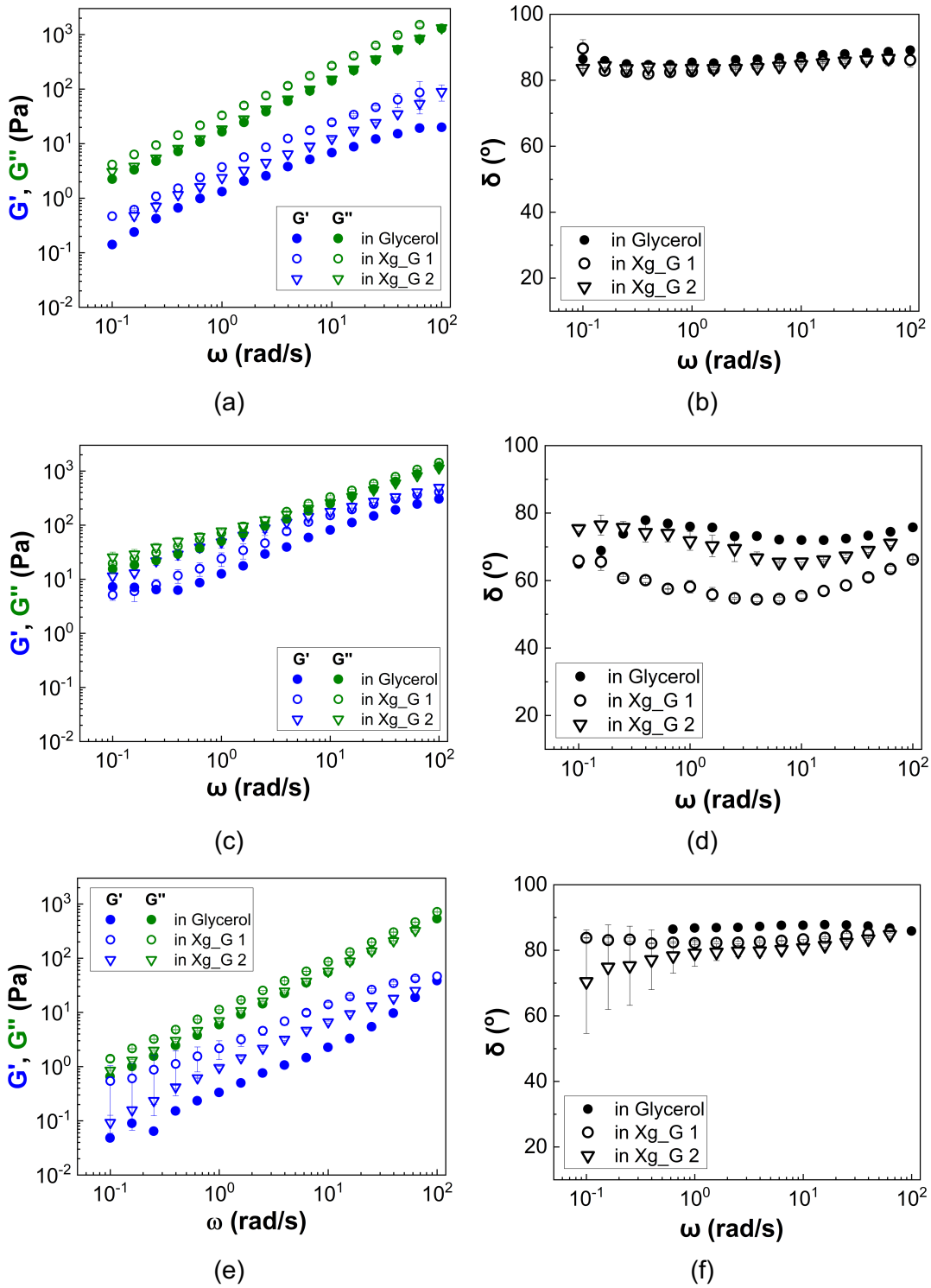

Figure II.5: Viscoelastic moduli (storage, G' and loss, G'' modulus) (left column) and phase angles (δ) (right column) of all suspensions in the Xanthan gum solutions as a function of angular frequency (ω) at 20°C. The corresponding data for the suspensions in pure glycerol are included for comparison. a) and b) 50% v/v glass spheres; c) and d) 30% v/v abrasive silicas; e) and f) 10% v/v filler silicas.

All suspensions in the Xanthan gum solutions exhibit viscous dominated response ($G' < G''$) and an almost linear increase with angular frequency, in agreement to the behaviour of the corresponding suspensions in glycerol. The addition of Xanthan gum to the suspensions also appears to increase both the G' and G'' values, compared to these obtained in the pure glycerol case. However, in the case of the glass spheres (Figure II.5a) the two moduli increase with the same rate as also evidenced by the values of the phase angles overlapping for the suspensions in the two Xanthan gum solutions but also with these of all suspension in pure glycerol (Figure II.5b). In contrast, the viscoelastic behaviour of the abrasive (Figure II.5c) and the filler silica (Figure II.5e) suspensions weakly increases in the presence of Xanthan gum compared to that obtained for the suspensions in the Newtonian solvent; this increase in viscoelasticity is also reflected through a decrease in the measured phase angles (Figure II.5d and f respectively).

The particle porosity might be responsible for the increase in suspension viscoelastic response in the Xanthan gum solutions; in this case part of the solvent absorbs into the pores leading to an increase in the effective volume fraction of both the particles and the polymer in the suspension. In fact, the abrasive silicas exhibit lower δ values compared to the filler silica suspensions, which might be associated to the higher apparent particle volume fraction of the former ($\varphi = 0.30$) compared to the latter ($\varphi = 0.10$).

As for the measurements under state, the rheology of the suspending media and the selected particle suspensions under oscillatory frequency sweeps were also studied at 60°C. Figure II.6 illustrates the viscoelastic moduli (Figure II.6a) and the phase angles (Figure II.6b) of the two Xanthan gum solutions as a function of ω at 60°C. The G' and G'' values decrease with temperature, while the crossover point between the two moduli (Figure II.6a) appears at higher ω values compared to 20°C (Figure II.4a) for both Xg_G 1 and Xg_G 2 solutions indicating shorter relaxation times. This agrees with the order-disorder transition of the long polymer chains at high temperature conditions. The phase angles of the Xanthan gum solutions at 60°C increase at $\omega \leq 1\, rad/sec$, while their values weakly decrease at higher angular frequencies compared to 20°C, especially for the Xg_G 1 solvent (Figure II.6b).

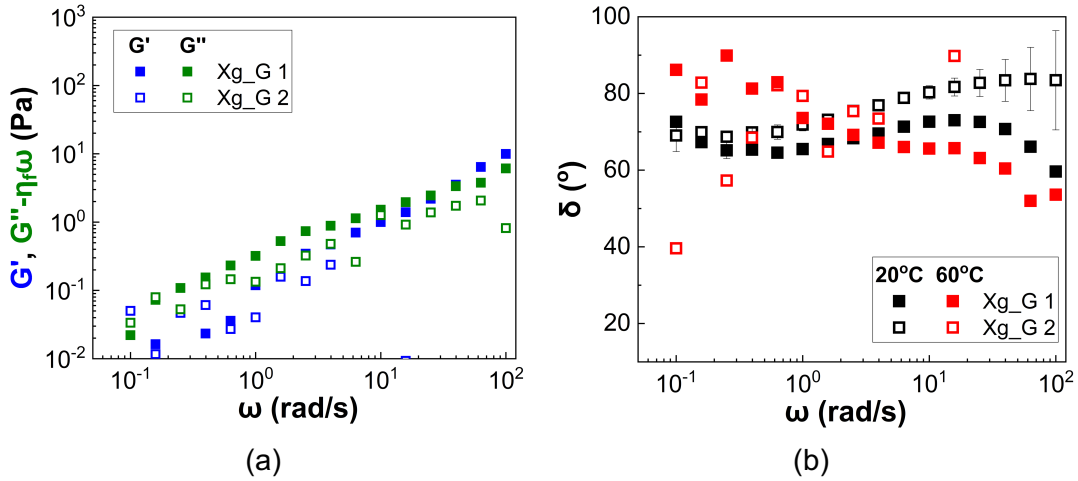

Figure II.6: a) Viscoelastic moduli (storage, G' and loss, G'' modulus) of the two Xanthan gum solutions in glycerol as a function of angular frequency (ω) at 60°C. The effect of the solvent (glycerol) has been subtracted from the viscous component (G'') to evaluate the elastic relaxation times of the fluid; b) Corresponding phase angles as a function of angular frequency (ω). The phase angles estimated at 20°C are also included.

Viscous dominated response is mainly observed for all suspensions in the Xanthan gum solution at 60°C as shown in Figure II.7a, c and e. The addition of Xanthan gum decreases the G' and G'' values (Figure II.7a) of the glass sphere suspensions followed by a subsequent decrease of the relative viscoelasticity, as described through the higher δ values (Figure II.7b) compared to the glycerol case; this contradicts the observations for the same suspensions at 20°C. The interparticle contacts enabled due to the disruption of the solvation layer of pure glycerol are likely to be hindered in the presence of Xanthan gum leading to a suppression of suspension viscoelasticity. In contrast, the relative viscoelasticity of the abrasive silica suspensions at 60°C (Figure II.7c) weakly increases in the presence of Xanthan gum, i.e. the δ values decrease (Figure II.7d) in agreement to 20°C. The viscoelastic properties of the filler silica suspensions in the Xanthan gum solutions at $\varphi = 0.10$ do not seem to be significantly affected by heating. Both moduli decrease with temperature (Figure II.7e) while the measured phase angles at 60°C (Figure II.7f) remain identical to these obtained at 20°C especially at angular frequencies $\omega \leq 10\, rad/s$. A slight decrease in δ is only observed at higher ω values; this might be related to changes in the polymer and particle dynamics/microstructure in the high frequency regime (high deformation rates).

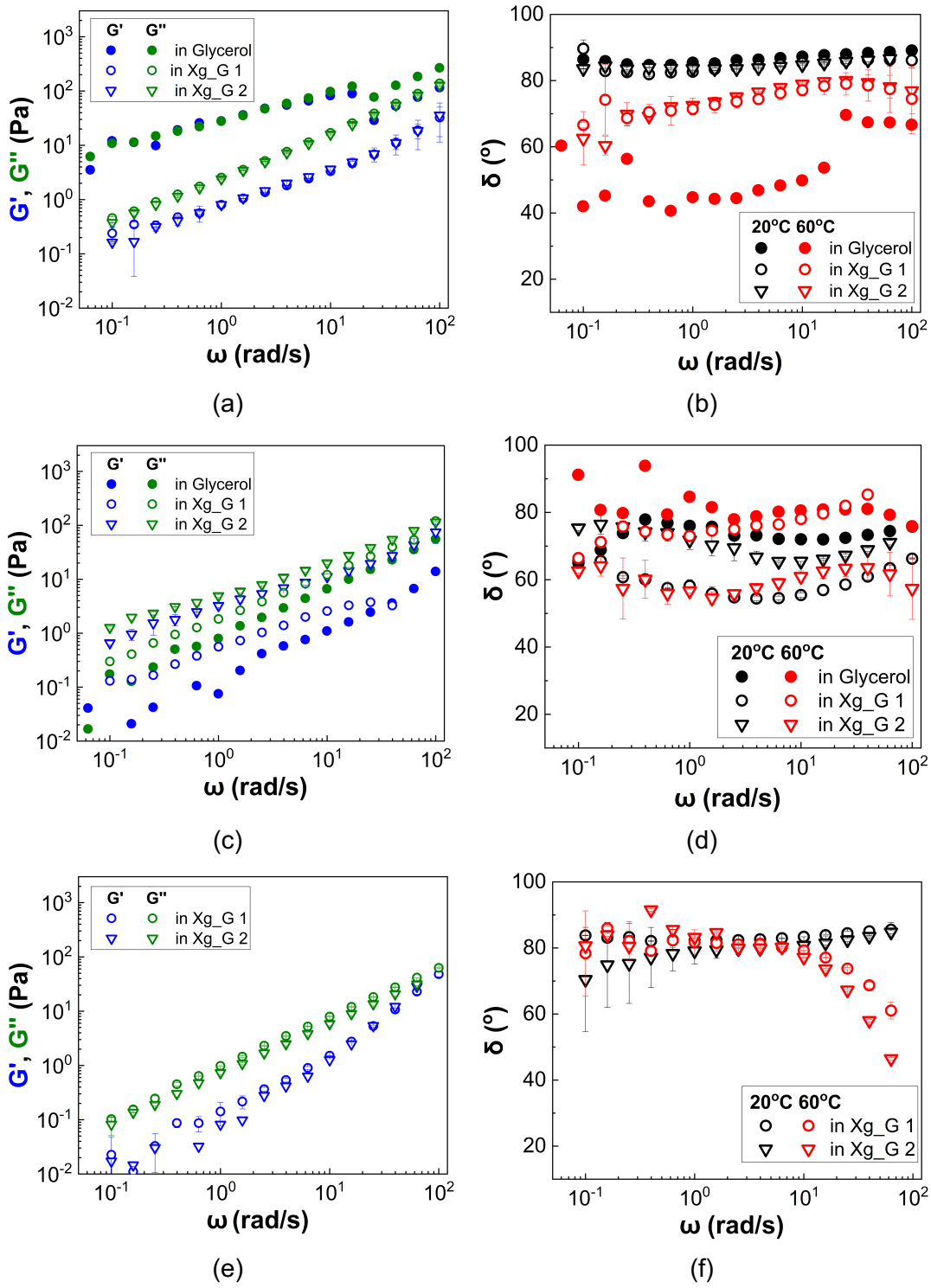

Figure II.7: a) Viscoelastic moduli (storage, G' and loss, G'' modulus) of the 50% v/v glass sphere suspensions in the two Xanthan gum solutions as a function of angular frequency (ω) at 60°C; b) Corresponding phase angles as a function of angular frequency (ω). Comparison with the suspensions in pure glycerol are also included. The phase angles estimated at 20°C are also included.

II.3 Large Amplitude oscillatory shear (LAOS)

Large amplitude oscillatory shear measurements (LAOS) were conducted to evaluate changes in the microstructure of the suspensions in the presence of Xanthan gum. Since the particle volume fraction for all suspensions is in the dense regime direct visualization of suspension microstructure cannot be obtained due to sample opacity limitations. The results obtained at 20°C using the second batch of the Xanthan gum solution for the three suspensions, i.e. 50% v/v glass spheres, 30% v/v abrasive silicas and 10% v/v filler silicas, are summarized in Figure II.8a, b and c respectively along with the raw viscoelastic moduli of the corresponding suspensions in glycerol. All suspensions in the Xanthan gum solution exhibit viscous dominated response ($G' < G''$) in agreement to the suspensions in the pure glycerol.

An increase in the G' is observed for the suspensions in the Xanthan gum solution followed by a weak decrease of the viscous modulus, G'' for all suspensions in Figure II.8. The linear viscoelastic region also seems to extend to a slightly wider range of strain amplitudes (γ) in the shear thinning suspending medium compared to the suspensions in the pure glycerol. A weaker strain thinning of the elastic moduli is observed as well for the glass sphere and filler silicas in the presence of Xanthan gum. A more stable polymer/particle network is likely to be formed under these conditions, as the Xanthan gum chains either attach on the silica surface causing steric stabilisation or entrap the particles into certain positions restricting their motility upon shear.

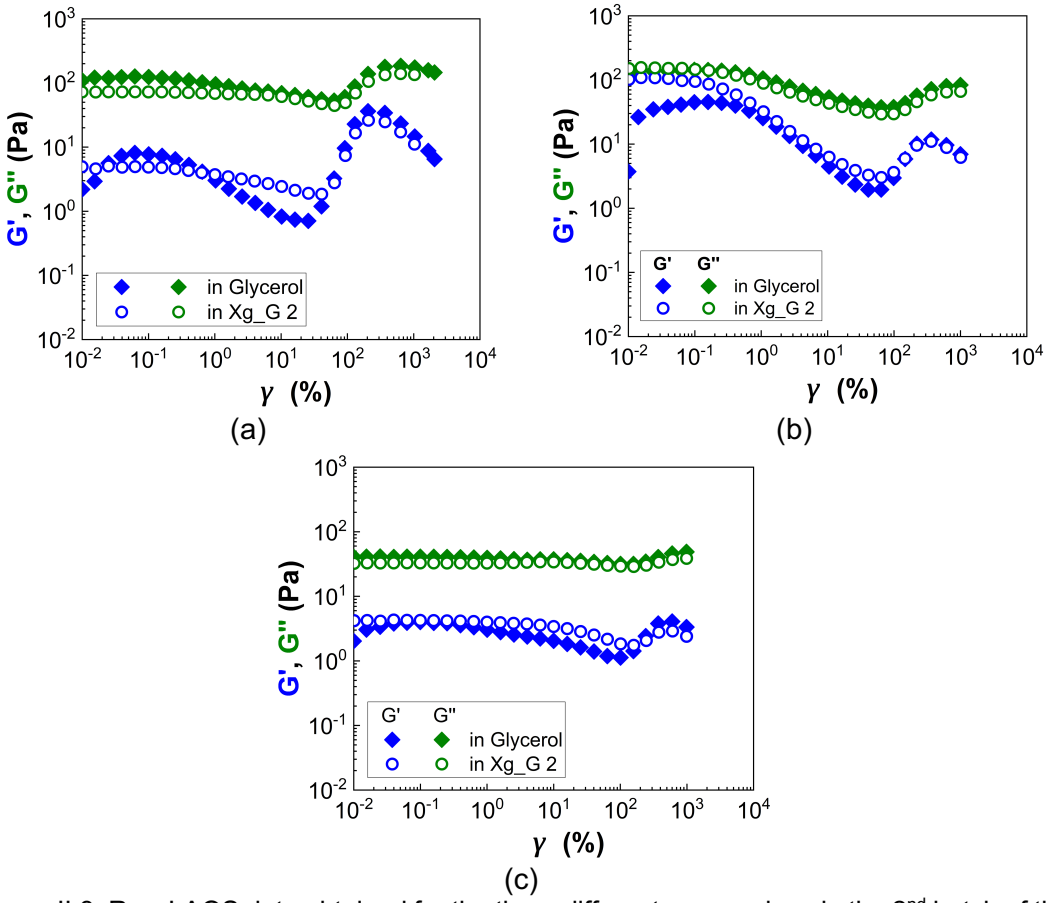

Figure II.8: Raw LAOS data obtained for the three different suspensions in the 2nd batch of the Xanthan gum solutions in glycerol at 20°C. The response of the corresponding suspensions in pure glycerol are also included for comparison. a) 50% v/v glass spheres; b) 30% v/v abrasive silicas & c) 10% v/v filler silicas.

The non-linear viscoelastic properties of the three suspensions under LAOS were obtained through the Fast Fourier Transform analysis of the raw stress signals. The estimated variables for all suspensions are summarized in Figure II.9. The non-linear elastic and viscous moduli of all cases follow the same trend as the moduli obtained for the 1st harmonic. The thickening ratio (T) of all suspensions depicted in Figure II.9g to i, do not show any apparent change between the suspension in pure glycerol and that in the Xanthan gum solution. This highlights the absence of any strain rate induced instabilities in the presence of Xanthan gum. In contrast, small deviations are observed for the stiffening ratio (S) values (Figure II.9g to i) between the suspensions in the Xanthan gum solution and these estimated for the suspensions in glycerol. The interactions between the particles and the Xanthan gum molecules might be responsible of enhancing the elastic nature of the suspensions, which weakly destabilizes under large applied deformations giving rise to strain induced non-linearities.

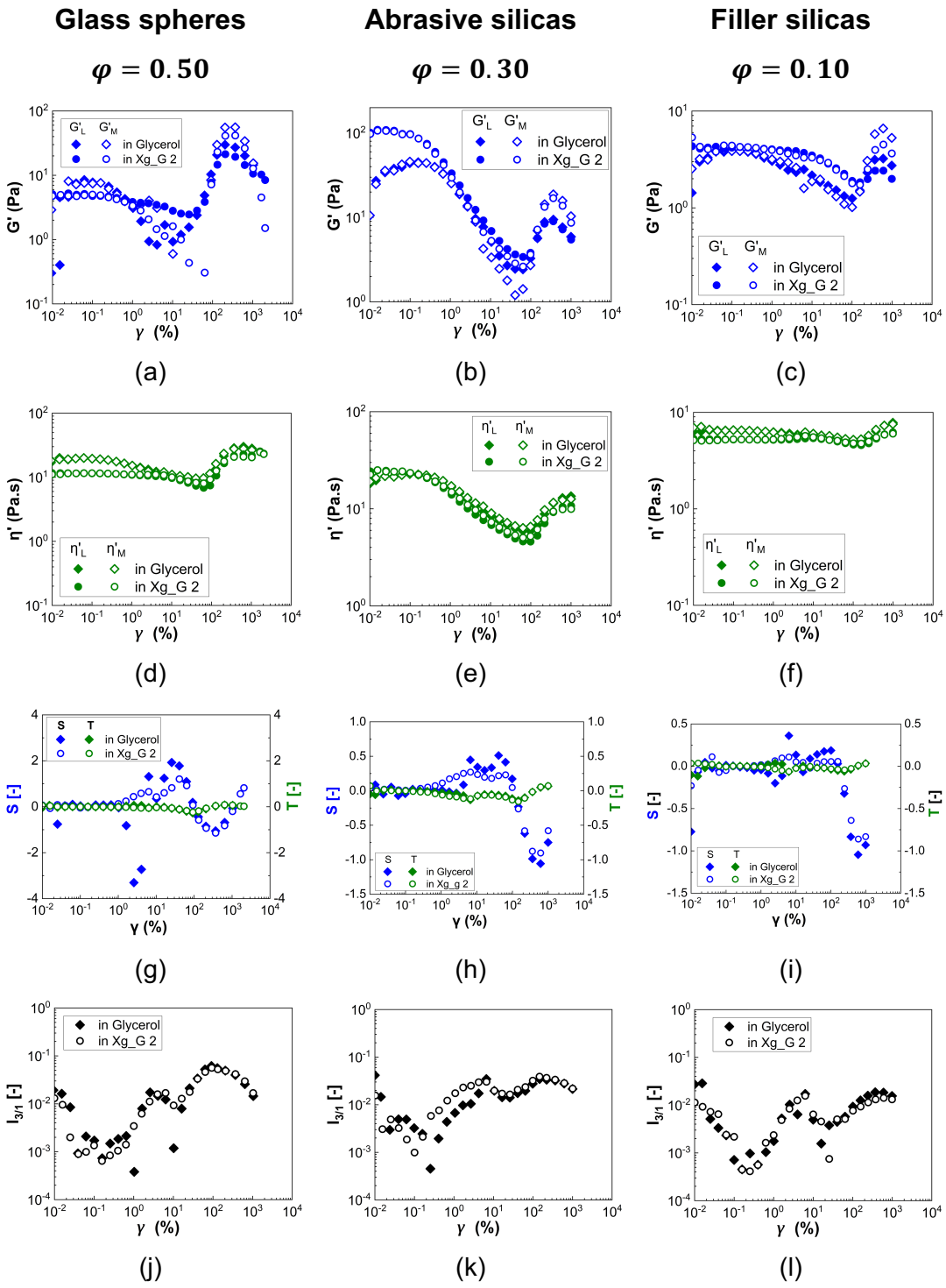

Figure II.9: Non-linear viscoelastic measures estimated from the elastic Lissajous curves as a function of % strain amplitude for the three suspensions in in the 2nd batch of the Xanthan solution in glycerol at 20°C and $f = 1Hz$. Dynamic minimum strain (G'_M) (hollow symbols) and large strain (G'_L) moduli (a, b, c), dynamic minimum strain rate viscosity (η_M) (hollow symbols) and large strain rate viscosity (η_L) (filled symbols) (d, e, f), stiffening ratio (S) and thickening ratio (T) (g, h, i), Fourier spectra (j, k, l) representing the intensity of the third harmonic relative to that of the first harmonic. The data of the suspensions in pure glycerol are also included for comparison.